NEUTRINO IN PHYSICS AND ASTROPHYSICS
(supplement)

COSMIC RAYS

A brief overview related to the sections "Atmospheric neutrinos" & "Astrophysical neutrinos"

V. Naumov

JINR, Fall Term 2023

v.02.11.2023

Victor Franz Hess, center, departing from Vienna about 1911

What are Cosmic Rays?

Cosmic Rays (CR) are high-energy particles of extraterrestrial origin

The astrophysical field of activity for particle and nuclear physics

"Classical" **CR** are nuclei or ionized atoms ranging from a single proton up to an iron nucleus and beyond, but being mostly **protons** (~90%) and α **particles** (~9%).

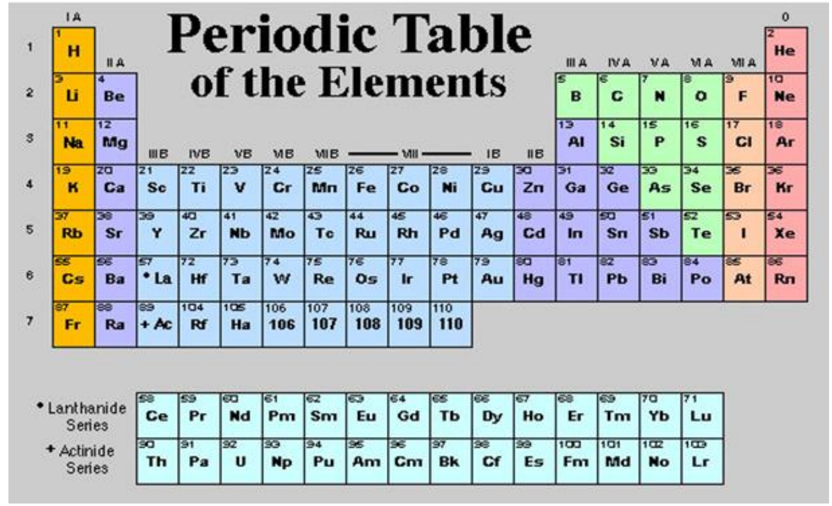

However the above "definition" is much wider and includes in fact all stable and quasistable (longlived) ultrarelativistic particles:

- **antiprotons & (maybe) antinuclei**
- **neutrons (e.g., from the Sun)**
- **hard gamma rays ($\lambda < 10^{-12}$ cm)**
- **electrons & positrons**
- **neutrinos & antineutrinos**
- **esoteric entities** (strangelets, relativistic WIMPs, magnetic monopoles, relic mini black holes, microscopic black holes & messengers of extra dimesions, mirror particles, ... whatever you want)

Secondary CR (produced by the primaries in the Earth's atmosphere) consist of essentially all elementary particles and nuclei (both stable and unstable). The most important are

nucleons, stable nuclei & radionuclides,
(hard) gamma rays,
mesons ($\pi^{\pm}, \pi^0, K^{\pm}, \ldots, D^{\pm}, \ldots$),
charged leptons ($e^{\pm}$, $\mu^{\pm}$, $\tau^{\pm}$),
neutrinos & antineutrinos (ν_e, ν_μ, ν_τ),
exotics.

Discovery of elementary particles

Particle	Year	Discoverer (Nobel Prize)	Method	
e^-	1897	Thomson (1906)	Discharges in gases	
p	1919	Rutherford	Natural radioactivity	
n	1932	Chadwik (1935)	Natural radioactivity	
e^+	1933	Anderson (1936)	Cosmic Rays	★
$\mu^\pm$	1937	Neddermeyer, Anderson	Cosmic Rays	★
$\pi^\pm$	1947	Powell (1950) , Occhialini	Cosmic Rays	★
$K^\pm$	1949	Powell (1950)	Cosmic Rays	★
π^0	1949	Bjorklund	Accelerator	
K^0	1951	Armenteros	Cosmic Rays	★
Λ^0	1951	Armenteros	Cosmic Rays	★
Δ	1932	Anderson	Cosmic Rays	★
Ξ^-	1932	Armenteros	Cosmic Rays	★
$\Sigma^\pm$	1953	Bonetti	Cosmic Rays	★
p^-	1955	Chamberlain, Segre' (1959)	Accelerators	
anything else	1955 $\Longrightarrow$ today	various groups	Accelerators	
$m_\nu \neq 0$	2000	KAMIOKANDE	Cosmic rays	★

Cosmic rays can be of either galactic (including solar) or extragalactic origin.

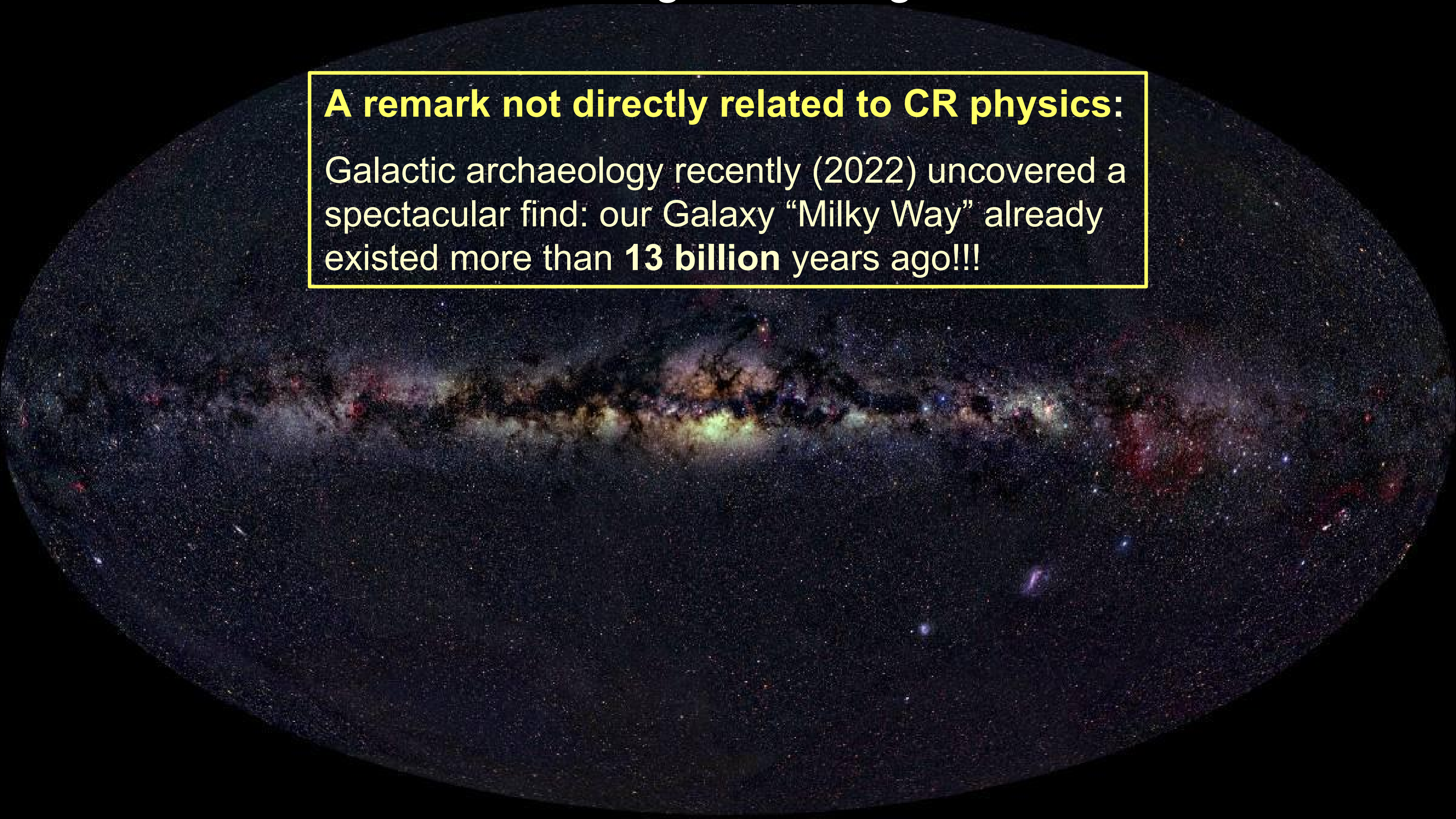

A remark not directly related to CR physics:

Galactic archaeology recently (2022) uncovered a spectacular find: our Galaxy “Milky Way” already existed more than **13 billion** years ago!!!

The deep sky © 2000, Axel Mellinger

Sketch of the Galaxy

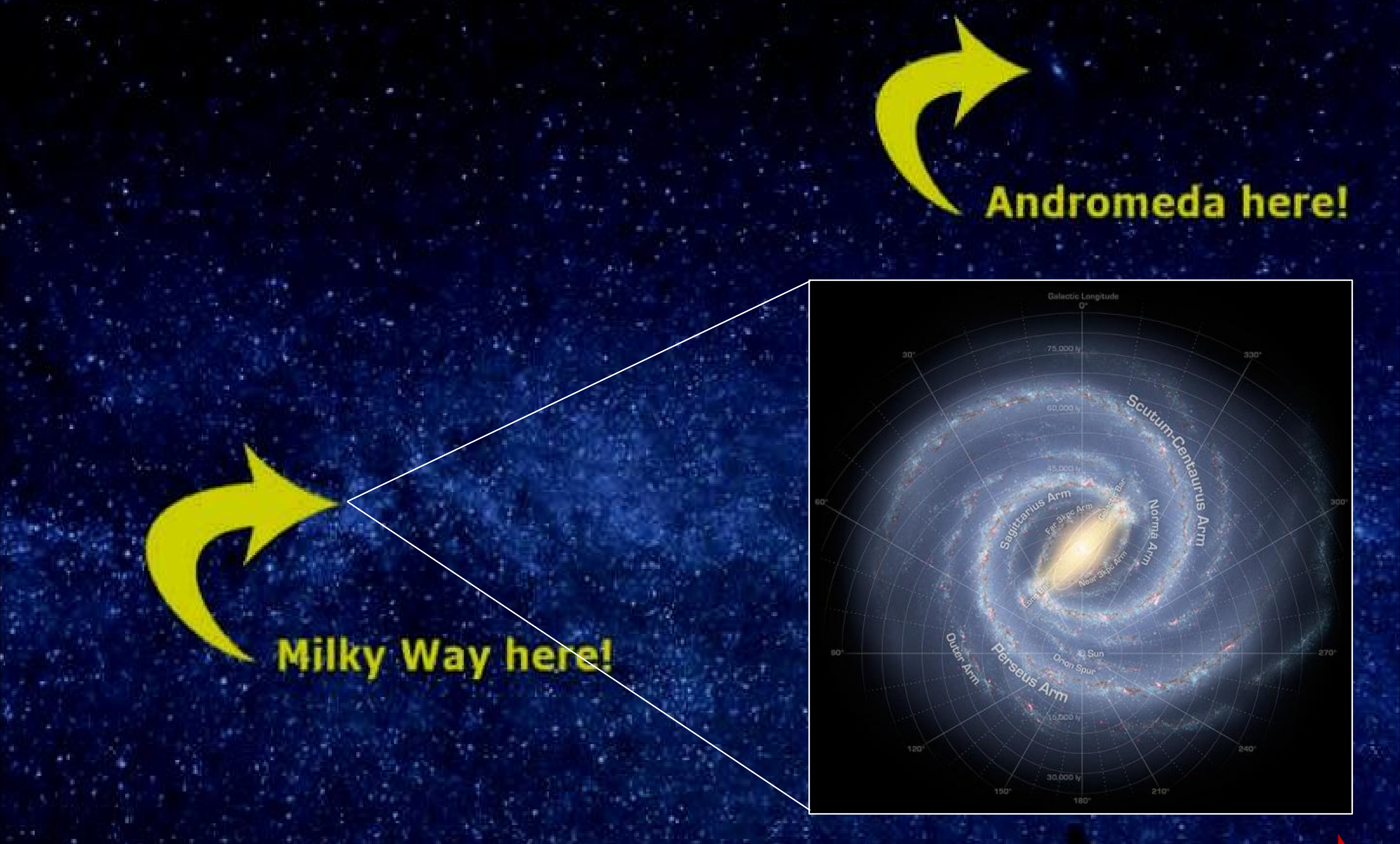

Note for pdf version: the arrows refer to the Backup slides.

The Milky Way

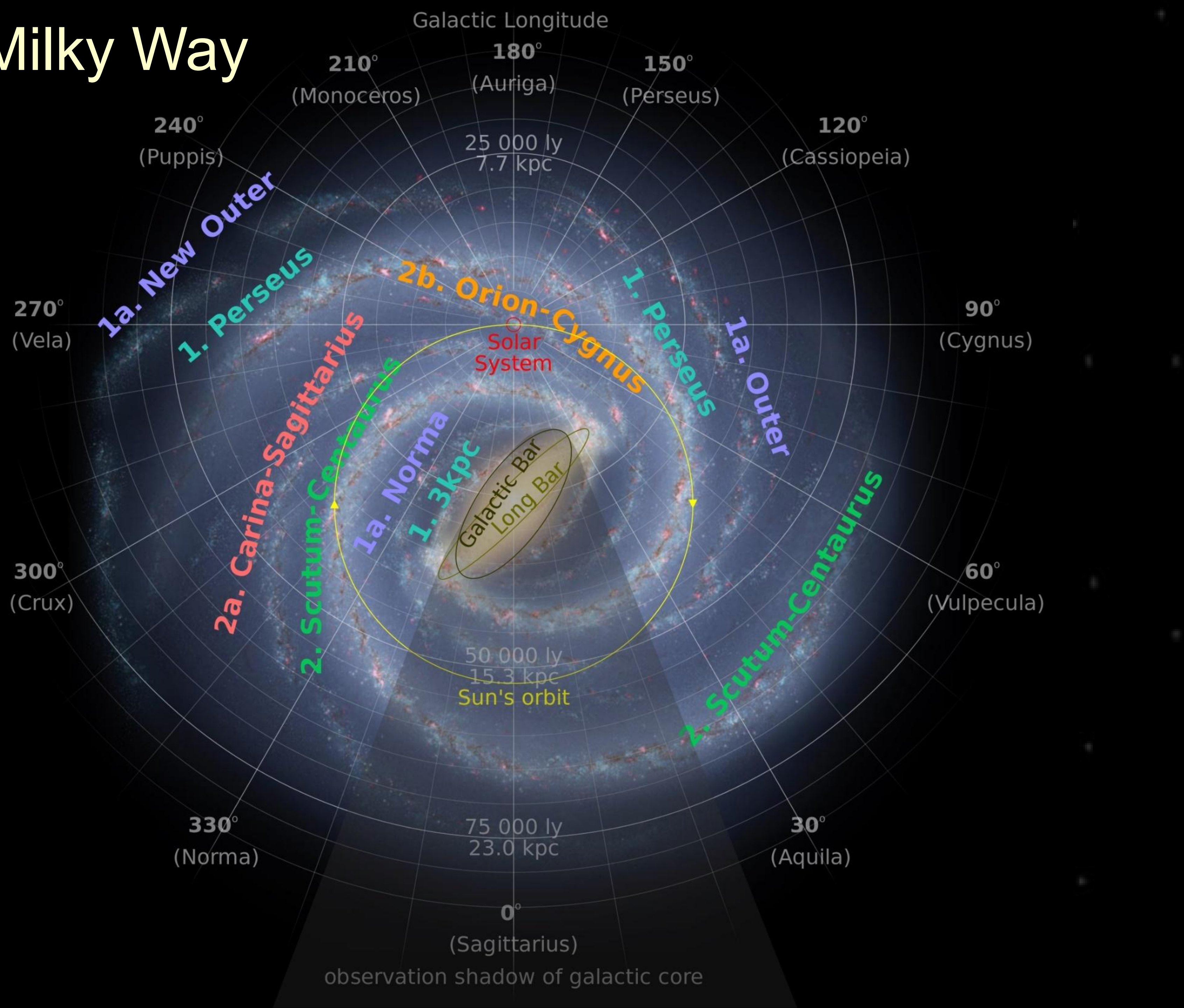

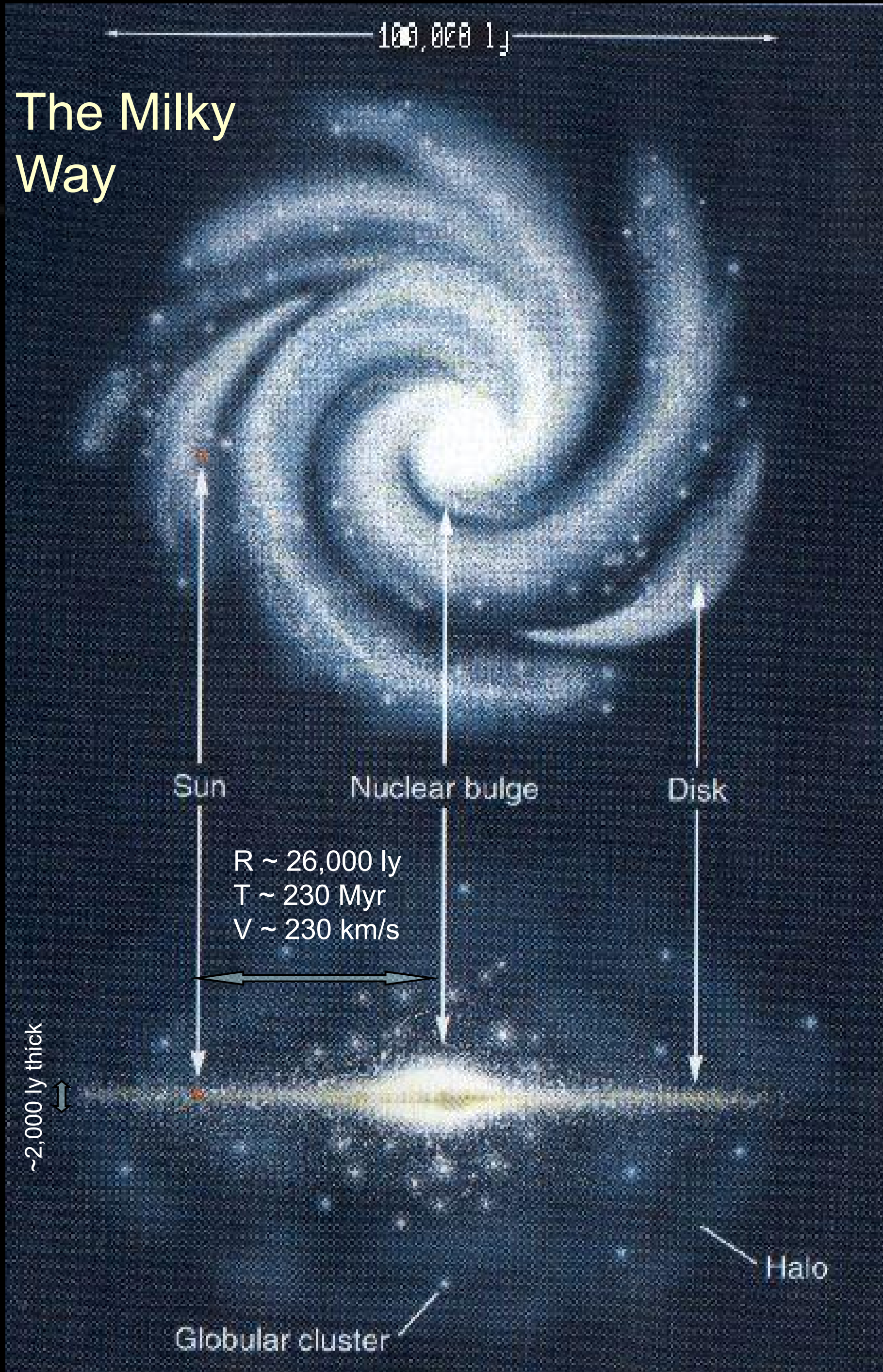

The mean concentration of the (classical) CR near the Earth $n_{CR} \sim 10^{-10}$ cm^{-3}.
The mean energy $<E_{CR}> \sim 10$ GeV.
Therefore, the mean energy density is

$$\varepsilon_{CR} = n_{CR}<E_{CR}> \sim 1 \text{ eV/cm}^3 \sim 10^{-12} \text{ erg/cm}^3$$

The mean density in the Galaxy is of the same order of magnitude and the full energy of CR in the Galaxy can be estimated

$$W_{CR}^{Disk} \sim \varepsilon_{CR} V_{Disk} \sim 10^{55} \text{ erg} \sim 10\, M_{Sun}c^2$$

$$W_{CR}^{Halo} \sim \varepsilon_{CR} V_{Halo} \sim 10^{56} \text{ erg} \sim 100\, M_{Sun}c^2$$

It is of the order of (or larger than) the kinetic energy of the interstellar gas and of the interstellar magnetic field!

CR is one of the factor affecting the energetics of the Galaxy.

The same is true for essentially all the “normal” galaxies. For the powerful radio-galaxies the full energy of CR is fantastically large:

$$W_{CR} \sim 10^{60\text{-}61} \text{ erg} \sim 10^7\, M_{Sun}c^2.$$

Honorable Mention to Cosmic Rays

In a sense, the solar system is built from Cosmic Rays.

Cosmic Rays affected (and maybe still affect) the evolution of the life on the Earth being during billions of years a catalyzer of mutations.

It might be that Cosmic Rays killed the dinosaurs (this is not the most popular hypothesis today, but thanks so much any case!).

Cosmic Rays probably affect the climate on the Earth.

Cosmic Rays produce fantastic Aurora Polaris (also thanks, mainly from Eskimos).

Cosmic Rays are associated with the extreme phenomena in the Universe (SNs, GRBs, radio-galaxies, quasars,…)

For pdf version: Let's remind that the arrows refer to the **Backup slides**.

In background: Mounted cast skeleton of Afrovenator, a predator that grew to a length of 30 feet. Sereno's team discovered Afrovenator in 130-million-year-old sediments during his 1993 expedition to Niger. Photo by Paul Sereno. **From <http://www-news.uchicago.edu/releases/photos/expedition2/>**

The range of energies of interest for neutrino astrophysics and cosmology is from ~ 1 μeV to ~ 1 YeV (~ 30 orders), of which for CR physics from ~ 100 MeV to a few ZeV (~ 13 orders)

International System of Units (SI)

(for more information on SI prefixes, see the next slide)

value	SI prefix	symbol
10	deca	da
10^2	hecto	h
10^3	kilo	k
10^6	mega	M
10^9	giga	G
10^{12}	tera	T
10^{15}	peta	P
10^{18}	exa	E
10^{21}	zetta	Z
10^{24}	yotta	Y

CR & CR Neutrinos

Well, for the sake of completeness...

SI prefixes

V·T·E

Prefix Name	Prefix Symbol	Base 1000	Base 10	Decimal	English word: Short scale	English word: Long scale	Adoption[nb 1]
yotta	Y	1000^{8}	10^{24}	1 000 000 000 000 000 000 000 000	septillion	quadrillion	1991
zetta	Z	1000^{7}	10^{21}	1 000 000 000 000 000 000 000	sextillion	trilliard	1991
exa	E	1000^{6}	10^{18}	1 000 000 000 000 000 000	quintillion	trillion	1975
peta	P	1000^{5}	10^{15}	1 000 000 000 000 000	quadrillion	billiard	1975
tera	T	1000^{4}	10^{12}	1 000 000 000 000	trillion	billion	1960
giga	G	1000^{3}	10^{9}	1 000 000 000	billion	milliard	1960
mega	M	1000^{2}	10^{6}	1 000 000	million		1873
kilo	k	1000^{1}	10^{3}	1 000	thousand		1795
hecto	h	$1000^{2/3}$	10^{2}	100	hundred		1795
deca	da	$1000^{1/3}$	10^{1}	10	ten		1795
		1000^{0}	10^{0}	1	one		–
deci	d	$1000^{-1/3}$	10^{-1}	0.1	tenth		1795
centi	c	$1000^{-2/3}$	10^{-2}	0.01	hundredth		1795
milli	m	1000^{-1}	10^{-3}	0.001	thousandth		1795
micro	μ	1000^{-2}	10^{-6}	0.000 001	millionth		1873
nano	n	1000^{-3}	10^{-9}	0.000 000 001	billionth	milliardth	1960
pico	p	1000^{-4}	10^{-12}	0.000 000 000 001	trillionth	billionth	1960
femto	f	1000^{-5}	10^{-15}	0.000 000 000 000 001	quadrillionth	billiardth	1964
atto	a	1000^{-6}	10^{-18}	0.000 000 000 000 000 001	quintillionth	trillionth	1964
zepto	z	1000^{-7}	10^{-21}	0.000 000 000 000 000 000 001	sextillionth	trilliardth	1991
yocto	y	1000^{-8}	10^{-24}	0.000 000 000 000 000 000 000 001	septillionth	quadrillionth	1991

1 eV →

CR & NA

Cosmological relic & solar neutrinos

Extension of the range of SI prefixes (18.11.2022)

Prefix	Quantity	Symbol
quetta	10^{30}	Q
ronna	10^{27}	R
ronto	10^{-27}	r
quecto	10^{-30}	q

Planck Scale [eV] & Big Data [bytes]

Very large (small) numbers end in “a” (“o”) with capital (lowercase) letters for the symbol

SEVERAL DEFINITIONS

One of the main characteristics of cosmic rays is their differential intensity = differential energy spectrum = differential flux:

$$F_a = \frac{dN_a}{dSdtd\Omega dE} \qquad \left([F_a] = \frac{\text{particles}}{\text{cm}^2 \cdot \text{s} \cdot \text{sr} \cdot \text{GeV}}\right).$$

So $dN_a = F_a dSdtd\Omega dE$ is the number of particles a with the total energies E to $E + dE$ which cross the area dS (perpendicular to the direction of observation) in time dt coming within the solid angle $d\Omega = d\varphi \sin\vartheta d\vartheta$.

In the general case, $F_a = F_a(E, \mathbf{\Omega}, \mathbf{r}, t) = F_a(\mathbf{p}, \mathbf{r}, t)$ with

$$\mathbf{\Omega} = (\sin\vartheta\cos\varphi, \sin\vartheta\sin\varphi, \cos\vartheta) = \frac{\mathbf{p}}{|\mathbf{p}|} = \frac{\mathbf{v}}{|\mathbf{v}|}$$

the unit vector directed along the particle momentum $\mathbf{p}$ (or velocity $\mathbf{v}$) and $\mathbf{r}$ the point of observation. But usually, for simplicity, we will write only the first argument.

The integral energy spectrum is defined by

$$F_a(>E) = \int_E^\infty F_a(E')dE'.$$

From this definition it follows that

$$F_a(E) = -\left[\frac{\partial F_a(>E)}{\partial E}\right].$$

Similar way one can define the differential and integral momentum spectra,

$$F_a(p) = \frac{dN_a}{dS\,dt\,d\Omega\,dp} \quad \text{and} \quad F_a(>p) = \int_p^\infty F_a(p')dp'$$

(where $p = |\mathbf{p}|$). These are related to the energy spectra as

$$F_a(p) = (p/E)F_a(E) \quad \text{and} \quad F_a(>p) = F_a(>E).$$

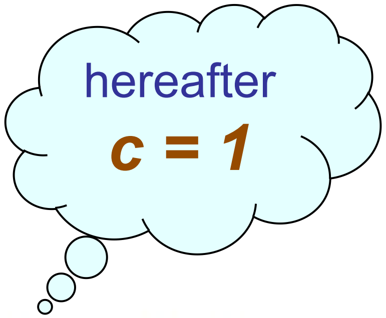

This immediately follows from the relation

$$pdp = EdE,$$

the consequence of the relativistic law $E^2 = p^2 + m_a^2$ (m_a is the mass of particle a).

In addition, one can introduce the differential and integral spectra

$F_a(E_\mathrm{k})$ and $F_a(>E_\mathrm{k})$, where $E_k \equiv E_\mathrm{kin} = E - m_a$ is the kinetic energy

and (for charged particles with the charge of $Z_a|e|$)

$F_a(R)$ and $F_a(>R)$, where $R = p/Z_a|e|$ is the magnetic rigidity ([R]=GV).

The flux of particles a whose differential intensity is $F_a(E)$ is defined by

$$\Phi_a(E, \boldsymbol{\Omega}, \mathbf{r}, t) = \int F_a(E, \boldsymbol{\Omega}', \mathbf{r}, t) \cos\vartheta d\boldsymbol{\Omega}',$$

In particular, for an isotropic radiation from a semisphere, the flux is

$$\Phi_a(E) = \int_0^{\pi/2} F_a(E) \cos\vartheta \sin\vartheta d\vartheta = \pi F_a(E).$$

Note

since (for the isotropic radiation) the value of Φ_a is simply proportional to the F_a, the term flux is frequently used also for F_a, instead of the correct term differential intensity or differential spectrum. Sometimes this can be a source of confusions.

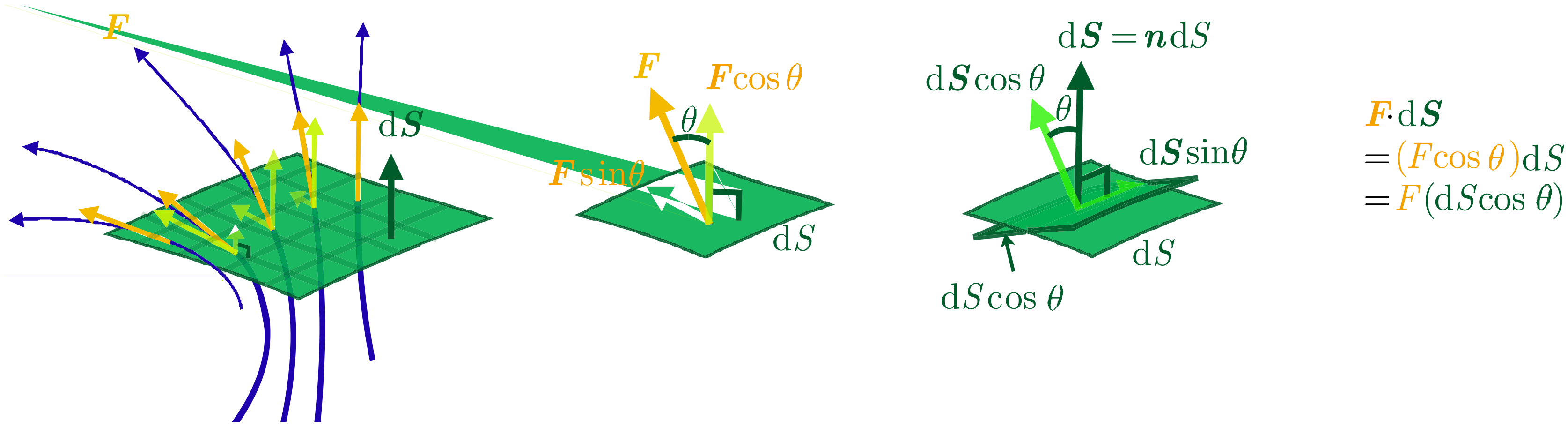

Astronomical coordinate systems

Coordinate system	Center point (origin)	Fundamental plane (0° lat.)	Poles	Coordinates: Latitude	Coordinates: Longitude	Primary direction (0° long.)
Horizontal or **Alt-azimuth**	Observer	Horizon	Zenith Nadir	Altitude (a) or elevation*	Azimuth (A or ϕ)	North or south point of horizon
Equatorial	Center of Earth (geocentric) or Sun (heliocentric)	Celestial equator	Celestial poles	Declination (δ)	Right ascension (α) or hour angle (h)	March (or vernal or spring) equinox
Ecliptic		Ecliptic	Ecliptic poles	Ecliptic latitude (β)	Ecliptic longitude (λ)	
Galactic	Center of Sun	Galactic plane	Galactic poles	Galactic latitude (b)	Galactic longitude (l)	Galactic center
Supergalactic	Barycenter of Superclaster	Supergalactic plane	Supergalactic poles	Supergalactic latitude (SGB)	Supergalactic longitude (SGL)	Intersection of Galactic & Supergalactic planes

*Zenith angle $\theta = \pi/2 - a$ in CR physics. Nadir angle is $\pi - \theta = \pi/2 + a$.

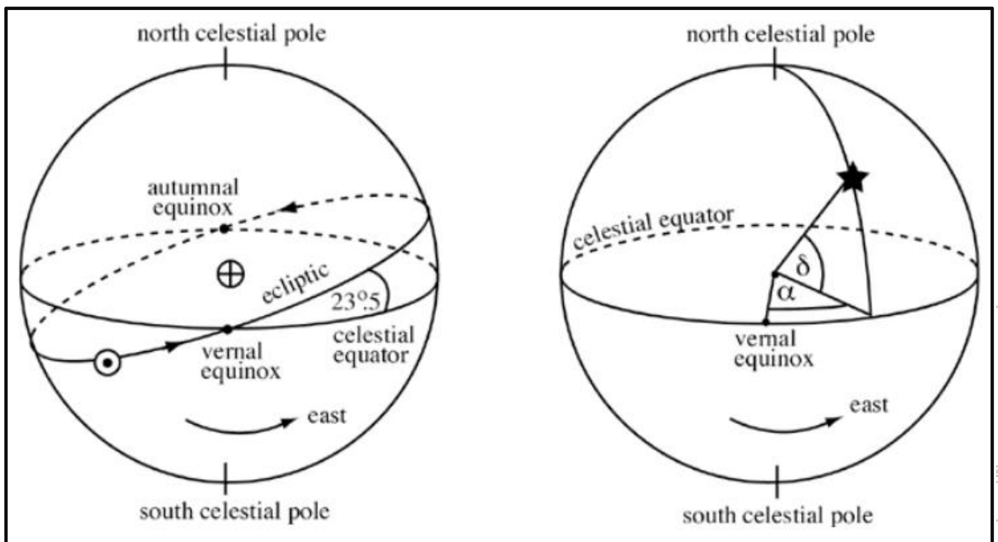

← Equatorial geocentric coodinate system

↓ Galactic coodinate system

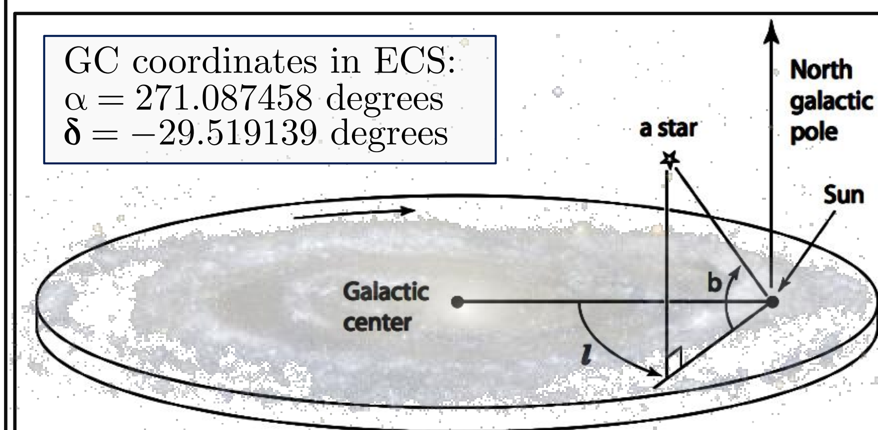

These two coordinate systems are commonly used in Cosmic-Ray Physics and Neutrino Astrophysics

CR Anisotropy measures

The observed CR anisotropy is expressed as the variation of j, where j can be differential/integral energy/momentum spectrum, or (usually) flux. Degree of anisotropy is characterized by the value

$$\delta_j = \frac{j_{\max} - j_{\min}}{2\langle j \rangle} \approx \frac{j_{\max} - j_{\min}}{j_{\max} + j_{\min}}.$$

- In the energy range $E \lesssim 10$ GeV, $\delta_\Phi < 10^{-3}$.
- At higher energies the situation changes radically and depends on many additional native factors.
  - direction of CR movement concentrates close to Galactic plane;
  - lower-energy particles come from the inner part of the Galaxy;
  - higher-energy particles come from both parts;
  - there are directions (e.g., galaxy cluster Virgo), along which these particles are concentrated so that δ_Φ increases up to ~ 1.

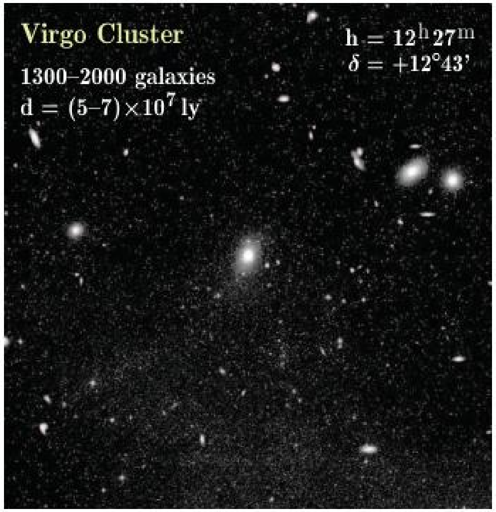

More detailed chracteristics are described using a spherical harmonic expansion (as for CMB)

$$\frac{j(b,l)}{\langle j \rangle} - 1 = \sum_{\ell=0}^{\infty} \sum_{m=-\ell}^{\ell} a_{\ell m} Y_{\ell m}\left(\frac{\pi}{2} - b, l\right)$$

← Galactic coordinate system

The coefficients of the angular power spectrum of the fluctuations are defined as

$$C_\ell = \frac{1}{2\ell+1} \sum_{m=-\ell}^{\ell} |a_{\ell m}|^2.$$

In particular, the amplitude of dipole anisotropy is defined as $\delta = 3\sqrt{C_1/4\pi}$.

Converting one coordinate system to another is not entirely trivial due to the complex motion of the Earth and Sun around the Galaxy...

...Fortunately, there are reference books and special computer programs.

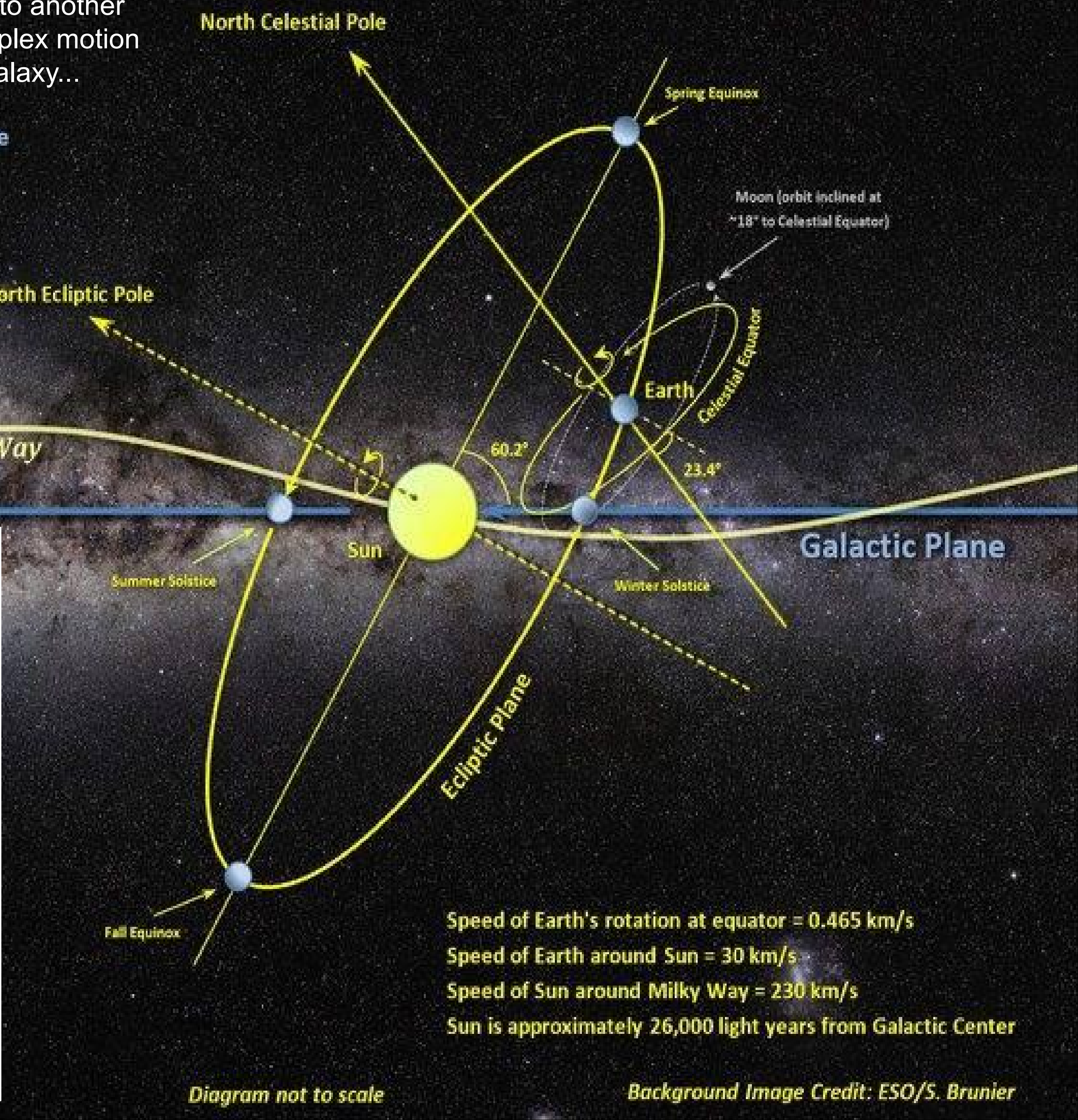

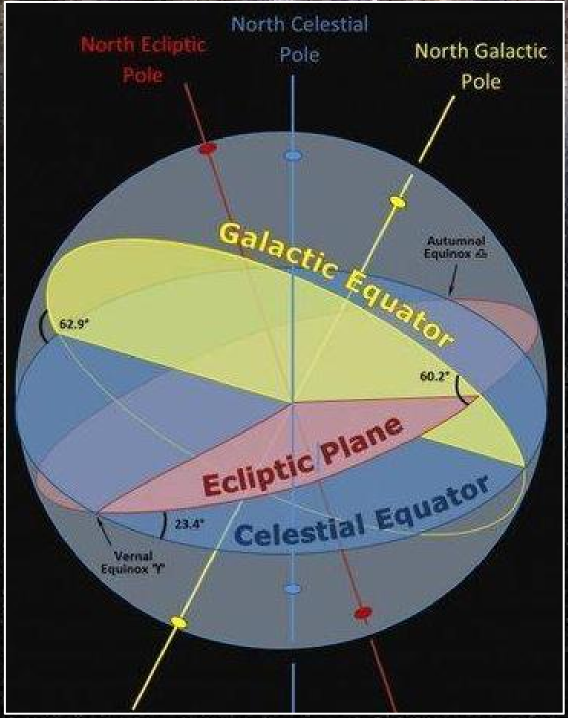

A bird's eye view of the all-nuclei CR spectrum

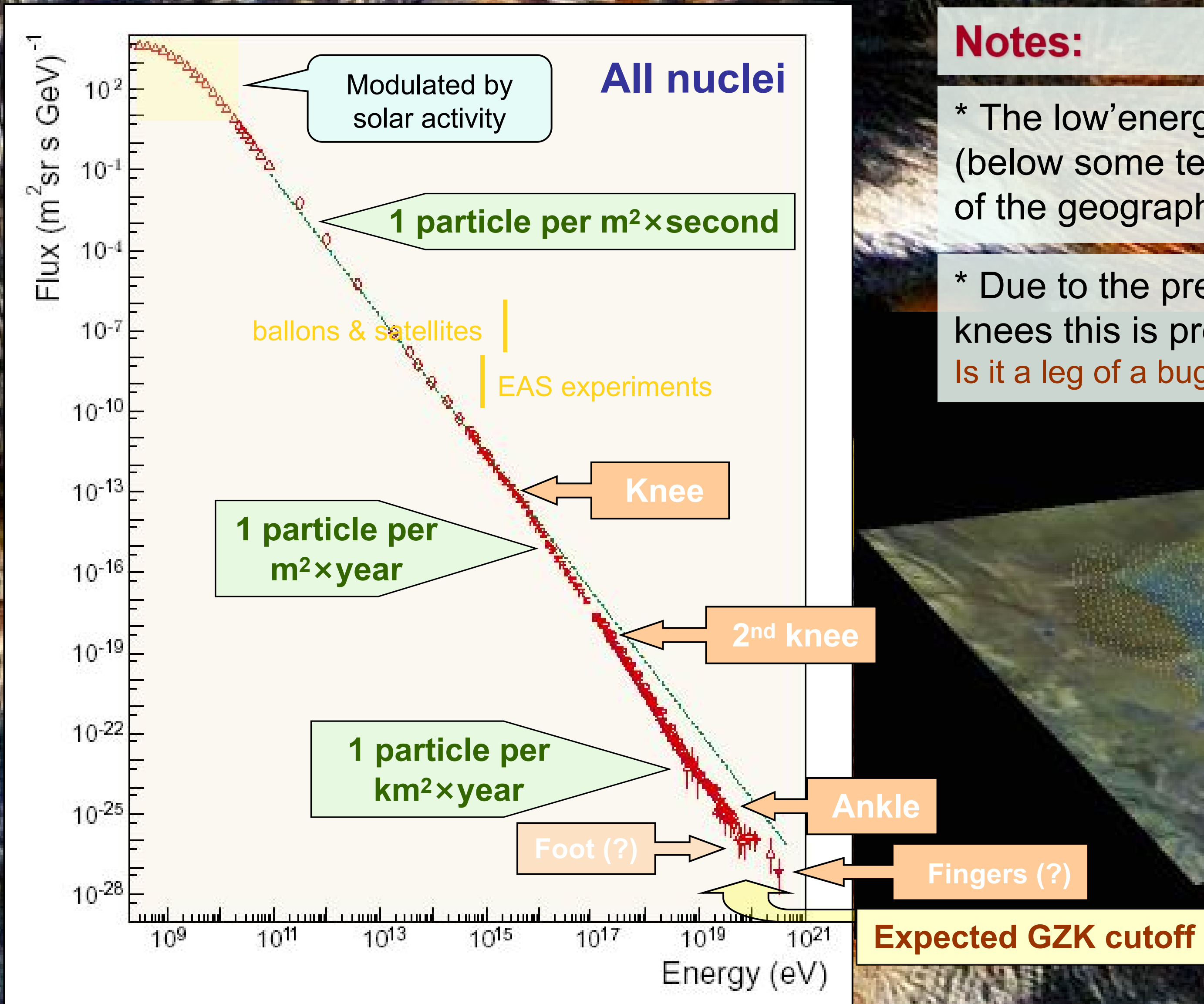

Notes:

* The low'energy part of the spectrum (below some tens of GeV) is dependent of the geographycal position.

* Due to the presence of (at least) two knees this is probably not a human leg. Is it a leg of a bug or the 2nd knee is a bug?

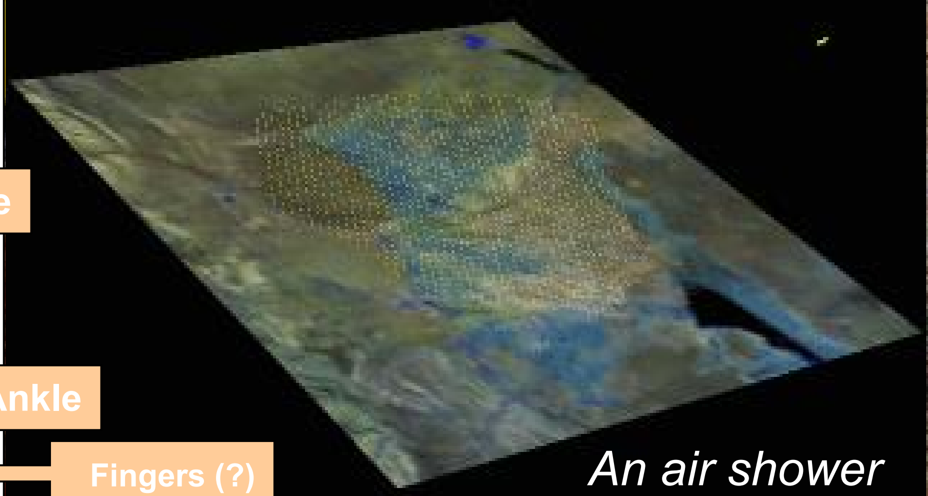

An air shower

Animation is taken from URL:
http://auger.org/education/Auger_Education/origincosmicrays.html

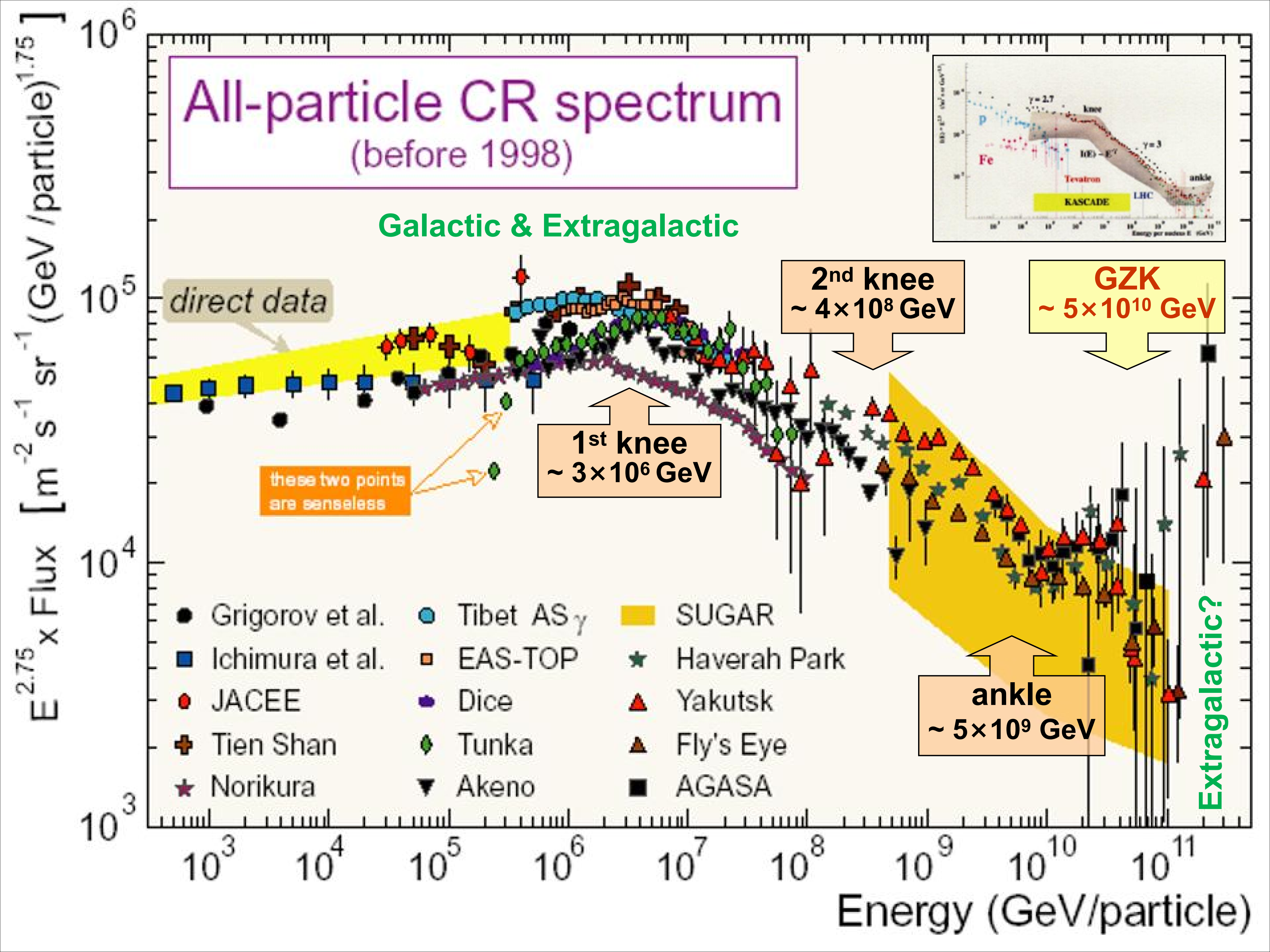

All-particle CR spectrum
(before 1998)
Galactic & Extragalactic
direct data
these two points are senseless
1st knee ~ 3×10^6 GeV
2nd knee ~ 4×10^8 GeV
GZK ~ 5×10^10 GeV
ankle ~ 5×10^9 GeV
Extragalactic?
Grigorov et al.
Ichimura et al.
JACEE
Tien Shan
Norikura
Tibet ASγ
EAS-TOP
Dice
Tunka
Akeno
SUGAR
Haverah Park
Yakutsk
Fly's Eye
AGASA
E^2.75 x Flux [m^-2 s^-1 sr^-1 (GeV/particle)^1.75]
Energy (GeV/particle)
p
Fe
knee
ankle
Tevatron
LHC
KASCADE

All-particle CR spectrum 2005

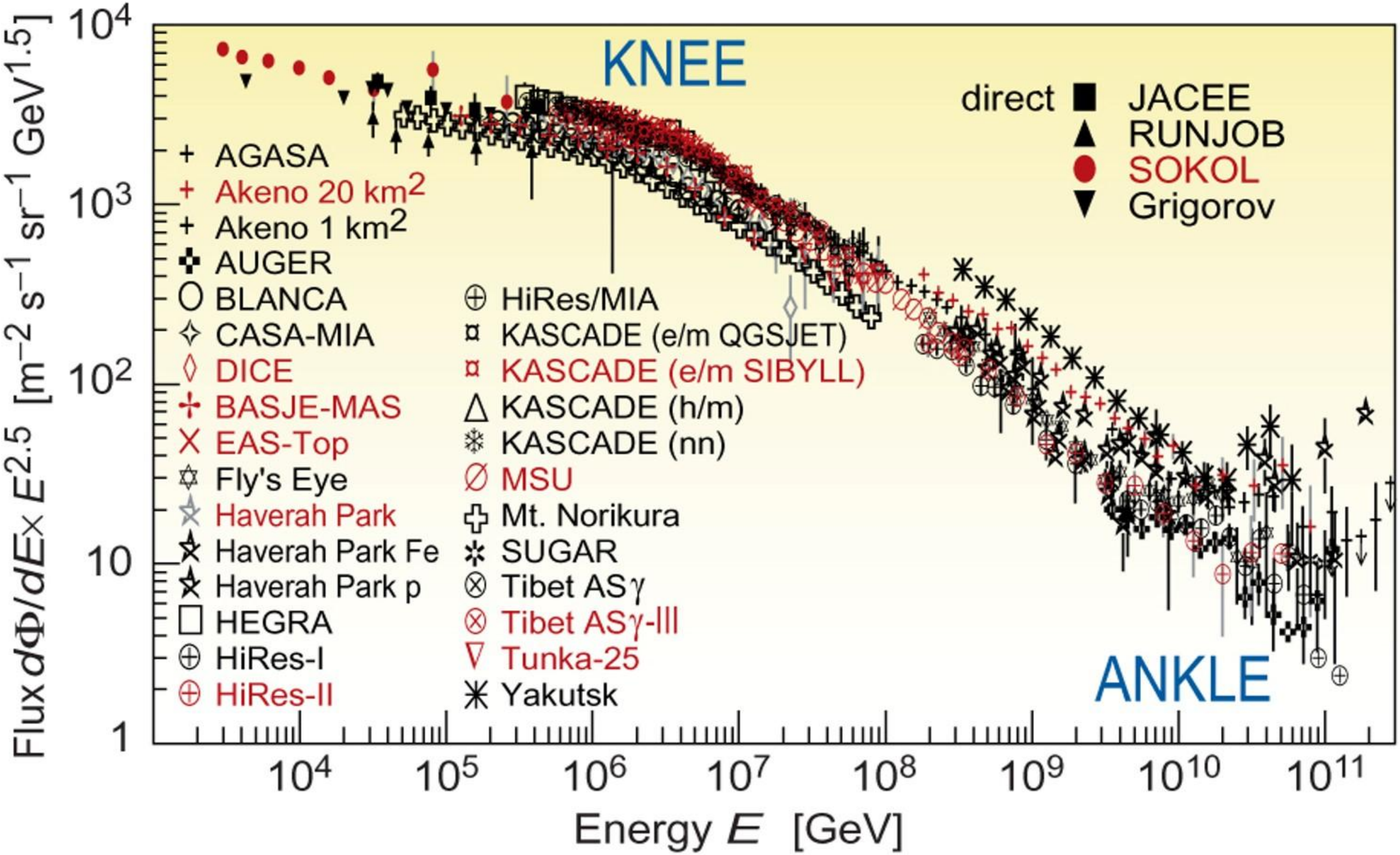

It looks like the main problem is in an absolute normalization of individual measurements. Indeed an adjusting (by Bartol team) helps to see a more realistic structure of the spectrum and composition.

All-particle CR spectrum & mass composition 2019

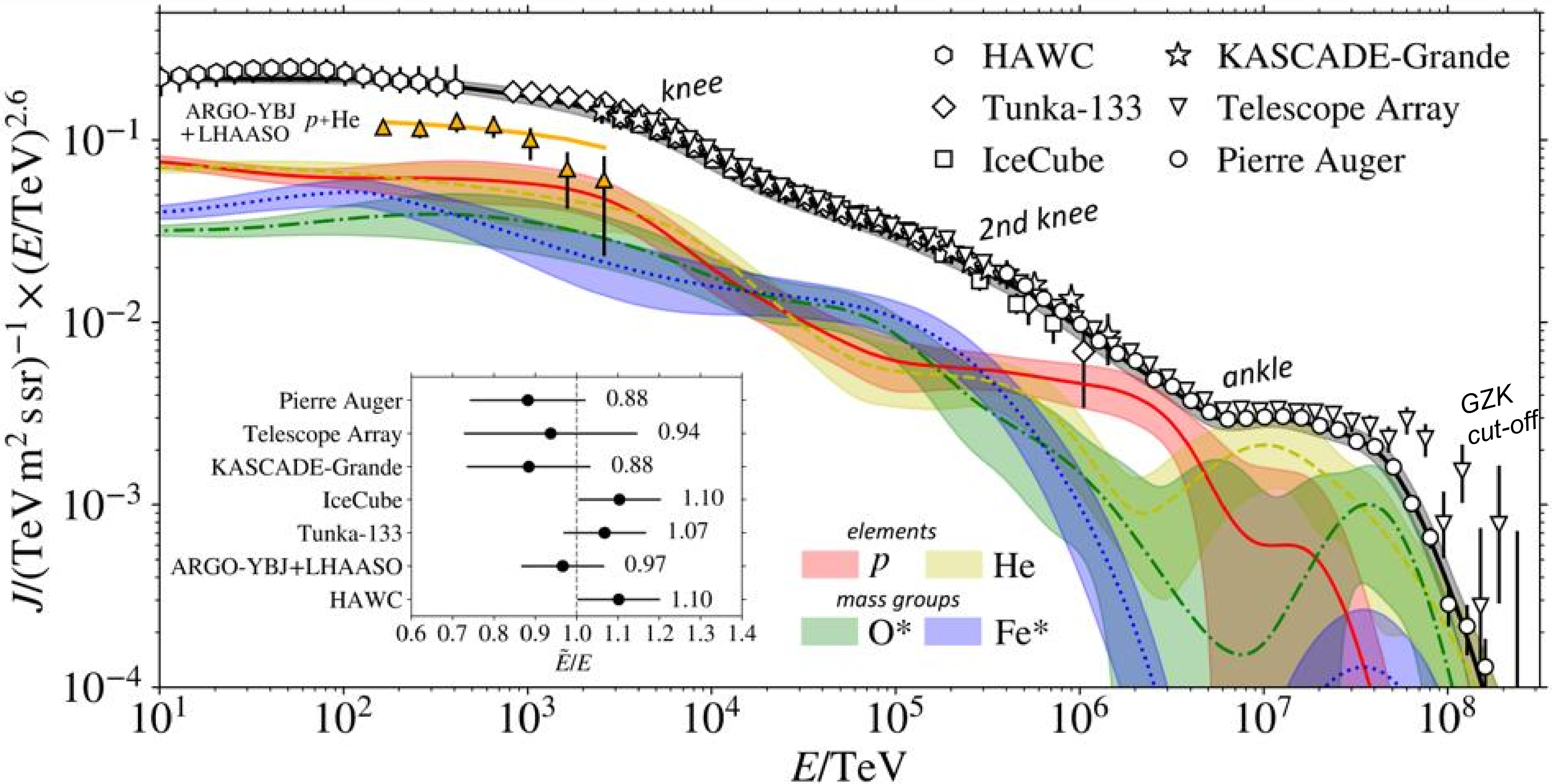

The plot reflects a recent attempt (**2019**) for a combined fit of flux and composition measurements by different experiments, where the individual spectra have been multiplied by a constant (inset) to adjust them to a common energy scale. The bands are 1σ uncertainties derived from published experimental data. Features such as the ***knee***, ***2nd knee***, and ***ankle*** mark softenings or hardenings of the spectrum which can be approximated by a power law in between these features. For future progress, it is important to reduce the uncertainties by improving hadronic interaction models and enhancing air-shower arrays to perform hybrid measurements. See below.

From F. G. Schroeder *et al.*, "High-Energy Galactic Cosmic Rays" (Astro2020 Science White Paper), arXiv:1903.07713 [astro-ph.HE].

All-particle Local Interstellar (LIS) CR spectrum & mass composition 2020

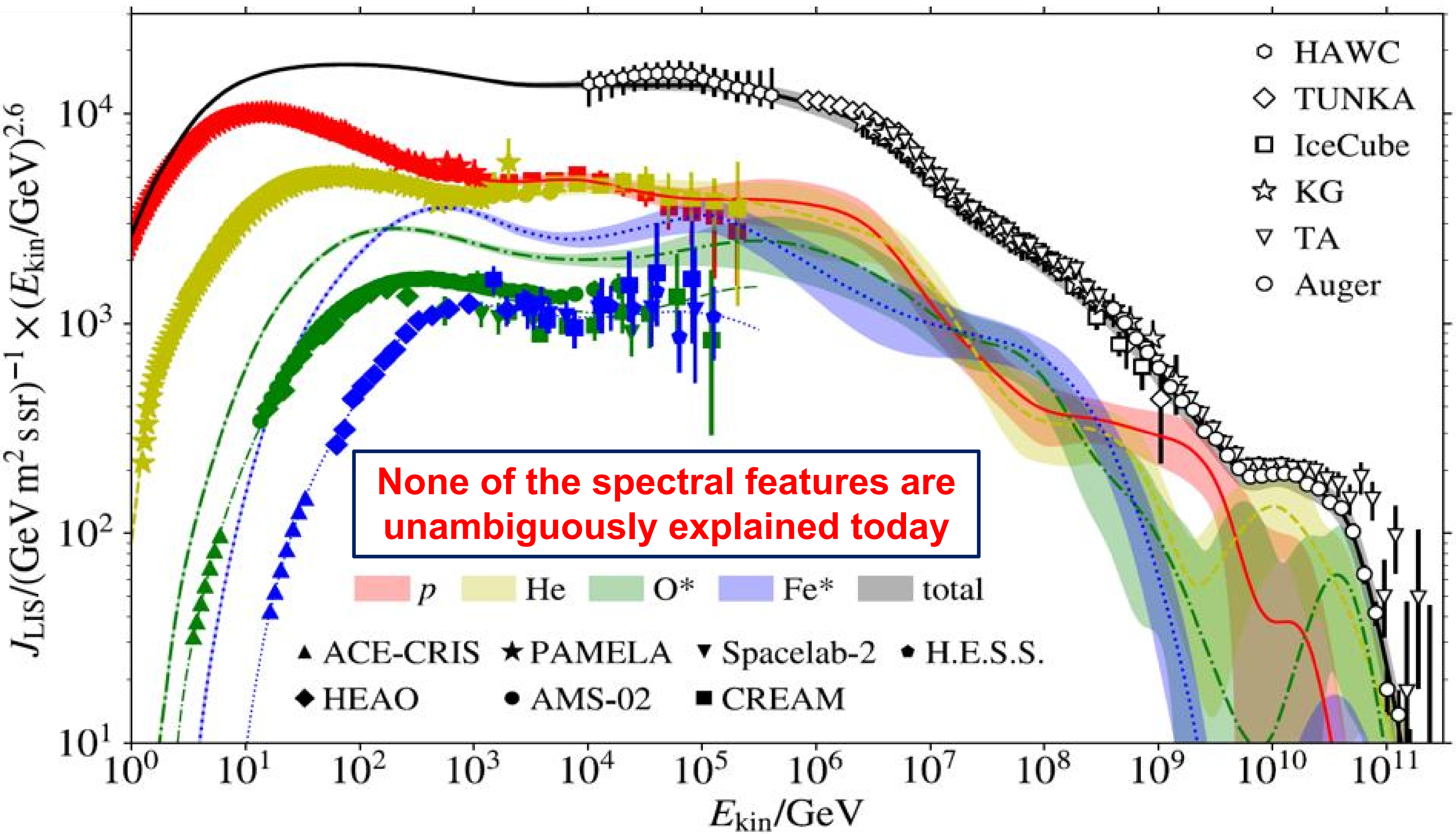

This is the global spline fit to direct & indirect observations (same as in the previous slide but in a wider energy range). Fit includes 4 independent mass groups. One leading element L per group is described by smooth spline curve, other elements j in the group kept in constant the ratio $J_j(R)/J_L(R)$.

From A. Fedynitch, "Conventional and prompt atmospheric neutrinos," Report @ Workshop `Cosmic Rays & Neutrinos in the Multi-Messenger Era' (Paris, December 8, 2020).

Truly all-particle cosmic-ray flux

(State of The Art 2023)

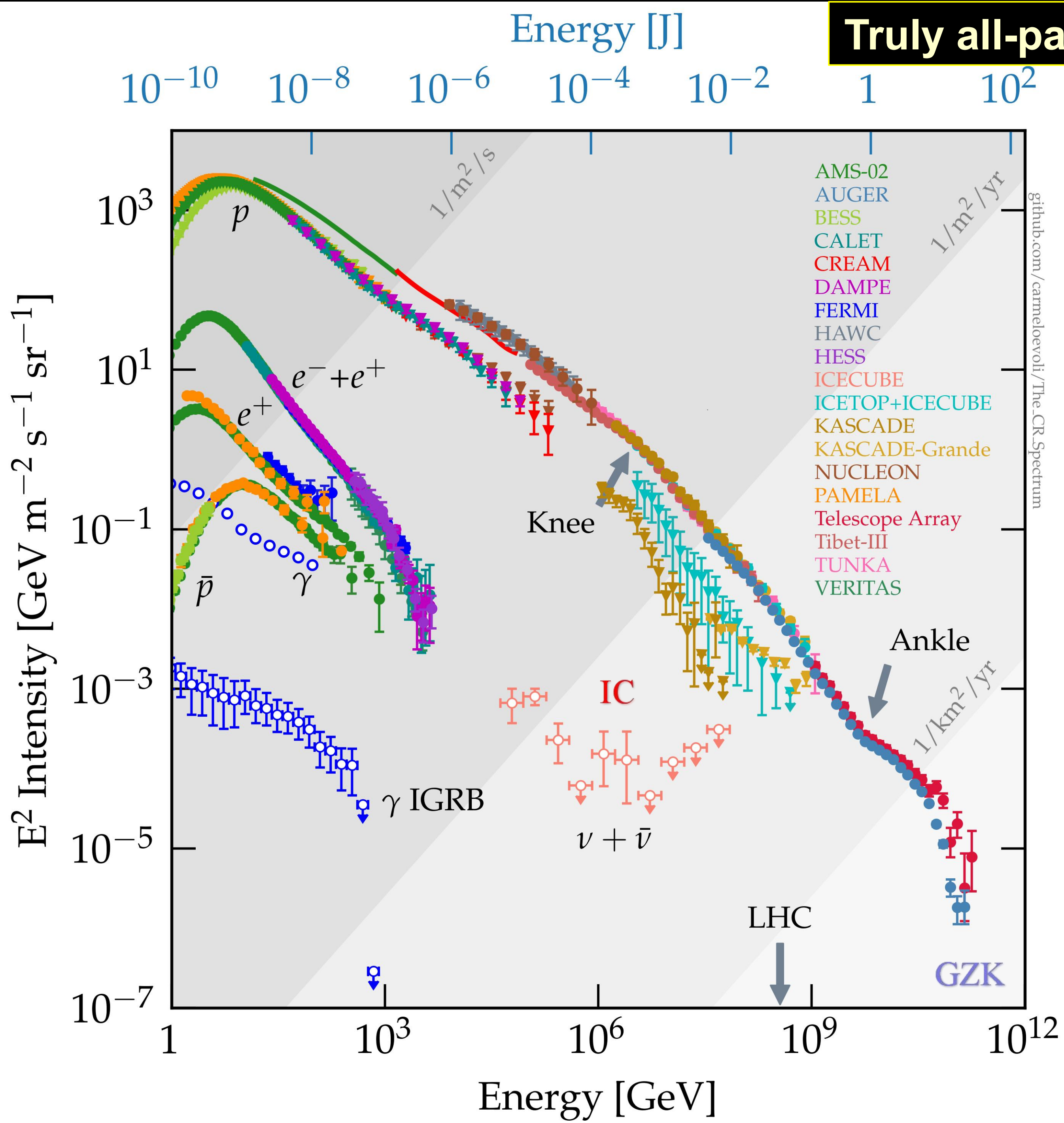

A compilation of the cosmic-ray energy spectra measured by several experiments (mainly after 2000).

No renormalization!

[From **Carmelo Evoli.** The Cosmic-Ray Energy Spectrum.

Zenodo. **URL**:https://zenodo.org/records/7948212 and **DOI**:10.5281/zenodo.1468852.

Version 6, Fall 2023

Plot routines, database and references are in the dedicated GitHub repository.]

A surprise from ultra-high energies

All particles, including meson and baryon resonances, become (quasi)stable.

Does our extrapolation of known physics of particle interactions remain correct in the UHE region?

Particle	Mass, m (MeV/c^2)	Mean life, τ (s)	$c\tau$ (cm)	Decay length at E = 100 EeV
n (neutron)	939.6	8.857×10^{2}	2.655×10^{13} (1.775 au)	2.826×10^{24} cm (0.916 Mpc)
μ (muon)	105.7	2.197×10^{-6}	6.586×10^{4}	6.234×10^{16} cm (4167 au)
τ (tauon)	1777	2.906×10^{-13}	8.711×10^{-3}	4.902×10^{8} cm (4902 km)
D^+	1869	1.051×10^{-12}	3.150×10^{-2}	1.685×10^{9} cm (16,851 km)
$\rho(770)$	771	9.82×10^{-20} (Γ = 149.2 MeV)	2.944×10^{-9}	382 cm
$\Delta(1232)$	1232	7.9×10^{-20} (Γ = 120 MeV)	2.368×10^{-9}	192 cm

1 au = 149 597 870 660 m, 1 pc = 1 au/(1 arc sec) = 3.085 677 580 7 $\times 10^{16}$ m = 3.262 ly

UHECR puzzles (before HiRes & Auger)

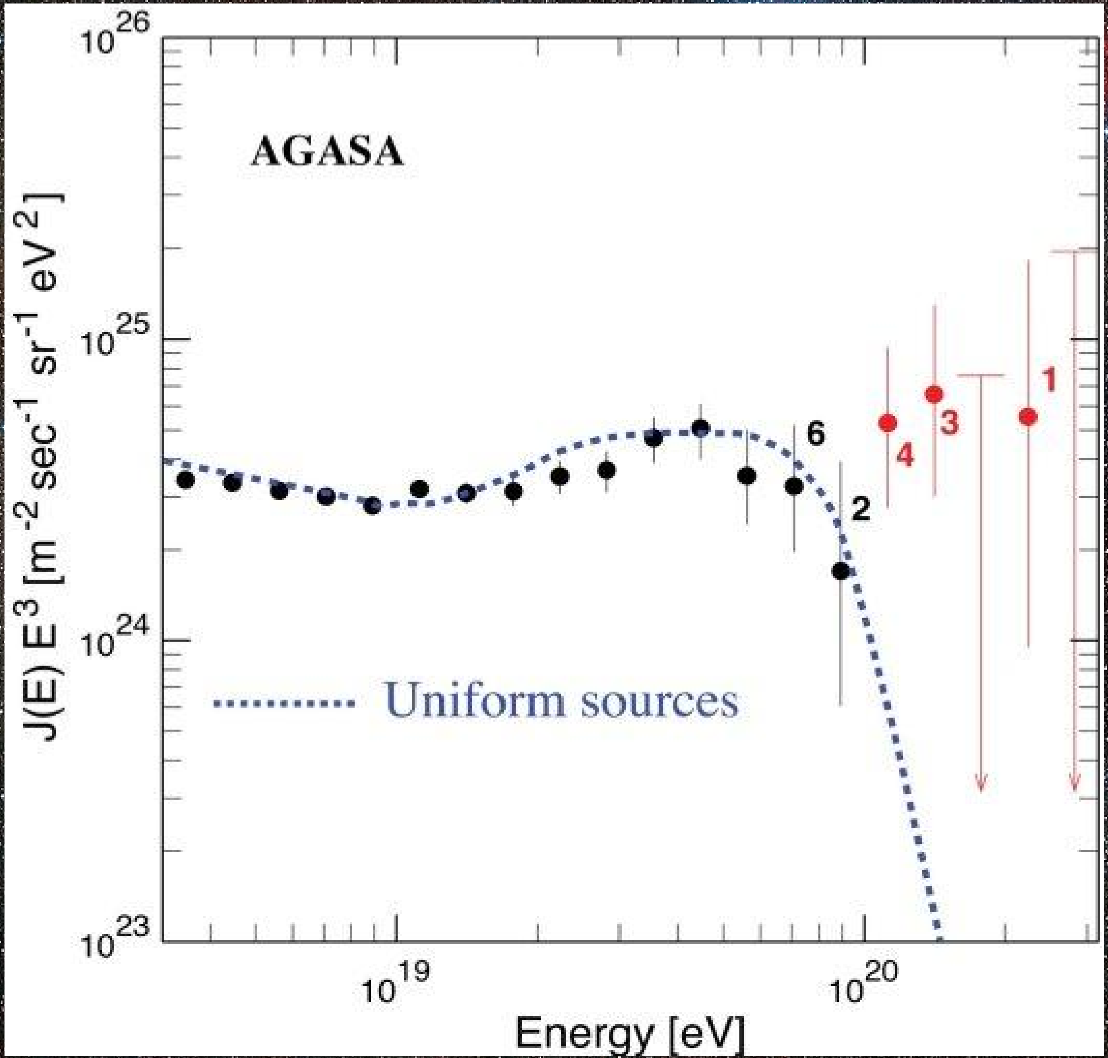

There were a few observational facts to prove that the UHECR are indeed a mystery.

The fact that their sources (whatever they are) are expected to be in our close neighbourhood and yet we do not see them.

That their energy is so huge that no conventional astrophysical acceleration mechanism seems capable of producing them;

That during more than four decades of observation we did not succeed in giving them an identity (what kind of particles they are?).

↑ A zoom on the highest energy range of the cosmic ray spectrum (from the AGASA experiment). The dotted line shows the expected cutoff if the cosmic ray sources were uniformly distributed in the universe. The few events above the cutoff have no explanation as to their origin in the framework of conventional astrophysics.

One piece of the Puzzle, the GZK feature

$$p + \gamma_{CMB} \rightarrow n + \pi^{+}$$
$$p + \gamma_{CMB} \rightarrow p + \pi^{o}$$
$$p + \gamma_{CMB} \rightarrow p + e^{+} + e^{-}$$

Pion photoproduction

Greisen (1966),
Zatsepin & Kuz'min (1966)

Pair production

(Blumenthal, 1970)

$$A + \gamma_{CMB} \rightarrow (A\text{-}1) + N$$
$$A + \gamma_{CMB} \rightarrow (A\text{-}2) + 2N$$
$$A + \gamma_{CMB} \rightarrow A + e^{+} + e^{-}$$

Photodisintegration

Puget *et al.* (1976)

Pair production

Blumenthal (1970)

As an example, if the largest energy cosmic ray ever detected (320 EeV, i.e. more that 50 joules!) was a proton produced with an initial energy of 10 ZeV, the distance of its source should be less than 50 Mpc (roughly 160 millions of light-years). Although such a distance may look immense, at cosmological scales it is more or less the size of the local supercluster of galaxies – our home supercluster Laniakea, the "suburbs" of the Milky Way galaxy. However, the latter is several thousand times smaller than Laniakea.

Let's try to understand the grandiosity and enormity of the GZK spatial scale.

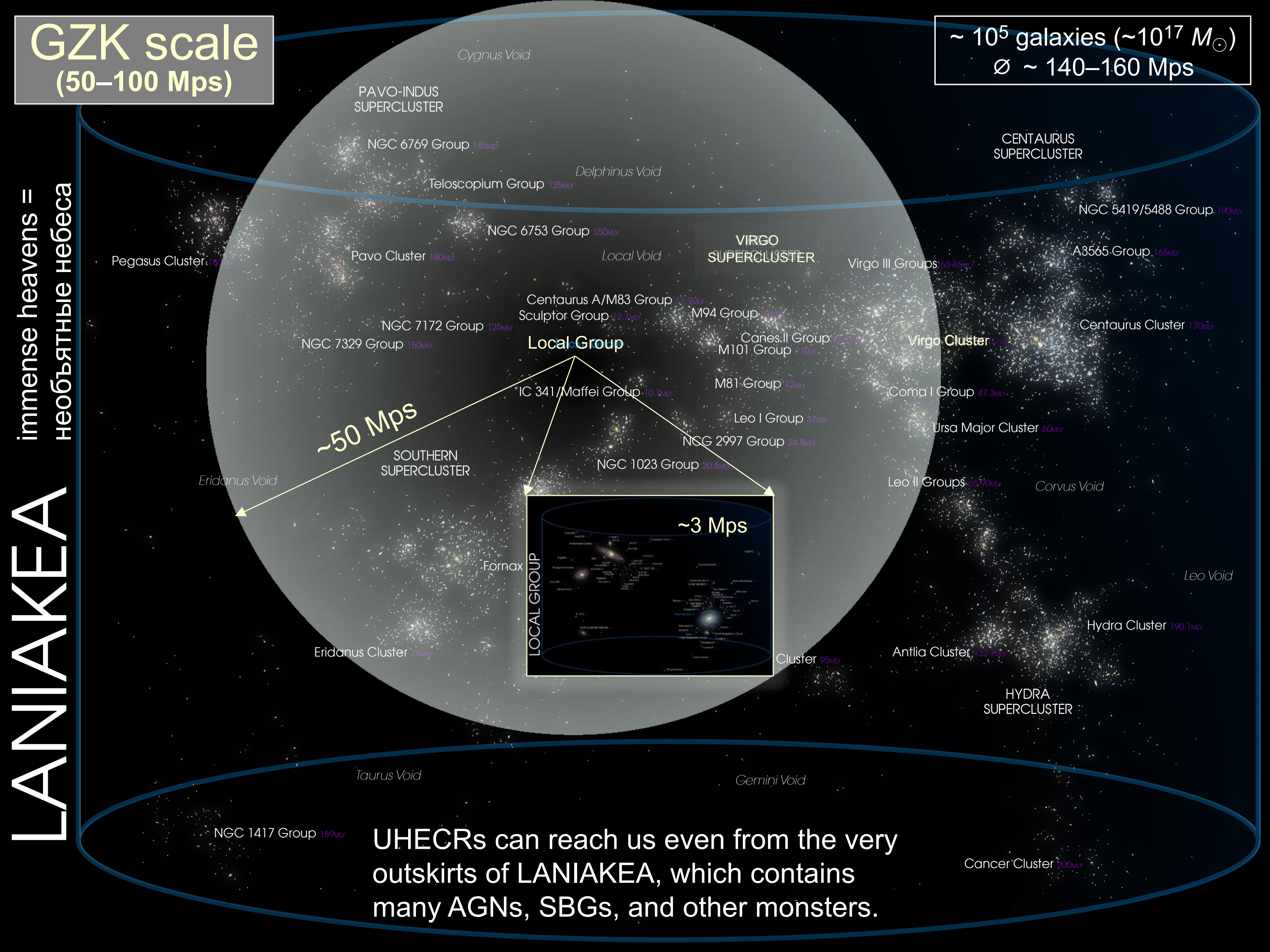

GZK scale
(50–100 Mps)
~ 10^5 galaxies (~$10^{17}\ M_\odot$)
∅ ~ 140–160 Mps
immense heavens = необъятные небеса
LANIAKEA
Cygnus Void
PAVO-INDUS SUPERCLUSTER
NGC 6769 Group
Delphinus Void
Teloscopium Group
CENTAURUS SUPERCLUSTER
NGC 5419/5488 Group
NGC 6753 Group
Pavo Cluster
Pegasus Cluster
Local Void
VIRGO SUPERCLUSTER
Virgo III Groups
A3565 Group
Centaurus A/M83 Group
Sculptor Group
M94 Group
NGC 7172 Group
NGC 7329 Group
Local Group
Canes II Group
M101 Group
Virgo Cluster
Centaurus Cluster
IC 341/Maffei Group
M81 Group
Coma I Group
~50 Mps
Leo I Group
Ursa Major Cluster
NGC 2997 Group
SOUTHERN SUPERCLUSTER
NGC 1023 Group
Eridanus Void
Leo II Groups
Corvus Void
~3 Mps
LOCAL GROUP
Fornax
Leo Void
Hydra Cluster
Eridanus Cluster
Cluster
Antlia Cluster
HYDRA SUPERCLUSTER
Taurus Void
Gemini Void
NGC 1417 Group
Cancer Cluster
UHECRs can reach us even from the very outskirts of LANIAKEA, which contains many AGNs, SBGs, and other monsters.

The Milky Way Galaxy forms part of a Local Group of galaxies within about a 10^7 ly diameter. The cluster features about **54** galaxies all of which are centred around two major clusters – the first with the Milky Way and its surrounding satellite galaxies, and the other around the Andromeda Galaxy – some 2.5 $\times 10^6$ ly away.

LOCAL GROUP

(part of Virgo supercluster)

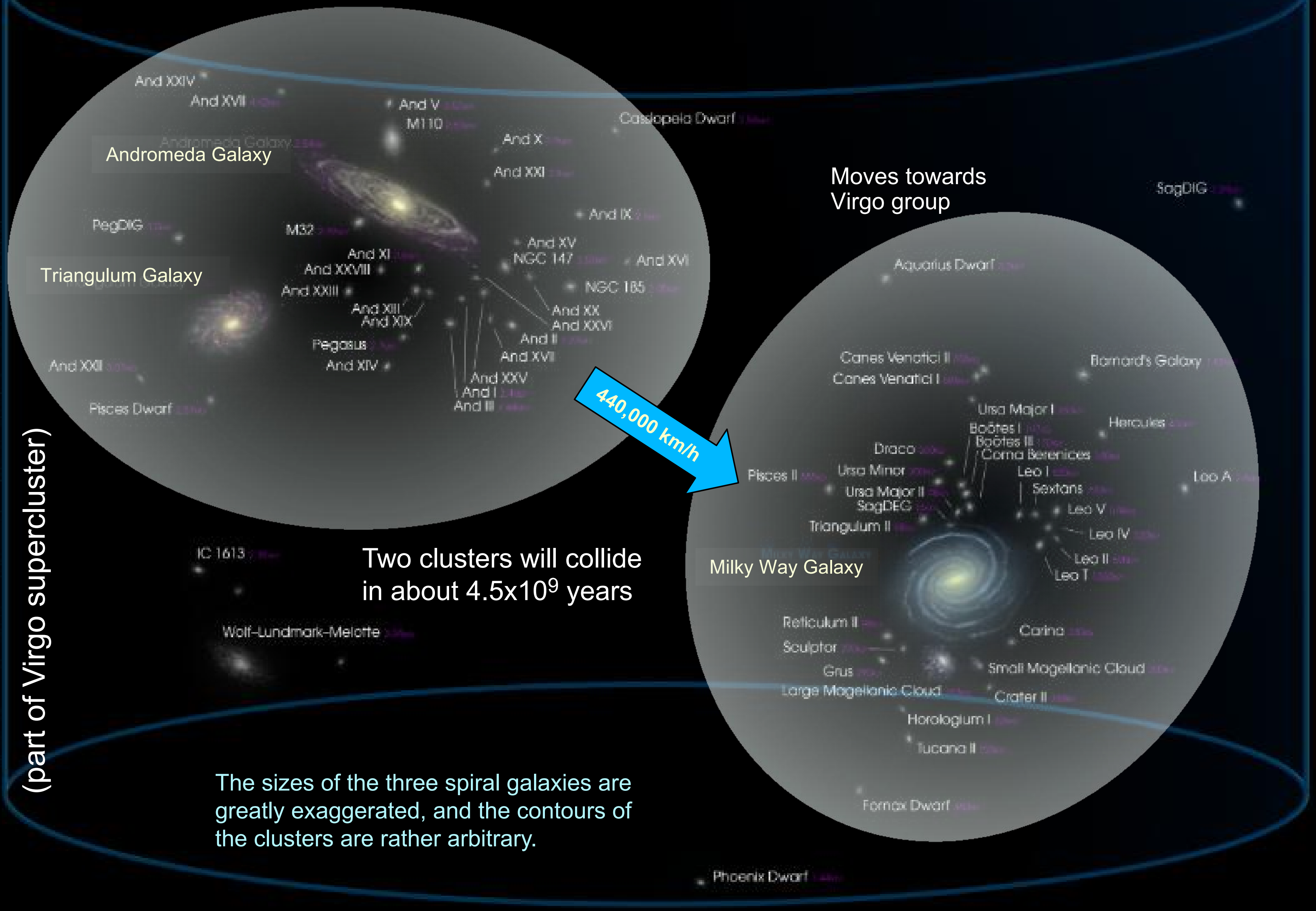

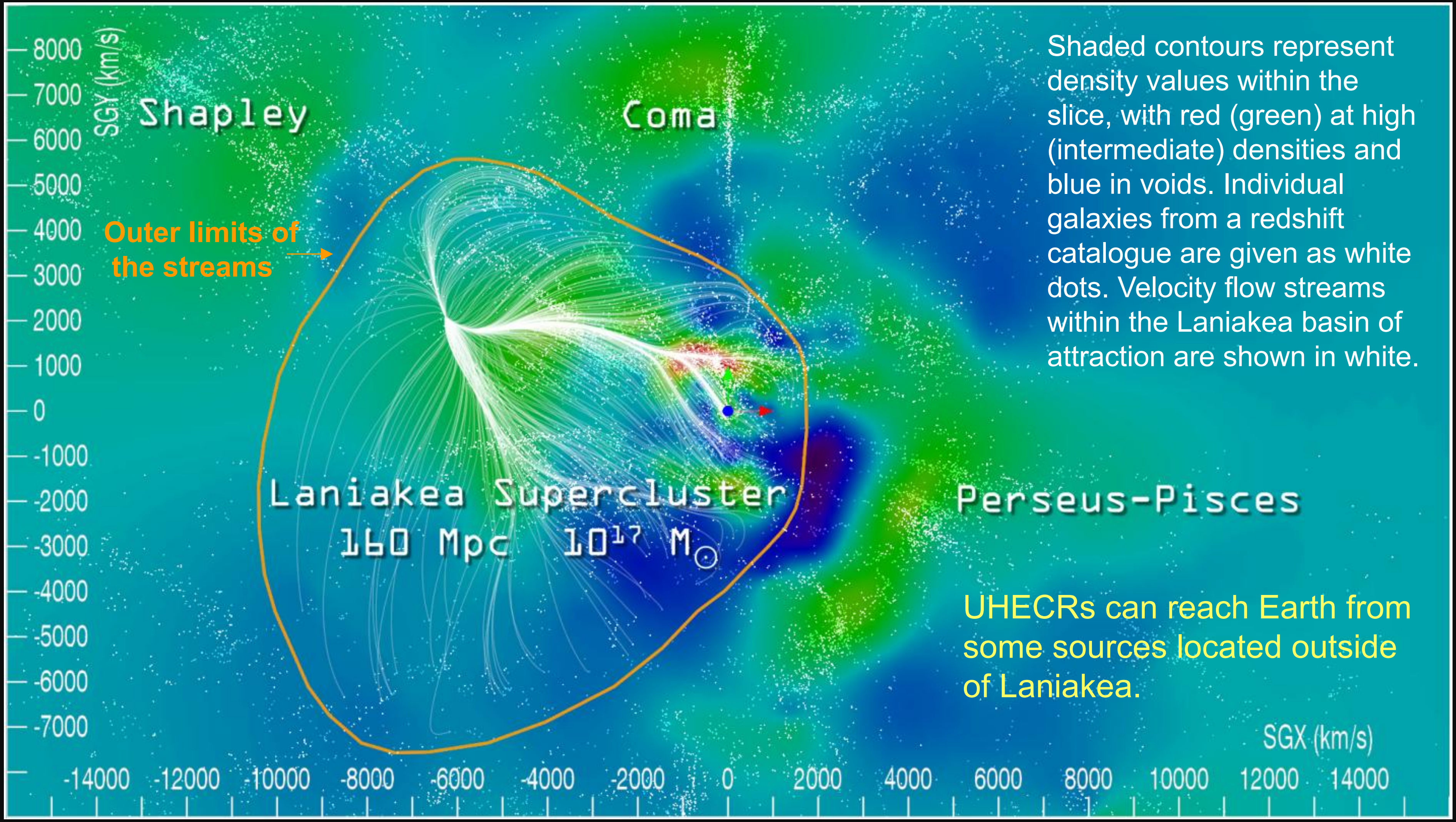

A slice of the Laniakea Supercluster in the supergalactic equatorial plane (SGX,SGY).

The cartesian supergalactic coordinates SGX and SGY are in units of redshift. Milky Way is located at the dark blue dot at the origin of the coordinate system.

Laniakea expands and will continue to expand but an imprint of it will remain in the galaxy peculiar velocities.

[**Reference:** R. Brent Tully, H. Courtois, Y. Hoffman & D. Pomarede, “The Laniakea supercluster of galaxies,” Nature **513** (September 2014) 71–73, arXiv:1409.0880 [astro-ph.CO].]

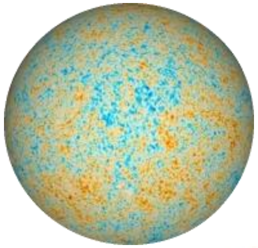

Cosmic Microwave Background

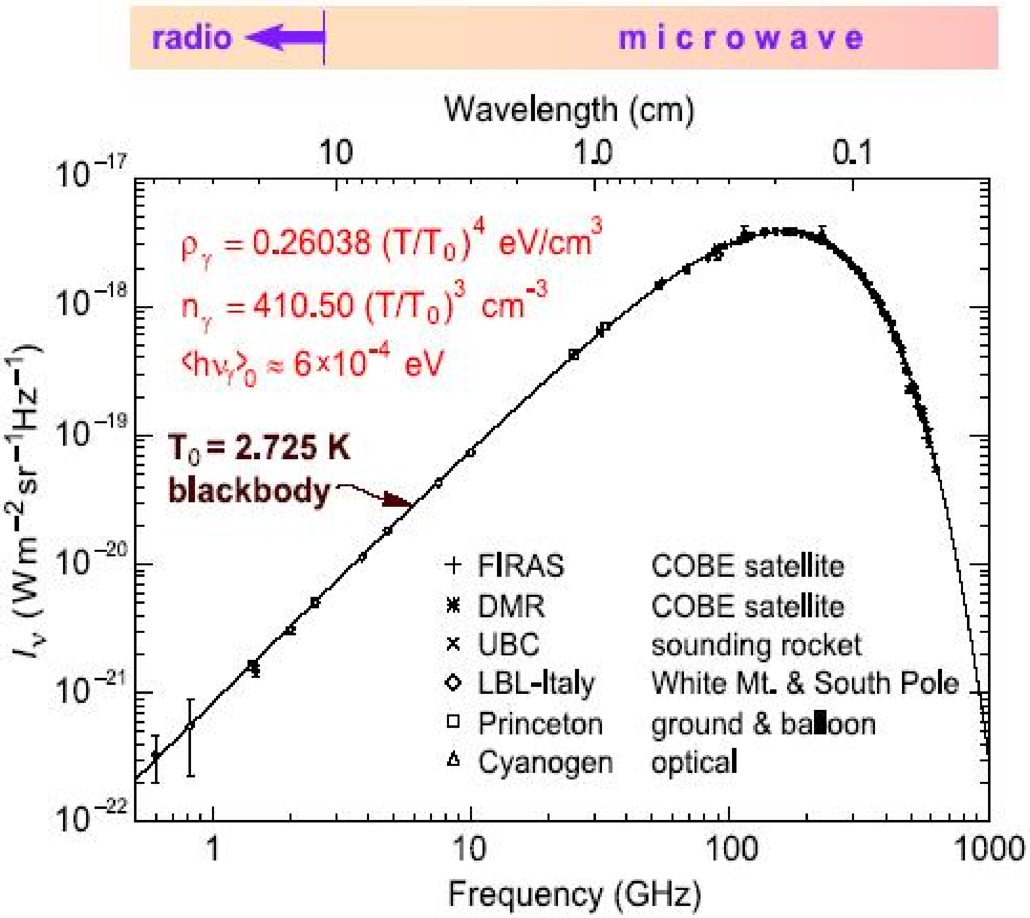

Precise measurements of the CMB (= CBR = RR) spectrum. The line represents a 2.73 K blackbody (present-day value), which describes the spectrum very well, especially around the peak of intensity. The spectrum is less well constrained at 10 cm and longer wavelengths.

When you tune your TV set between channels, *a few percent* of the "snow" that you see on your screen is noise caused by the background of microwaves.

Solar velocity with respect to CMB is 369.3 ± 2.5 km/s.

GZK Kinematics

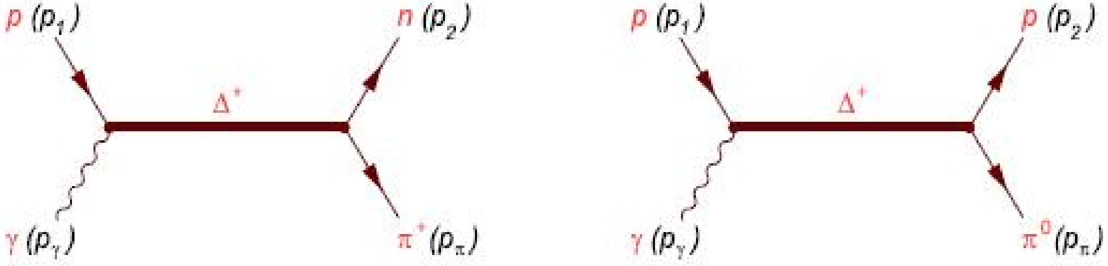

The reaction threshold can be found from the condition

$$s = (p_1 + p_\gamma)^2 = m_p^2 + 2E_\gamma \left(E_1 - P_1 \cos\theta\right) \geq (p_2 + p_\pi)^2_{\min} = (m_p + m_\pi)^2 \,.$$

The minimum occures for head-on collisions ($\cos\theta = -1$). Neglecting $\mathcal{O}\left(m^2/E_1^2\right)$ contributions yields

$$E_1 > \frac{2m_p m_\pi + m_\pi^2 + m_N^2 - m_p^2}{4E_\gamma} \simeq \frac{m_\pi \left(m_p + m_\pi/2\right)}{2E_\gamma}.$$

Therefore, taking $\langle h\nu_\gamma \rangle = 6 \times 10^{-4}$ eV (CMB) we have

$$E_{\text{th}} \simeq \begin{cases} 1.13 \times 10^{20} \, \dfrac{\langle h\nu_\gamma \rangle}{E_\gamma} \text{ eV} \quad \text{for} \quad p\gamma \to n\pi^+ \\ 1.17 \times 10^{20} \, \dfrac{\langle h\nu_\gamma \rangle}{E_\gamma} \text{ eV} \quad \text{for} \quad p\gamma \to p\pi^0. \end{cases}$$

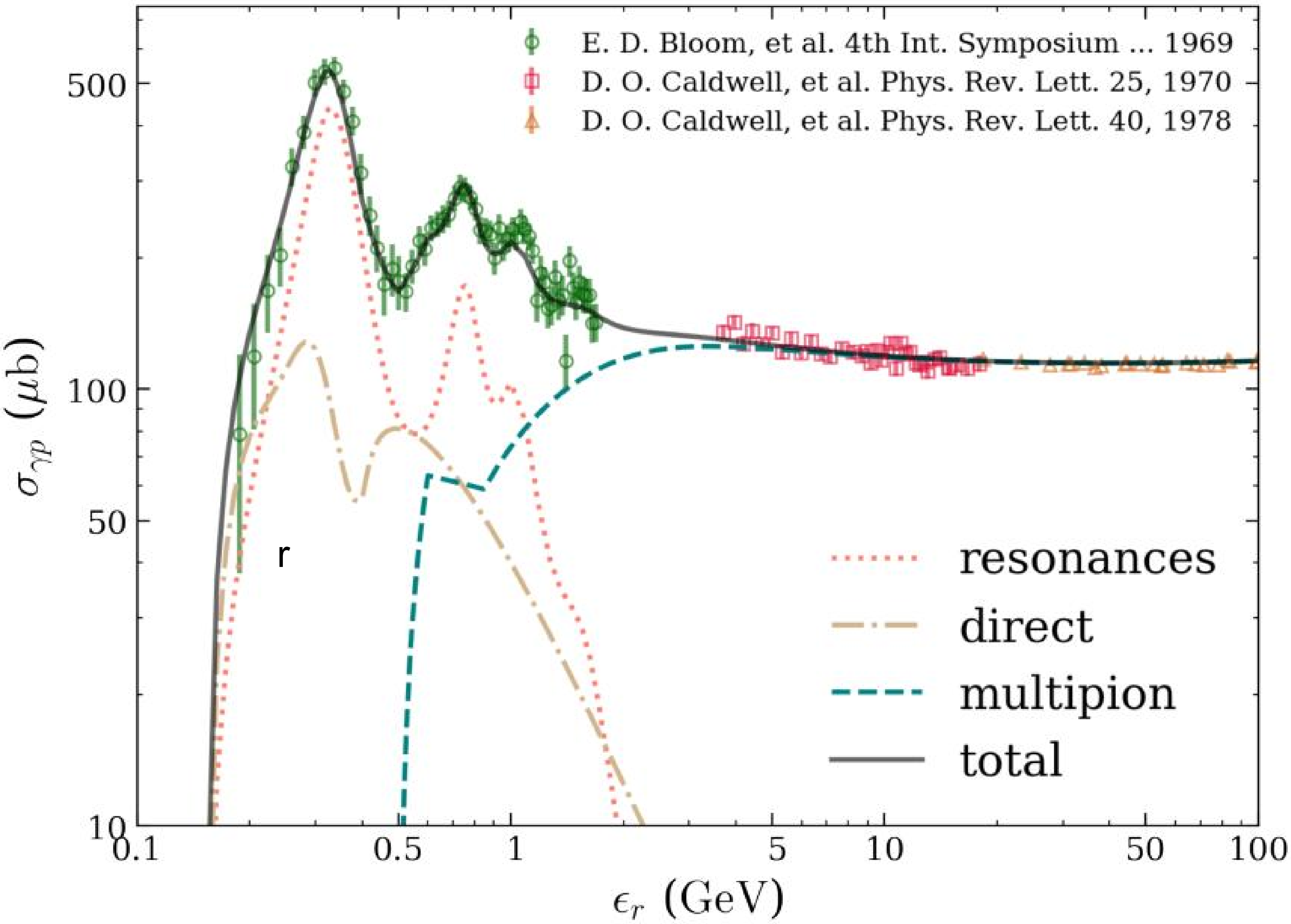

The cross section for inelastic scattering of photons by protons as a function of photon energy in the proton rest frame ϵ_r. The curves correspond to the theoretical estimates of different processes.

[**Reference**: L. Morejon, A. Fedynitch, D. Boncioli, D. Biehla, and W. Wintera, "Improved photomeson model for interactions of cosmic ray nuclei," JCAP11(2019)007, arXiv:1904.07999 [astro-ph.HE].]

GZK Dynamics (UHECR horizon)

$$\frac{\Delta E_p^{(1\pi)}}{E_p} \sim \frac{m_\pi}{m_p} \approx 0.15, \quad \frac{\Delta E_p^{(\text{multi}-\pi)}}{E_p} \sim \frac{\sum m_\pi}{m_p} \approx 0.5$$

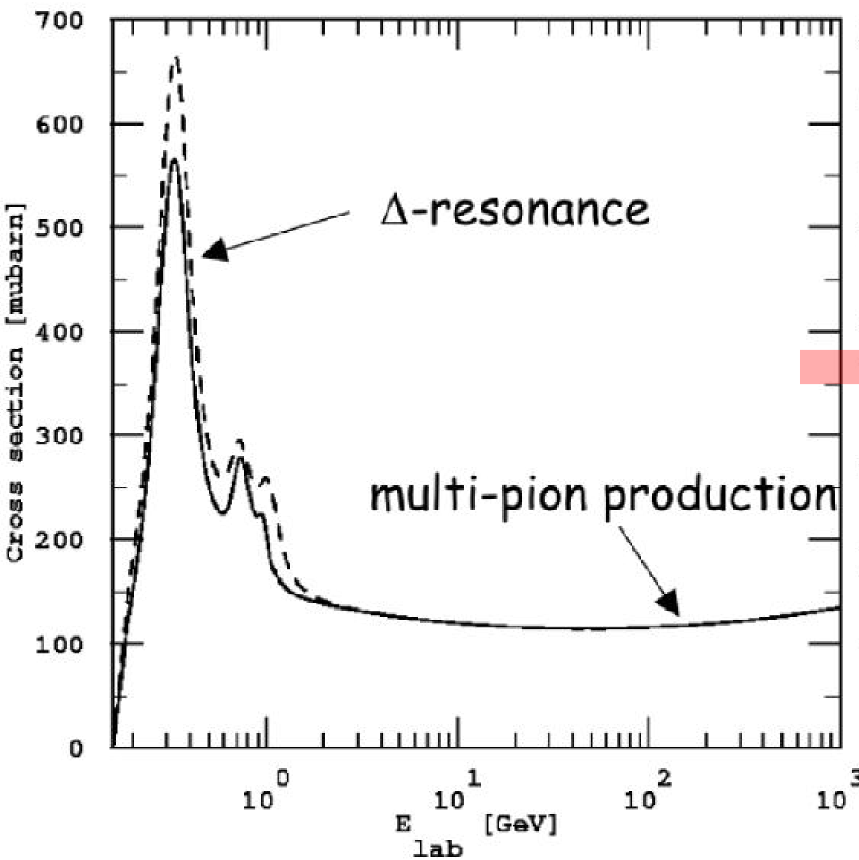

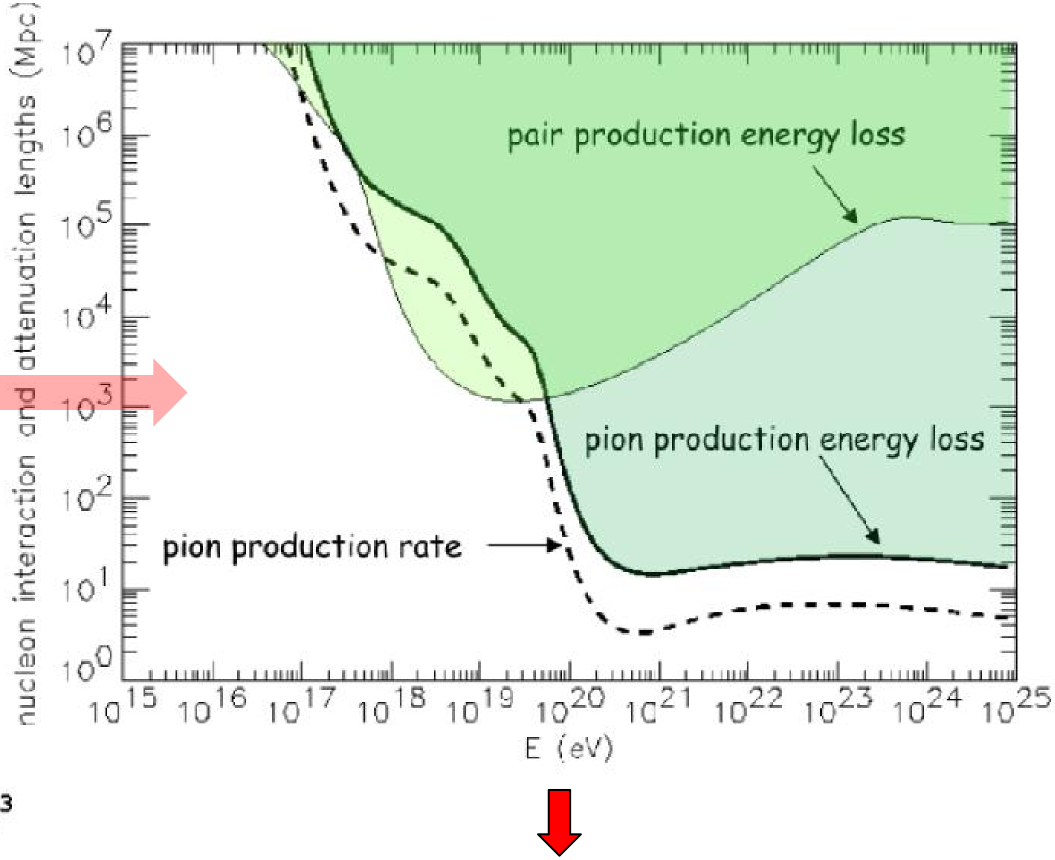

UHECR sources should be closer to 50-100 Mpc from Earth (cf. with the horizon radius of ~5 Gpc).

Gamma-Ray Absorption by CMB (GSJ cutoff)

Similar way one can find the thereshold for $\gamma\gamma_{\text{CMB}} \to e^+e^-$ [R. J. Gould & G. P. Schréder (1966), J. V. Jelley (1966)]:

$$E_{\text{th}} = \frac{m_e^2}{E_\gamma} \simeq 4.35 \times 10^{14} \frac{\langle h\nu_\gamma \rangle}{E_\gamma} \text{ eV}.$$

The total cross section is well known:

$$\sigma_{\gamma\gamma} = \frac{1}{2}\pi r_0^2 (1 - v^2) \left[(3 - v^4) \ln\left(\frac{1+v}{1-v}\right) - 2v(2 - v^2) \right],$$

where $r_0 = e^2/m_e$ is the classical electron radius and v is the electron (and positron) velocity in the center-of-mass system. The differential CMB photon density at energy ϵ and angle θ is (for an isotropic distribution)

$$dn = \frac{1}{2} n(\epsilon) \sin\theta d\epsilon d\theta, \quad \text{where} \quad n(\epsilon) = \frac{\epsilon^2}{\pi^2 \left(e^{\epsilon/kT} - 1\right)}.$$

Then the absorption probability per unit path length is

$$\frac{d\tau_{\text{abs}}}{dx} = \int\int \frac{1}{2} \sigma_{\gamma\gamma} n(\epsilon)(1 - \cos\theta) d\epsilon d\cos\theta,$$

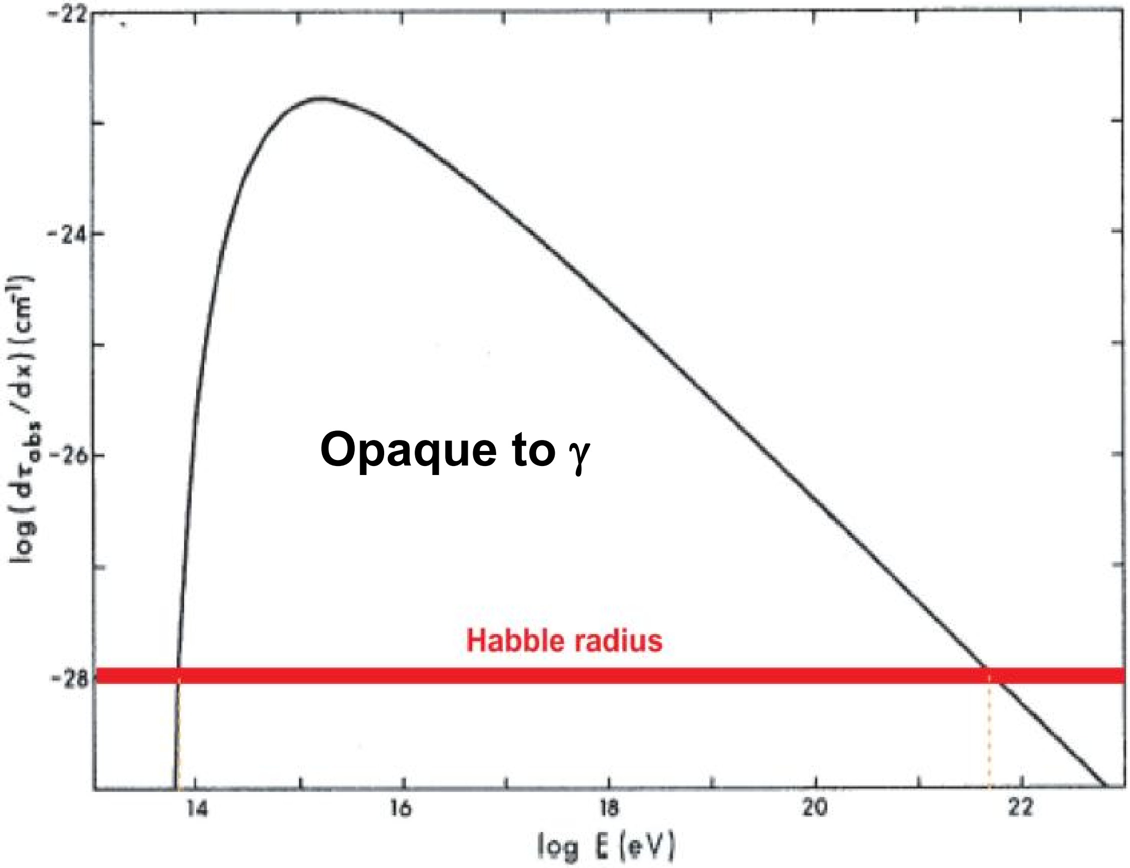

It is seen that the absorption probability is greater than the reciprocal of the "Hubble radius" ($\sim 10^{28}$ cm) or "radius of the Universe" for $10^{14} \lesssim E \lesssim 10^{22}$ eV. For photons in this energy range, the absorption optical depth to the edge of the Universe would be > 1.

That is, we could "see" only out to a distance $d \sim (d\tau_{\mathsf{abs}}/dx)^{-1}$ in the Universe.

Note: The figure[a] is a bit obsolete since (a) it has been calculated for $T = 3.5\ K$ and (b) it takes no account for the redshift. However the qualitative result remains the same.

---

[a] Borrowed from R. J. Gould & G. P. Schréder, "Opacity of the universe to high-energy photons," Phys. Rev. Lett. **16** (1966) 252–254.

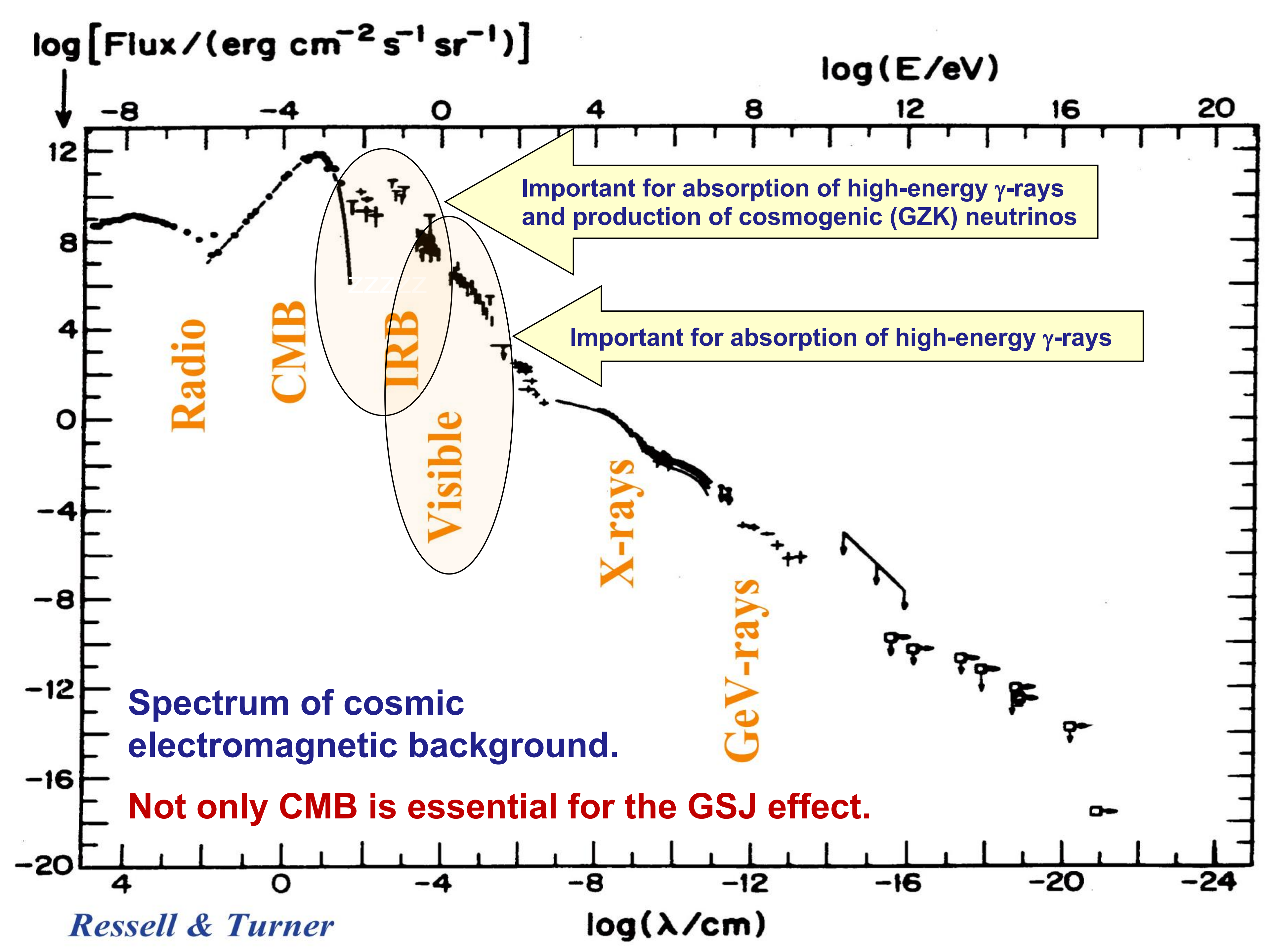
log [Flux/(erg cm^{-2} s^{-1} sr^{-1})]
log(E/eV)
−8
−4
0
4
8
12
16
20
12
8
4
0
−4
−8
−12
−16
−20
4
0
−4
−8
−12
−16
−20
−24
log(λ/cm)
Radio
CMB
IRB
Visible
X-rays
GeV-rays
Important for absorption of high-energy γ-rays and production of cosmogenic (GZK) neutrinos
Important for absorption of high-energy γ-rays
Spectrum of cosmic electromagnetic background.
Not only CMB is essential for the GSJ effect.
Ressell & Turner

Cosmic Infrared Background

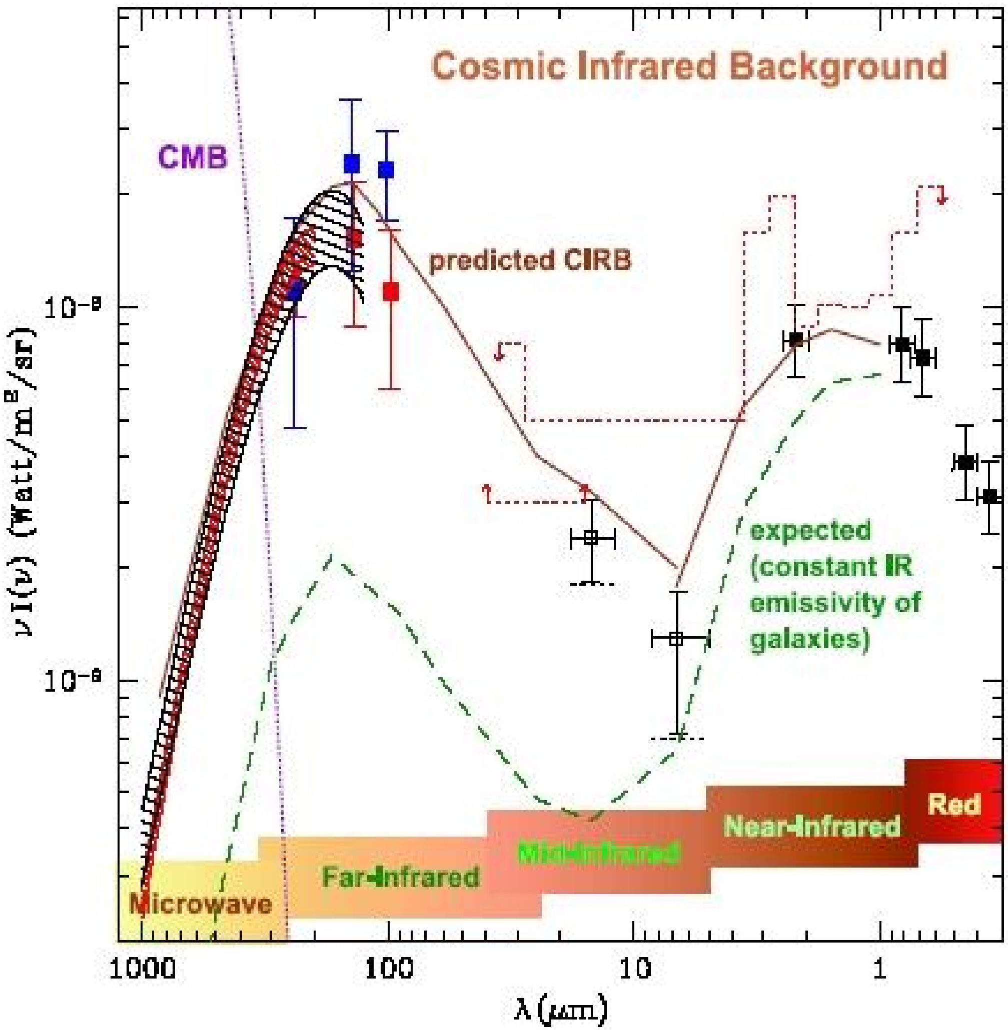

The CIRB spectrum as measured by independent groups in the all-sky COBE maps, compared with estimates of the optical extragalactic background based on ultradeep optical integrations by the Hubble Space Telescope. The dashed histograms are limits set by TeV cosmic opacity measurements. The lower dashed line is the expected intensity based on the assumption that the IR emissivity of galaxies does not change with cosmic time. The thick line is the predicted CIRB spectrum of a model for IR galaxy evolution.

[From A. Franceschini *et. al.*, "A long-wavelength view on galaxy evolution from deep surveys by the infrared space observatory," astro-ph/0108292.]

Optical view of the Galactic Center

[From Howard McCallon]

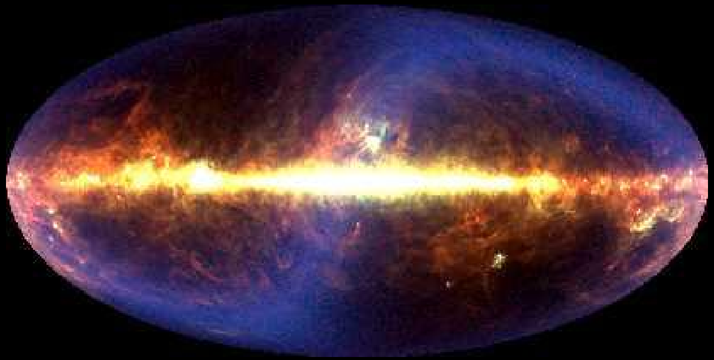

The Galaxy taken by the COBE satellite as a composite of Far-IR wavelengths of 60, 100, and 240 μm. The Galactic Center shines brightly in the Far-IR because of the thick concentration of stars embedded in dense clouds of dust. These stars heat up the dust and cause it to glow.

[From Michael Hauser, COBE/DIRBE Sci. Team & NASA]

Near-IR view of the Galactic Center

[from the 2 Micron All Sky Survey "2MASS"]

Spectral Region	Wavelength Range (μm)	Temperature Range (K)	What we see
Near-Infrared	**(0.7-1) to 5**	**740 to (3,000-5,200)**	Cooler red stars Red giants Dust is transparent
Mid-Infrared	**5 to (25-40)**	**(92.5-140) to 740**	Planets, comets, asteroids Dust warmed by starlight Protoplanetary disks
Far-Infrared	**(25-40) to (200-350)**	**(10.6-18.5) to (92.5-140)**	Emission from cold dust Central regions of galaxies Very cold molecular clouds

[From IPAC, NASA , URL: http://www.ipac.caltech.edu/Outreach/Edu/Regions/irregions.html]

Cosmic X-ray & γ-ray Backgrounds

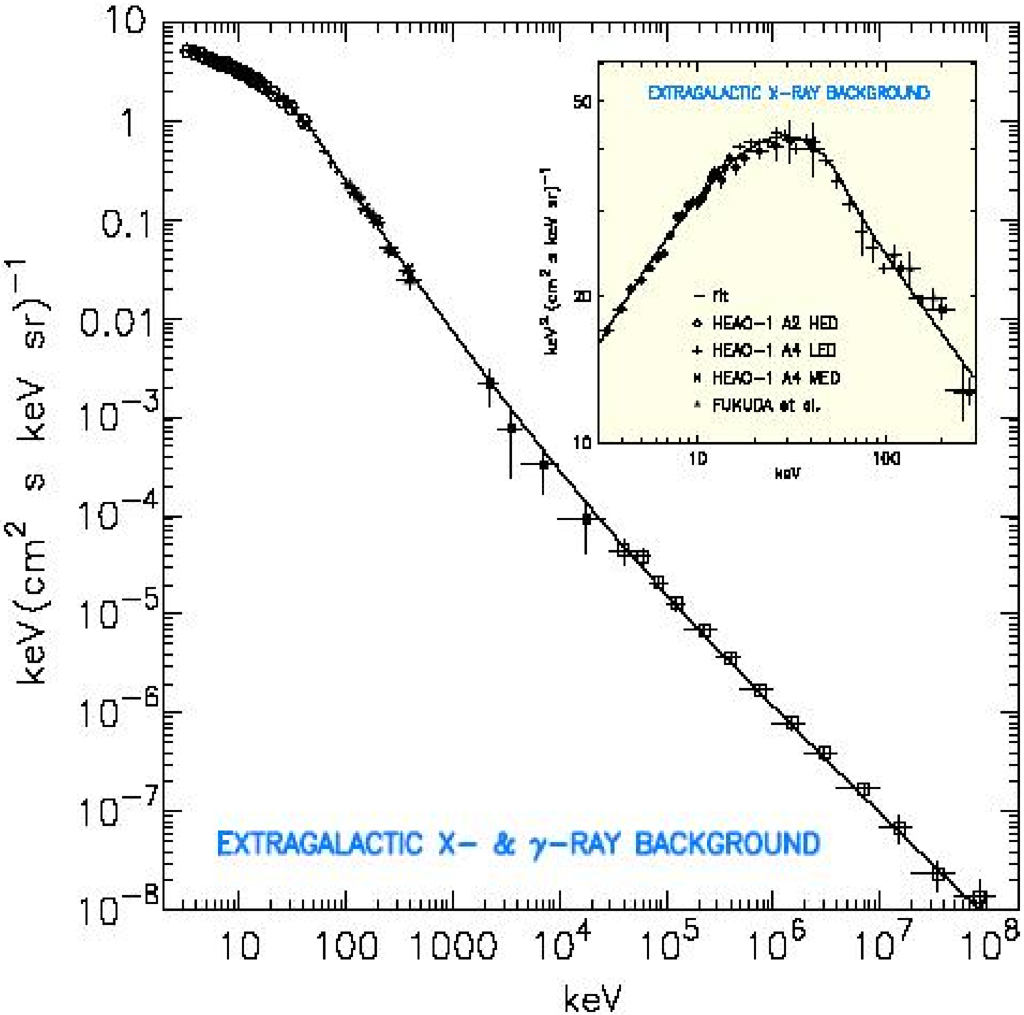

Selected results on the intensity spectrum of the diffuse cosmic component over the 3 keV to 100 GeV range. The results are fitted to simple empirical exponential and power-law functions. The reduced χ^2 of the fit is about 1.3, over almost eight decades of photon energy. Various source classes and physical processes are postulated to dominate in different spectral ranges. Comptel and Egret data are marked with filled and open squares, respectively. The data in inset are multiplied with energy.

[From D. E. Gruber *et. al.*, "The spectrum of diffuse cosmic hard X-rays measured with HEAO-1," ApJ **520** (1999) 124 (astro-ph/9903492).]

More recent look on γ-ray horizon

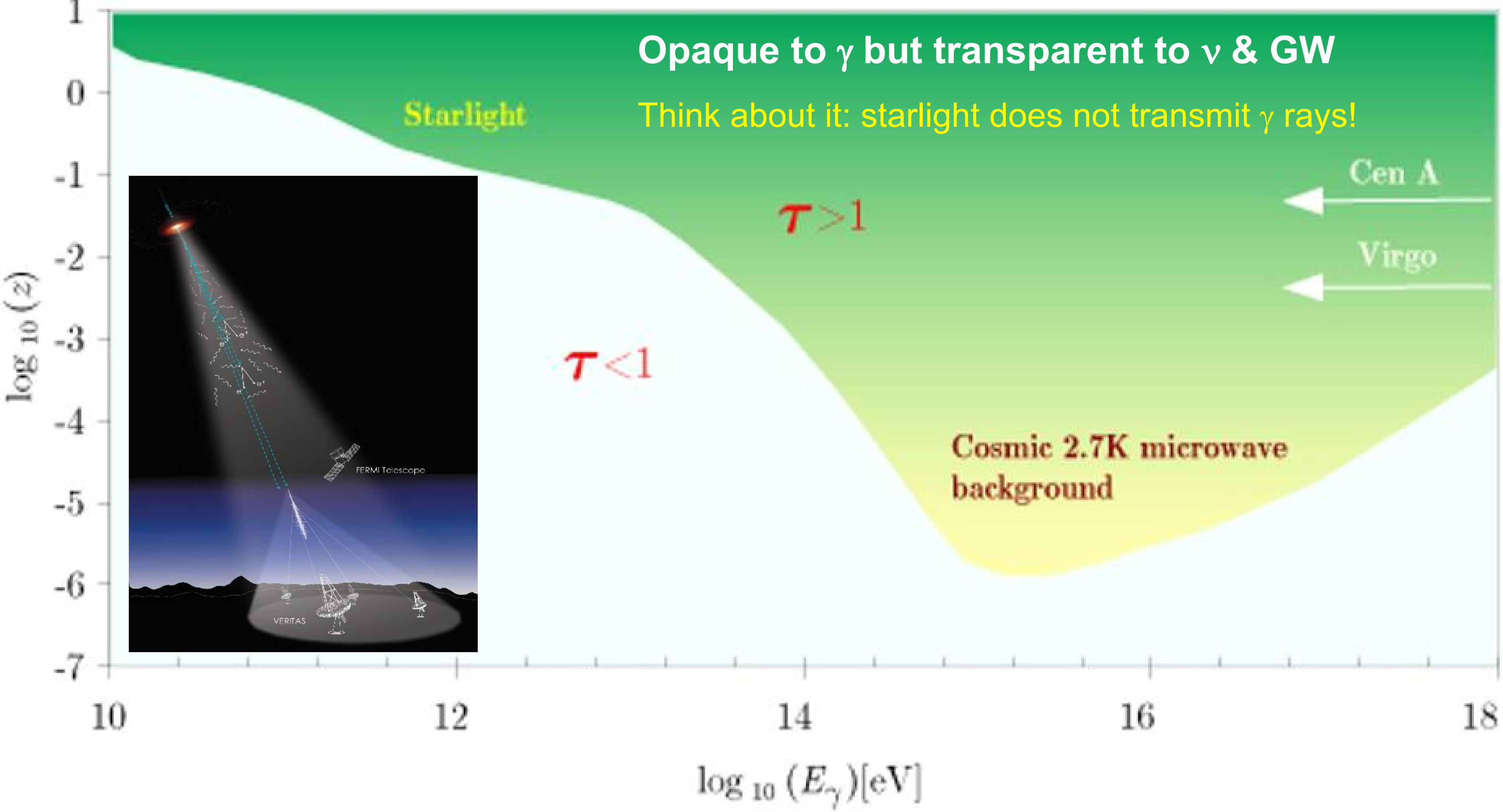

The horizon of high-energy γ-rays in terms of **redshift** *z*. The shaded region marks the regime of large optical depth, i.e., γ-rays at these energies from sources at these redshifts will not reach us. The basis for this curve is an ambient photon distribution and intensity composed of the **cosmic microwave background** and average **starlight**. The contribution of each component to the absorption from γγ -pair production is indicated.

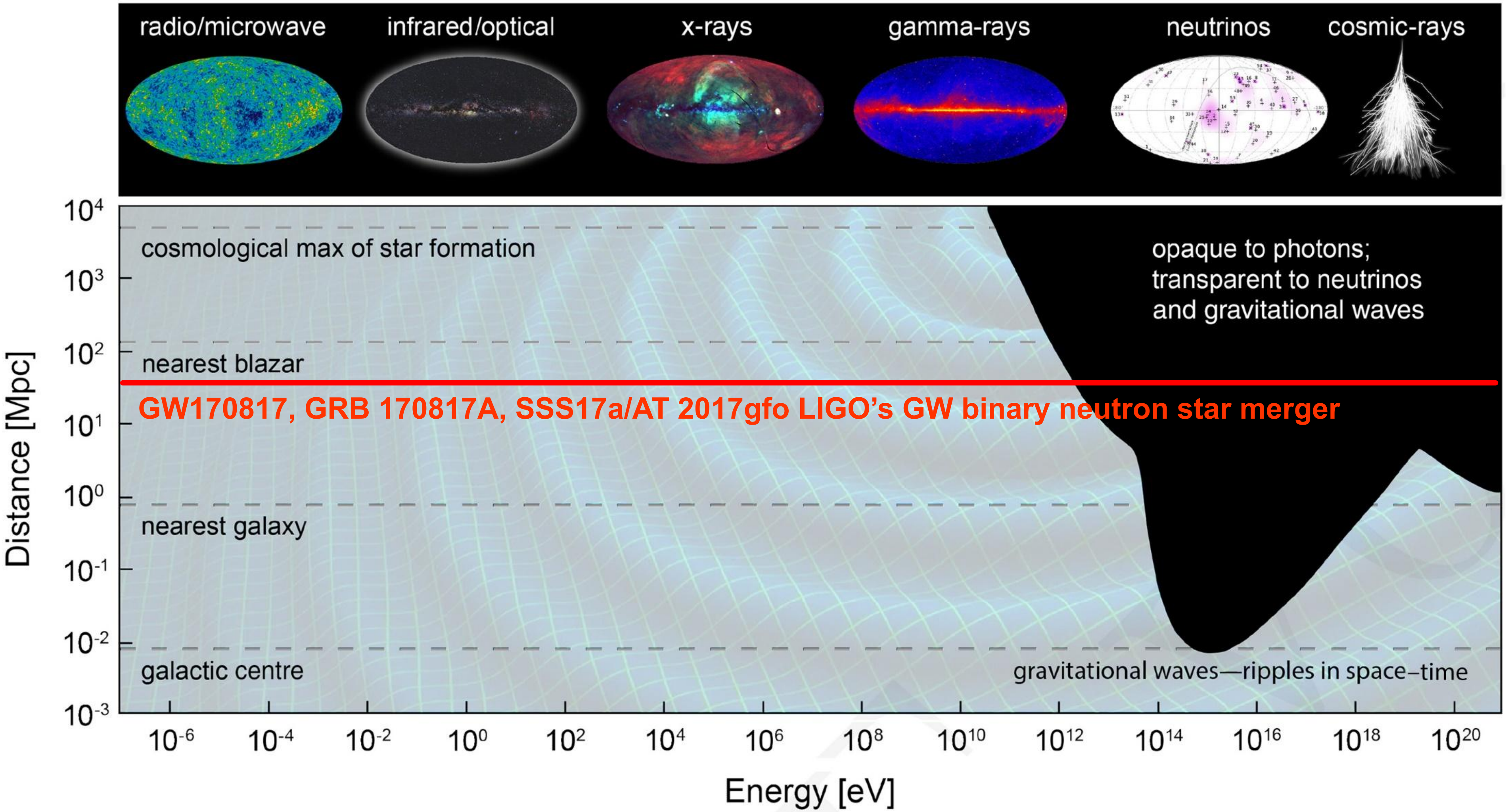

The horizon of γ-rays in terms of distance for a wide energy range. While lower-energy photons can travel to us from the farthest corners of the Universe, the highest energy photons and cosmic rays are attenuated after comparatively short distances due to the GSJ and GZK cutoffs obscuring our view of the most energetic cosmic events.

[From I. Bartos & M. Kowalski, "Multimessenger Astronomy" (Physics World Discovery, IoP Publishing, Bristol, 2017).]

Two classes of UHECR production models

- **Bottom-up (BU)** scenario:

  UHECRs are assumed to be accelerated in electromagnetic fields of astrophysical objects (known or exotic).

  ⇒ charged particles (protons, nuclei, electrons).

  Secondaries: photons & neutrinos.

  Disadvantages:
  - acceleration above 10^{20} eV difficult
  - no visible sources

- **Top-down (TD)** scenario:

  It is the umbrella term for all models in which the observed UHECR are formed as decay products of some superheavy X particles. These hypothetical particles could either be metastable (lifetime > age of Universe) or emitted by relic topological defects in the present epoch. In both cases, the range of masses suggested by the AGASA excess is very narrow, $m_X = 10^{12-14}$ GeV .
  The lower limit follows from the highest observed CR energies, $E_{max} = (2-3)\times10^{11}$ GeV, while the upper limit is model-dependent, it can be derived by comparing the integral flux predicted in the TD model with the non-observation of UHECRs above E_{max} ; usually $m_X^{max} = (2-3)\times10^{13}$ GeV.

  Fragmentation products: mainly photons & neutrinos.

  Advantages:
  - no acceleration problem
  - if X = CDM, no GZK cutoff

Partial list of "explanations" for the AGASA mystery

- Origin in nearby ($z<0.01$) Seyfert galaxies.
- Origin in distant radio galaxy jets and hot spots.
- Origin in colliding galaxy systems.
- Origin in large-scale structures (pancakes, filaments, flow shocks to clusters of galaxies).
- Links with (cosmological) gamma-ray bursts.
- Compact astrophysical sources like microquasars, magnetars, quark novae.
- Photons, electrons and nucleons initiated by UHE cosmic neutrinos on relic neutrino background (Z-bursts).
- Decay of metastable superheavy relic particles trapped in the Galactic halo.
- UHE SUSY candidates (gluinos, glubolinos, neutralinos, shadrons, sgoldstionos, etc.)..
- Evaporation of primordial black holes.
- Decay of topological defects (such as monopoles, vortons, superconducting cosmic strings, hybrid defects like necklaces, etc.) created in the early Universe.
- Symmetry broken by wormhole or instanton effects.
- Topological defects (quasistable monopoles, etc.) themselves as UHECR particles.
- Space-time's unseen dimensions, KK-modes, branes, and all that.
- Lorentz symmetry violations with anomalous kinematics, modified dispersion relation from *q*-deformed noncommutative theory.
- Other exotic and Sci-Fi :
  - ✓ Stranglets / quark nuggets / nuclearities;
  - ✓ New hadrons, uchecrons, superbaryons made of color sextet quarks;
  - ✓ WIMPZILLAs and other superheavy relic X particles (X-bursts);
  - ✓ Crcryptons (fractionally charged and confined particles) of SUSY theories;
  - ✓ Photon-Axion mixing (for UHE photons);
  - ✓ Non-linearity in quantum mechanics, discrete space, quasi-static Universe,…

← More generally: active galaxies

Intriguing opportunity:

Z-bursts resulting from the resonant annihilation of ultrahigh-energy cosmic neutrinos on relic antineutrinos are among proposed wittily explanations of the UHECR puzzle.

This solution has the same drawback as the explanation of the origin of life by panspermia…

Note: **3C279** a gamma-ray quasar, is one of the few known blazars in existence. It is located at a redshift of $z = 0.5362$.

The name signifies that it was the 279th object (ordered by right ascension) of the Third Cambridge Catalog of Radio Sources (**3C**), published in 1959.

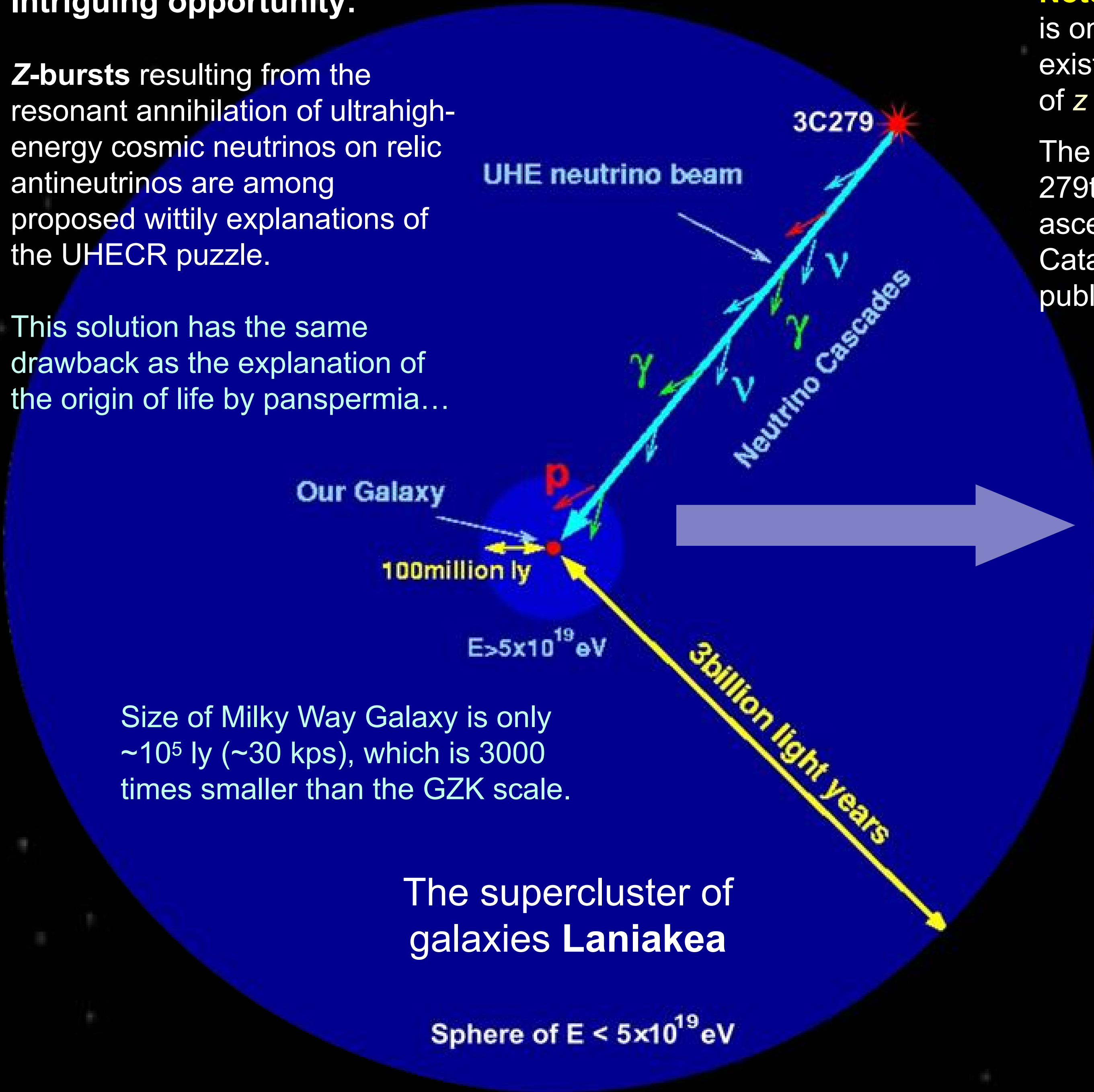

Size of Milky Way Galaxy is only ~10^5 ly (~30 kps), which is 3000 times smaller than the GZK scale.

The supercluster of galaxies **Laniakea**

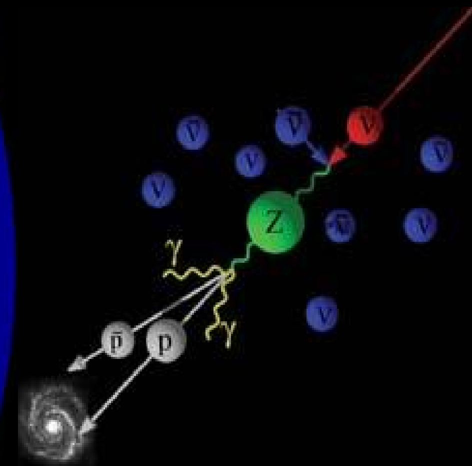

It seems the gale subsided (state on 2005)

after HiRes | after Pierre Auger

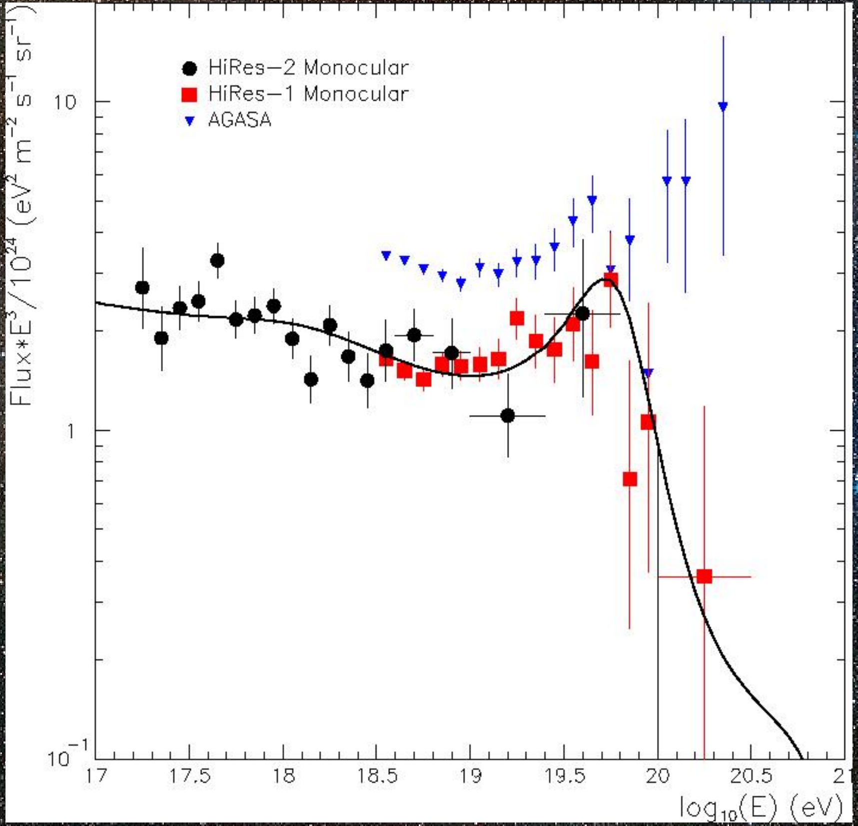

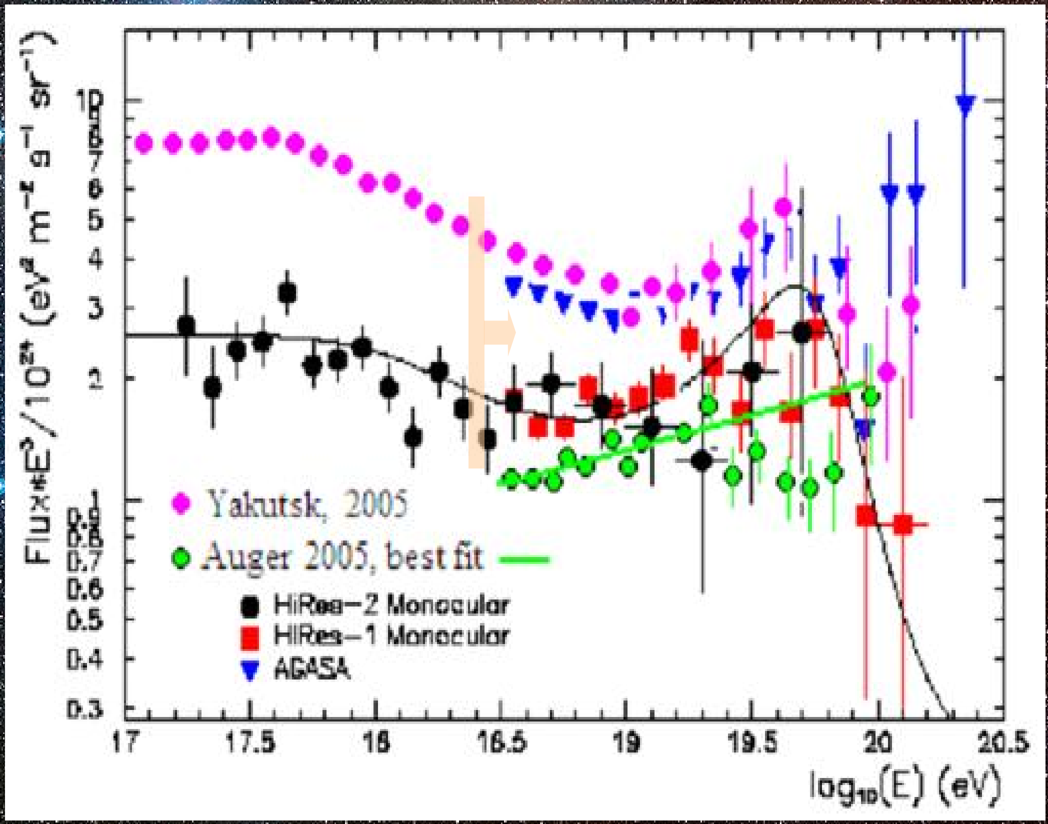

Number of events above 3 EeV:

Yakutsk – 1303 Auger – 3525
AGASA – 7000 HiRes 1 – 1616

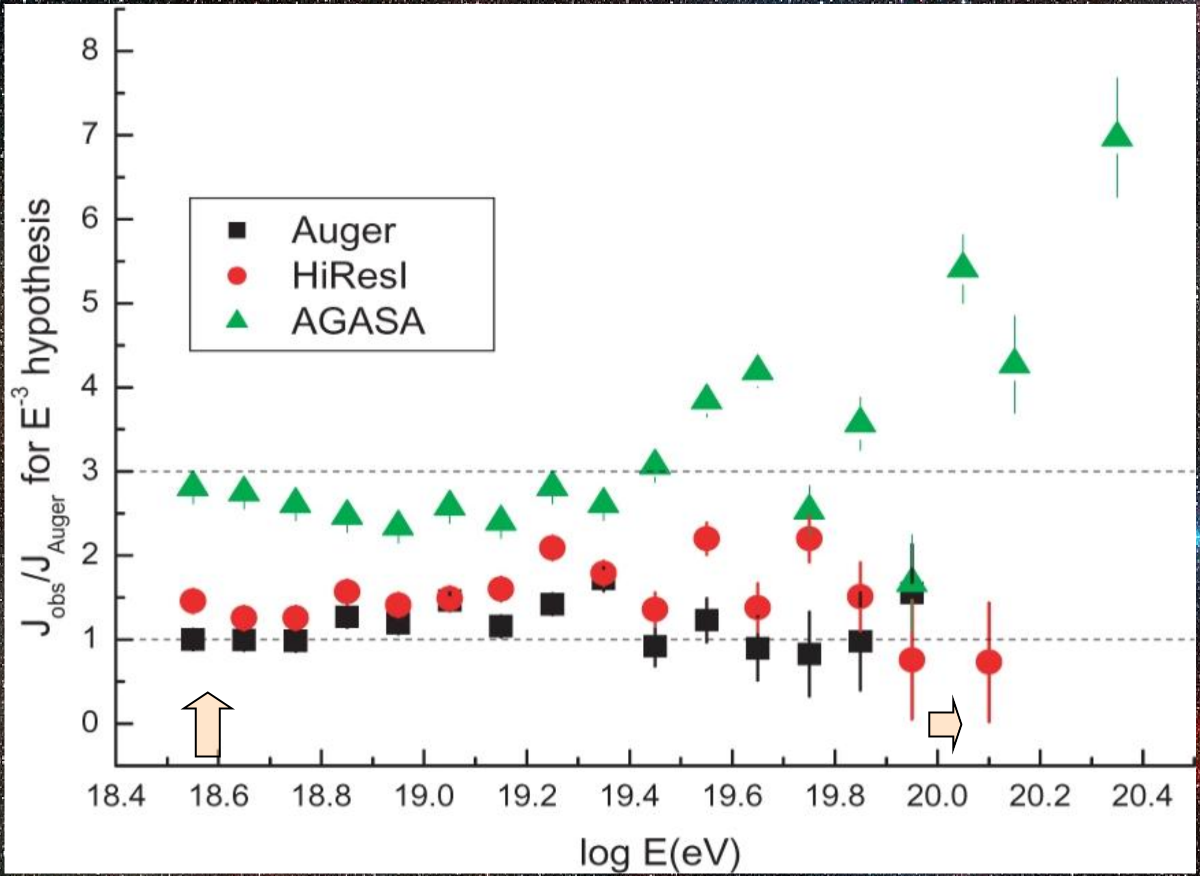

The ratio of the values of each point with respect to a fit of E^{-3} to the first point of the **Auger** spectrum at **3.55 EeV** which contains **1216 events**.

The purpose of the plot is to illustrate the differences between the different measurements in a straight-forward manner.

Yakutsk data are not included in this plot as they are so discordant (see previous slide).

The differences between the fluorescence measurements by **Auger** and **HiRes I** are relatively small except at the highest energies where the **Auger** statistics are presently too low to comment on the flux above 100 EeV.

The difference between **AGASA** and the fluorescence measurements probably arises, at least in part, because of the mass and hadronic model assumptions.

[**Reference:** A.A. Watson, "Observations of Ultra-High Energy Cosmic Rays," a talk given at 9th International Conf. on Astroparticle & Underground Physics ("TAUP 2005"), Zaragoza, September 10-14, 2005 (astro-ph/0511800).]

State of the Art — 2019: UHECR spectrum

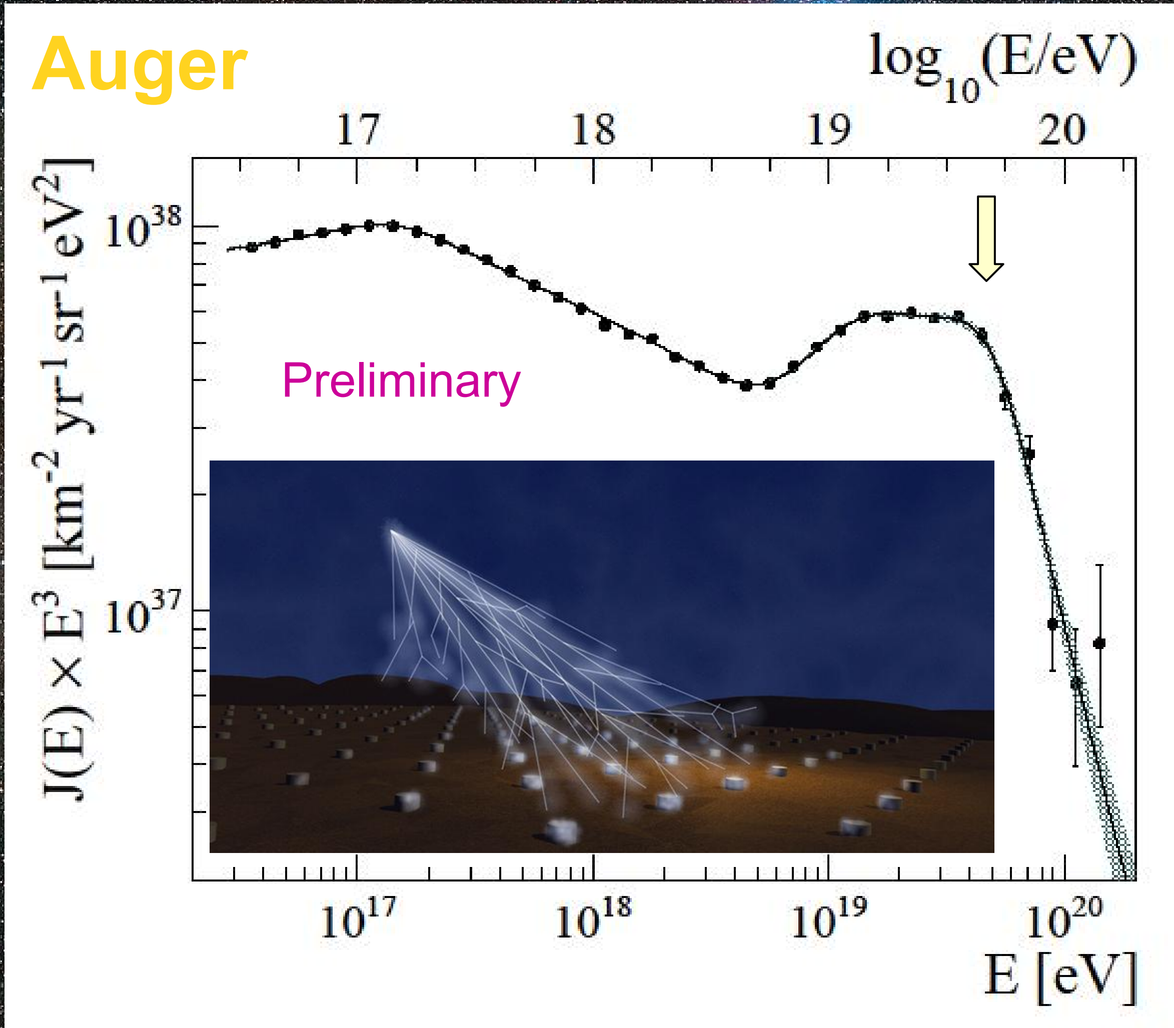

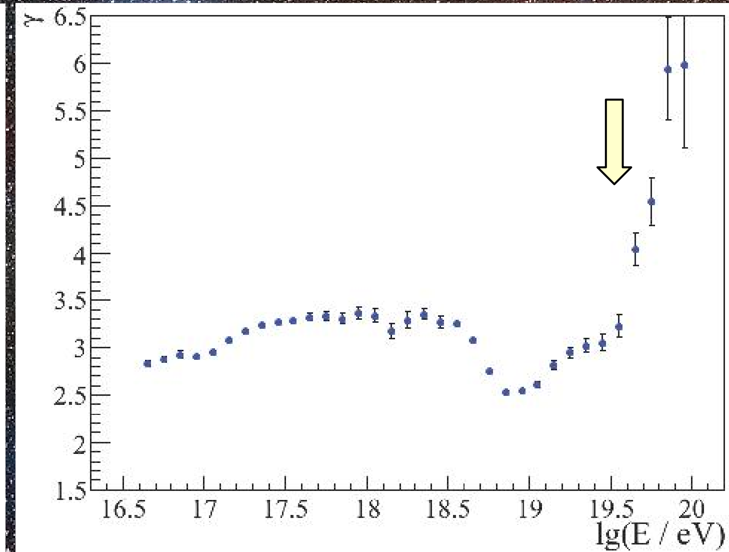

Evolution of the spectral index vs. energy. The spectral indexes are obtained from power law fits to the spectrum over sliding windows of 3 bins in log(E/eV).

The Auger data confirm the suppression of the flux above ~ **5×10^{19} eV**.

The energy spectrum (multiplied by E^3) from the combination of the different measurements with the Pierre Auger array.

[**Reference:** A. Castellina, "Highlights from the Pierre Auger Observatory", PoS(ICRC2019)004, arXiv:909.10791 [astro-ph.HE].]

Some questions disappear, but new ones appear…

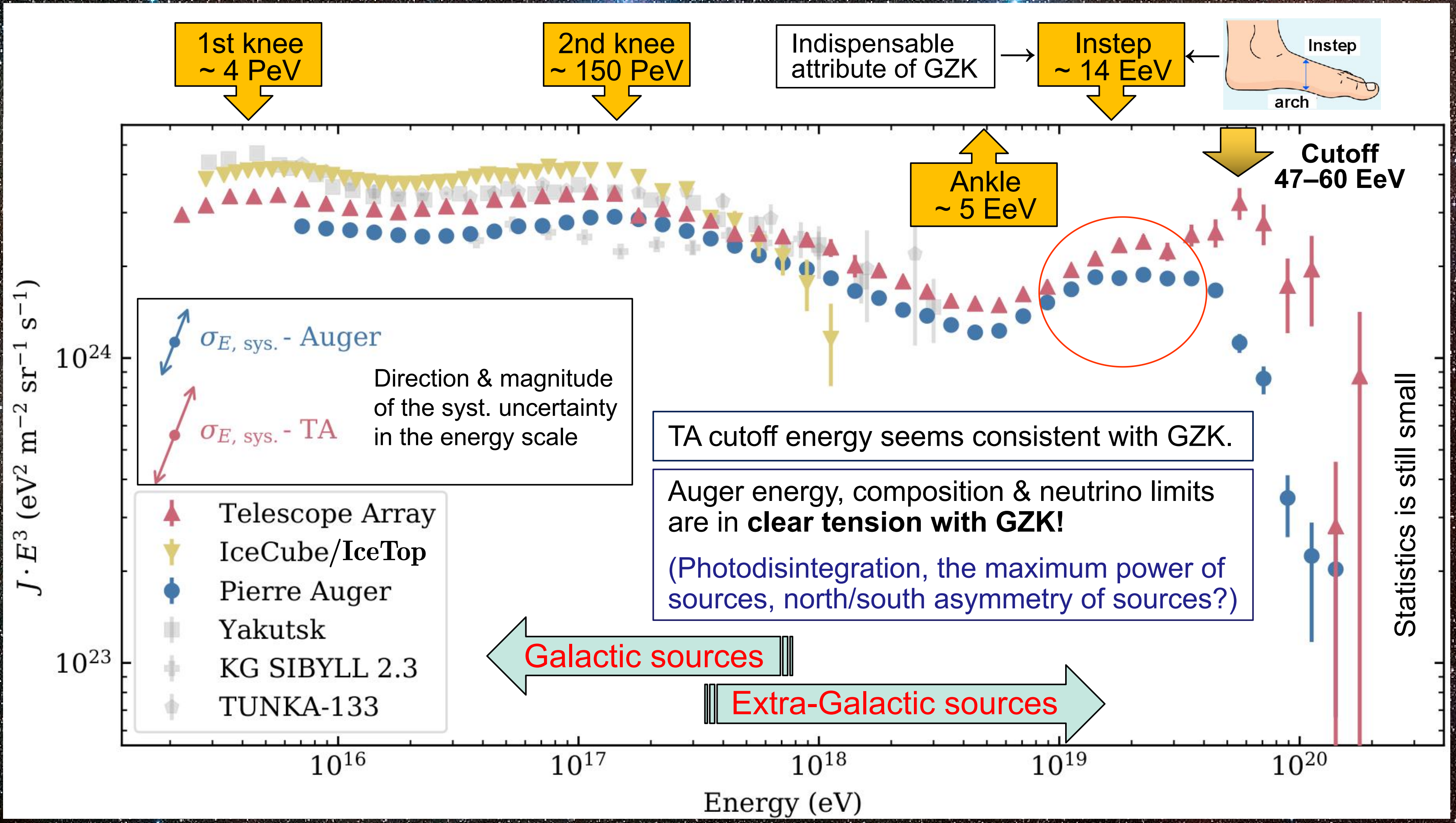

Recent measurements of the all-particle CR flux, which define the spectral features in the UHE region.

[**References**: A.Coleman et al., "Ultra-high-energy cosmic rays," Astropart. Phys. 149 (2023) 102819, arXiv:2205.05845 [astro-ph]; E. Mayotte, "Observations of Ultra-High-Energy Cosmic Rays", report at TAUP XVIII, Vienna, September 1, 2023).]

Telescope Array (TA)
Delta, UT, USA
507 detector stations, 680 km²
36 fluorescence telescopes

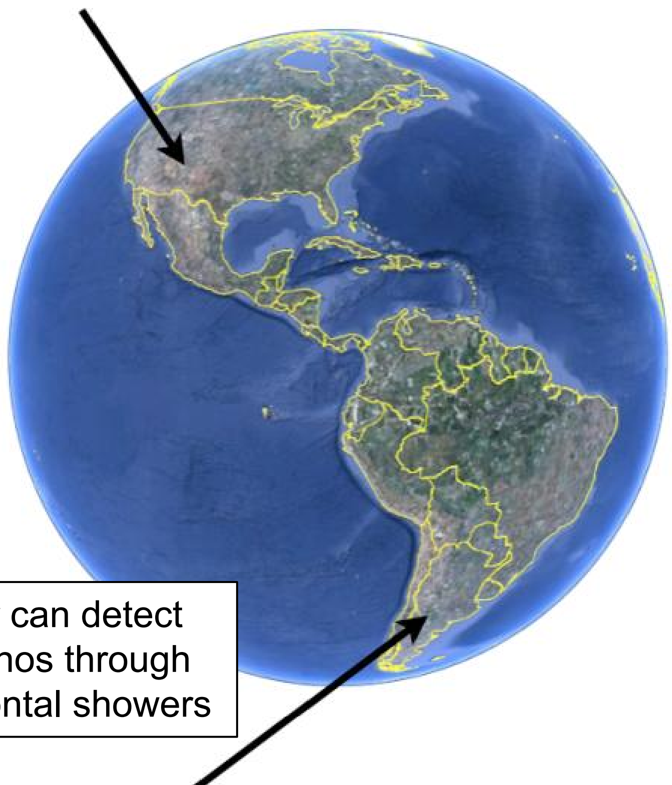

Auger can detect neutrinos through horizontal showers

Pierre Auger Observatory
Province Mendoza, Argentina
1660 detector stations, 3000 km²
27 fluorescence telescopes

[From A. Castellina, a report on INAF, 26-05-2021.]

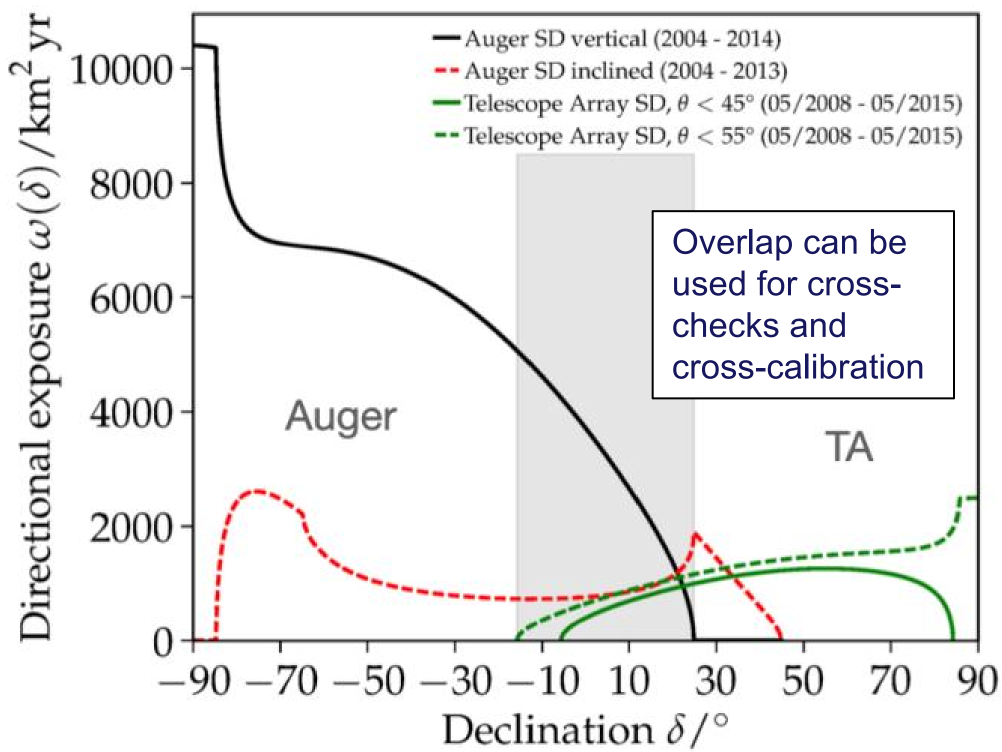

↑ Telescope Array
← Pierre Auger Observatory

UHECR anisotropy by Auger — State of the Art 2022

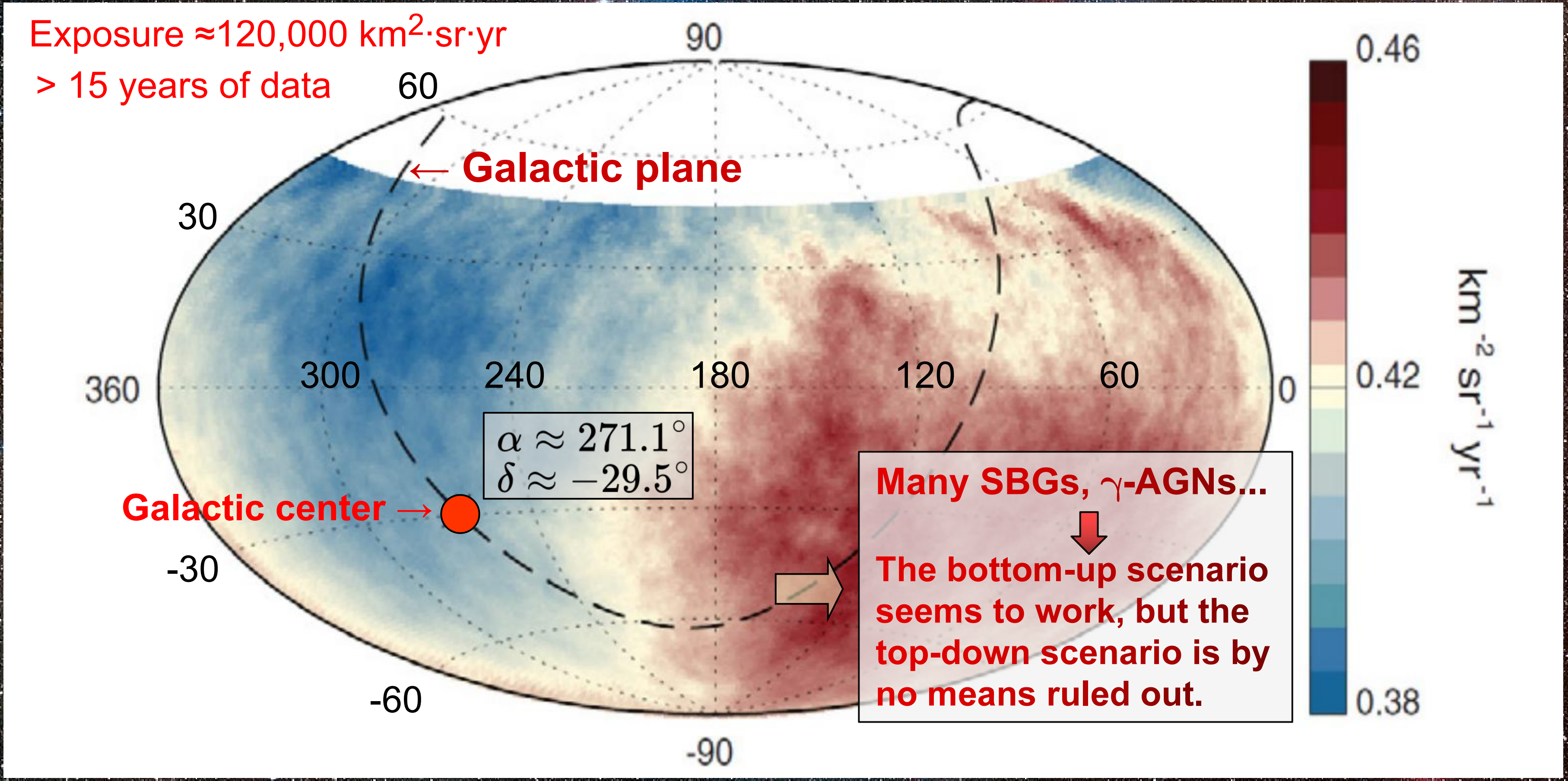

The CR flux above 8 EeV, averaged on top-hat windows of 45° radius (equatorial coordinates).

Under the assumption that higher multipoles are negligible, Auger Collaboration founds a total dipolar amplitude for $E \geq 8$ EeV of $\delta = 0.066 \pm 0.012$, pointing about 113° away from the direction of the Galactic center, as such **indicating an extragalactic origin of the modulation**. A combined analysis of the Pierre Auger and Telescope Array collaborations is consistent with that obtained by Auger alone, with smaller uncertainties when allowing for non-vanishing quadrupole moments.

[**Reference:** L. Perrone (for the Pierre Auger Collaboration), "Ultra-high energy cosmic rays with the Pierre Auger Observatory," EPJ Web Conf. **280** (2023) 01002. (a report at RICAP-22)]

Sculptor Galaxy (also known as the **Silver Coin**, **Silver Dollar Galaxy**, **NGC 253**, or **Caldwell 65**) — the closest starburst galaxy to the Milky Way.

A starburst galaxy (SBG) is a galaxy that exhibits an exceptionally high star formation rate (SFR) compared to the average long-term SFR of the galaxy or the SFR observed in most other galaxies.

For example, the SFR in the Milky Way galaxy is about $3M_\odot$ /year, while in SBG the SFR can reach $100M_\odot$ /year or even more. Such a large SFR means that the galaxy will consume its entire reservoir of star-forming gas in a timescale, T_{SBG} , much shorter than the age of the galaxy (namely T_{SBG} << 1 Gyr).

Thus, star formation is a phase that occupies a short period of galaxy evolution. Perhaps it is during this period that the formation of UHECR occurs. Most SBGs are in the process of merging or having a close collision with another galaxy, ... possibly generating shock waves ... but this is just a naive hypothesis.

More observational data on Galactic CR spectrum and composition

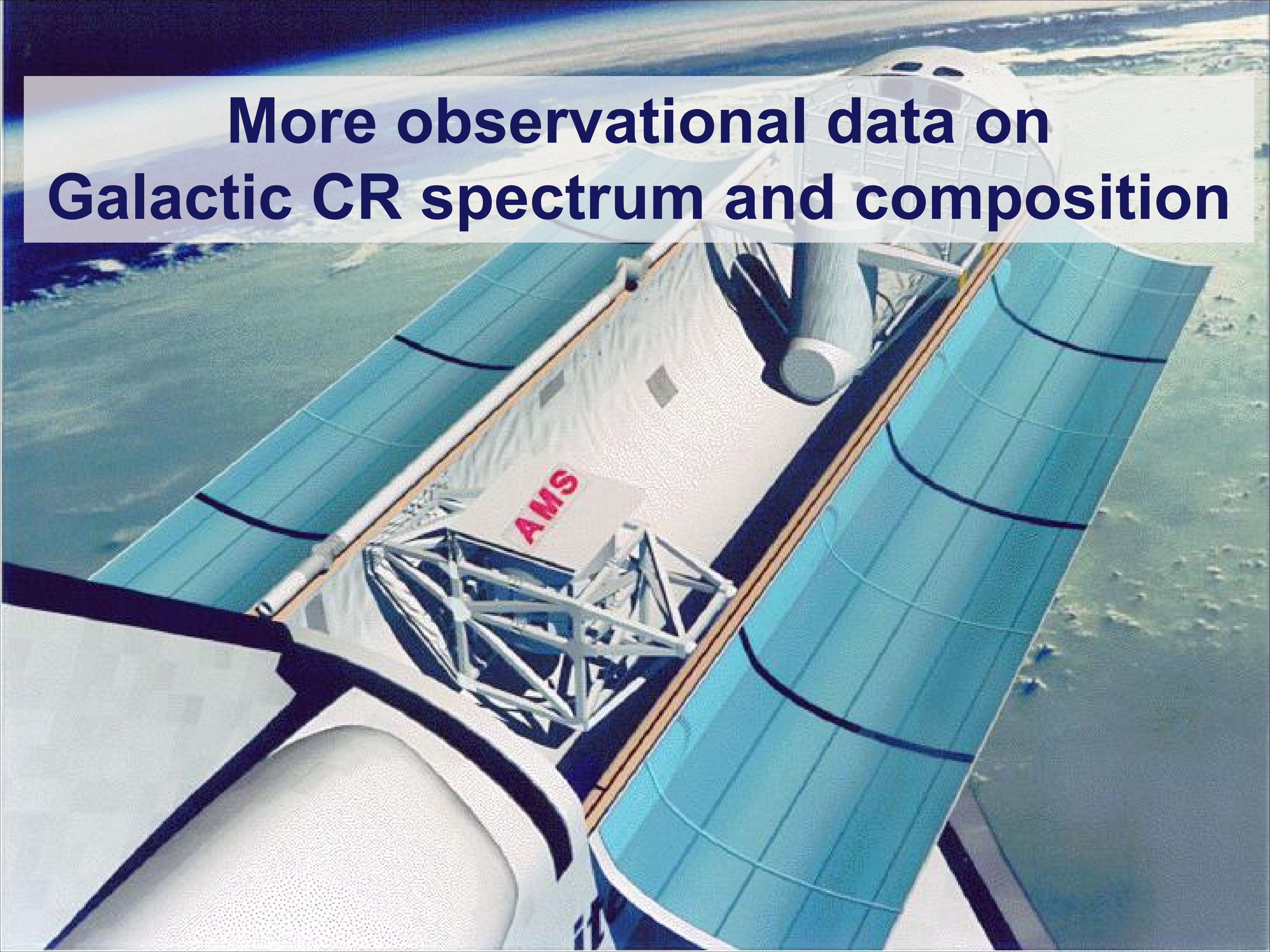

CR composition at low energies

Particle abundances in CR (at E > 2.5 GeV/particle, minimum SA) and in Universe

Nuclear group	Particle charge, Z	Integral Intensity in CR ($m^{-2}\,s^{-1}\,sr^{-1}$)	Number of particles per 10^4 protons	
			CR	Universe
Protons	1	1300	10^4	10^4
Helium	2	94	720	1.6×10^3
L	3-5	2	15	10^{-4}
M	6-9	6.7	52	14
H	10-19	2	15	6
VH	20-30	0.5	4	0.06
SH	>30	10^{-4}	10^{-3}	7×10^{-5}
Electrons	-1	13	100	10^4
Antiprotons	-1	>0.1	5	?

The abundances of primary CR is essentially different from the standard abundances of nuclei in the Universe. The difference is biggest for the light nuclear group **L** (Li, Be, B).

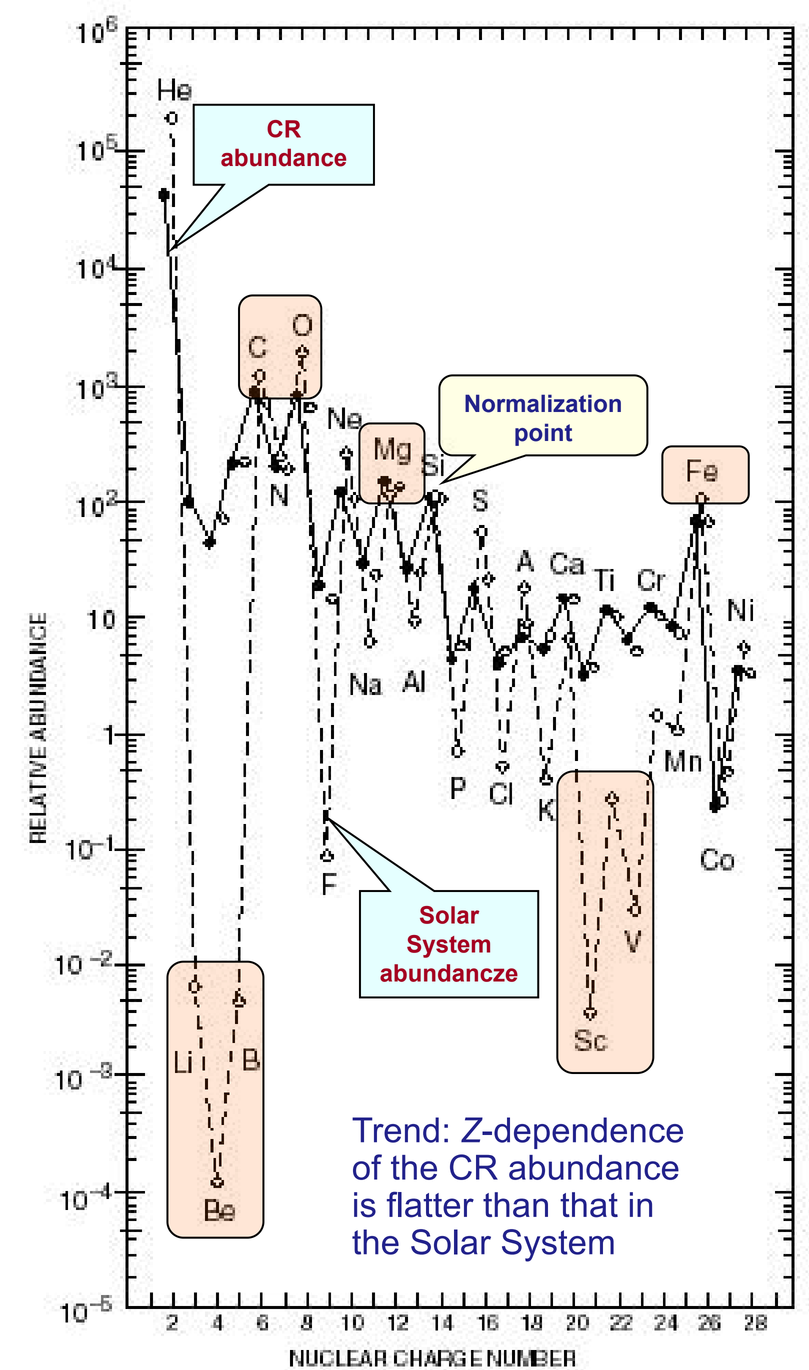

Over the charge region Z=1–28 (H–Ni), CR experiments in space can resolve the individual elements over an extended energy range. A summary of these data shows the relative abundance of CR at ~1 AU (solid line) along with the Solar System abundance (dashed line) for two different energy regimes, 70–280 MeV/nucleon and 1–2 GeV/nucleon. All abundances are normalized at one for silicium (**Si**) and the later is taken to be 100.

[**Reference:** J.A. Simpson, Ann. Rev. Nucl. Part. Sci. **33** (1983) 323.]

- Hydrogen (**H**) and helium (**He**) are the dominant elements, constituting some 98% of the CR ions, but are still under-abundant in the CR relative to the Solar System abundance.

There is reasonably good agreement between the CR and Solar System abundance data for most of the even elements particularly for carbon (**C**), oxygen (**O**), magnesium (**Mg**) and iron (**Fe**).

The light elements lithium (**Li**), beryllium (**Be**) and boron (**B**) as well as scandium (**Sc**) and vanadium (**V**) in the sub-iron region are greatly over-abundant when compared to the Solar System abundance. This is a result of nuclear spallation (or x-process) in interstellar space by nuclei of higher charge. The daughter nuclei generated by these reactions with the interstellar gas will have essentially the same velocity as the primary nuclei and hence the same energy per nucleon. Their energy spectra tend to be steeper than those of the primaries due to energy-dependent escape of the higher-energy primaries from the Galaxy.

Nuclear reactions in lab, space and astrophysical media

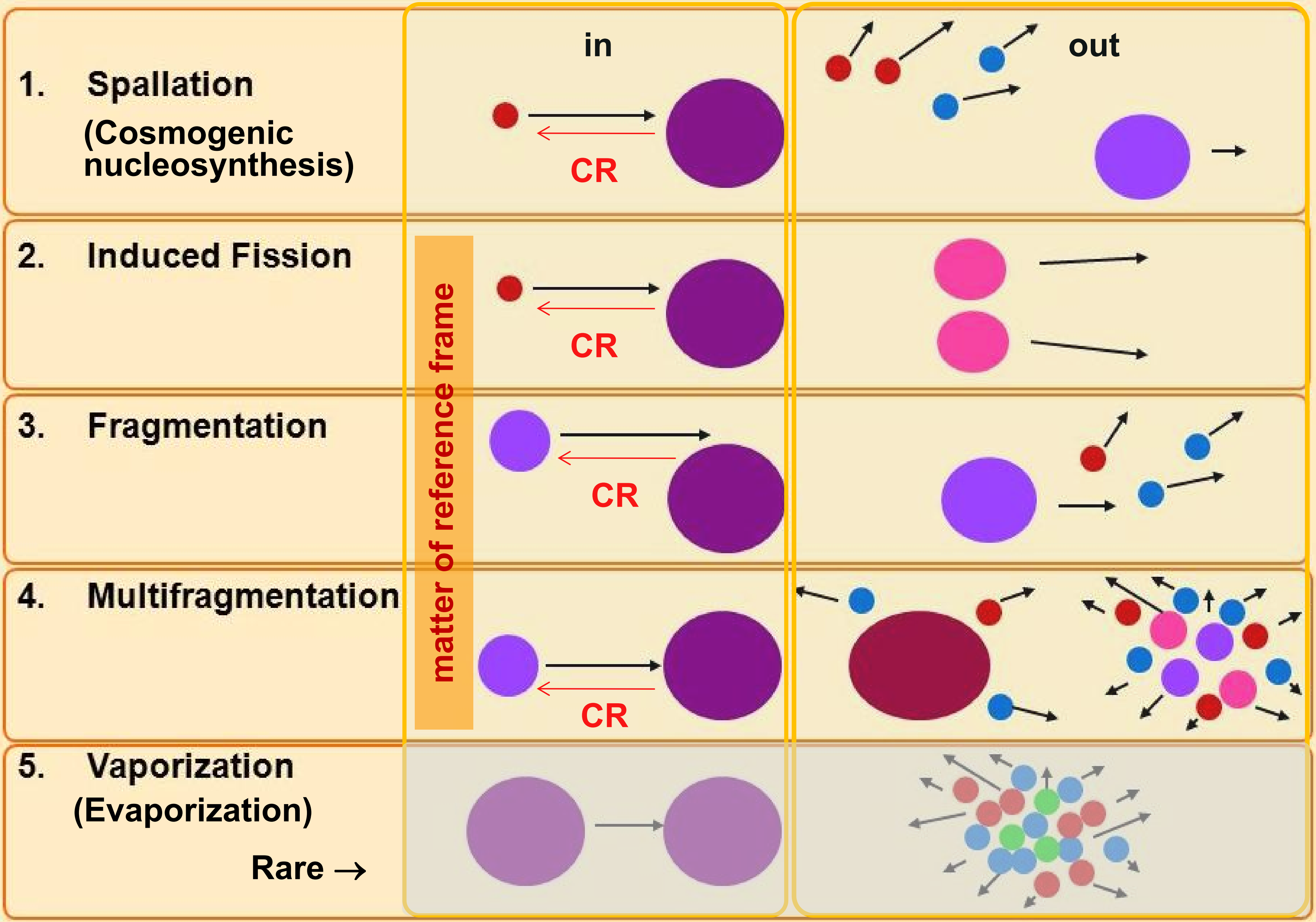

In fact, nuclear reactions can occur in conjunction:

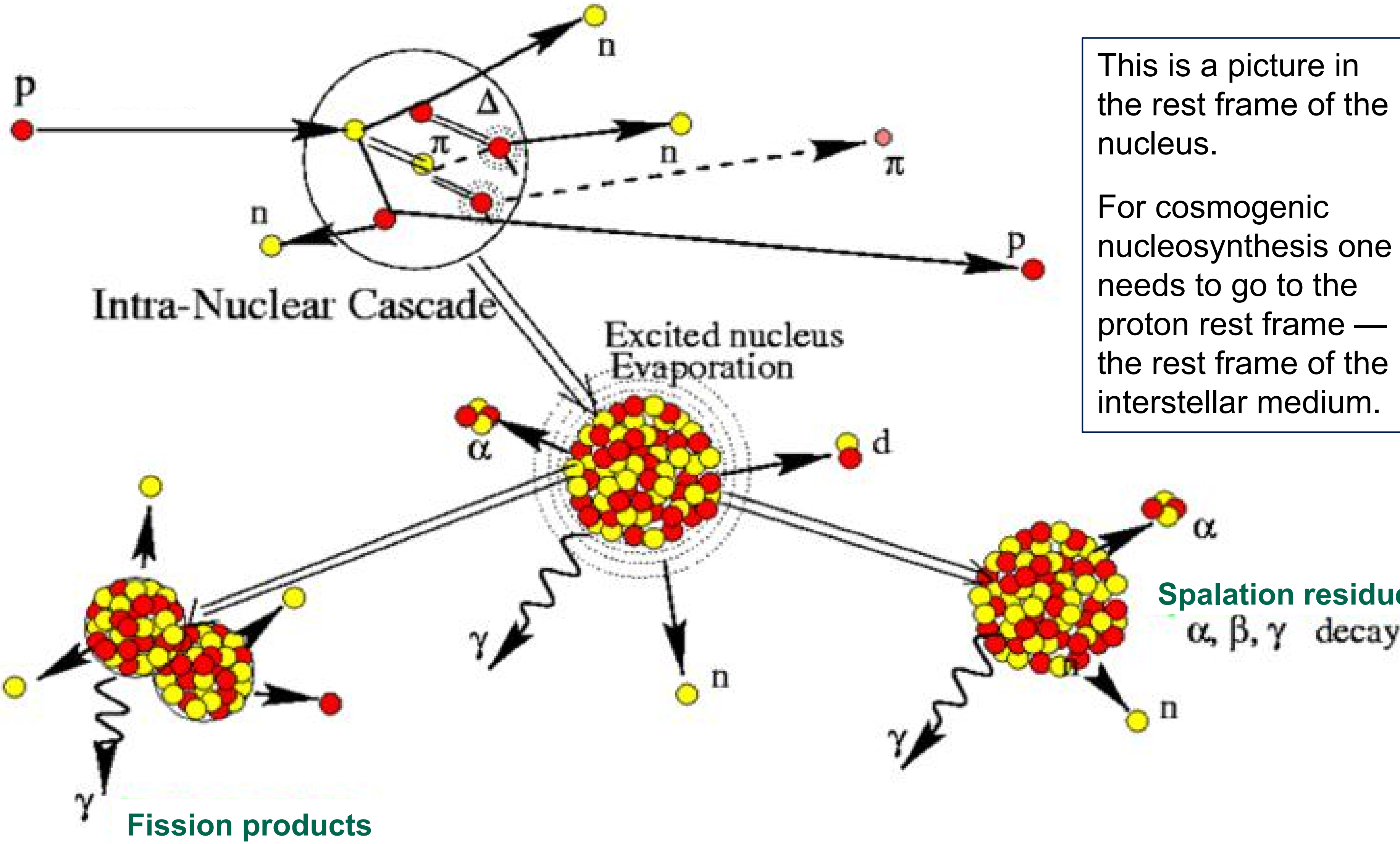

This is a picture in the rest frame of the nucleus.

For cosmogenic nucleosynthesis one needs to go to the proton rest frame — the rest frame of the interstellar medium.

This is why the daughter nuclei will have essentially the same (ultrarelativistic) velocities as the primary CR nucleus, and therefore almost the same energy per nucleon.

Old but not obsolete data

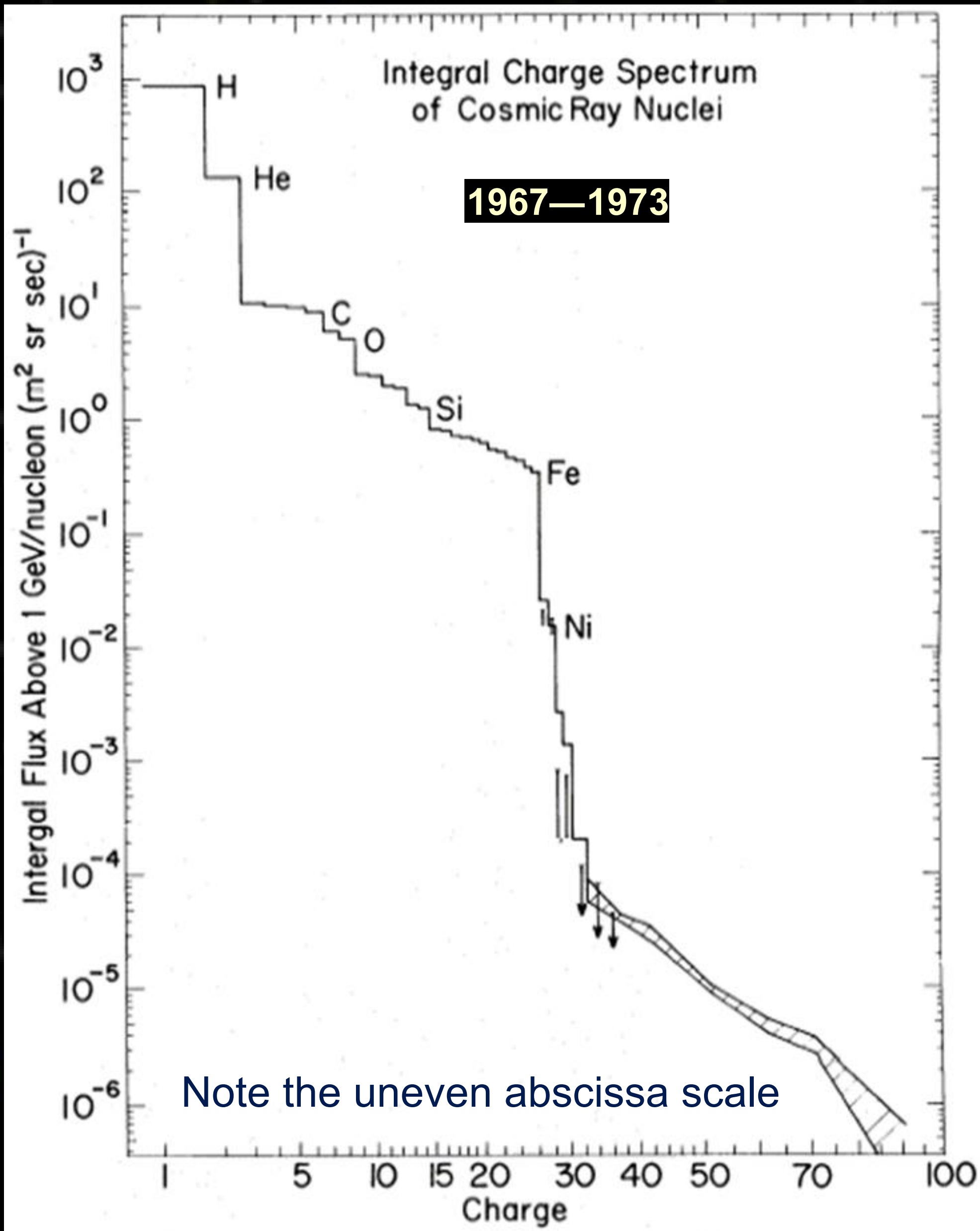

← The integral charge spectrum of CR nuclei having kinetic energies above 1 GeV per nucleon. Compiled from several earlier works.

[**Reference**: E. Juliusso and P. Meyer, ApJ **201** (1975) 76.]

Z	Element	F	Z	Element	F
1	H	540	13–14	Al-Si	0.19
2	He	26	15–16	P-S	0.03
3–5	Li-B	0.40	17–18	Cl-Ar	0.01
6–8	C-O	2.20	19–20	K-Ca	0.02
9–10	F-Ne	0.30	21–25	Sc-Mn	0.05
11–12	Na-Mg	0.22	26–28	Fe-Ni	0.12

Relative abundances *F* of cosmic-ray nuclei at 10.6 GeV/nucleon normalized to oxygen (=1). The oxygen differential flux at kinetic energy of 10.6 GeV/nucleon is 3.26 10^{-6} cm^{-2} s^{-1} sr^{-1} $(GeV/nucleon)^{-1}$.

[**Reference**: T.K. Gaisser & T. Stanev, “Cosmic rays,” pages 228-234 of the Review of Particle Physics, Phys. Lett. B **592** (2004) 1.]

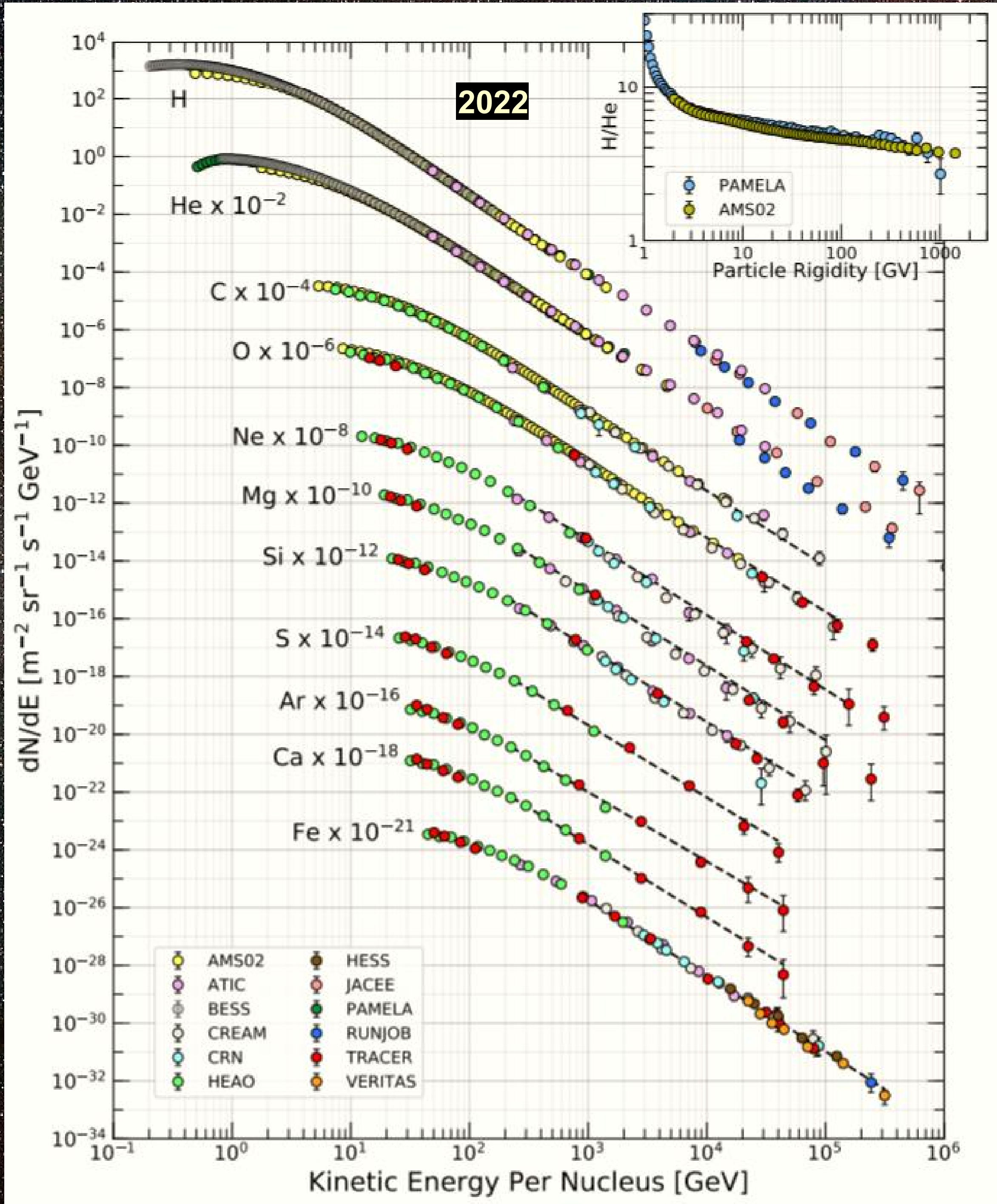

Modern status:

Differential fluxes of the major nuclear components of the primary
cosmic radiation in particles per energy-per-nucleus are plotted vs kinetic energy-per-nucleus.

Pay attention to scale factors.

The inset shows the H/He ratio as a function of rigidity.

[From y J.J. Beatty, J. Matthews & S.P. Wakely, "Cosmic rays", RPP review; see in P.A. Zyla et al. (Particle Data Group), Prog. Theor. Exp. Phys. **2020** (2020) 083C01 (**RPP-2020**) or in R.L. Workman et al. (Particle Data Group), Prog. Theor. Exp. Phys. **2022** (2022) 083C01 (**RPP-2022**). This review paper includes a lot of other useful data and references.]

The Sun in short

Why is the Sun interesting for CR & neutrino astrophysics?

- **Solar neutrinos (from nuclear fusion inside the Sun).**
- **High-energy neutrinos from cosmic ray interactions in the solar atmosphere.**
- **High-energy neutrinos from annihilation of cold dark matter particles (CDM) captured in the Sun.**
- **Neutrinos from powerful (X-class) solar flares.**
- **Solar modulation of cosmic rays, which affects the low-energy atmospheric neutrino fluxes at Earth.**
- **A good “calibrator” for cosmic-ray spectrometers**

Below we’ll consider in short photospheric features, sunspot cycle, etc. relevant to the CR modulation.

The Sun in short

Sun Facts

Solar radius = 695,990 km = 109 Earth radii
Solar mass = 1.989×10^{30} kg = 333,000 Earth masses
Solar luminosity (energy output of the Sun) = 3.846×10^{33} erg/s
Surface temperature = 5780 K
Surface density = 2.07×10^{-7} g/cm^3 = 1.6×10^{-4} Air density
Surface composition = 70% H + 28% He + 2% (C, N, O, ...) by mass
Central composition = 35% H + 63% He + 2% (C, N, O, ...) by mass
Central temperature = 15,600,000 K
Central density = 150 g/cm^3 = 8 × Gold density
Solar age = 4.57×10^9 yr

Sunspots

Sunspots appear as dark spots on the surface of the Sun. Temperatures in the dark centers of sunspots drop to **3000—4500 K** (compared to **5780 K** for the surrounding photo-sphere). They typically last for several days, although very large ones may live for several weeks.

Sunspots are magnetic regions on the Sun with magnetic field strengths **thousands** of times stronger than the geomagnetic field [22,000 — 67,000 nT = 2.2 — 6.7 Gauss]. Sunspots usually come in groups with two sets of spots. One set will have **positive** or **north** magnetic field while the other set will have **negative** or **south** magnetic field.

The field is strongest in the darker parts of the sunspots — the **umbra**. The field is weaker and more horizontal in the lighter part — the **penumbra**.

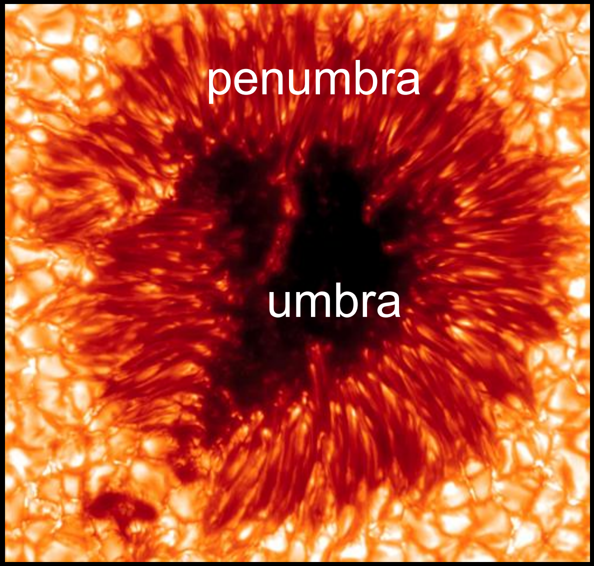

Watch as an enormous and extremely energetic group of sunspots complete their trek across the face of the Sun. Known as Active Region 1967 (AR1967), the sunspot complex is roughly 180,000 kilometers across, making it larger than the planet Jupiter. Another smaller group of sunspots can be seen rotating above it.

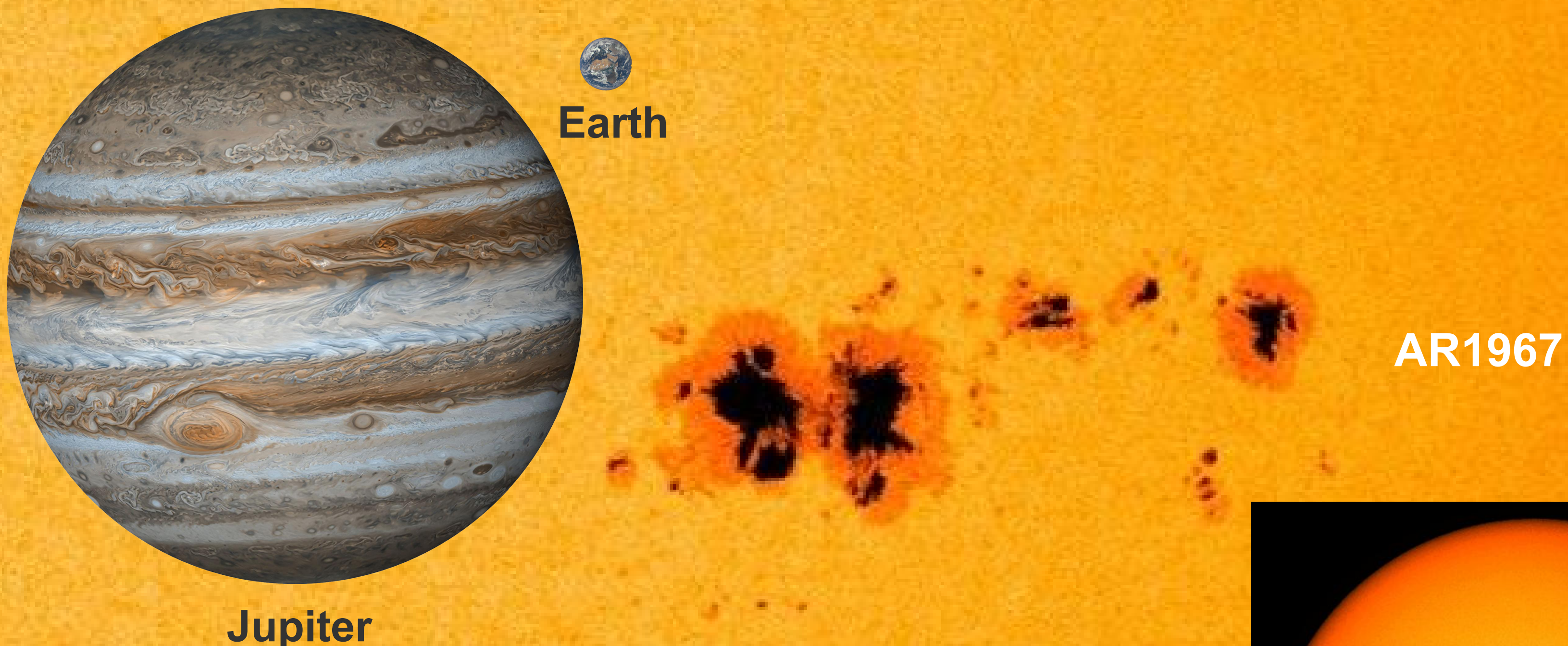

Active regions usually produce powerful bursts of radiation known as solar flares. AR1967 has been quite active, erupting a great deal of mid-size flares on Feb. 3 and an intense X-class flare, the most powerful type of solar flare, on Jan. 30.

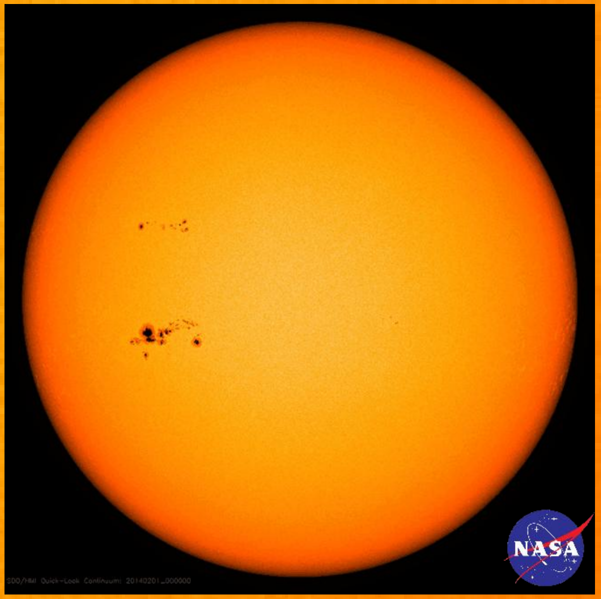

Images by NASA's Solar Dynamics Observatory (SDO) are taken from URL: https://www.wired.com/2014/02/sunspot-active-jupiter/

Sunspot structure
(simulation)


Active region (simulation)

An active region (AR) on the Sun is an area with an especially strong magnetic field. Most solar storms - solar flares and coronal mass ejections - blast forth from ARs. Magnetic fields in ARs can be 1,000 or more times stronger than the average magnetic field of the Sun. Sunspots are visual indicators of ARs, although not all ARs produce the sunspots. The latter are usually surrounded by lighter-shaded areas of mild magnetic disturbance called faculae (see below). Some less intense ARs show up as just faculae without sunspots. ARs are most common during the peak of the sunspot cycle when the Sun's magnetic field is highly disturbed. ARs appear bright in X-ray and UV images of the Sun. The powerful magnetic fields around ARs release intense bursts of energy, which often take the form of high-energy X-ray and UV photons. Many types of dramatic solar features, including solar prominences and coronal loops, frequently appear around ARs.

[See UCAR/Center for Science Education: <https://scied.ucar.edu/sun-active-region>]

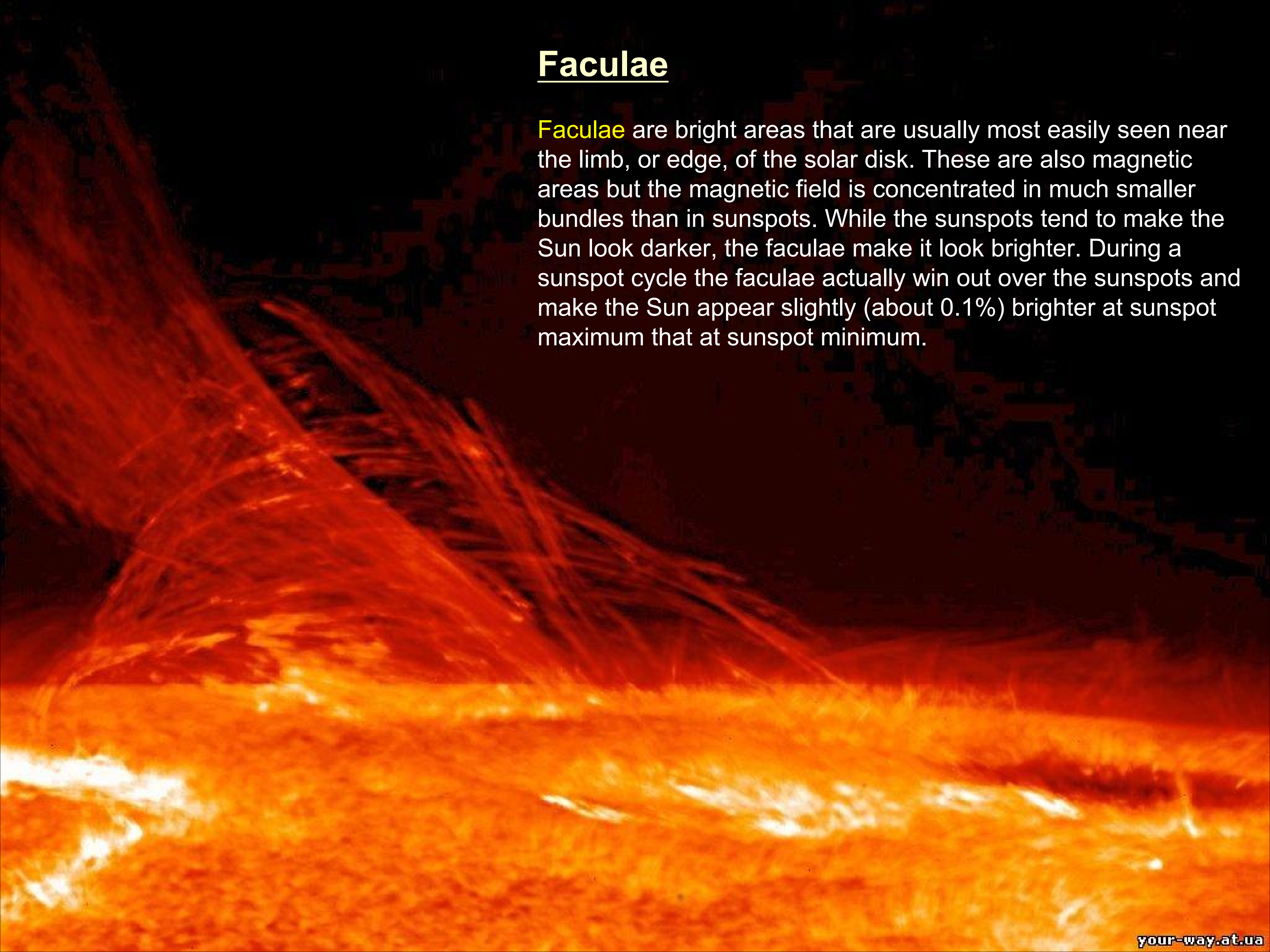

Faculae

Faculae are bright areas that are usually most easily seen near the limb, or edge, of the solar disk. These are also magnetic areas but the magnetic field is concentrated in much smaller bundles than in sunspots. While the sunspots tend to make the Sun look darker, the faculae make it look brighter. During a sunspot cycle the faculae actually win out over the sunspots and make the Sun appear slightly (about 0.1%) brighter at sunspot maximum that at sunspot minimum.

Granules

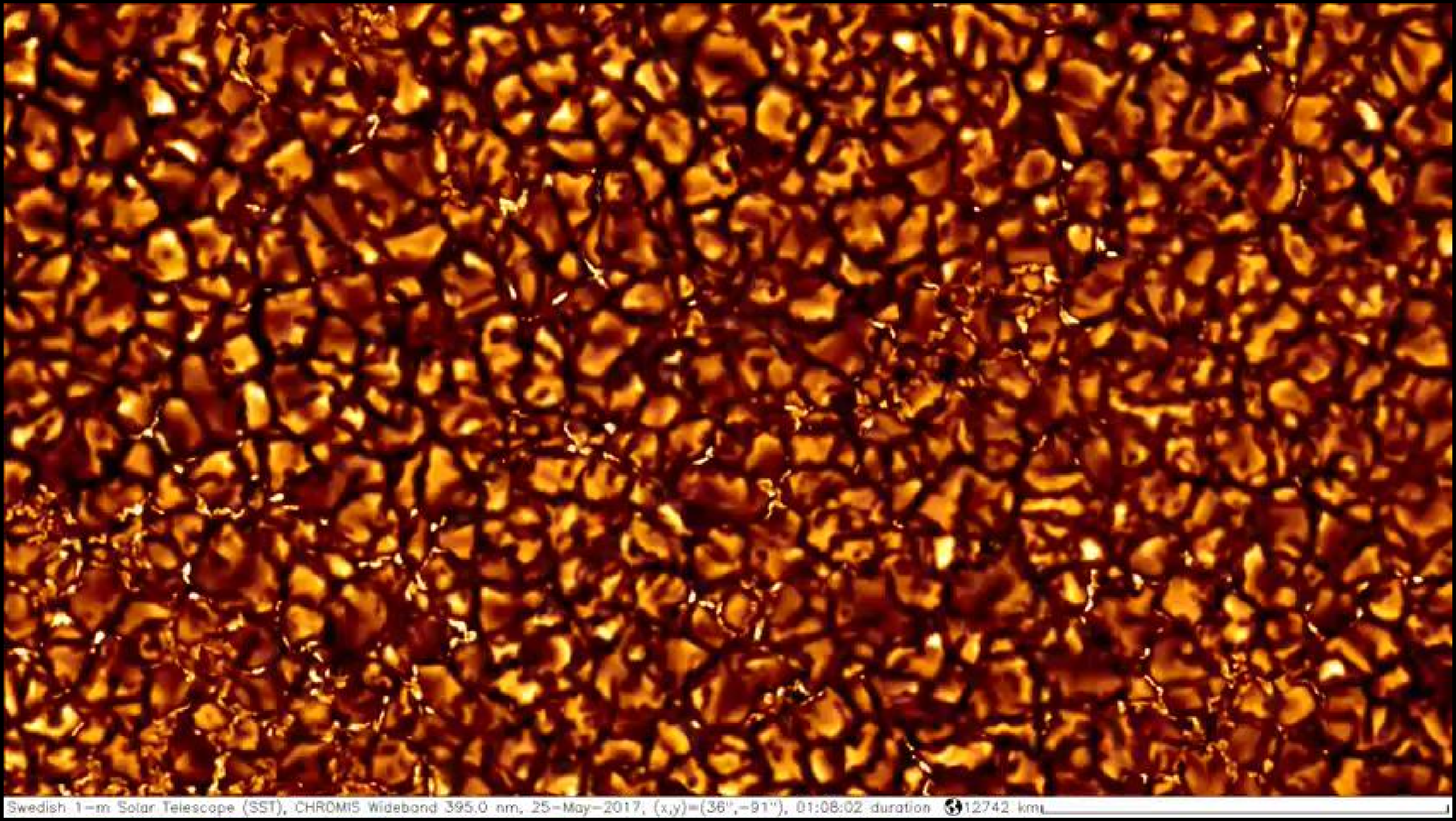

Granules are small (about **1,000 km** across) cellular features that cover the entire Sun except for those areas covered by sunspots. These features are the tops of convection cells where hot fluid rises up from the interior in the bright areas, spreads out across the surface, cools and then sinks inward along the dark lanes. Individual granules last for only about **20 minutes**. The granulation pattern is continually evolving as old granules are pushed aside bynewly emerging ones. The flow within the granules can reach supersonic speeds of more than 7 km/s and produce sonic "booms" and other noise that generates waves on the Sun's surface. [From Swedish 1m Solar Telescope (SST).]

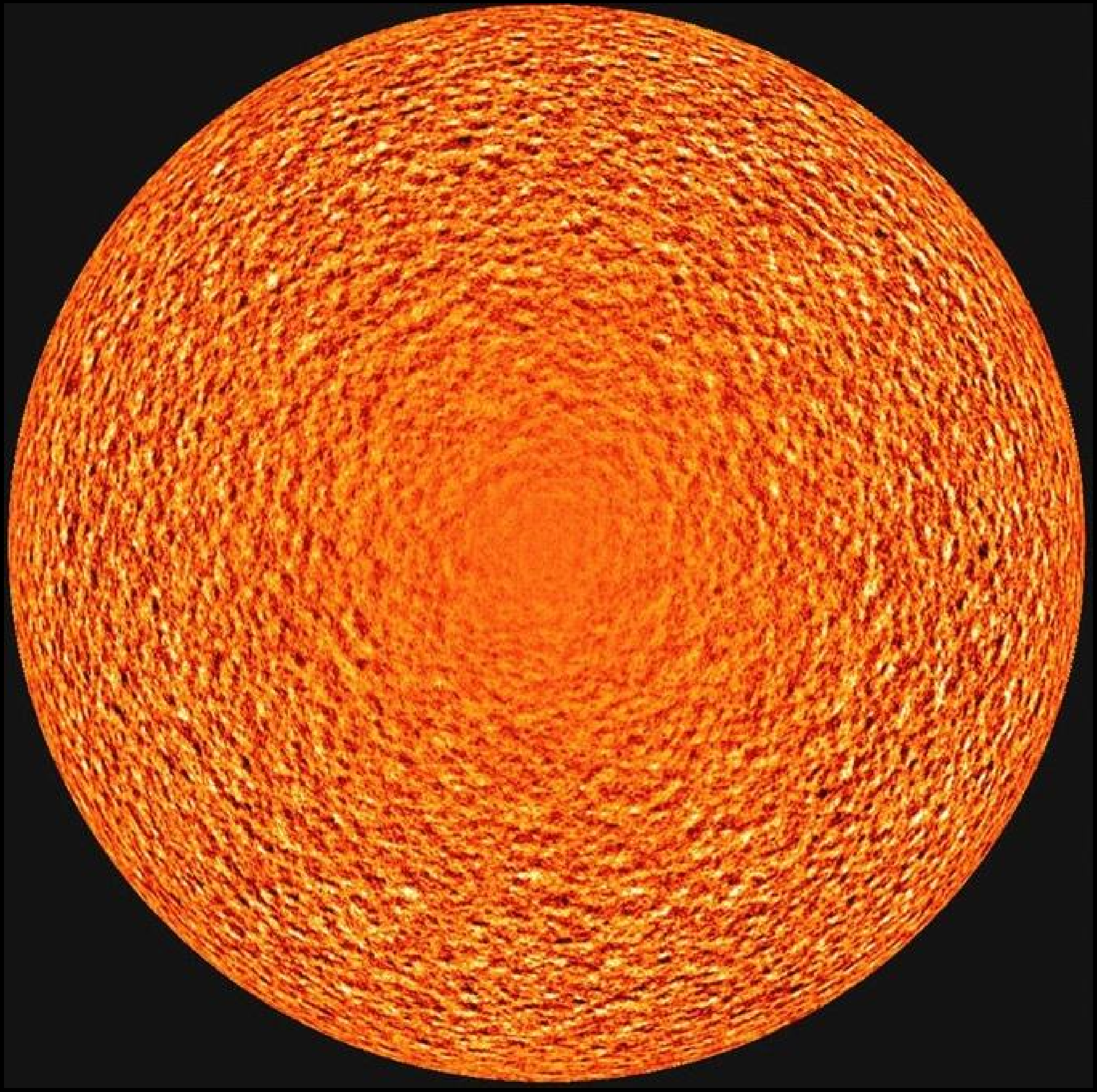

Supergranules

Supergranules are much larger versions of granules (~ **35,000 km** across) but are best seen in measurements of the Doppler shift where light from material moving toward us is shifted to the blue while light from material moving away from us is shifted to the red. These features also cover the entire Sun and are continually evolving.

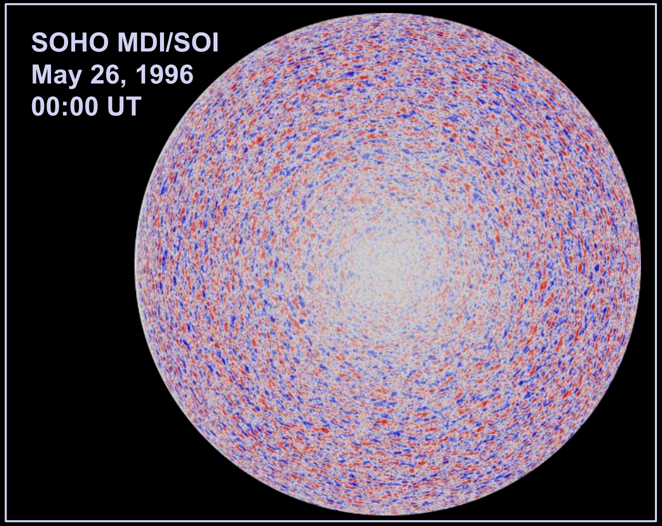

Individual supergranules last for a day or two and have flow speeds of about **0.5 km/s**.

The fluid flows observed in supergranules carry magnetic field bundles to the edges of the cells where they produce the chromospheric network.

Solar wind/flares → magnetic reconnection → aurora

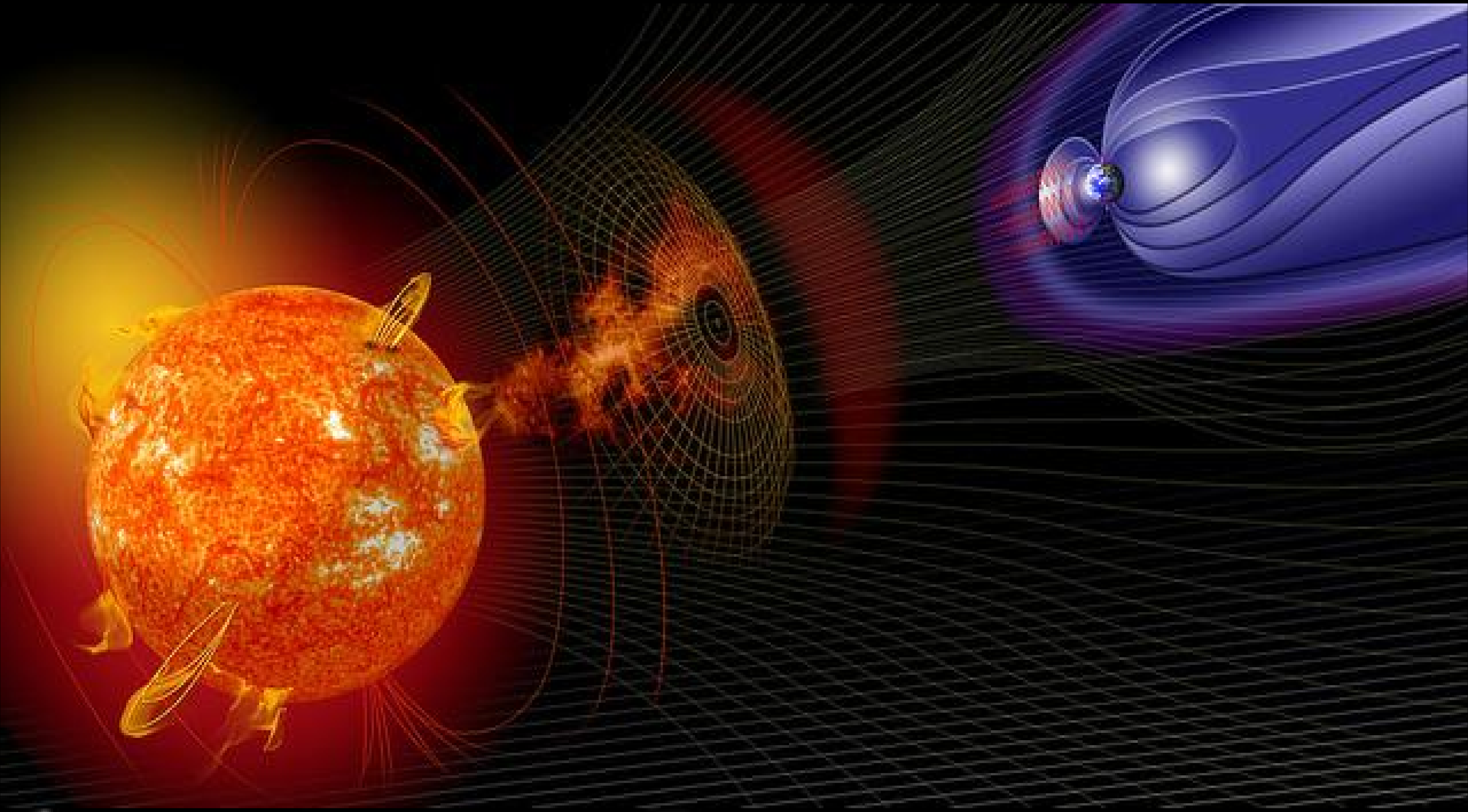

Solar wind consists of ionized hydrogen (protons) and electrons with a dash of helium and a very small proportion of heavier ions.

The average speed of the solar-wind particles in Earth's orbital plane is about 400 km/s with variations from 300 to 800 km/s. The particle energies are too low to create visible auroras. But their speed fluctuations perturb Earth's magnetosphere, leading to diverse interactions between the wind and geomagnetic field.

Specifically, the solar wind generates reconnections in the geomagnetic field. Particles leak in from equatorial rediation belts and from areas around the magnetic field lines, producing the auroras.

For more details, see, e.g., “Atmospheric Optics”, URL: https://atoptics.co.uk/blog/magnetosphere-and-aurora/

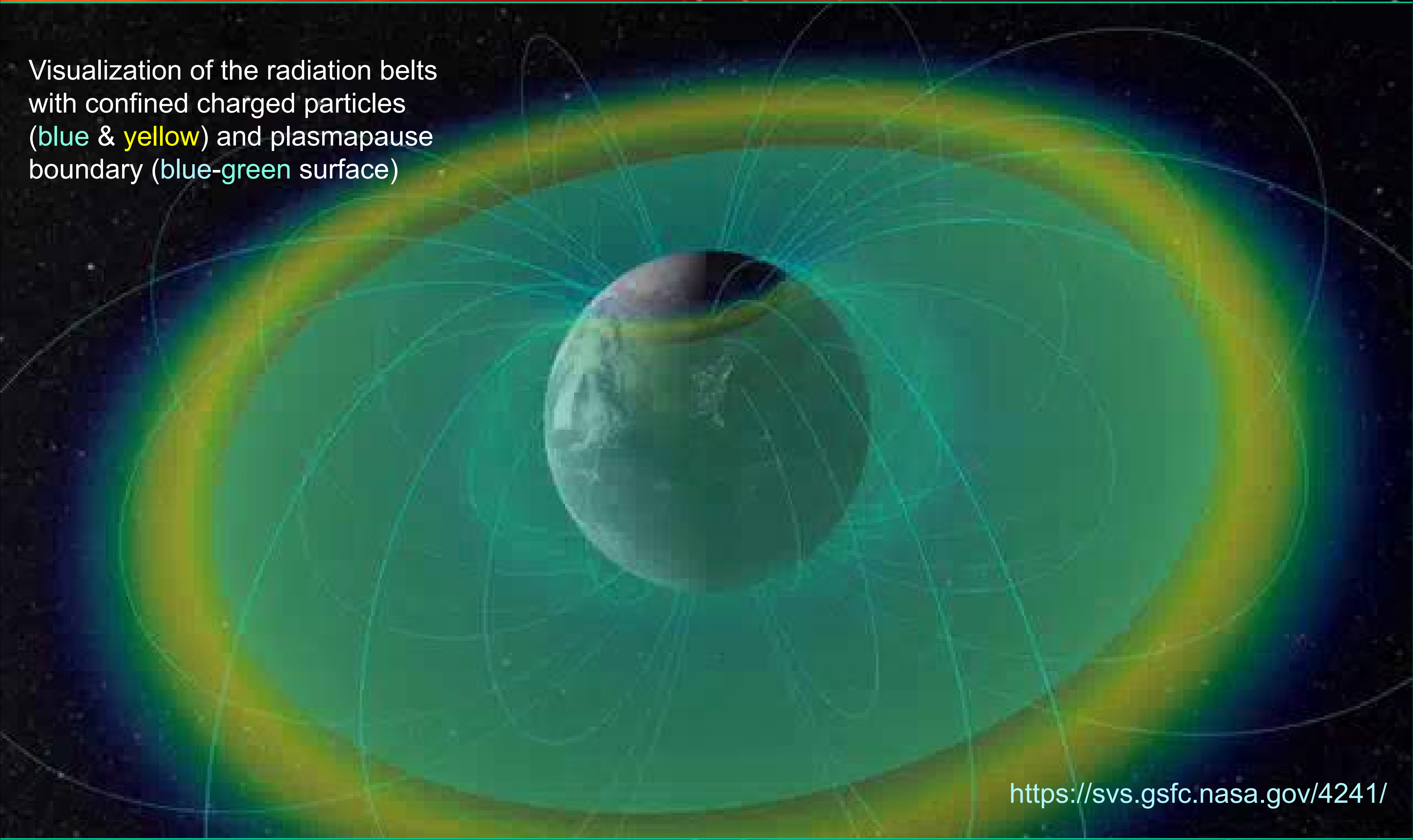

The near-Earth space enviroment is a complex interaction between geomagnetic field, cool plasma moving up from Earth's ionosphere, and hotter plasma of the solar wind. This interactions maintain the radiation belts.


Solar flare
Solar wind
Geomagnetic field
Steele Hill/NASA

Differential rotation

The Sun rotates on its axis once in about 27 days.

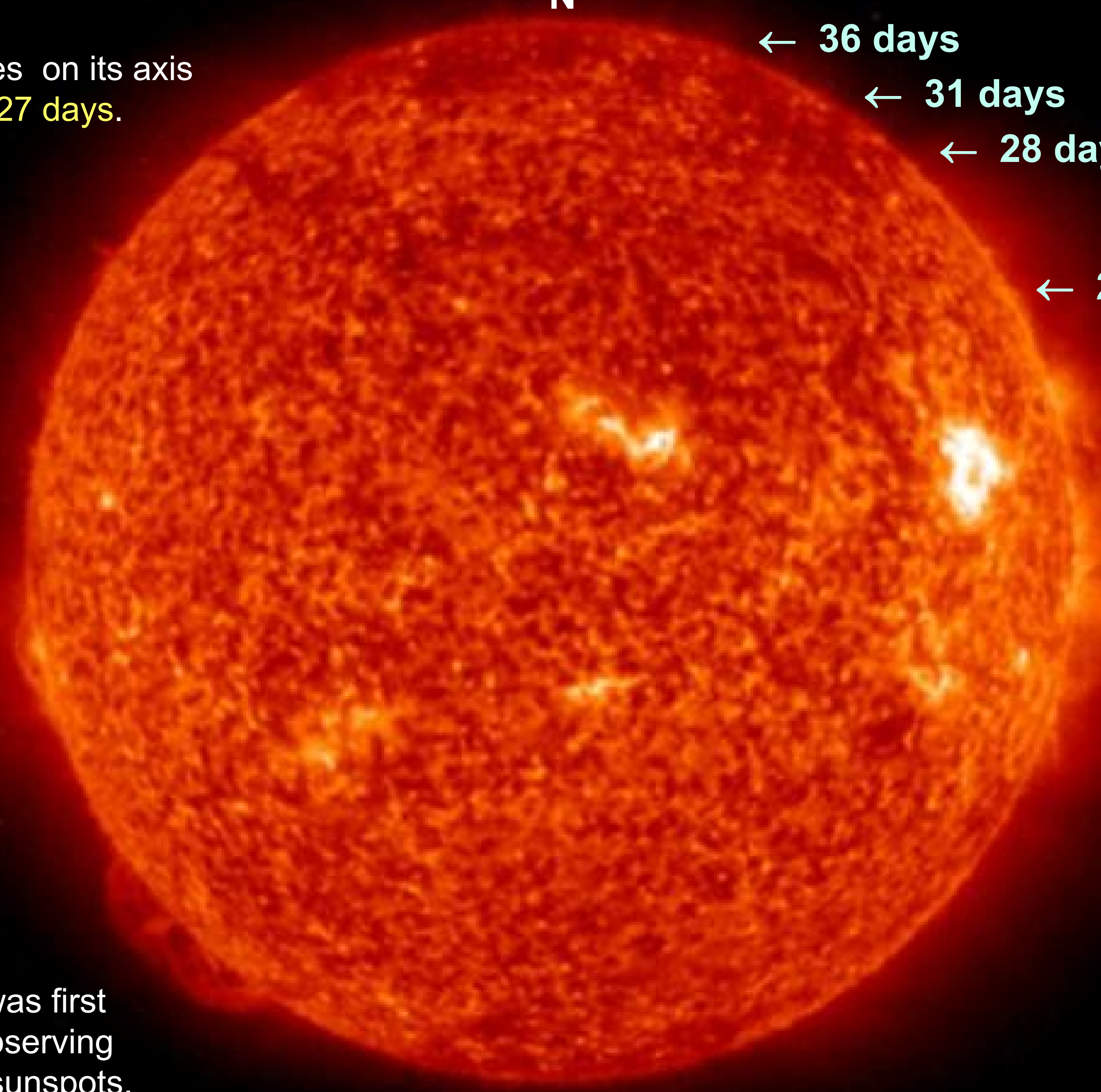

In equator

v ≈ 2 km/s

The rotation was first detected by observing the motion of sunspots.

The Sun's rotation axis is tilted by about 7.25 ^{o} from the axis of the Earth's orbit so we see more of the Sun's north pole in Septembe of each year and more of its south pole in March.

[From Stanford Solar Center, URL: http://solar-center.stanford.edu/].

Solar Magnetism

Sun is a ball of electrically-charged hot gas (plasma) which moves, generating a powerful magnetic field whose configuration evolves with a 22 year cycle. It's all caused by

magnetic dynamo {
- differential rotation or "Ω effect" (the Sun rotates faster at its equator)
- convection (α effect)
- meridional flows

Solar minimum

- **dipole field**
- **no sunspots**

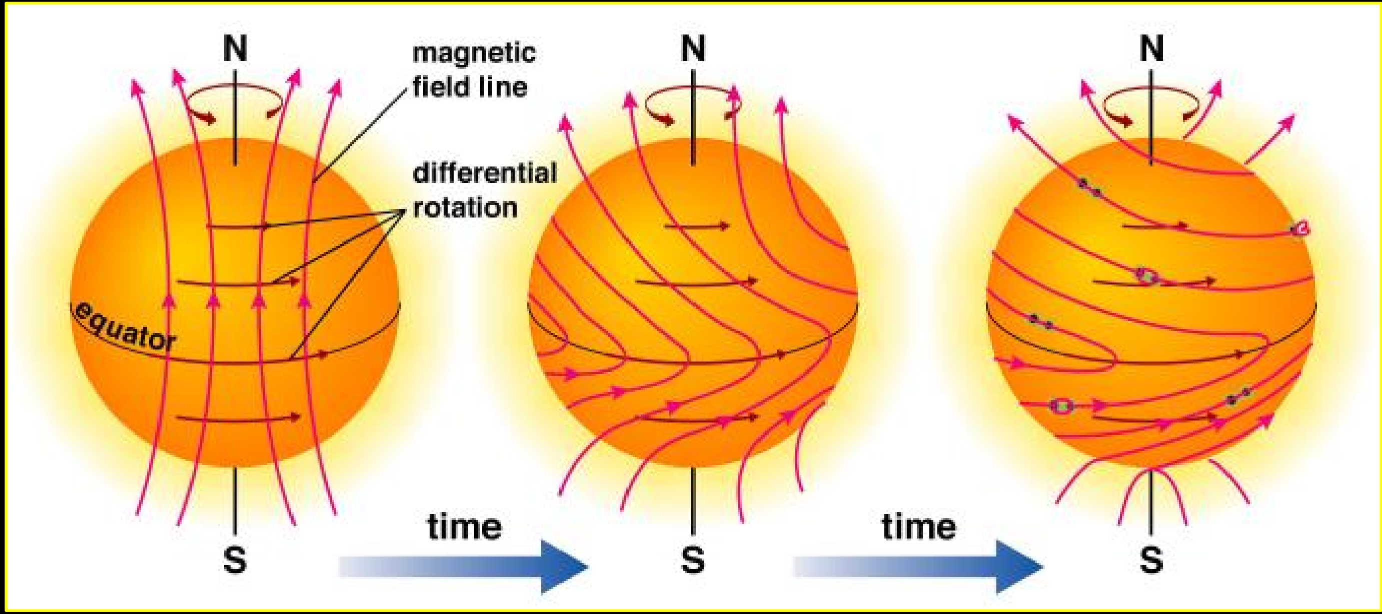

Solar maximum

- **toroidal field**
- **many sunspots**

The field becomes more and more twisted and complex from differential rotation. It finally breaks and flips every **11 years**. So the total cycle is really **22 years** from start to finish.

The sunspot cycle also comes about because of the Ω effect, which stretches the magnetic field lines around the solar surface, turning a poloidal ("bar magnet") field into a toroidal one. Ultimately, the poles switch and the cycle begins again. Of course, this is a super-simplified picture...

Evolution of the solar magnetic field from 1997 to 2013.

The **white** magnetic field lines are considered 'closed'. They move upward, and then return to the solar surface. The **green** and **violet** lines represent field lines that are considered 'open'. **Green** (**violet**) represents **positive** (**negative**) magnetic polarity. These field lines do not connect back to the Sun but with more distant magnetic fields in space.

The animation is constructed using the Potential Field Source Surface model and magnetograms from the **SOHO/MDI** and **SDO/HMI** instruments.

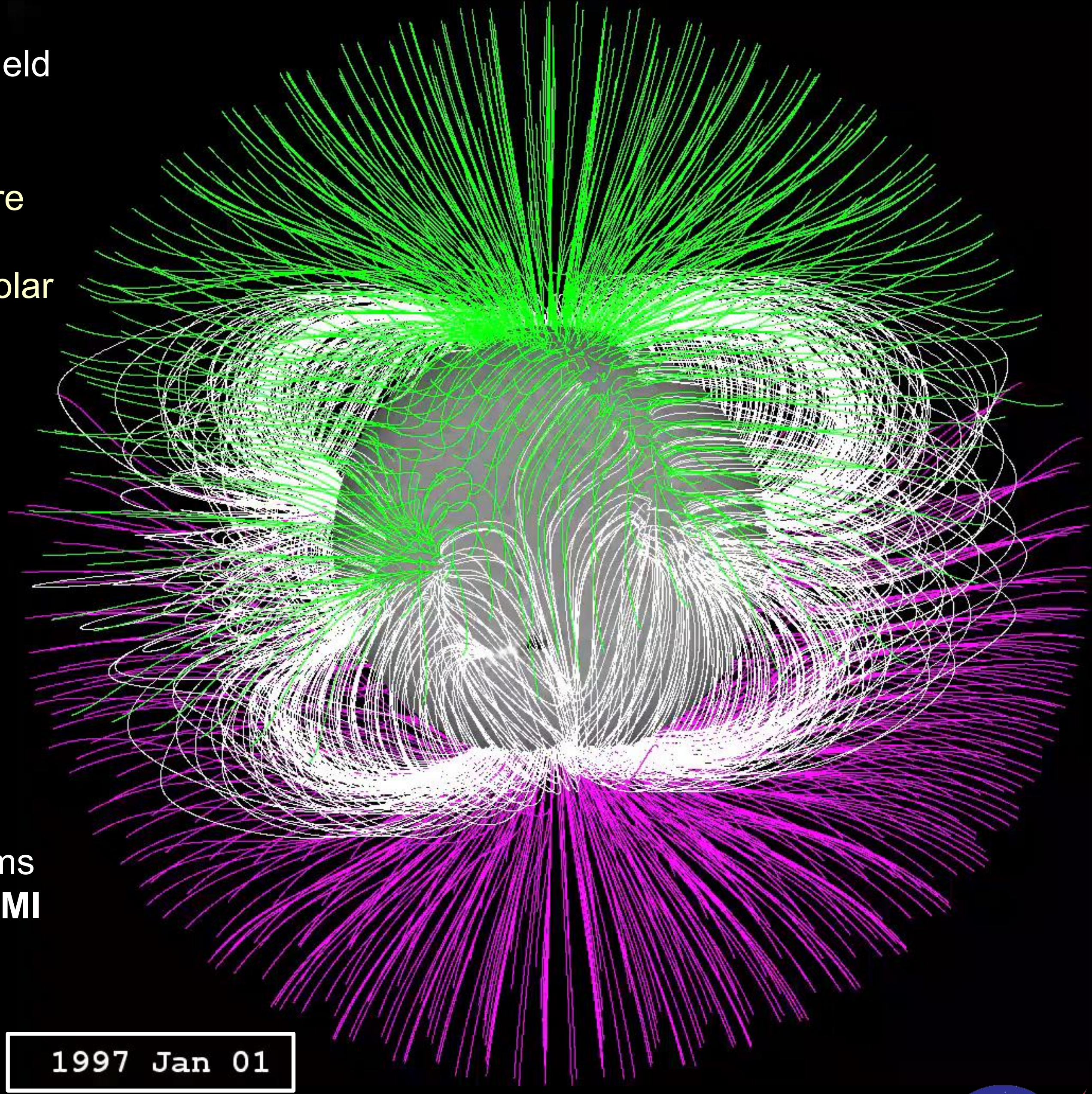

[From NASA Scientific Visualization Studio, URL: https://svs.gsfc.nasa.gov/4124]

Solar modulation of primary cosmic rays

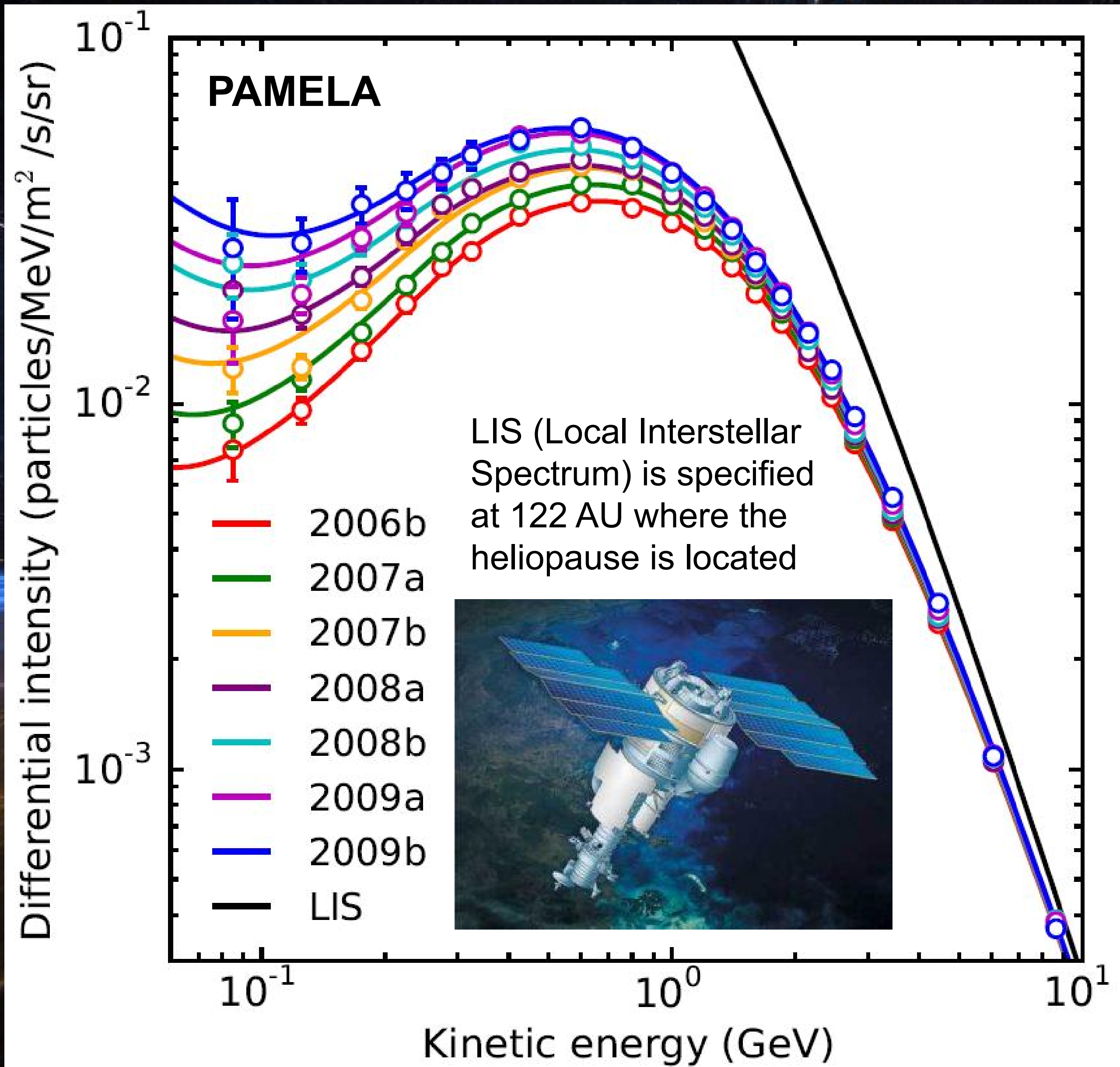

Variations of electron energy spectra observed by the PAMELA mission, shown as six-month averages for seven semesters, starting from 2006b, indicating the second semester of 2006 (July to December), up to 2009b as the second semester of 2009.

[**Reference**: M.S. Potgieter et al., “Modulation of galactic electrons in the heliosphere during the unusual solar minimum of 2006 to 2009: A modelling approach”, ApJ 810 (2015) 141.]

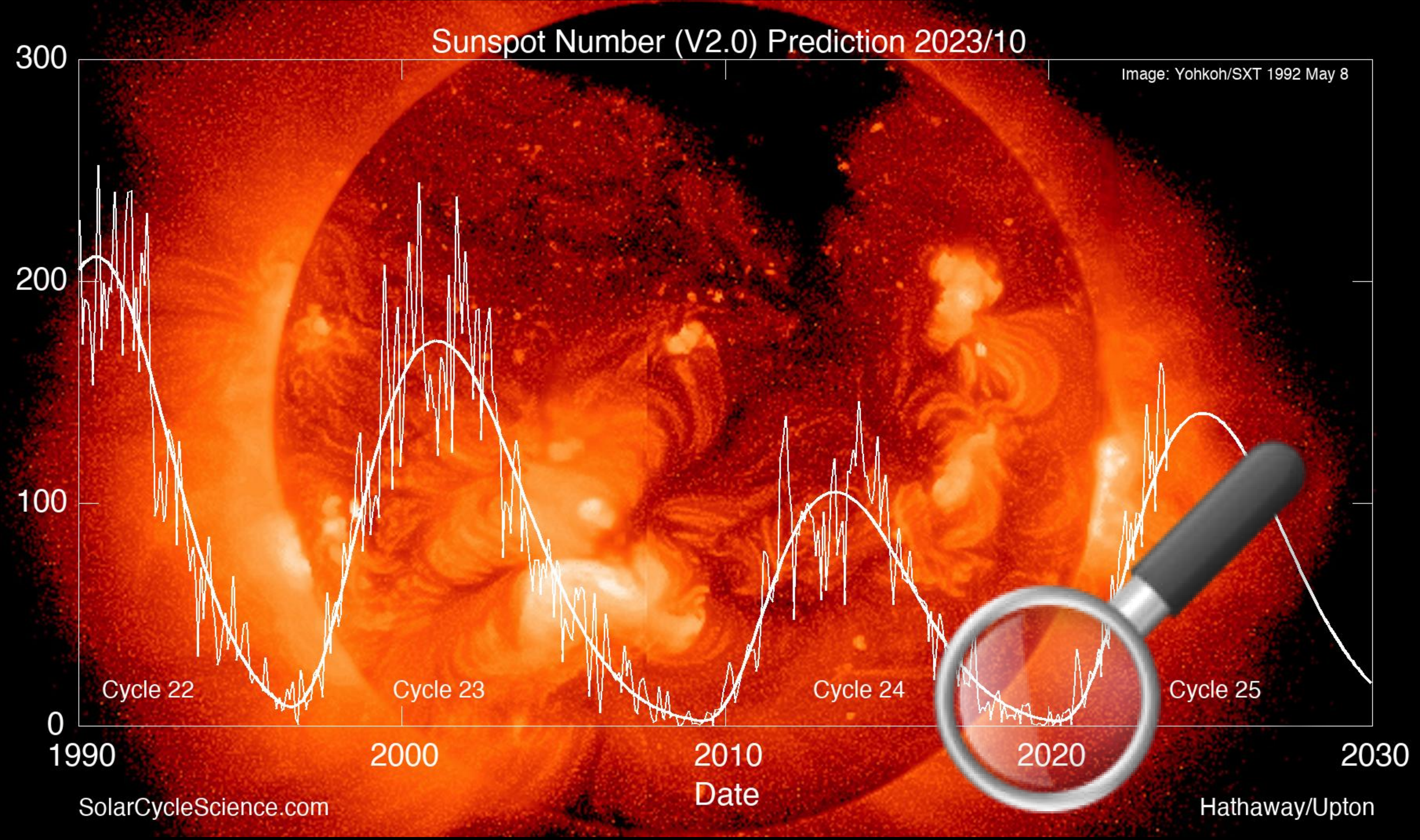

Several years ago, it was predicted that the 25th cycle would be the next (after the 24th) small cycle, the amplitude of which would be somewhat smaller (~95-97%) than the magnitude of the 24th cycle. However, the forecast turned out to be erroneous. Using the polar field strength at cycle 24/25 minimum in December of 2019 indicates a maximum sunspot number of 120 for the cycle 25.

[From URL: http://solarcyclescience.com/forecasts.html]

Unusual, but not unique (“*Nil novi sub sole*”). Let's wait awhile...

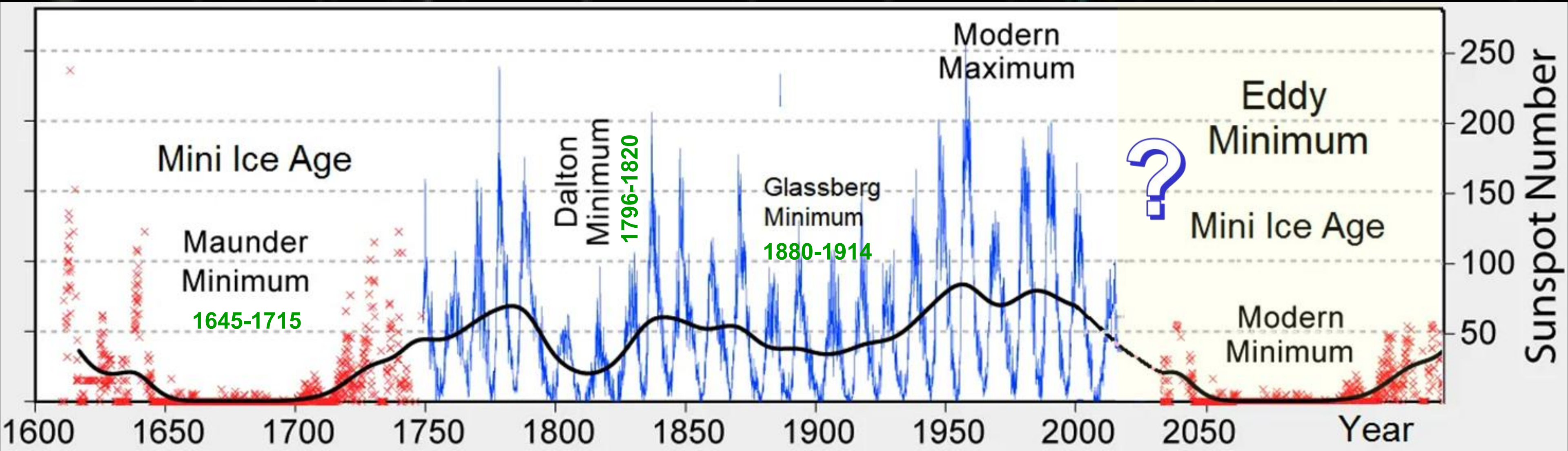

The most recent Grand Solar Minimum (GSM) was the **Maunder Minimum** which ran from **1645-1715**. Our Modern “Eddy” GSM that we are entering now will most-likely run for a similar duration — around 70 years (though theories are numerous — from cooling to warming — and it’s really anyone’s guess).

During the **Maunder**, “*temperatures across much of the Northern Hemisphere plunged*,” say NASA. “*Europe and North America went into a deep freeze: alpine glaciers extended over valley farmland; sea ice crept south from the Arctic; and the famous canals in the Netherlands froze regularly — an event that is rare today.*”

Along with GSMs, there are also **multidecadal** periods of low solar activity that don’t quite cut it as their grander counterparts. The most recent examples of these include the **Centennial** (**Glassberg** or **Gleissberg**) **Minimum (1880-1914)** and the **Dalton Minimum (1796-1820)**.

[Figure is from URL: https://electroverse.net/solar-minimum-aint-over-yet/]

Sun is a variable star!

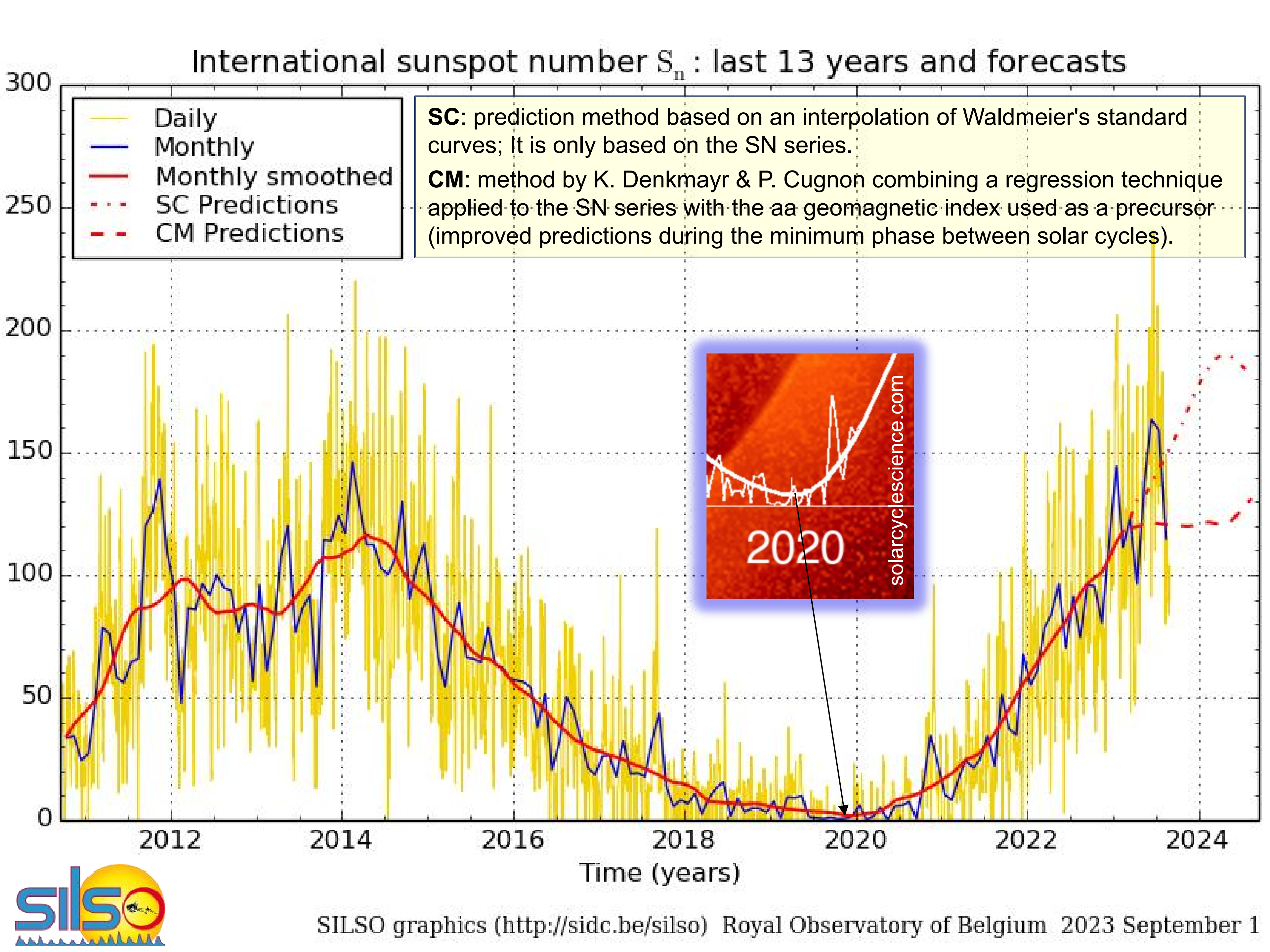
International sunspot number S_n : last 13 years and forecasts
Daily
Monthly
Monthly smoothed
SC Predictions
CM Predictions
SC: prediction method based on an interpolation of Waldmeier's standard curves; It is only based on the SN series.
CM: method by K. Denkmayr & P. Cugnon combining a regression technique applied to the SN series with the aa geomagnetic index used as a precursor (improved predictions during the minimum phase between solar cycles).
300
250
200
150
100
50
0
2012
2014
2016
2018
2020
2022
2024
Time (years)
2020
solarcyclescience.com
silso
SILSO graphics (http://sidc.be/silso) Royal Observatory of Belgium 2023 September 1

CR Neutron monitoring

A neutron monitor is an instrument that measures the number of high-energy particles impacting Earth from space. Because the intensity of cosmic rays hitting Earth is not uniform, it is important to place neutron monitors at multiple locations in order to form a complete picture of cosmic rays in space.

The cosmic ray lab of University of Delaware at McMurdo Station, Ross Island, Antarctica. →

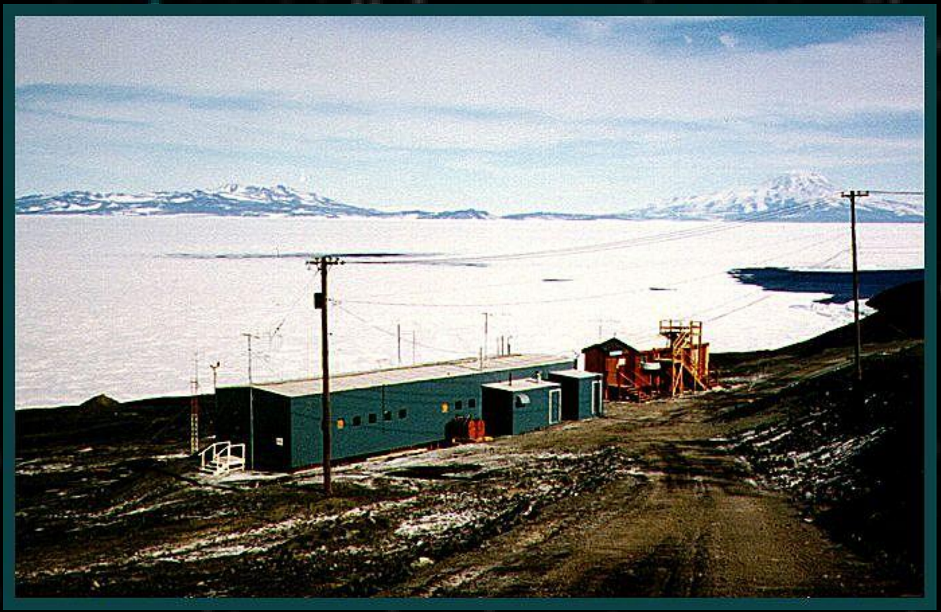

University of New Hampshire cosmic ray labs at Huancayo, Peru (**left**) and at Haleakala, Hawaii (**right**).

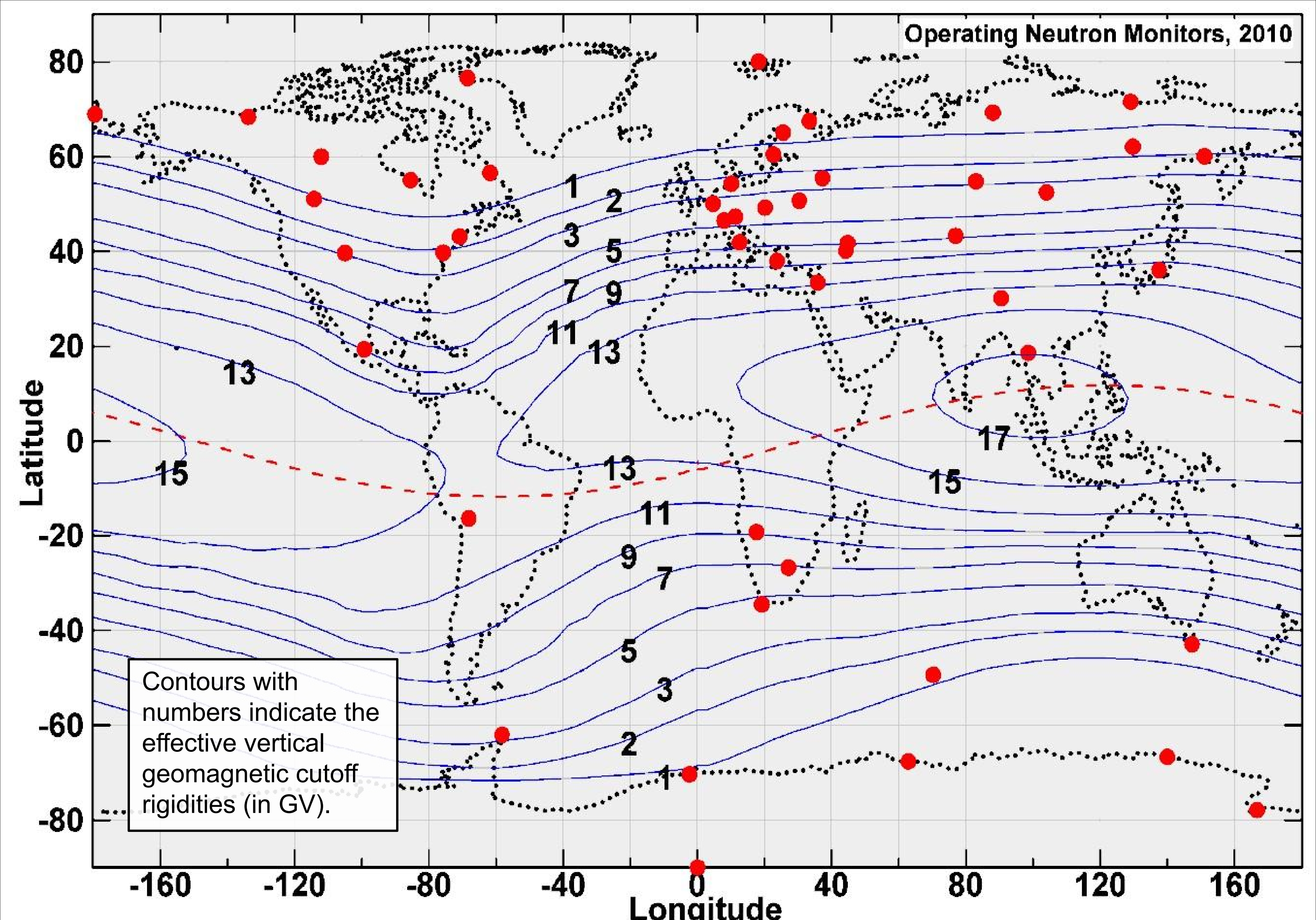

From D.Ruffolo, J. Phys. Conf. Ser. 1572 (2020) 012087

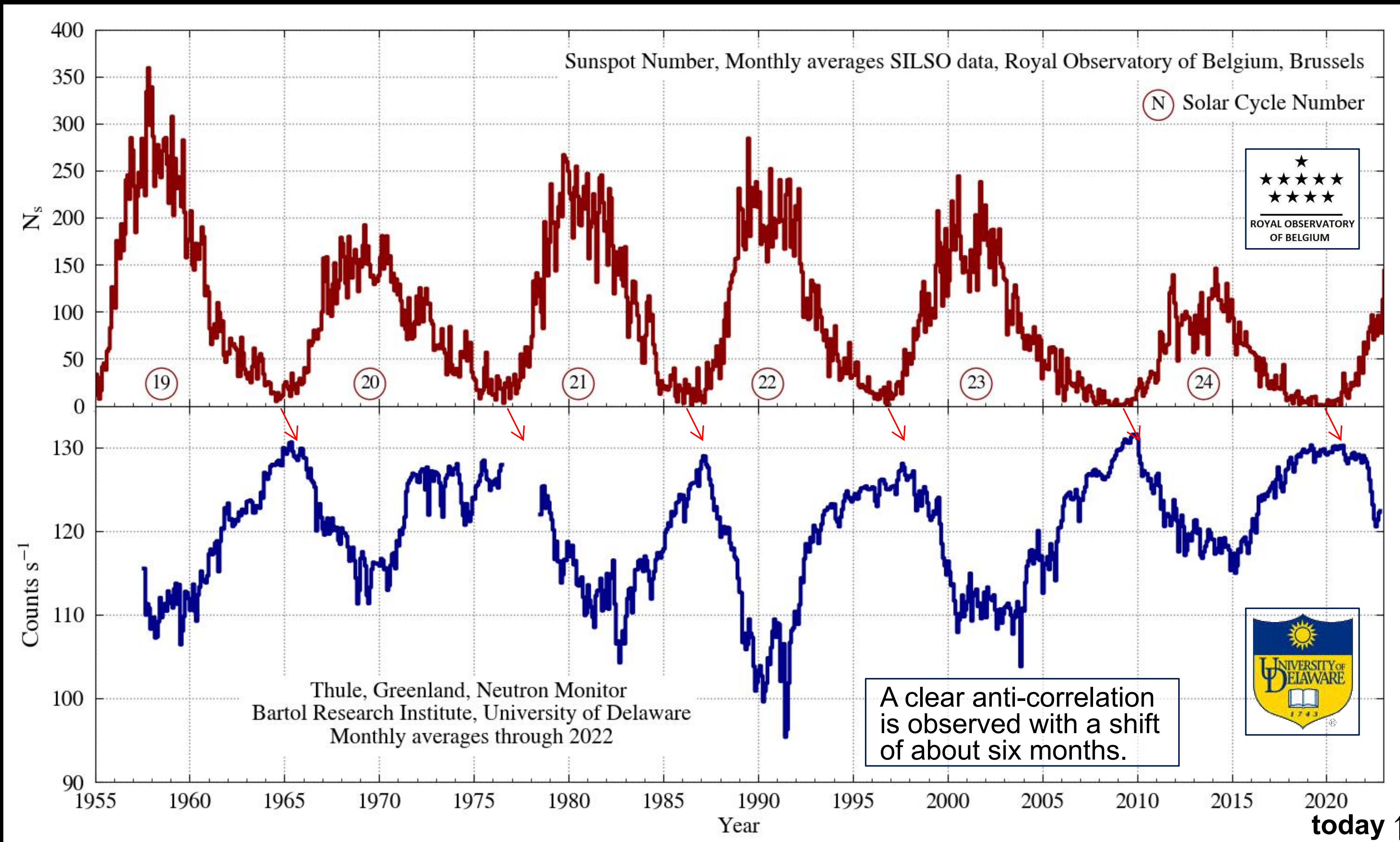

Solar modulation refers to the influence the Sun exerts upon the intensity of galactic cosmic rays. As solar activity rises (top panel, Source: WDC-SILSO Royal Observatory of Belgium, Brussels), the count rate recorded by a neutron monitor in Inuvik, Canada decreases (bottom panel, Source: Bartol Research Institute, University of Delaware, USA).

[From URL: http://neutronm.bartol.udel.edu/]

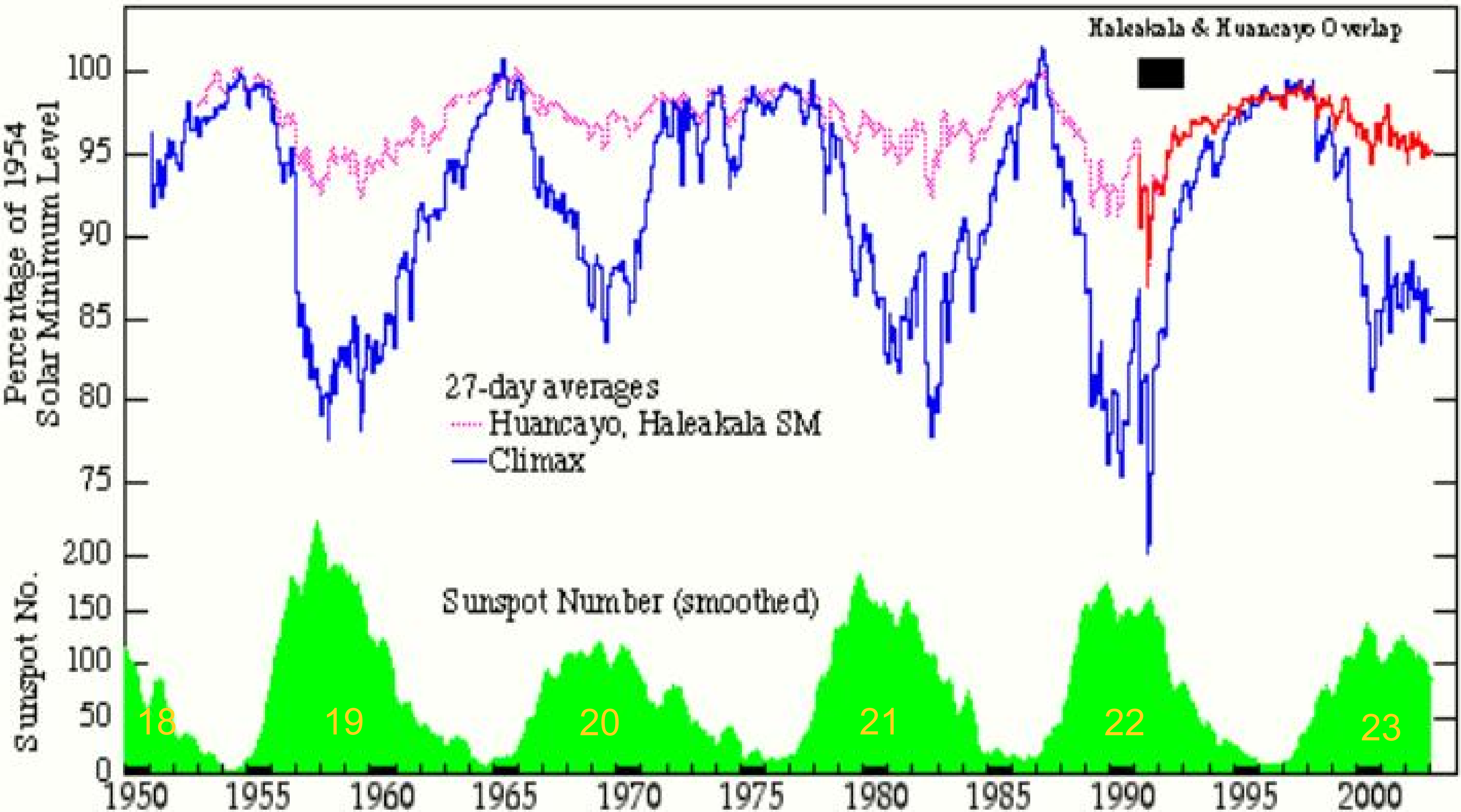

The Univ. of New Hampshire Neutron Monitors

CL February 2003

Cosmic Ray Intensity (Bartels solar-rotation averages through SR 2312):

>3 GV	—	Climax, CO (IGY Monitor, 1951-present)
>13 GV	·····	Huancayo, Peru (IGY Monitor, 1953-1992)
>13 GV	—	Haleakala, HI (Supermonitor, 1991-present)
■		Smoothed Int'l Sunspot Number (monthly)

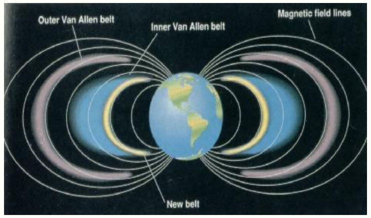

Early measurements of the CR effect of solar activity

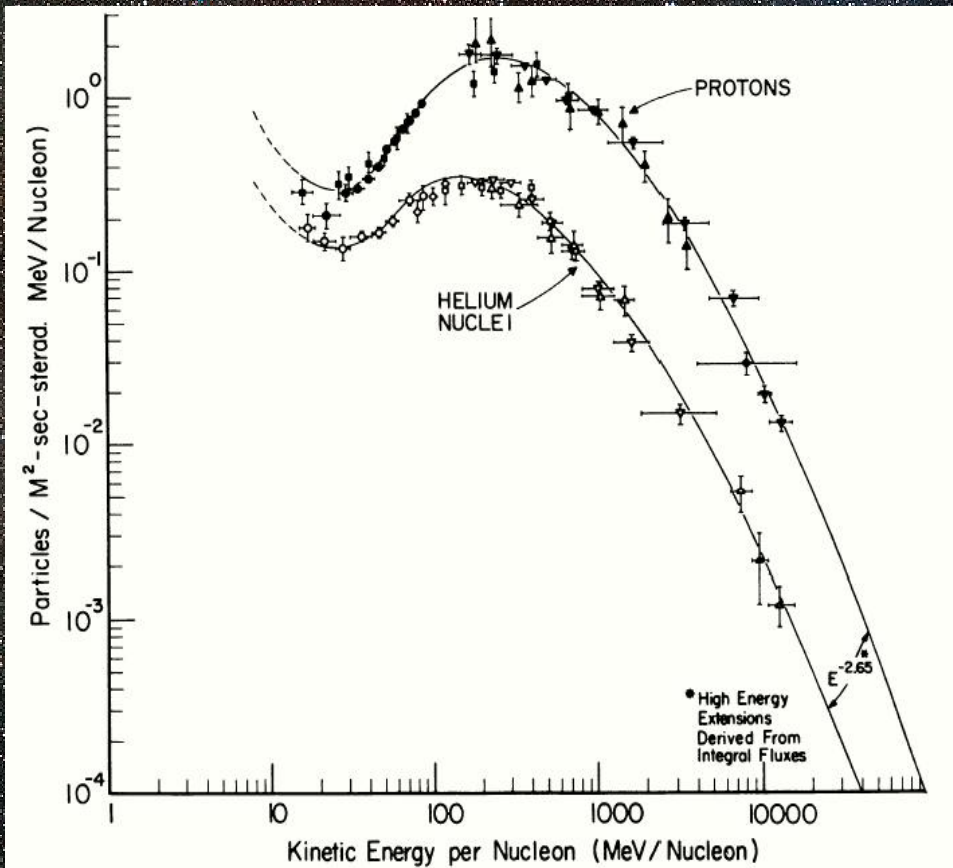

Primary differential kinetic-energy/nucleon spectra of CR protons and helium nuclei obtained near Earth near the solar minimum in 1965.

[**Reference**: G. Gloeckler & J.P. Jokipi, ApJ **148** (1967) L41.]

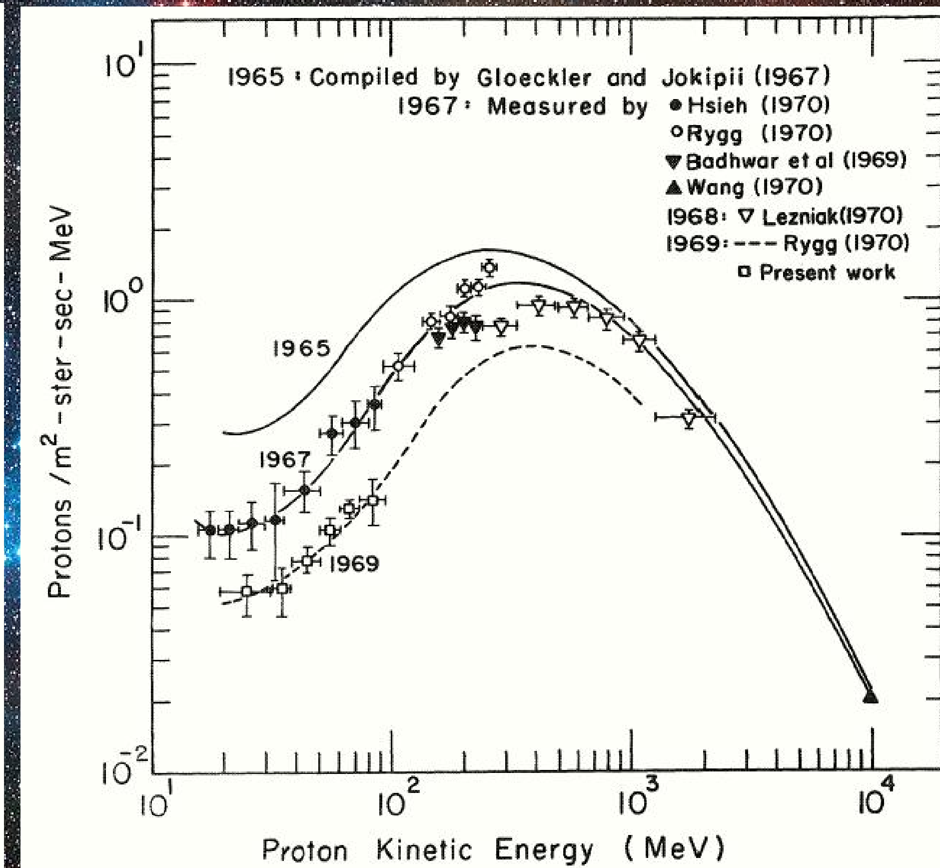

Primary differential kinetic-energy spectra of protons in 1965, 1967, and 1969. The 1965 spectrum is taken from the compilation of Gloeckler and Jokipi.

[**Reference**: K.C. Hsieh et al., ApJ **166** (1971) 221.]

Absolute differential energy spectra of primary protons and helium nuclei at ToA measured in several recent experiments.

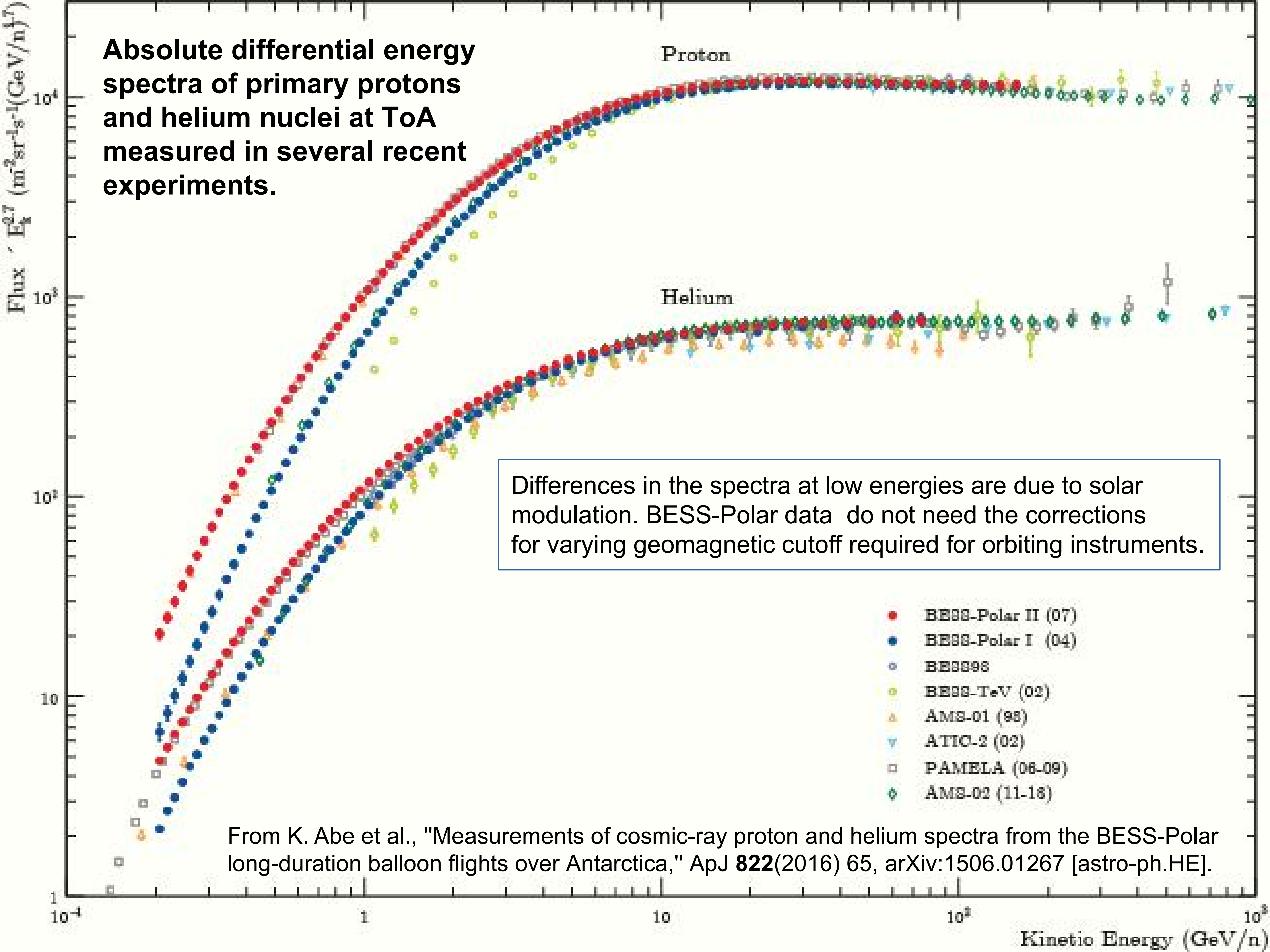

Differences in the spectra at low energies are due to solar modulation. BESS-Polar data do not need the corrections for varying geomagnetic cutoff required for orbiting instruments.

From K. Abe et al., "Measurements of cosmic-ray proton and helium spectra from the BESS-Polar long-duration balloon flights over Antarctica," ApJ **822**(2016) 65, arXiv:1506.01267 [astro-ph.HE].

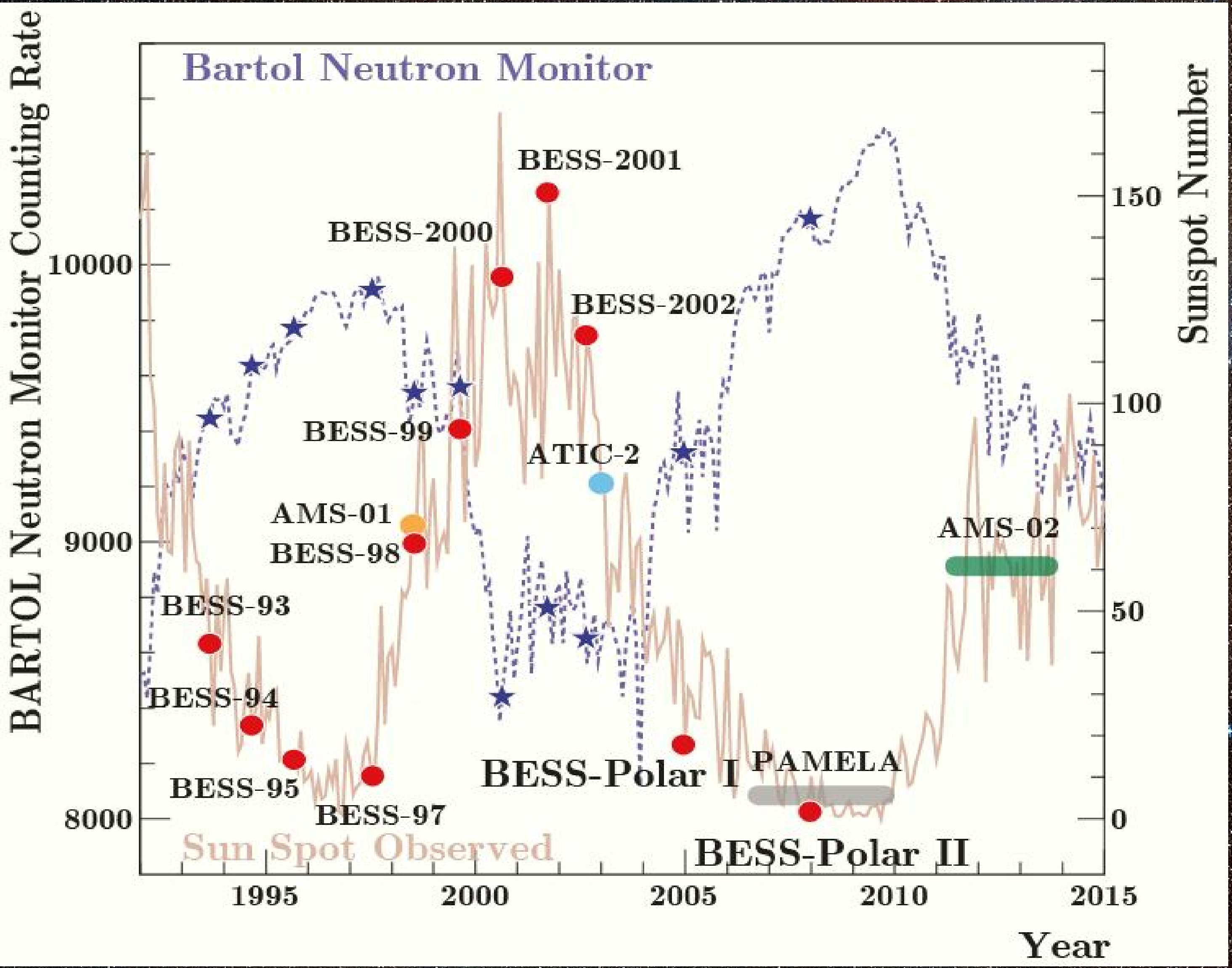

Variation of Bartol neutron monitor counts and sunspot number from 1991 to 2015.

The BESS-Polar II Flight was carried out very near the deepest solar minimum.

The **BESS**, **AMS-01**, **ATIC-2** and **BESS-Polar** flights are marked as circles at the corresponding sunspot number. The periods for which **PAMELA** and **AMS-02** proton and helium spectra have been reported are shown as bars at the approximate average sunspot number.

[**Reference**: K. Abe et al., "Measurements of cosmic-ray proton and helium spectra from the BESS-Polar long-duration balloon flights over Antarctica," ApJ **822** (2016) 65, arXiv:1506.01267 [astro-ph.HE].]

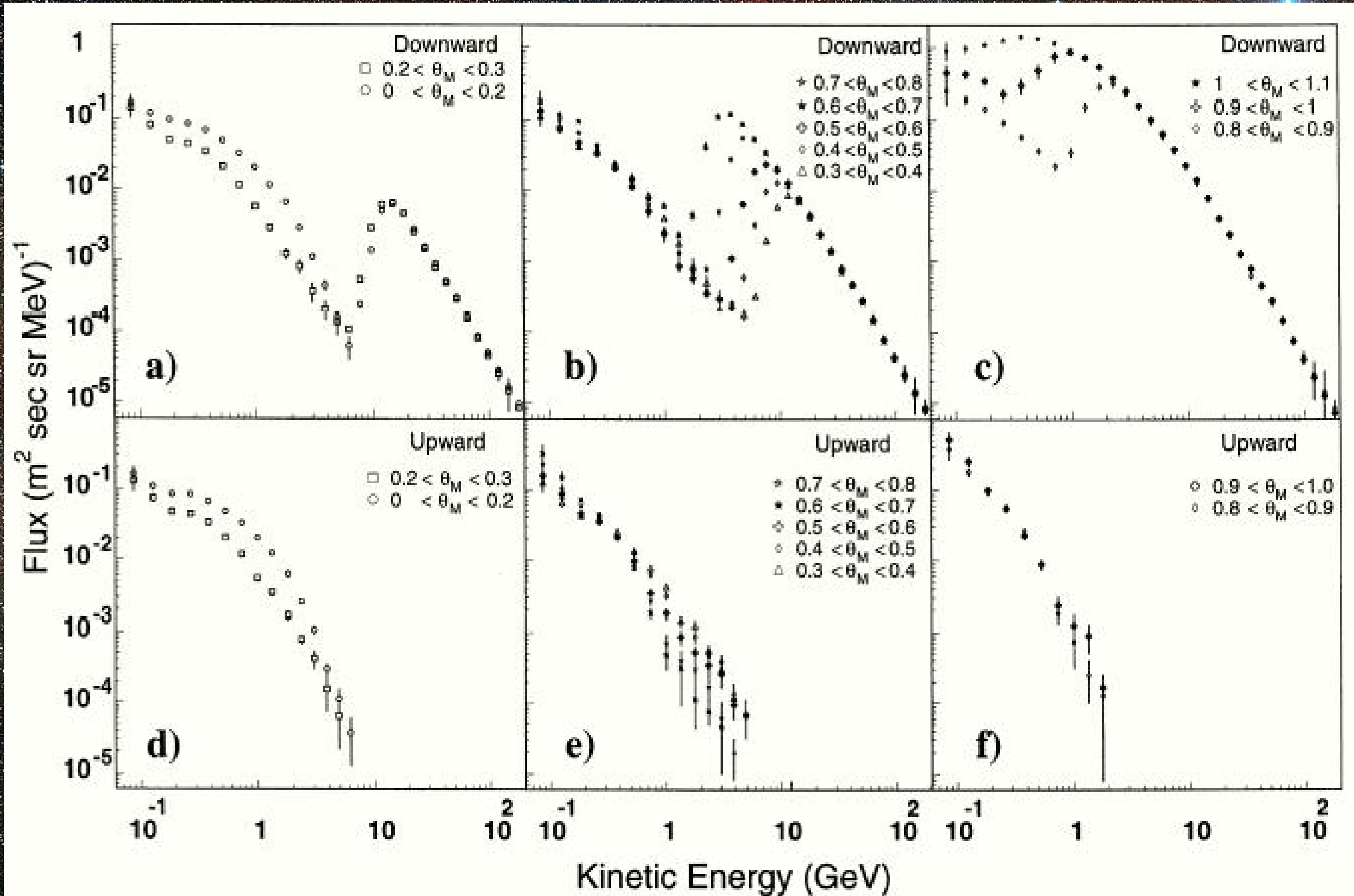

Spectra of downward going (**a,b,c**) and upward going (***d,e,f***) protons separated according to the geomagnetic latitude, Q_M, at which they were detected with AMS during the space shuttle flight STS-91 at an altitude of 380 km.

[**Reference**: J. Alcaraz et al. (AMS Collaboration), Phys. Lett. B **472** (2000) 215-226 (hep-ex/0002049); M. Aguilar etl. (AMS Collaboration), Phys. Rep. 894 (2021) 1-116.]

Electrons & Positrons

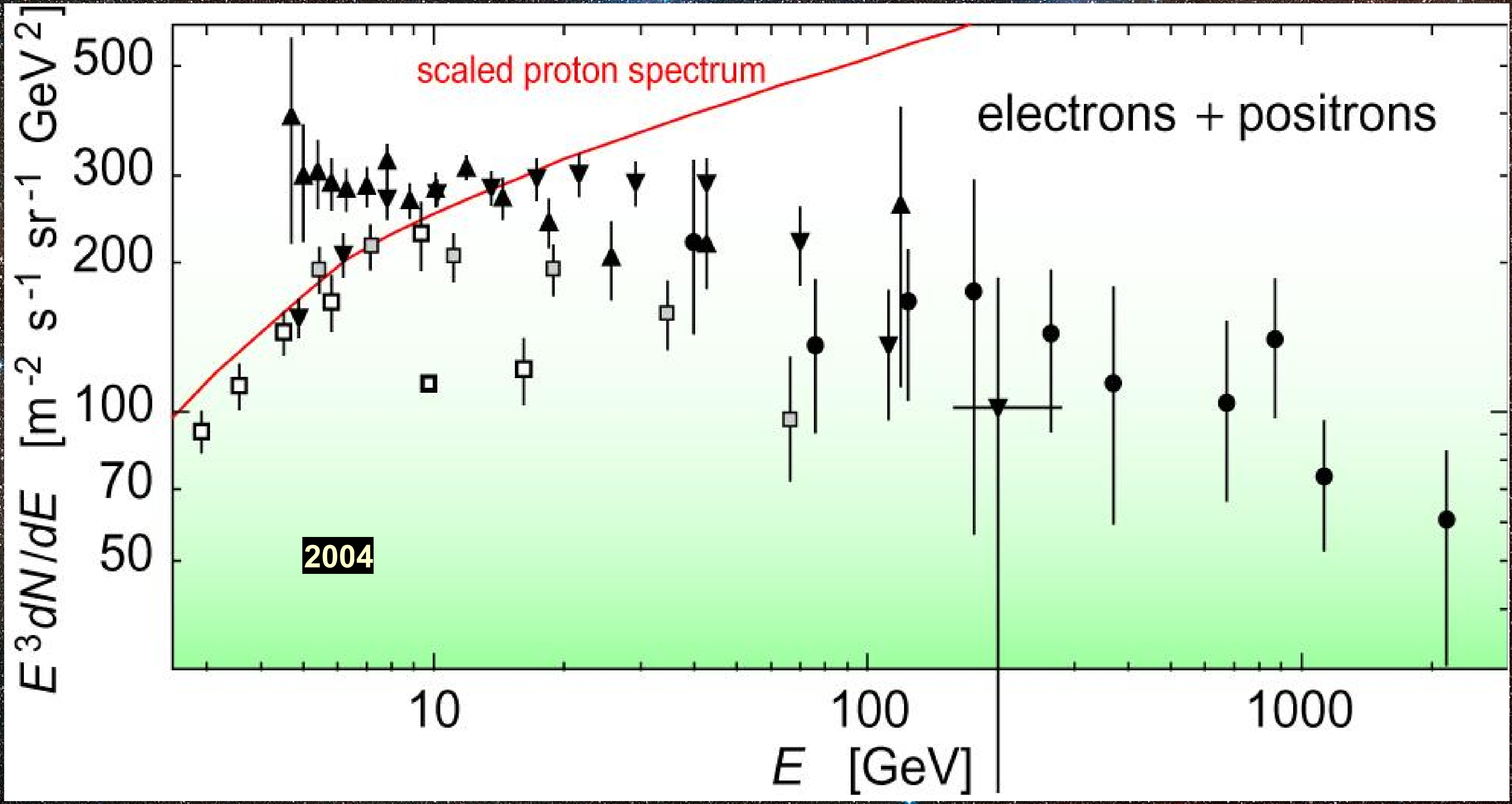

Differential energy spectrum of electrons plus positrons multiplied by E^3 (incomplete data set). The solid line shows the proton spectrum multiplied by 0.01.

[**Reference**: T.K. Gaisser & T. Stanev, “Cosmic rays,” pages 228-234 of the Review of Particle Physics, Phys. Lett. B **592** (2004) 1.]

Golden age of direct CR measurements

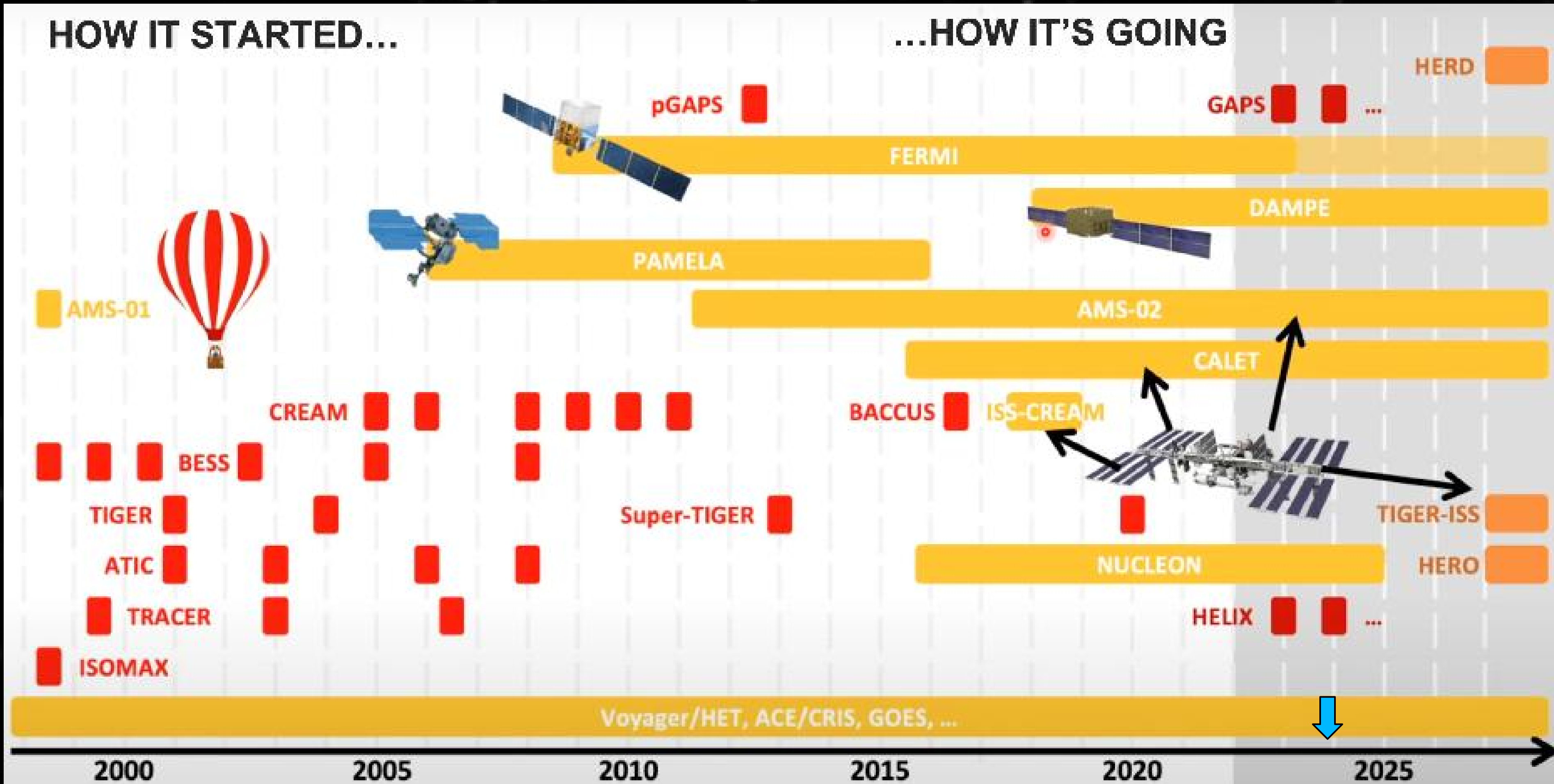

A timeline of the accomplished, ongoing, and planned experiments of direct CR detection in space (orange) or on stratospheric balloons (red) in the 3rd millennium. (Credit: Alberto Oliva)

[Reference: N.Tomassetti, "Direct Measurements of Galactic Cosmic Rays," arXiv:2301.10255v3 [astro-ph.HE].]

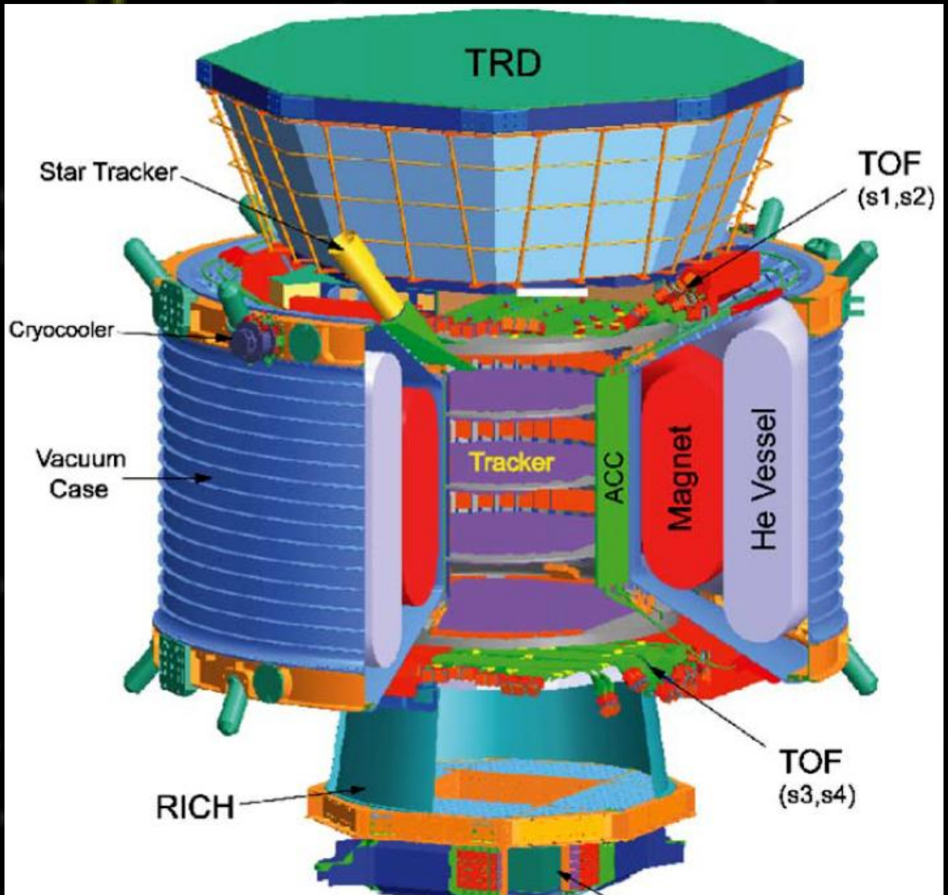

The AMS-02 detector configuration

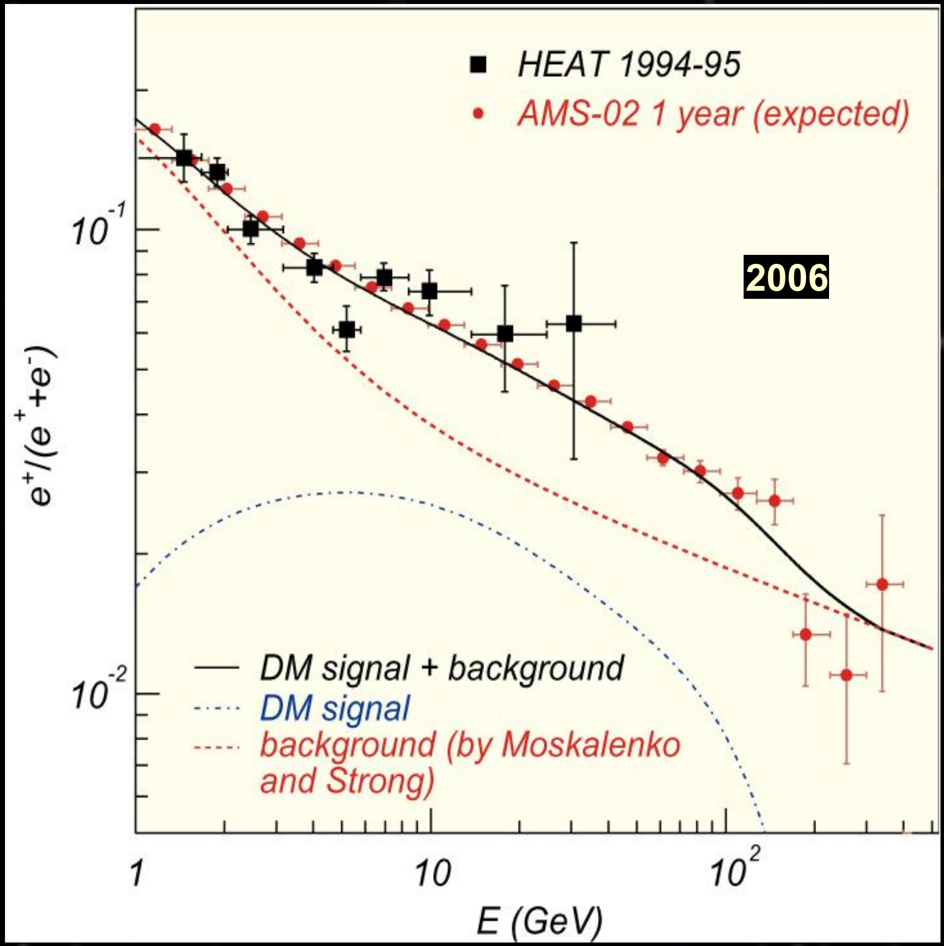

ISS

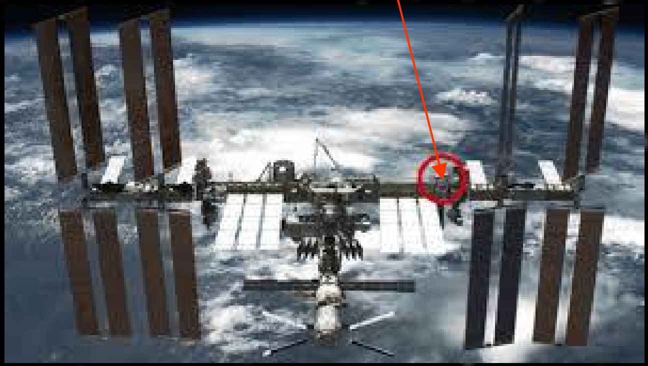

The expected positron fraction accuracy from the AMS-02 after 1 year on the ISS compared to available data from the HEAT collaboration. The error bars reflect the particle identification power estimated from AMS subdetector beam test data. See next slide for the modern data.

[Reference: Ph. von Doetinchem *et al*., "Performance of the AMS-02 transition radiation detector," Nucl. Instrum. Meth. A **558** (2006) 526–535.]

Current status of AMS measurements of lepton spectra (March 2022)

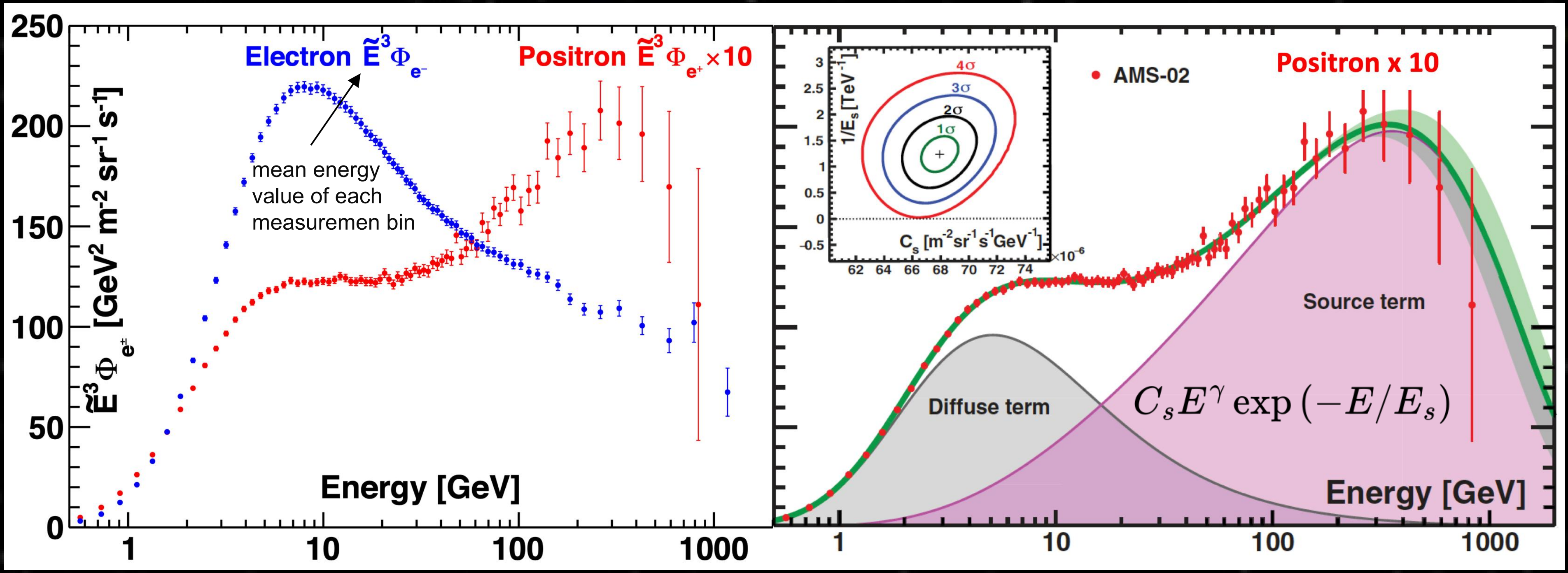

In the right panel, the positron spectrum is shown which is fitted with a diffused (power law) term plus a source (power law with exponential cutoff) term. To account for the solar modulation, force field approximation are used to modify the function form. The insert shows different significance contours for the source tem model.

The highest energy bins of the AMS spectra are with large errors and therefore not yet sufficient to distinguish different models conclusively. The AMS experiment will continue collecting data till the end of the ISS operation.

[Reference: Y.-H. Chang (on behalf of the AMS collaboration), “Latest Results from the AMS Experiment”, JPS Conf. Proc. **39** (2023) 011006.]

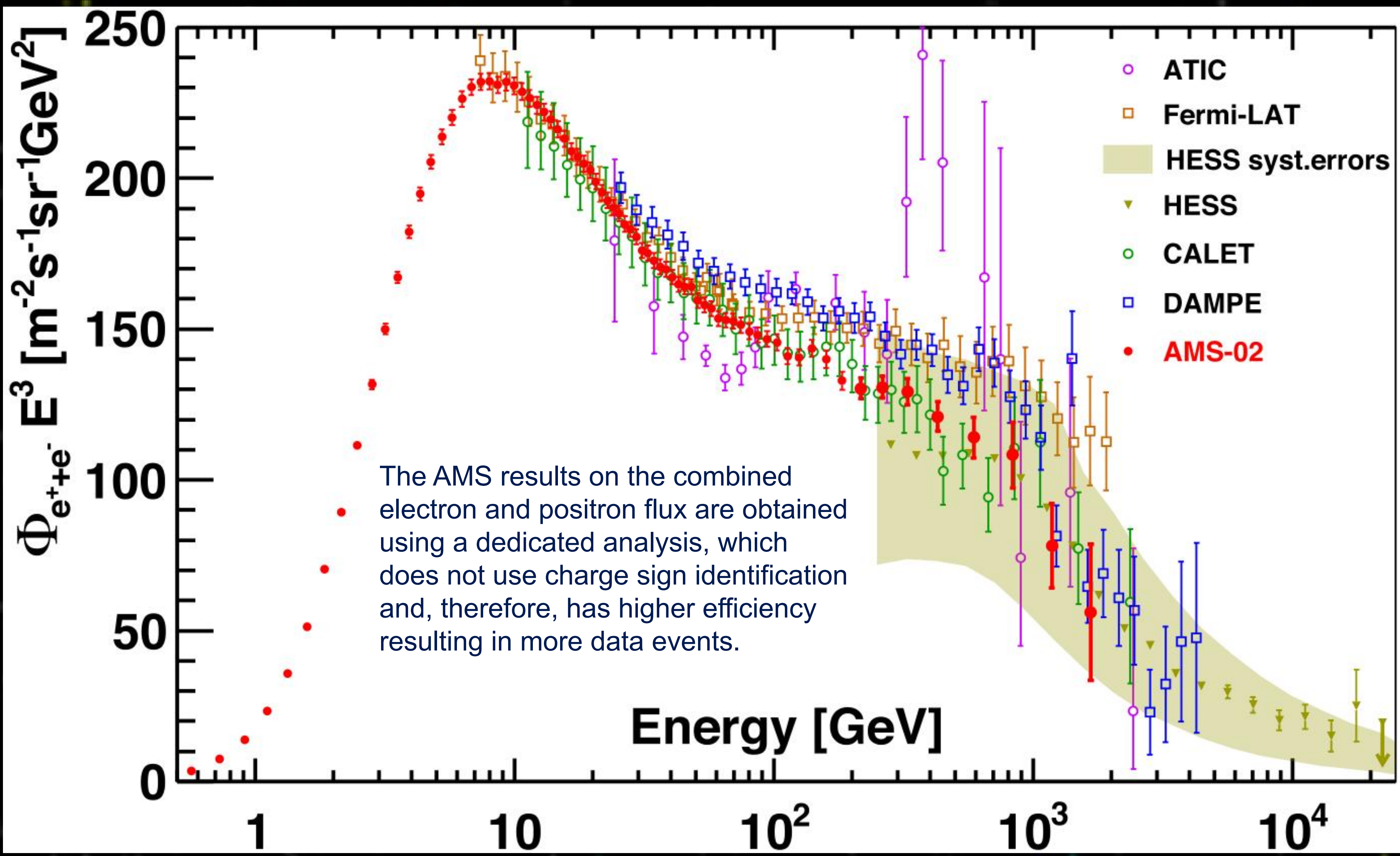

The AMS combined electron and positron flux, multiplied by E^3, together with the measurements from other modern experiments that use non-magnetic calorimeters.

[Reference: M. Aguilar et al., The Alpha Magnetic Spectrometer (AMS) on the international space station: Part II — Results from the first seven years," Phys. Rep. 894 (2021) 1-116.]

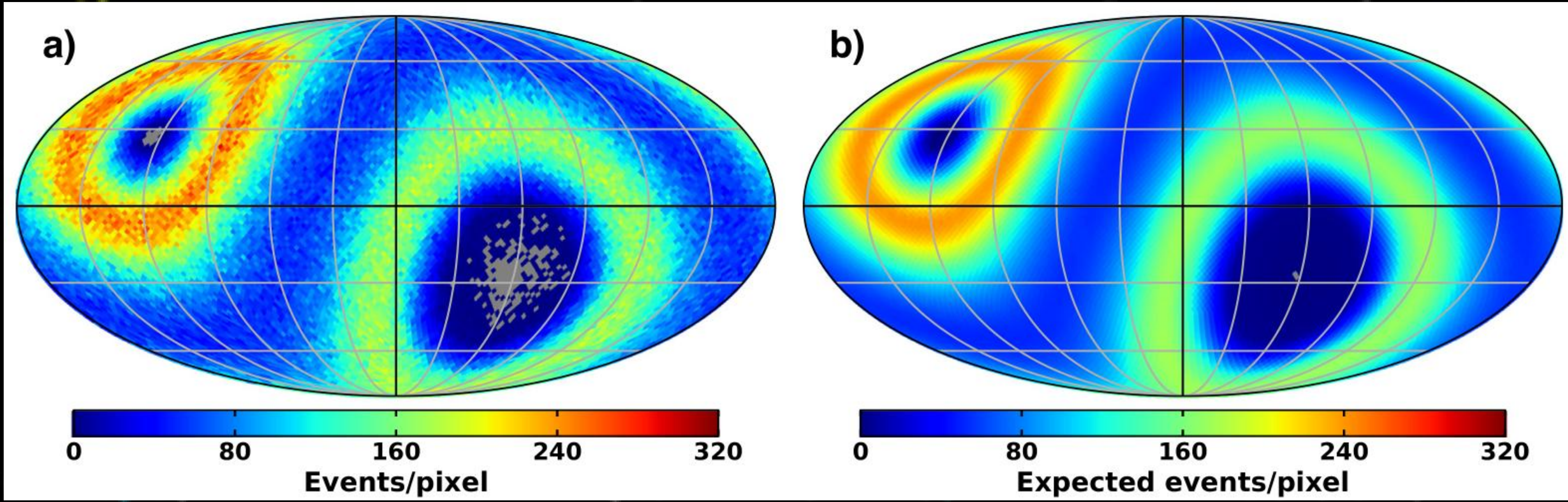

(a) Map of the incoming electron directions in galactic coordinates observed by AMS on the ISS. Analysis of the electron arrival directions was performed using the data in the energy range above **16 GeV**.

(b) Expected map of the incoming electron directions for an isotropic distribution of positrons in galactic coordinates. The dipole anisotropy δ is defined in terms of the dipole moment C_1. The AMS data show that

$$\delta = 3(C_1/4\pi)^{1/2} < 0.005$$

at the 95% C.L. that is consistent with isotropy.

[Reference: M. Aguilar et al., The Alpha Magnetic Spectrometer (AMS) on the international space station: Part II — Results from the first seven years," Phys. Rep. 894 (2021) 1-116.]

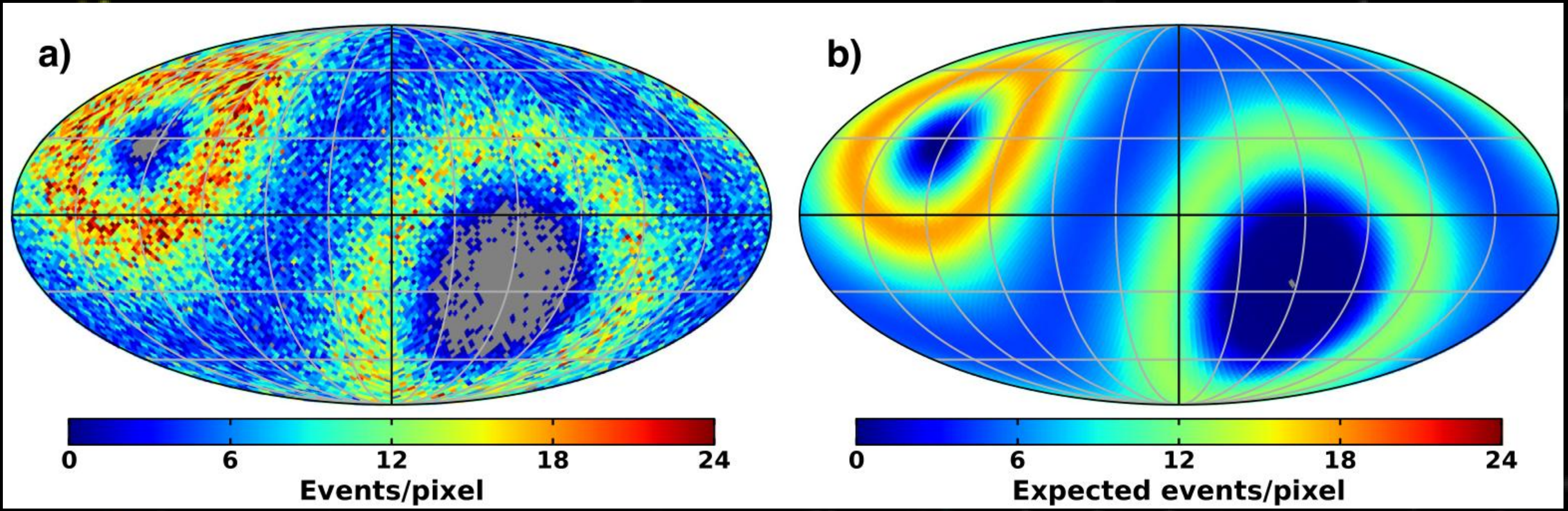

(a) Map of the incoming positron directions in galactic coordinates observed by AMS on the ISS. The analysis was performed using the positron data in the energy range above 16 GeV.

(b) Map of the expected positron directions for an isotropic distribution of positrons in galactic coordinates. The dipole anisotropy δ is defined in terms of the dipole moment C_1. The AMS data show that

$$\delta = 3(C_1/4\pi)^{1/2} < 0.019$$

at the 95% C.L. that is consistent with isotropy. Astrophysical point sources like pulsars will imprint a higher anisotropy on the arrival directions of energetic positrons than a smooth dark matter halo.

[Reference: M. Aguilar et al., The Alpha Magnetic Spectrometer (AMS) on the international space station: Part II — Results from the first seven years," Phys. Rep. 894 (2021) 1-116.]

Antiprotons and antinuclei in CR

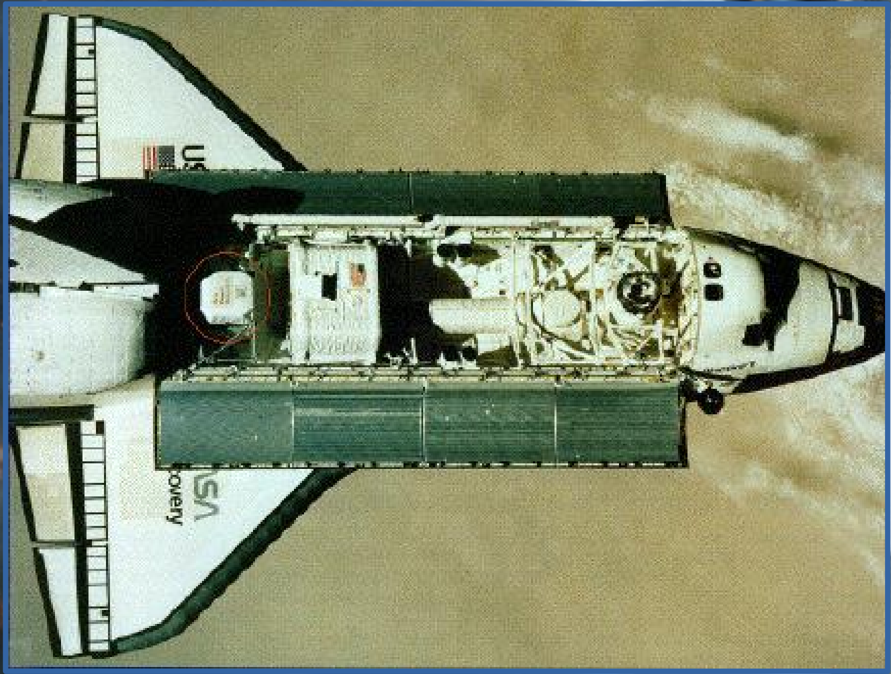

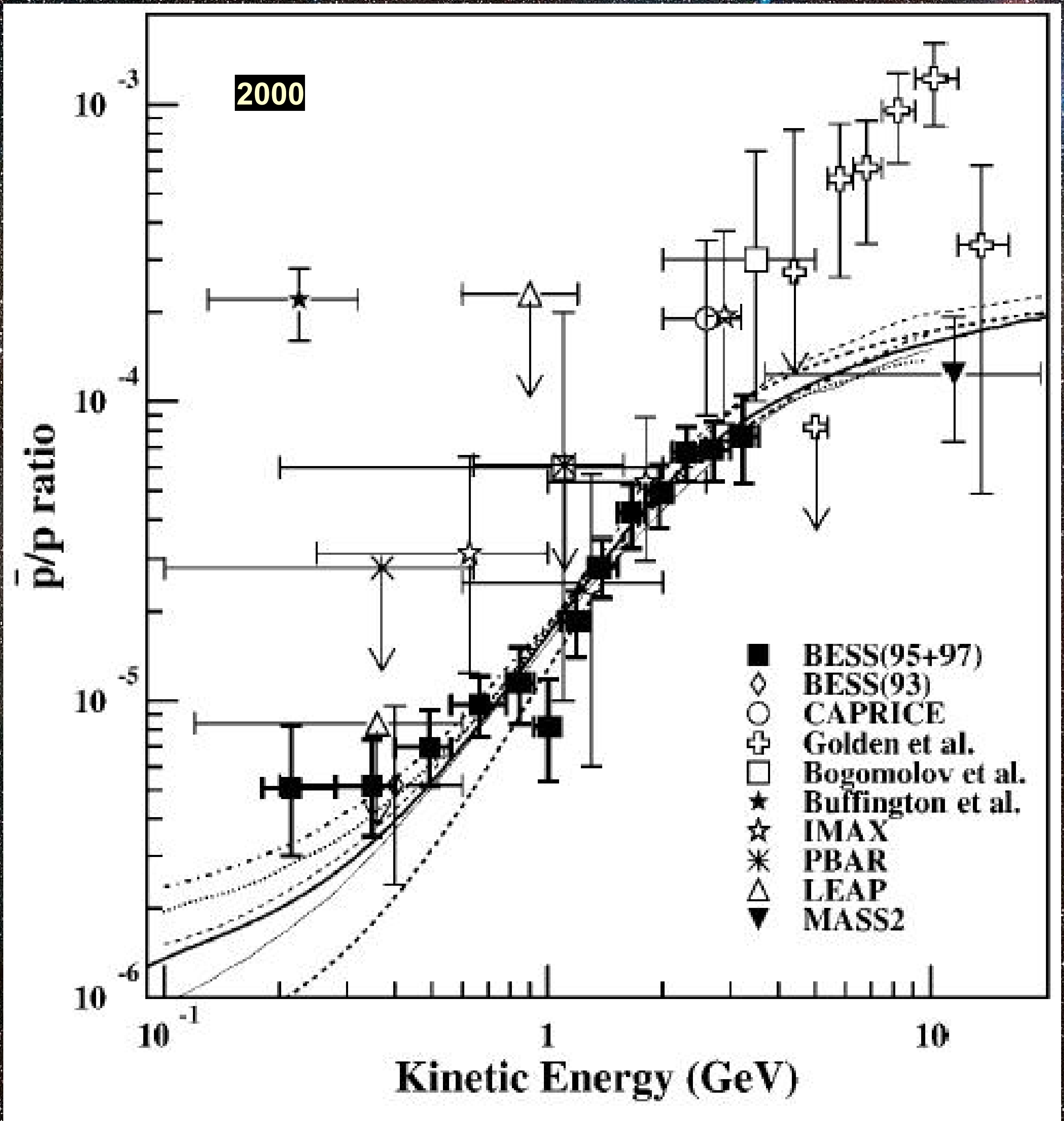

CR antiproton to proton ratio measured in different experiments.

[**Reference**: S. Orito et al. (BESS Collaboration), Phys. Rev. Lett. "Precision measurement of cosmic-ray antiproton spectrum", **84** (2000) 1078-1081.]

Antiproton flux measurements with the L3 detector at LEP CERN

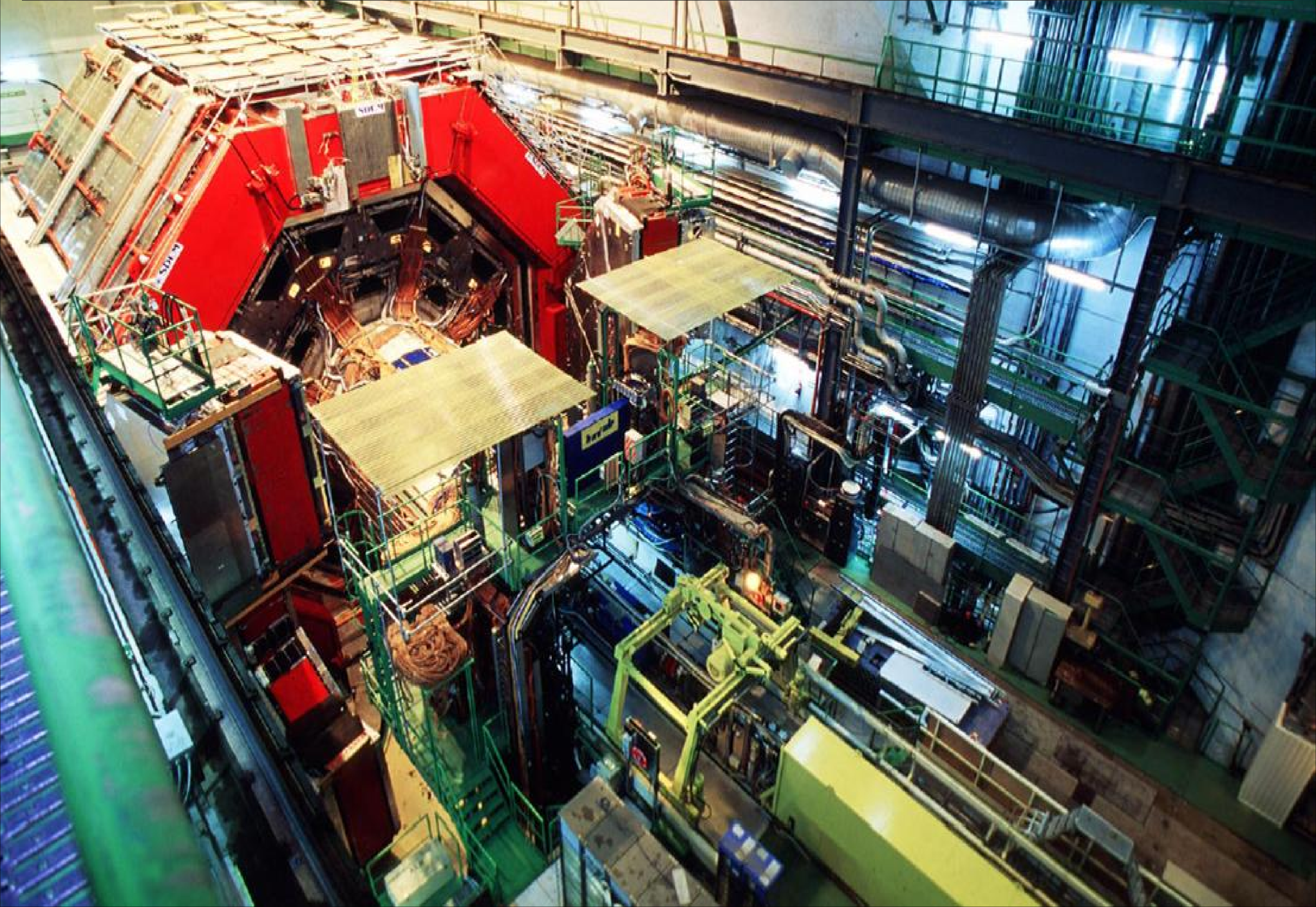

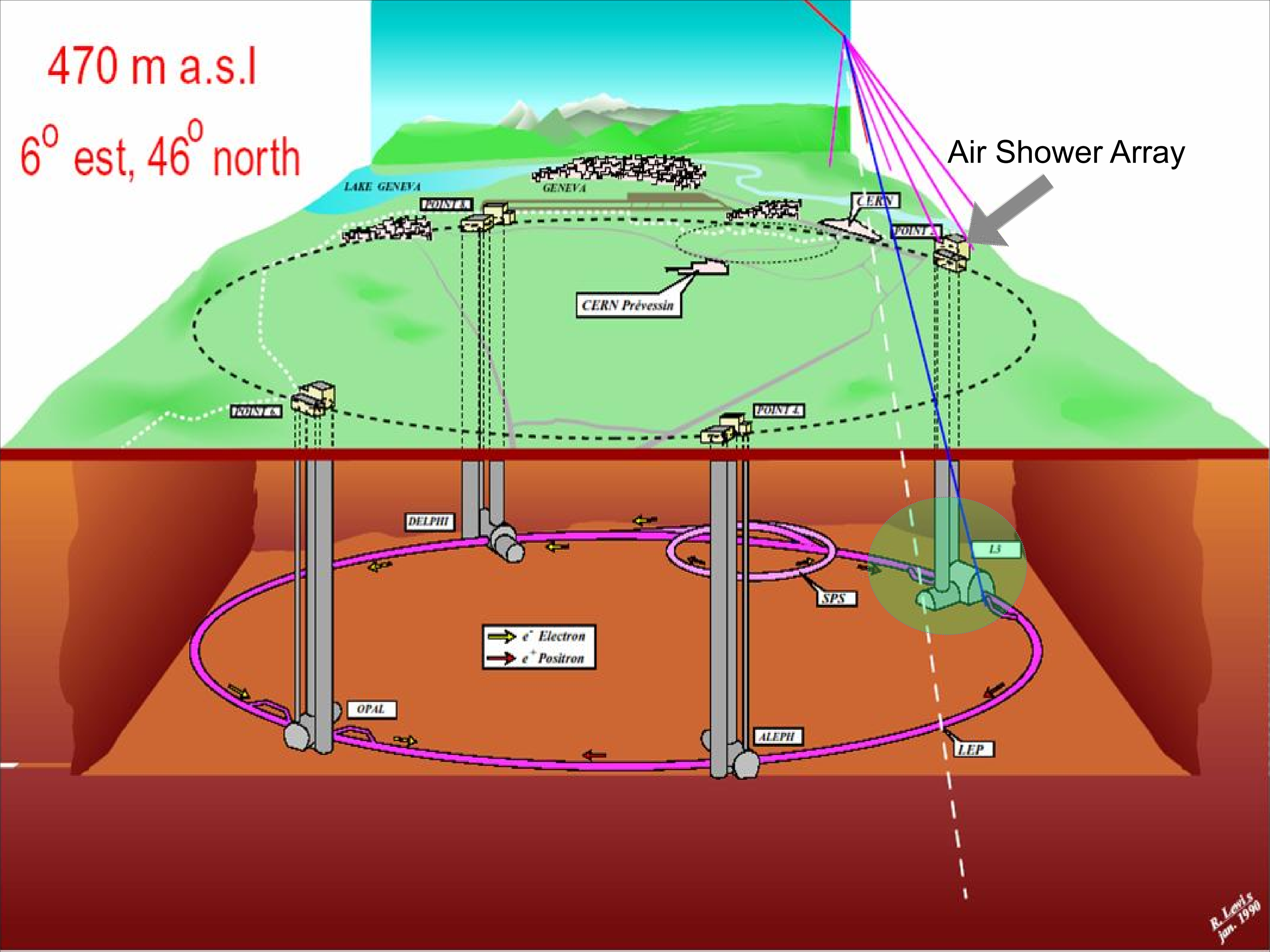
470 m a.s.l
6° est, 46° north
Air Shower Array
LAKE GENEVA
GENEVA
POINT 8
CERN
POINT 2
CERN Prévessin
POINT 6
POINT 4
DELPHI
L3
SPS
e⁻ Electron
e⁺ Positron
OPAL
ALEPH
LEP
R. Lewis
jan. 1990

The L3+C: Air Shower Array

47 scintillators ($50 \times 50 \times 1 cm^3$), area = 1800 m^2, offline coincidence with muon detector (27×10^6 triggers)

The L3+C: Muon detector

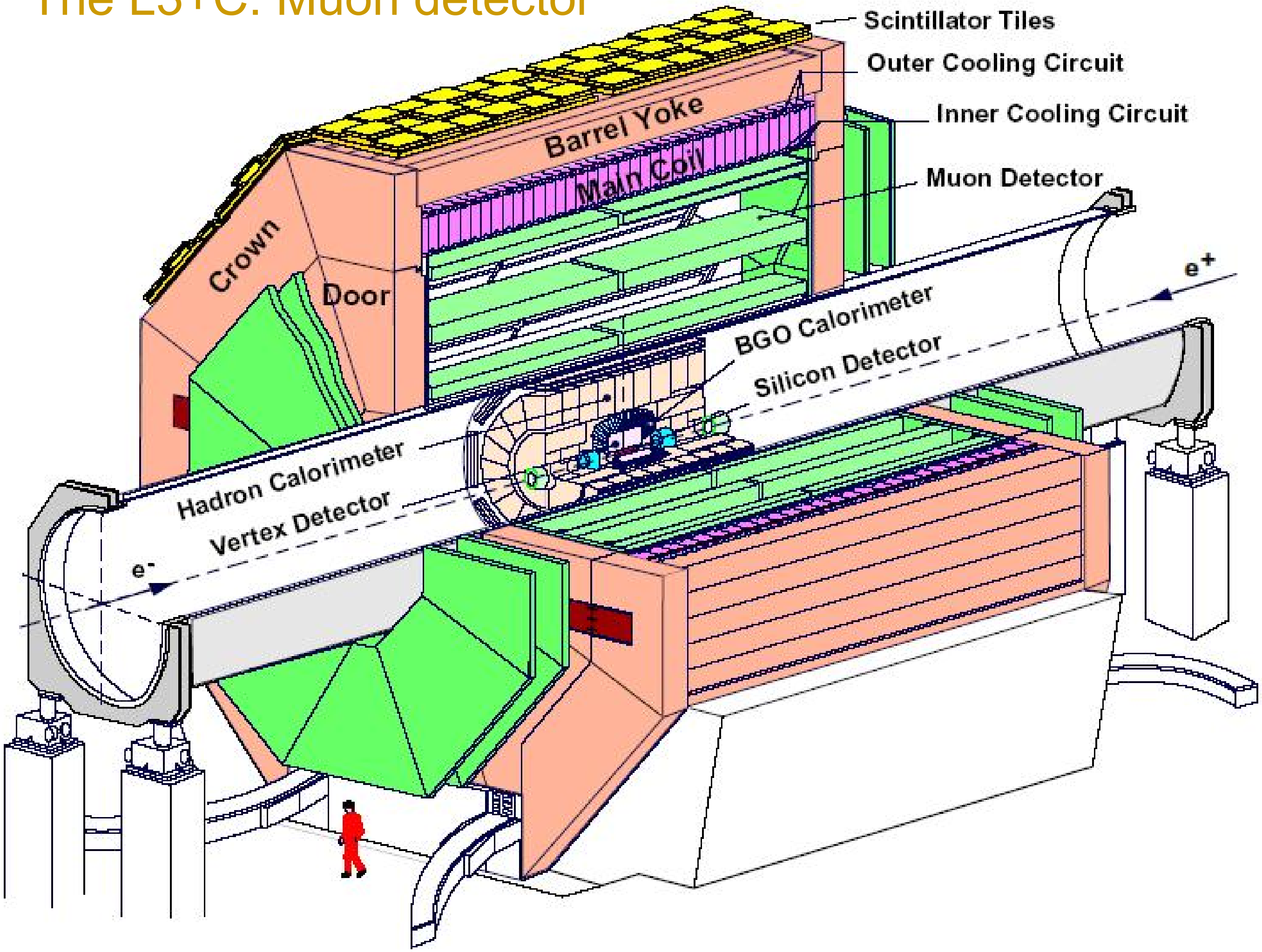

- 30 m below the surface,
- drift chambers in 1000 m³ magnetic volume (0.5T),
- 200 m² scintillator area,
- data acquisition indepen-dent from L3,
- 11 billion muon triggers collected.

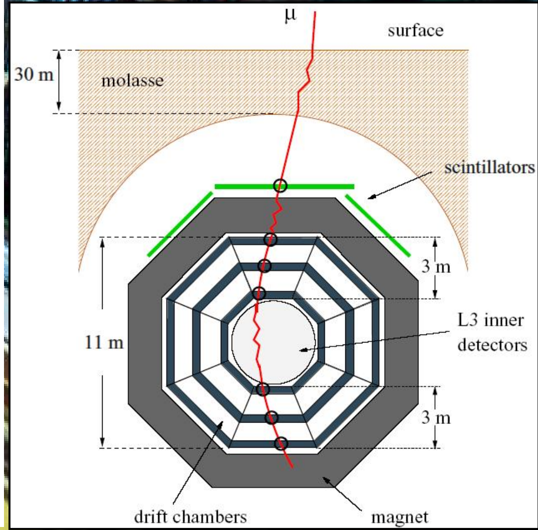

Moon Shadow

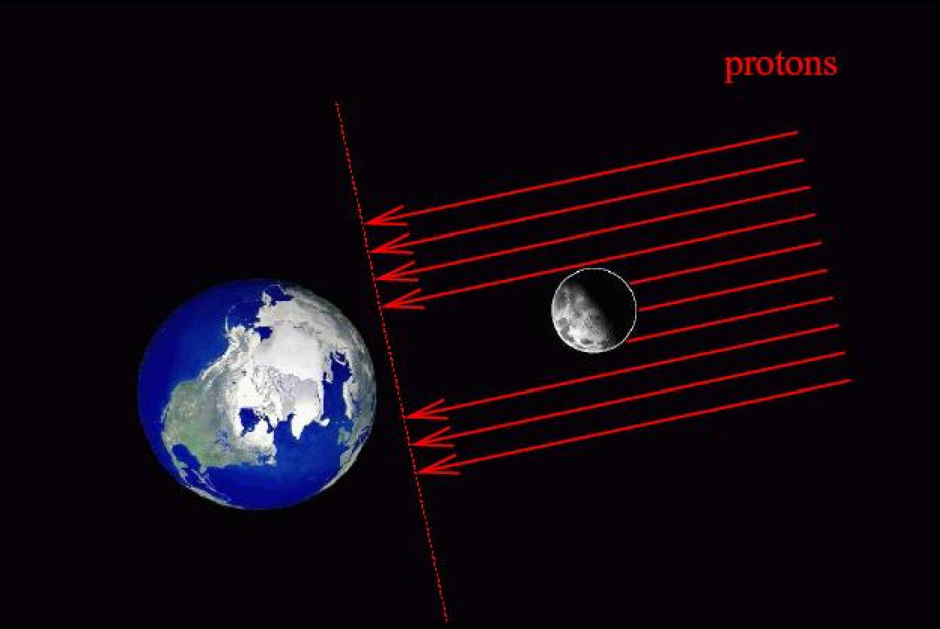

The moon is an absorber for primary cosmic rays. Therefore the moon shadow can be used for verification of experimental pointing accuracy.

The earth magnetic field shadow shifts from optical moon position eastwards for protons and westwards for antiparticles (“anti shadow”).

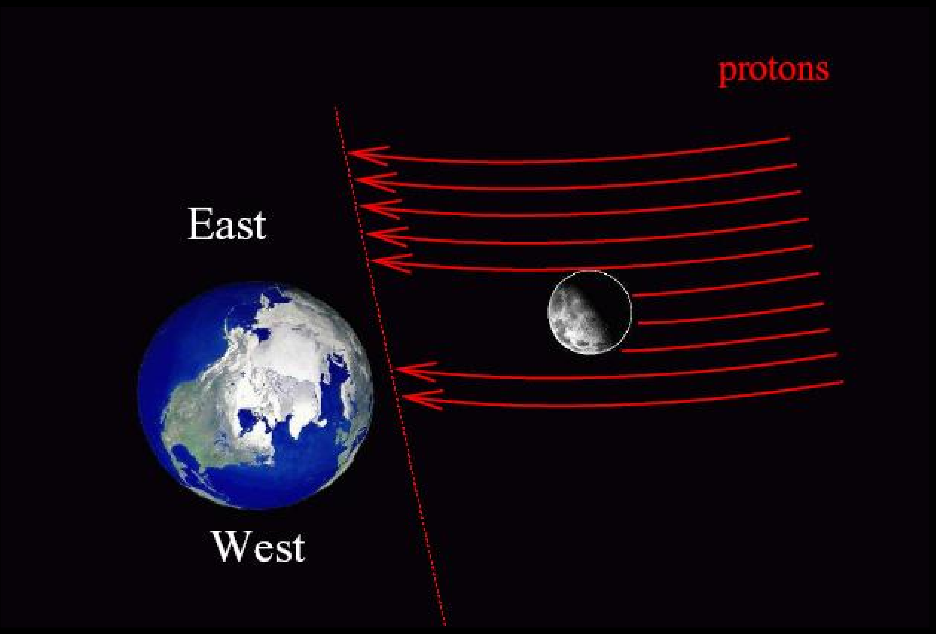

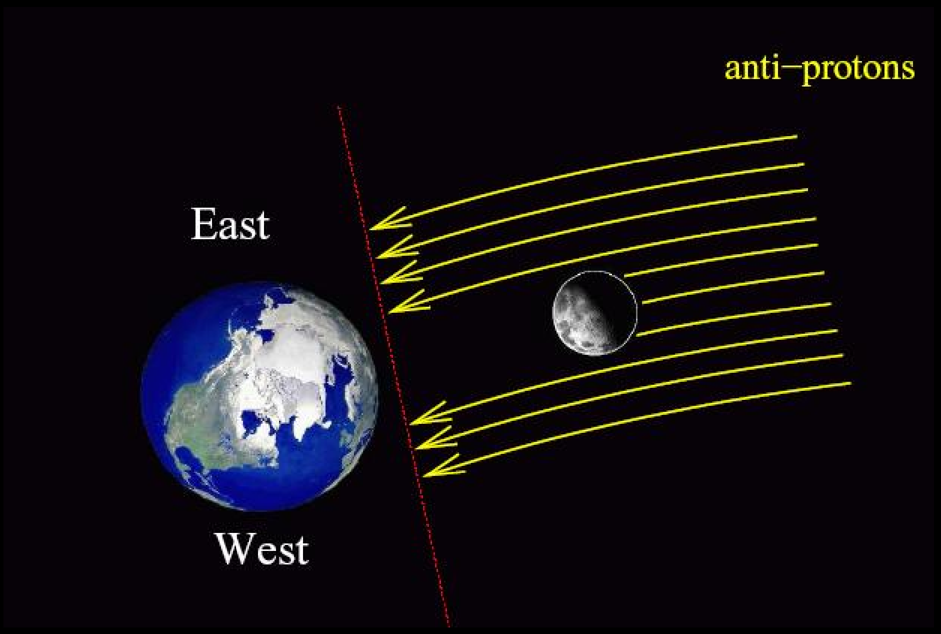

Pointing precision - The Earth-Moon system as a spectrometer

Cosmic rays are blocked by the Moon.
$\Longrightarrow$ deficit of cosmic rays when looking at the Moon (Clark 1957).

- Size of the deficit $\longrightarrow$ effective angular resolution
- Position of the deficit $\longrightarrow$ pointing error

Geomagnetic field: positively charged particles deflected towards the East and negatively charged particles towards the West. $\Longrightarrow$ ion spectrometer

- Advantage of L3+C:
  - Excellent angular resolution and pointing
  - Precise momentum measurement
  - Low p_{min} (high rate, large deflection)
  - Real sensitivity on the earth magnetic field.

Pointing precision: obtained from the comparison of the observed Moon shadow in the local coordinate system and a Monte Carlo simulation. $\Rightarrow$ $< 0.1^\circ$

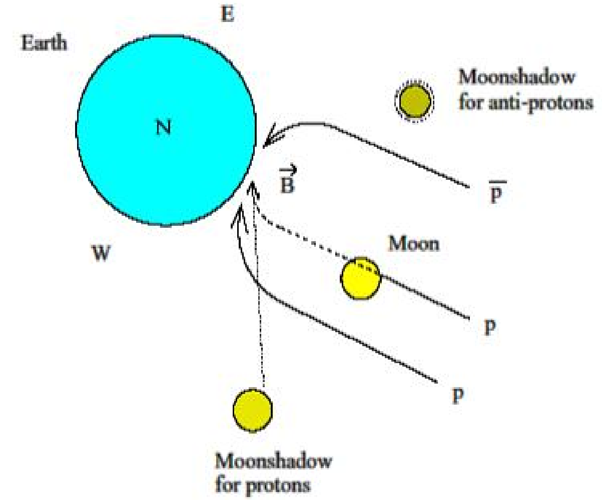

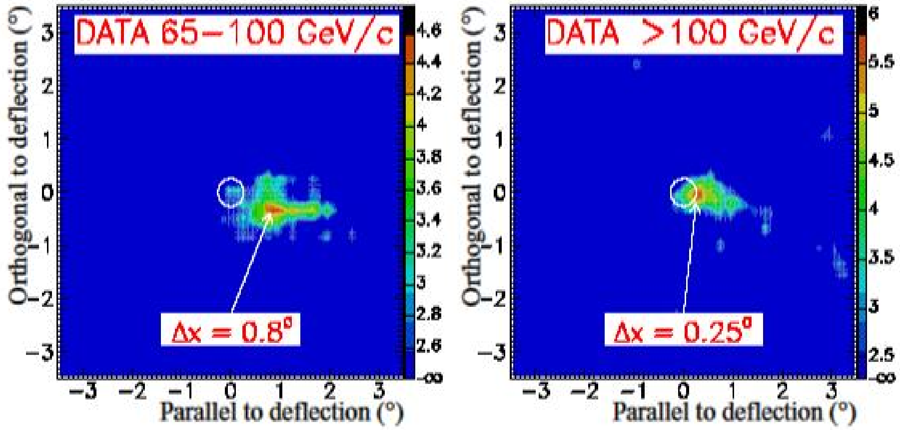

Shadow (in deflection coordinate system)

Angular distributions for events/Moon-solid-angle

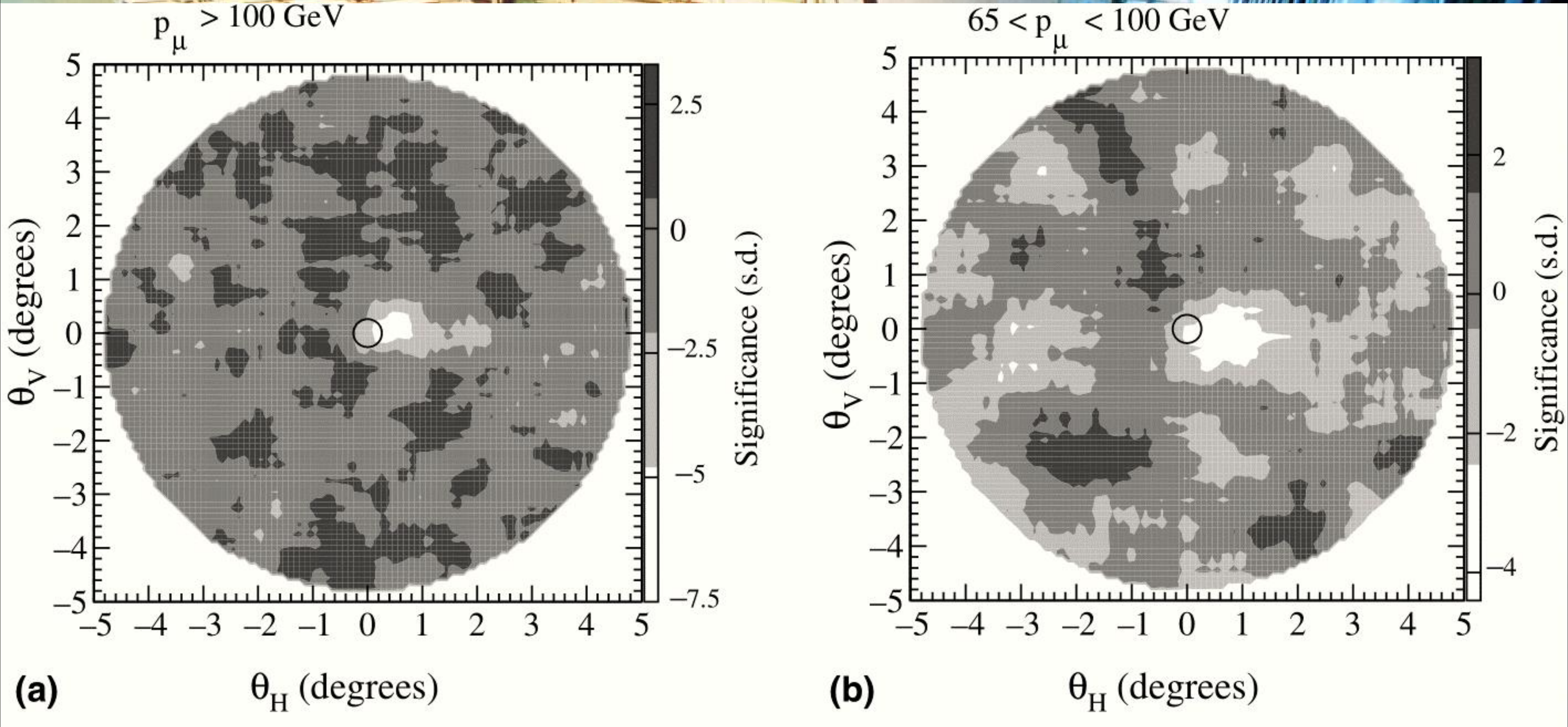

L3+C results obtained in the deflection system for: (a) the high-energy sample, (b) the low-energy sample. In both cases, smoothing techniques have been applied. A circle indicates the true position of the Moon. The vertical grey scale shows the significance in standard deviation units; negative values correspond to an event deficit.

[Reference: P. Achard et al. (L3 Collaboration), Astropart. Phys. **23** (2005) 411–434 (astro-ph/0503472).**]**

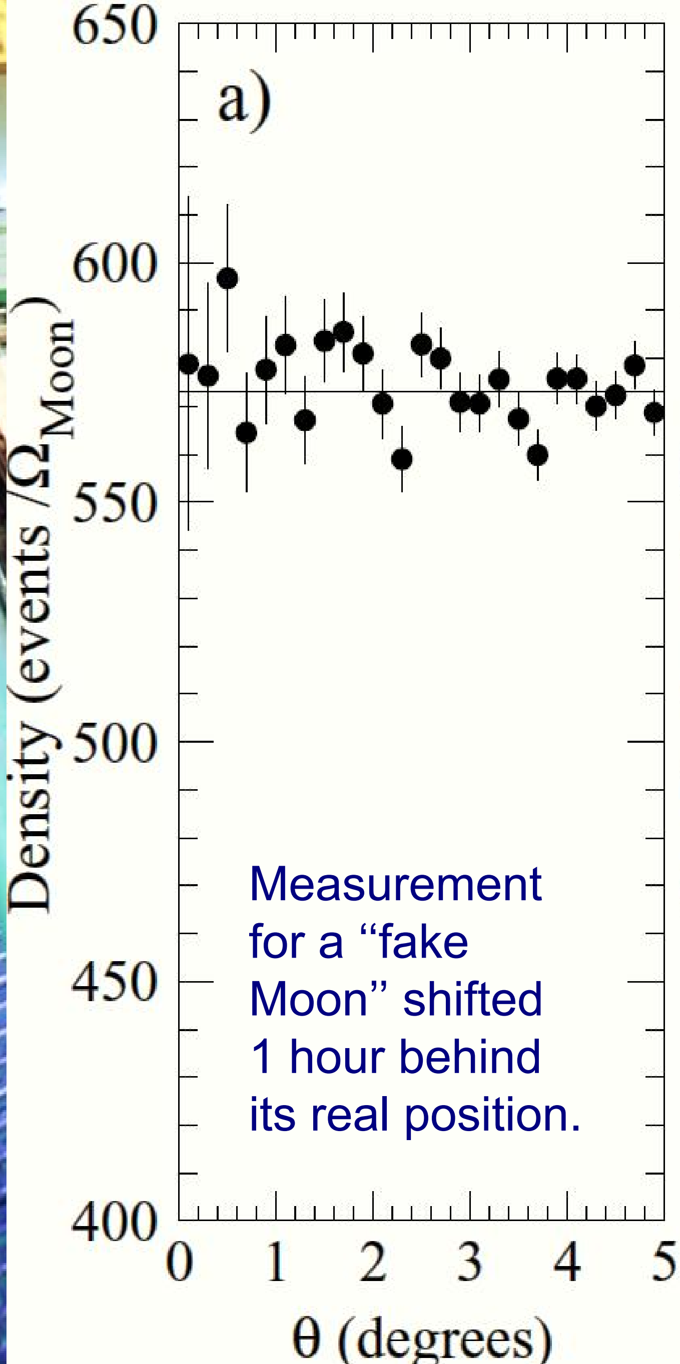

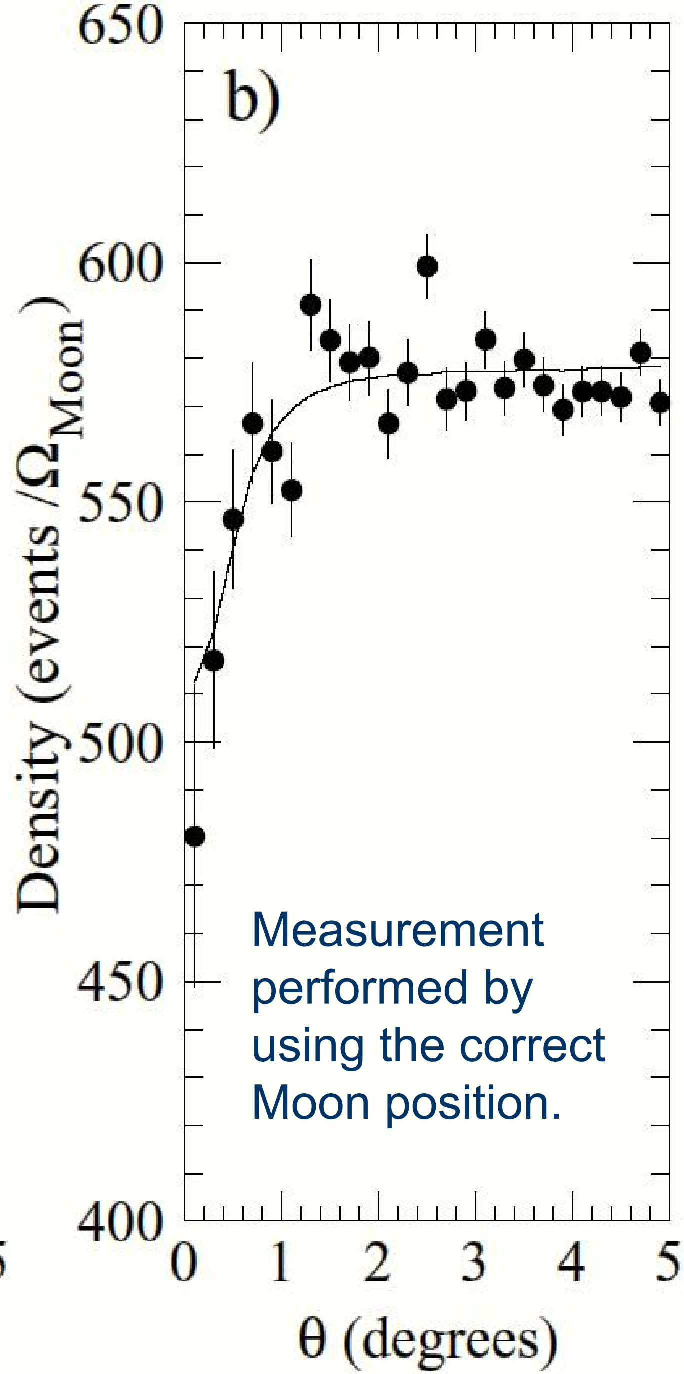

Angular distributions for events/Moon-solid-angle with E_μ > 100 GeV.

Solid lines are the results of the simulation, including the angular resolution deduced from the study of di-muon events.

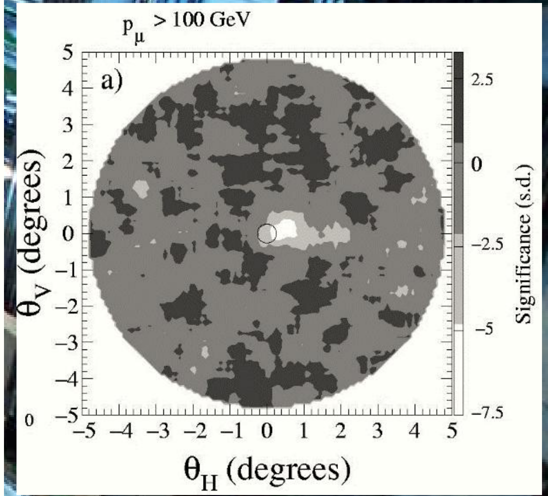

[Reference: P. Achard et al. (L3 Collaboration), Astropart. Phys. **23** (2005) 411–434 (astro-ph/0503472).]

See also news from IceCube

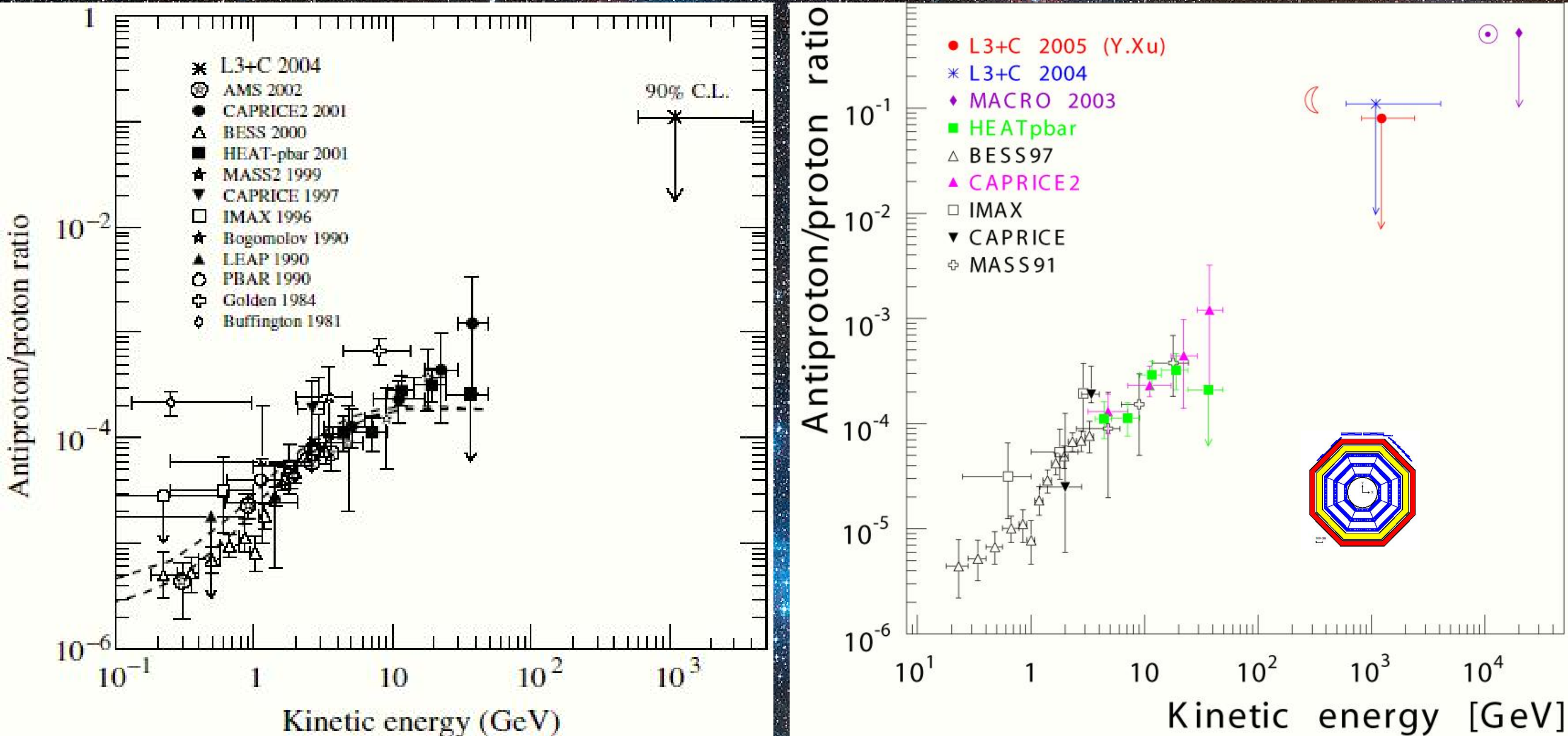

Measurements of the ratio of the antiproton and proton fluxes versus the primary energy, including the L3+C limit around 1 TeV. The dashed lines (left) show the range of the theoretical expectations according to I.V. Moskalenko, Astrophys. J. **565** (2002) 280. An upper limit obtained in the MACRO experiment at Gran Sasso [M. Ambrosio et al. (MACRO Collaboration), Astropart. Phys. **20** (2003) 145-156 (astro-ph/0302586)] from observation of the moon and sun shadows is also shown (right).

[**References**: P. Achard et al. (L3 Collaboration), Astropart. Phys. **23** (2005) 411–434 (astro-ph/0503472); Yupeng Xu, PhD, ETH Zürich (2005).]

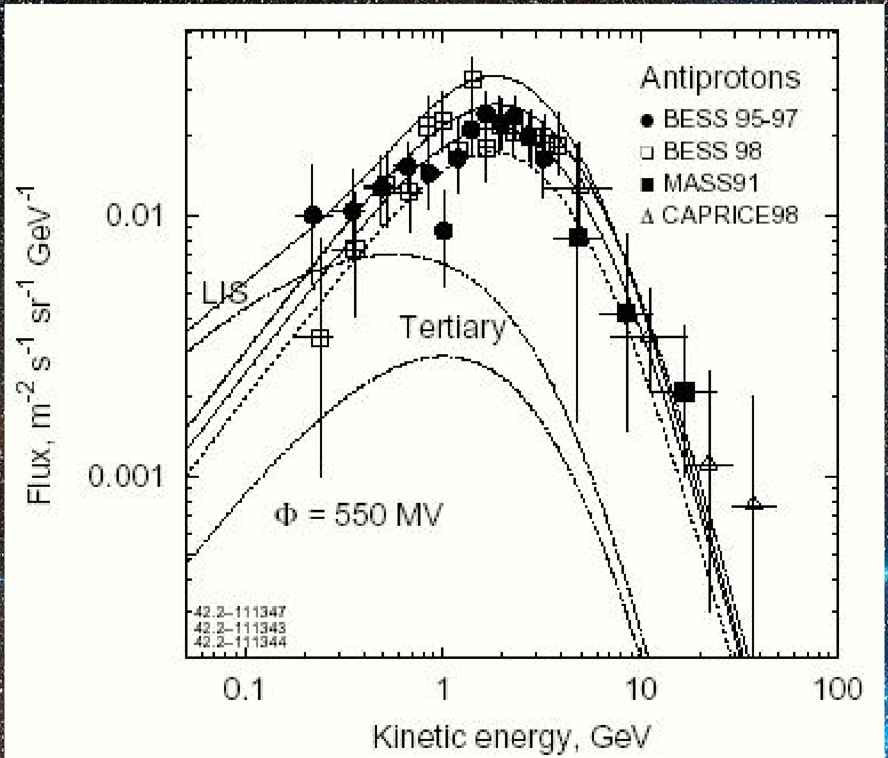

Calculated antiproton flux in a model with the spatial diffusion coefficient $D_{xx} = \beta D_0 (\rho/\rho_0)^\delta$; for $\delta = 0.47$ and different normalization factors D_0 ($\times 10^{28}$ cm s^{-2}). ***Solid curves*** – $D_0 = 3.3$ at $\rho_0 = 3$ GV, upper curve – local interstellar spectrum (LIS), lower curve – modulated (with modulation parameter of 550 MV). ***Dots*** – $D_0 = 2.6$, ***dashes*** – $D_0 = 4.3$.
Data: BESS 95-97 (Orito et al., 2000), BESS 98 (Asaoka et al., 2002), MASS 91 (Basini et al., 1999), CAPRICE 98 (Boezio et al., 2001).

[**Reference**: I.V. Moskalenko et al., ApJ **586** (2003) 1050.]

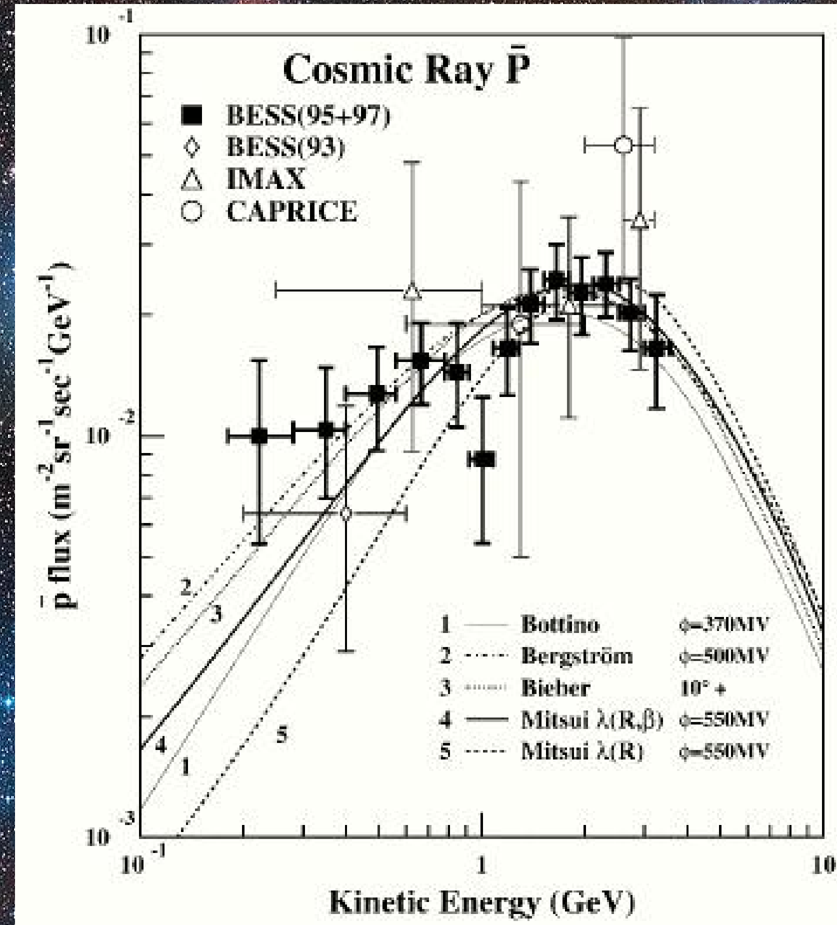

BESS 1995 and 1997 (solar minimum) antiproton fluxes at the top of the atmosphere together with previous data. The curves are recent calculations of the secondary antiproton spectra for the solar minimum period.

[**Reference**: S. Orito et al. (BESS Collaboration), Phys. Rev. Lett. **84** (2000) 1078.]

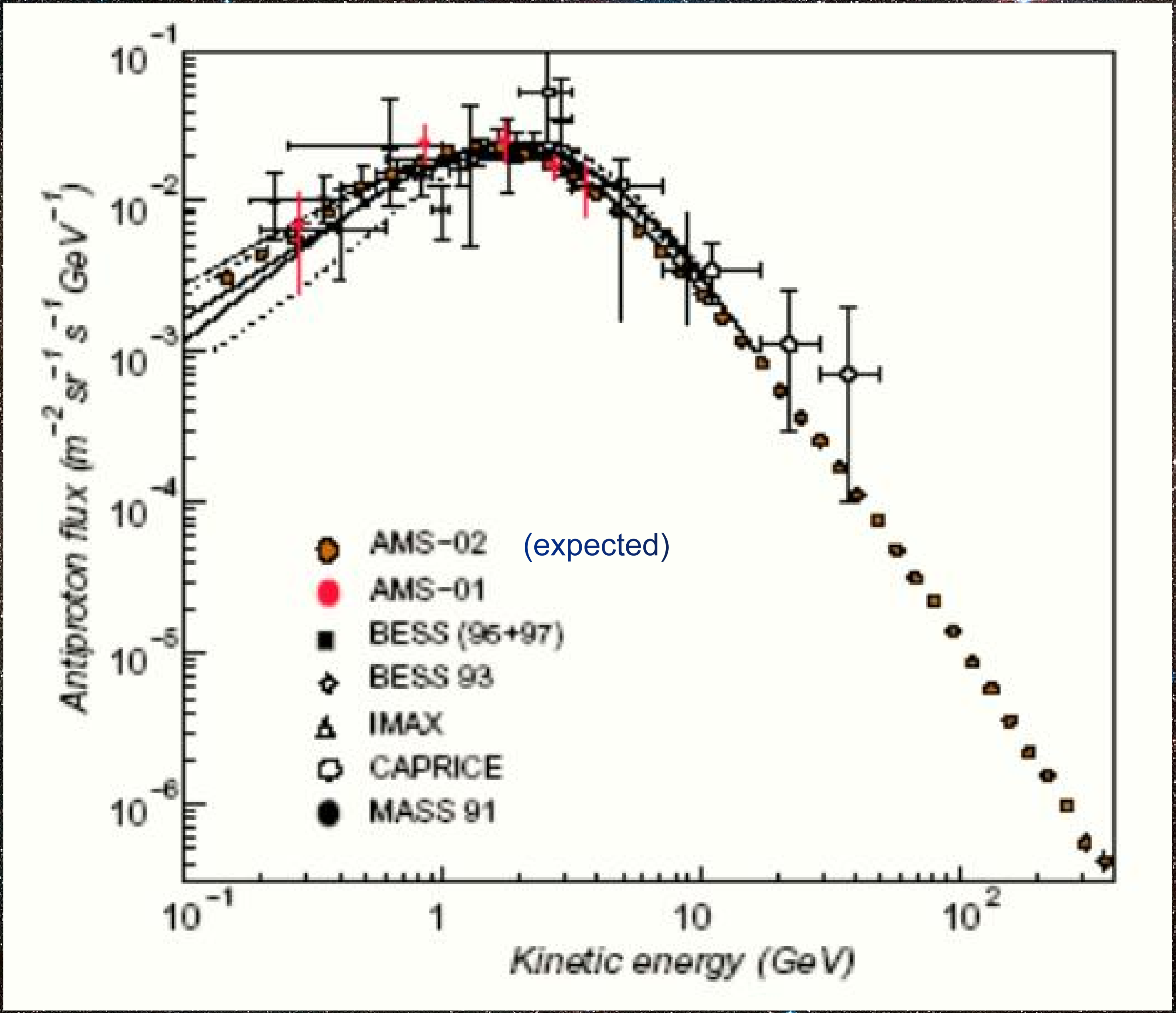

CR antiproton flux measured in different experiments.

The plot also shows expected statistics for the AMS-02 that has the potential to discover high-energy bumps that could be produced by exotic sources like the annihilation of neutralinos, the SUSY candidate for the dark matter.

[**Reference**: D.Casadei (for the AMS Collaboration), "Cosmic ray astrophysics with AMS-02," astro-ph/0404529.]

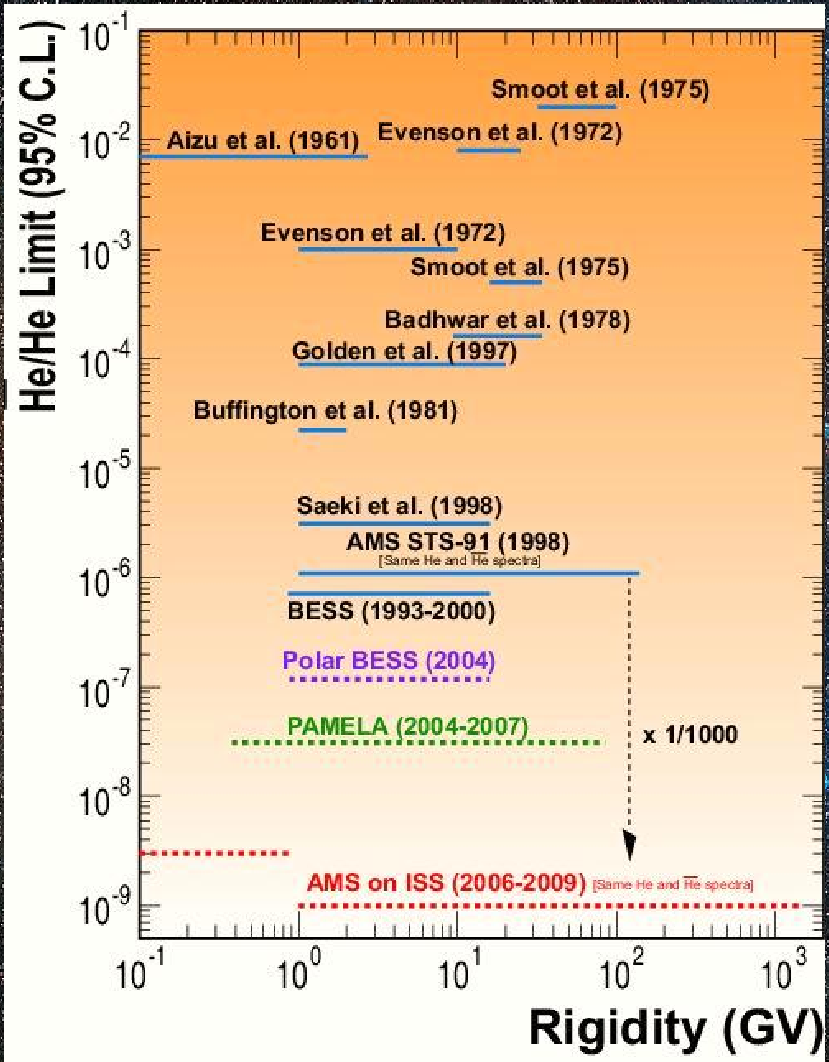

Upper limits on the antihelium to helium ratio in CR.

[**References:** M. Nozaki et al. (BESS Collab.), ICRC 26, OG.1.1.23; T. Saeki et al. (BESS Collab.), Phys. Lett. B **422** (1998) 319; *R. Battiston*, J. Phys. G: Nucl. Part. Phys. **29** (2003) 891; P. Picozza and A. Morselli, *ibid.*, 903.]

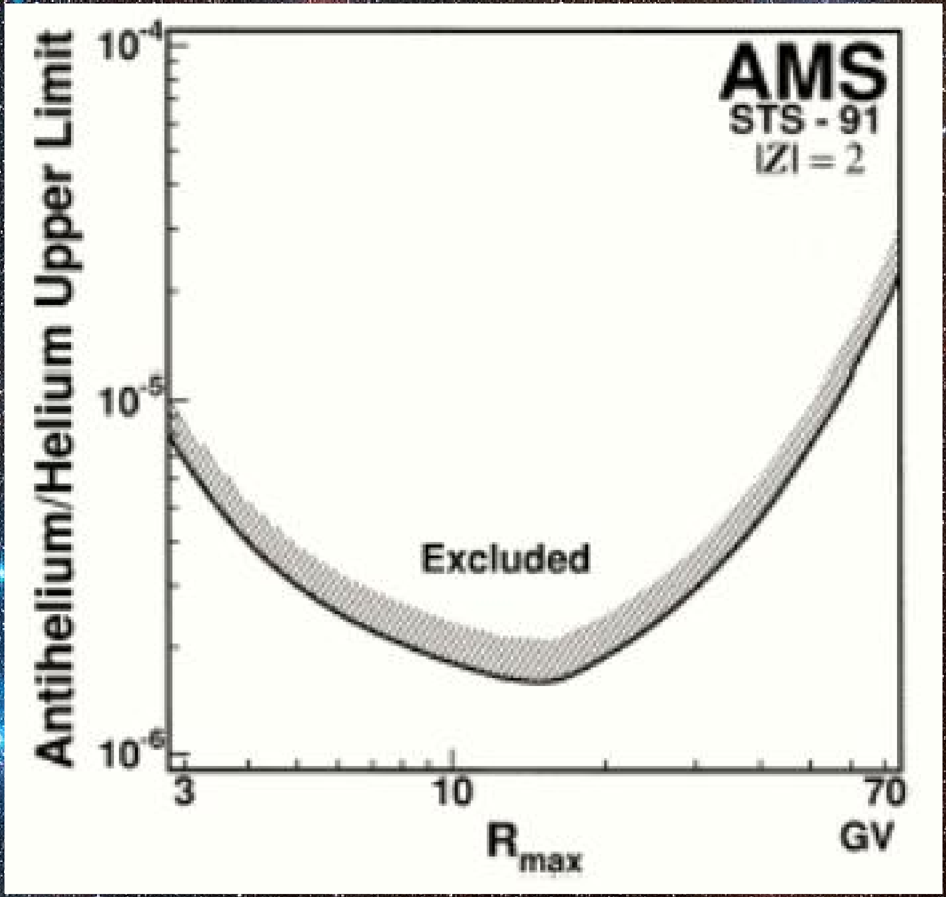

Upper limits on the relative flux of antihelium to helium in CR, obtained with the AMS Cosmic Ray Detector during STS-91 precursor flight (at the 95% confidence level), as a function of the rigidity range from R_{min} = 1.6 GV to R_{max}. In contrast with the AMS upper limits shown in the **left panel**, these results are independent of the assumptions about the incident antihelium spectrum.

[**Reference:** J. Alcaraz et al. (AMS Collaboration), Phys. Lett. B **461** (1999) 387.]

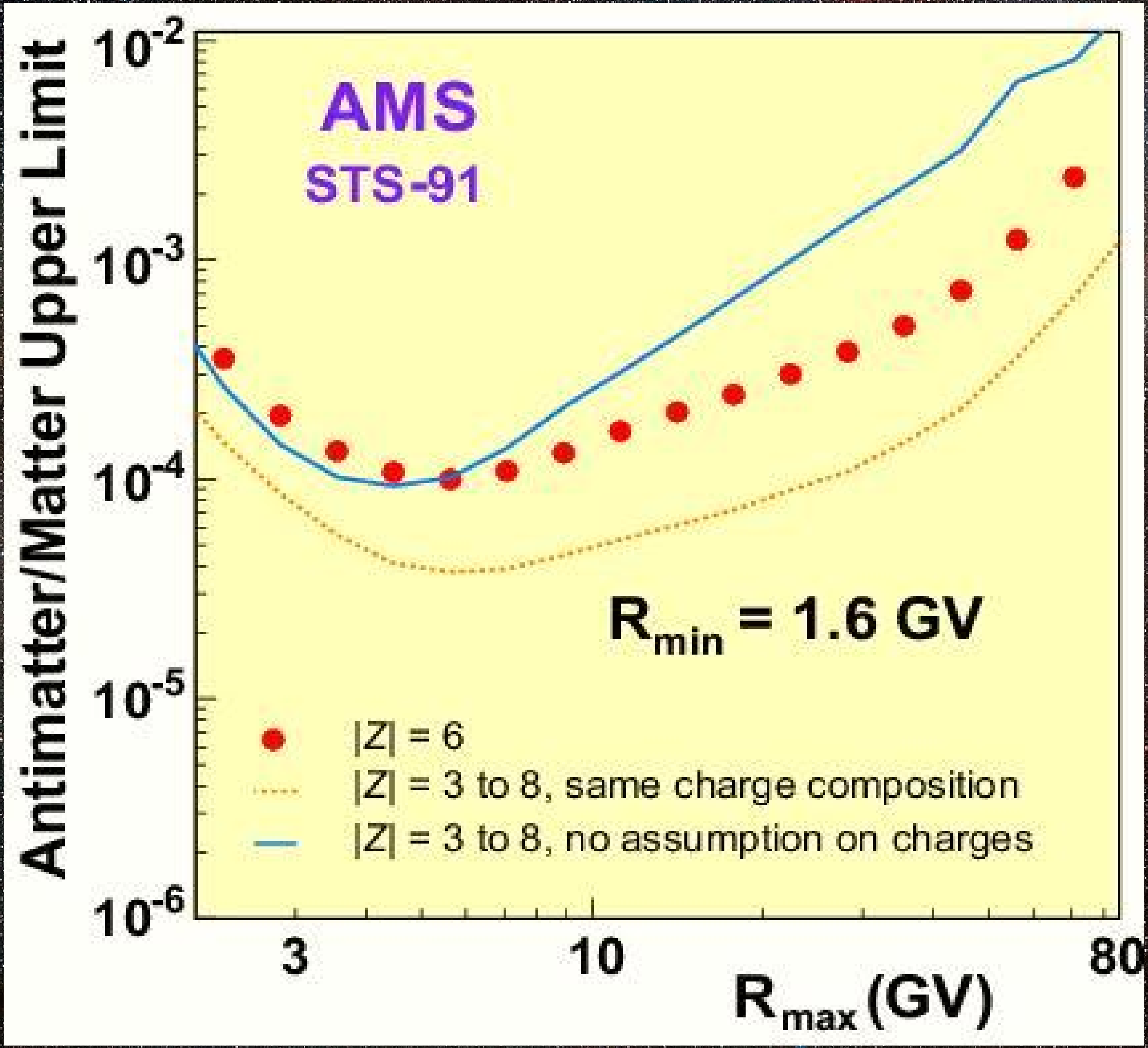

Upper limits on the antimatter-to-matter flux ratio under the conservative approach obtained with the AMS Cosmic Ray Detector during STS-91 precursor flight.

Integrating over the rigidity range (from R_{min} = 1.6 GV to R_{max}), the limit curves are shown as a function of the maximal rigidity R_{max}.

[**Reference:** M. Cristinziani, Nucl. Phys. B (Proc. Suppl.) **114** (2003) 275; astro-ph/0303641]

A few slides below [labeled "Ting 2023"] contain data from recent report by Samuel Ting "Latest Results from AMS on the International Space Station (ISS)" (CERN Colloquium, June 8, 2023).

Antinuclei in AMS on ISS

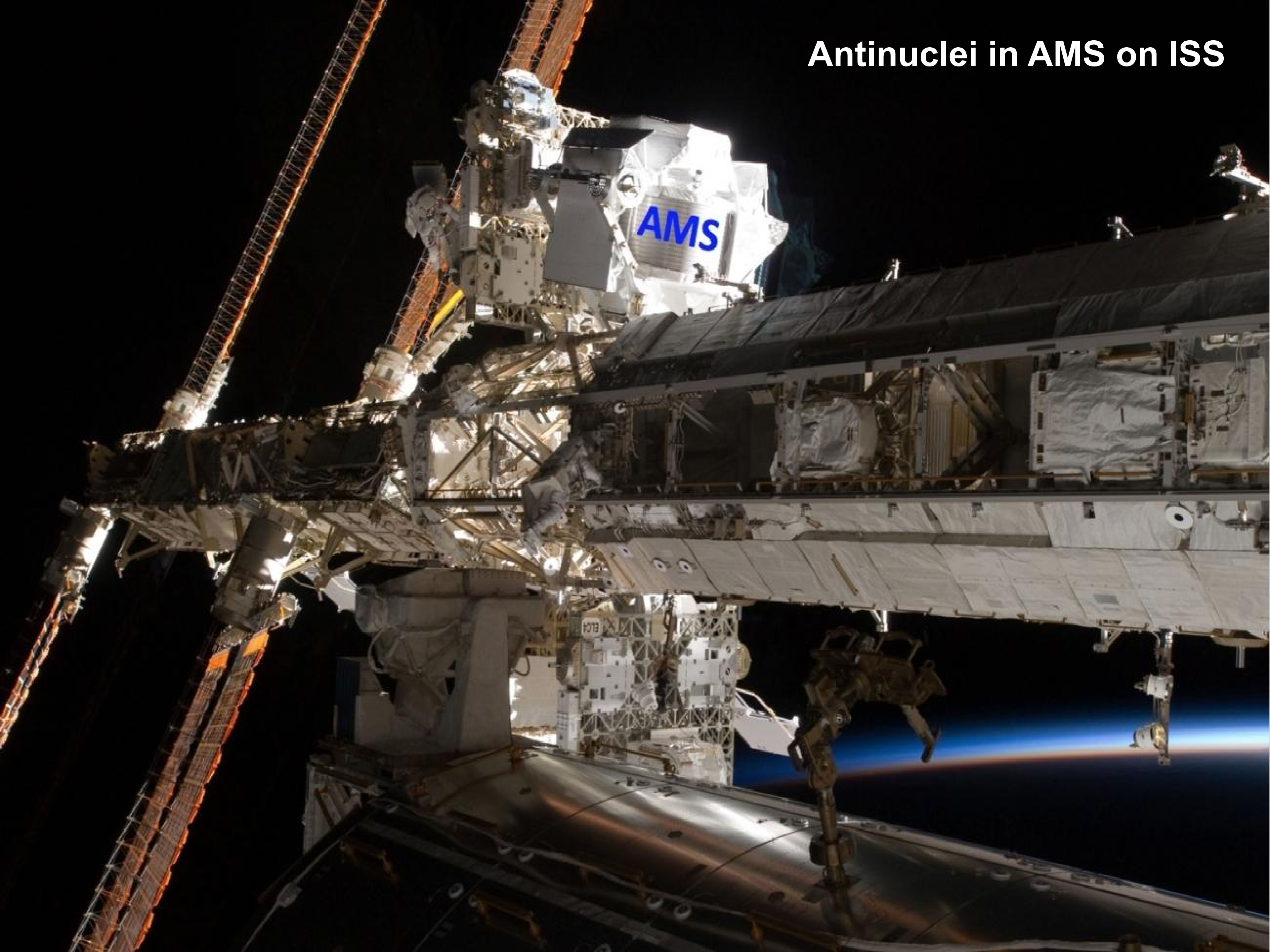

Current AMS Anti-Deuteron Results

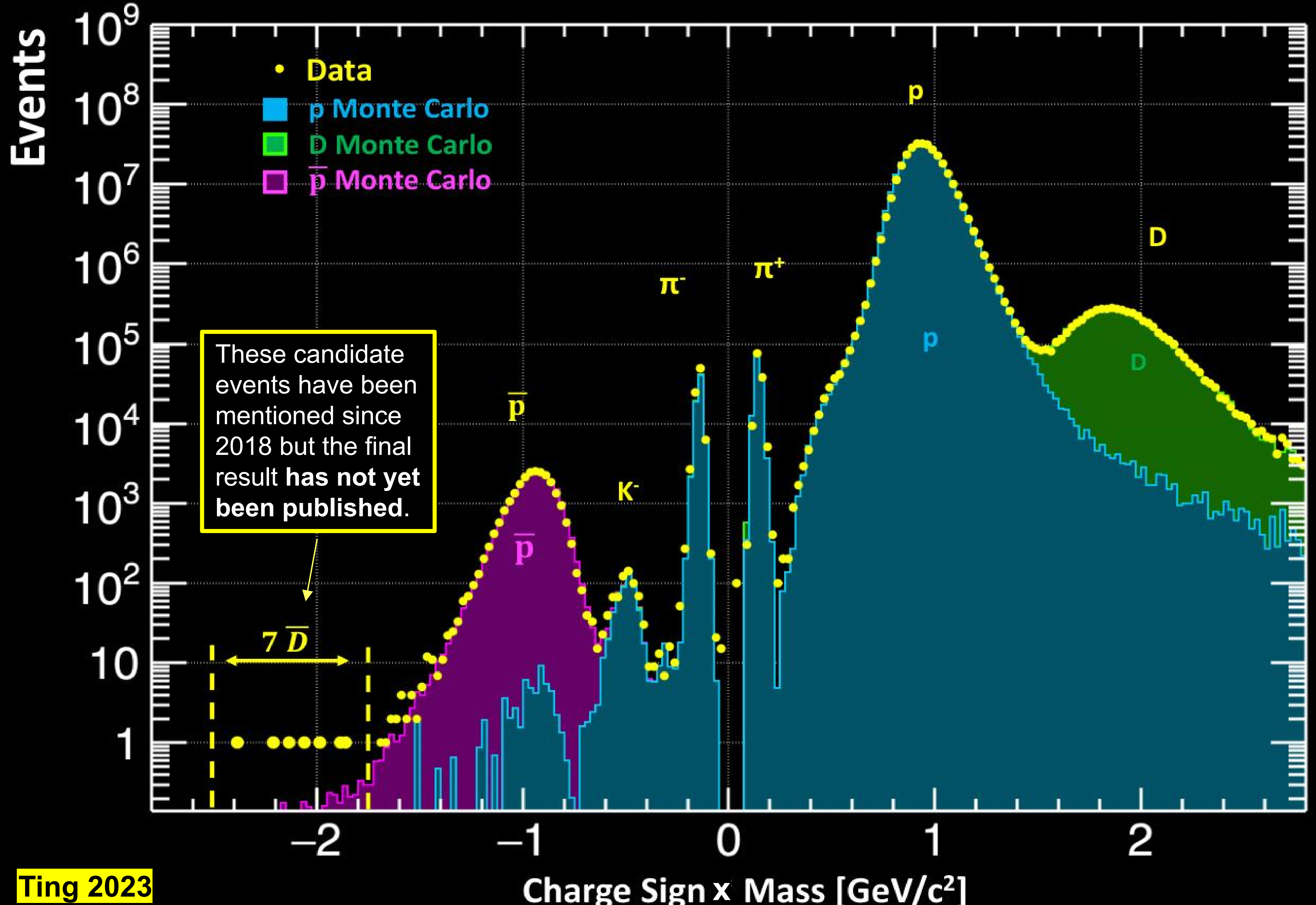

Ting 2023

Current Matter and Antimatter Statistics

Ting 2023

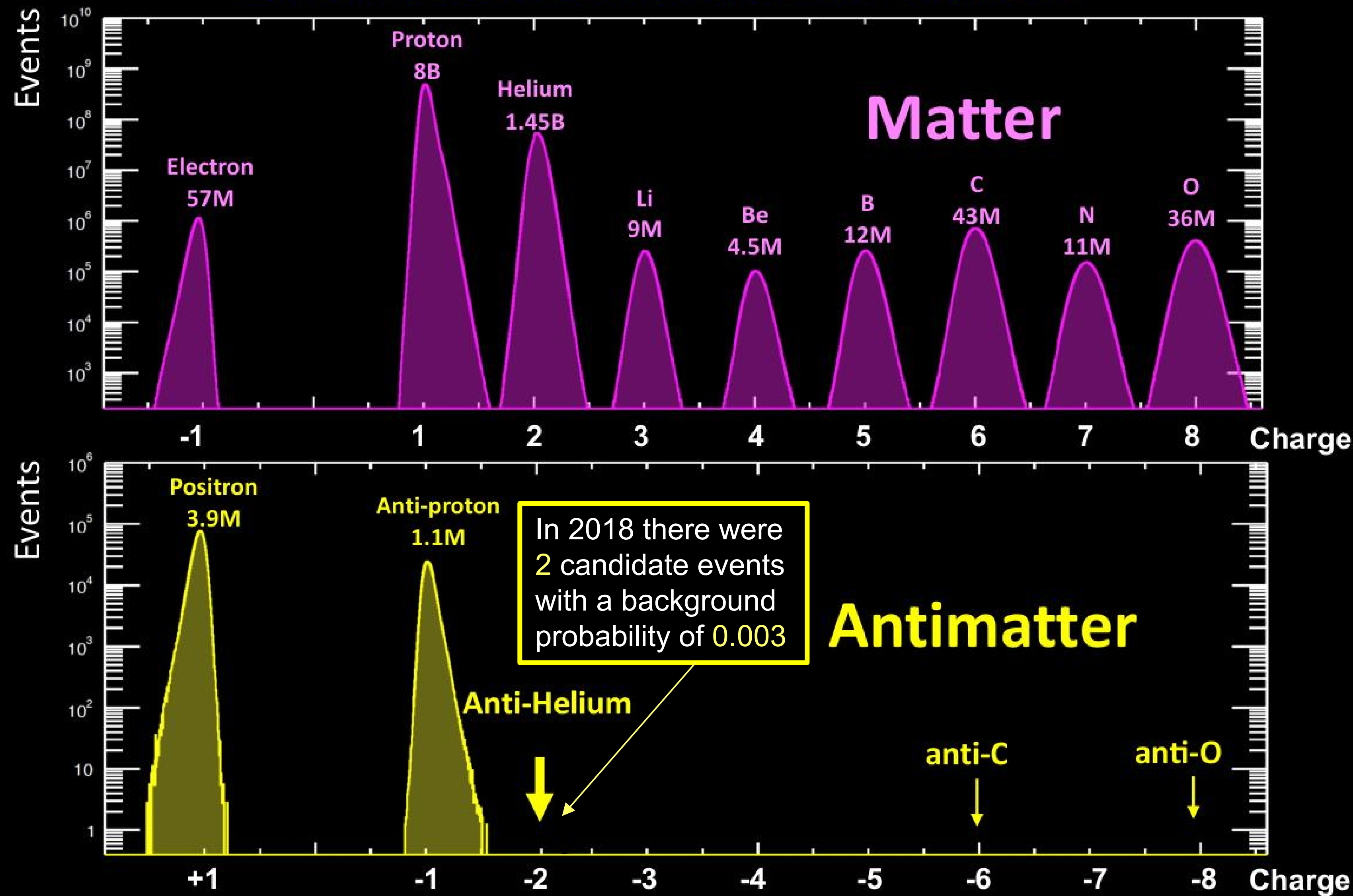

By 2030, AMS will have additional measurement points in the study of antimatter: anti-deuterons, anti-helium, anti-carbon and anti-oxygen.

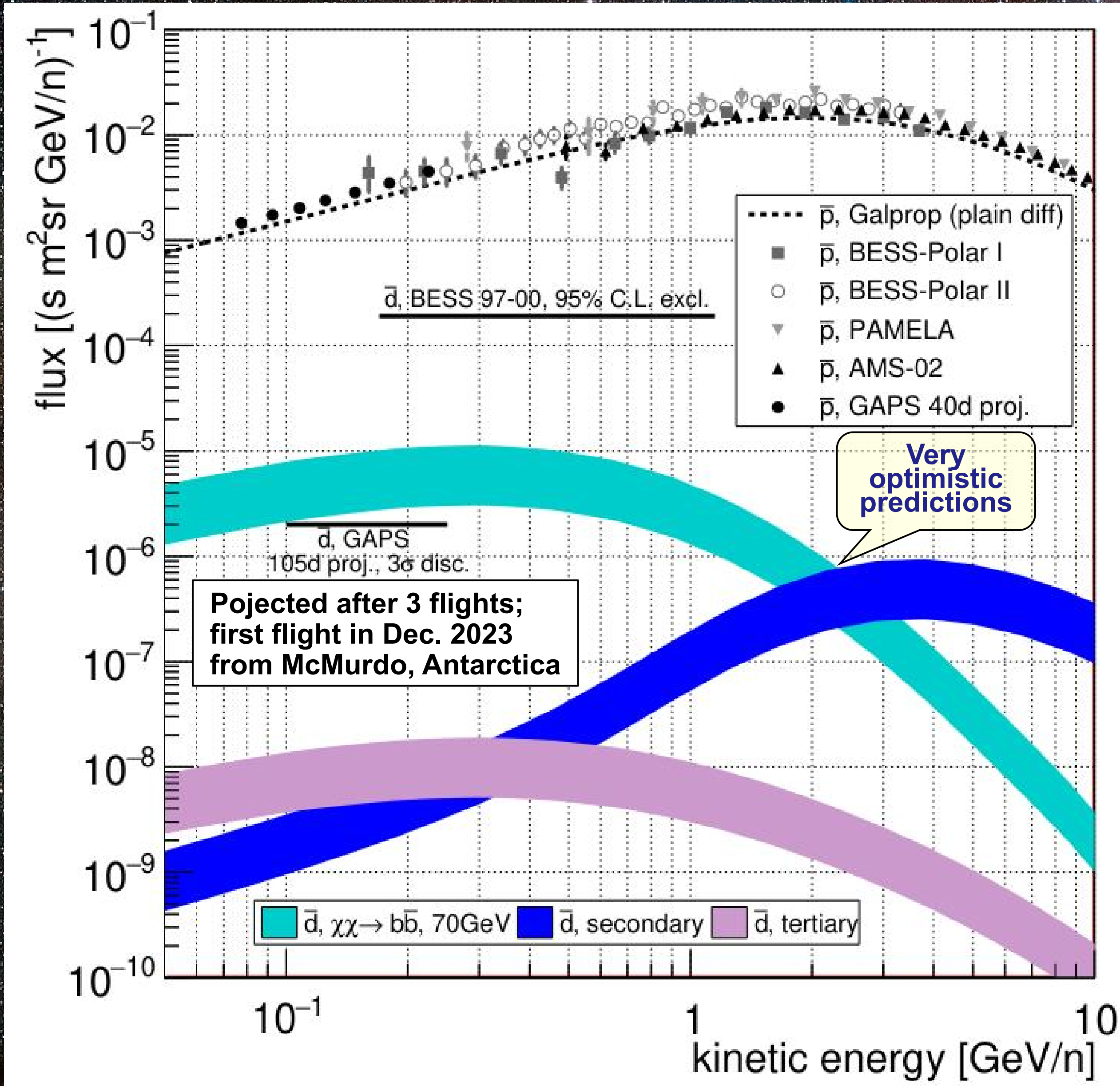

Antiproton flux data from AMS-02 at ISS, BESS-Polar I and II, and PAMELA, as well as projections for the GAPS antiproton flux measurements after 40 days, in comparison with the GALPROP plain diffusion prediction.

Also shown are the predicted **antideuteron** flux from DM, corresponding to the DM parameters indicated by AMS antiproton signal, interpreted as annihilation into purely $b\bar{b}$, as well as the predicted secondary and tertiary astrophysical antideuteron flux. Bands indicate antideuteron formation uncertainty.

The anticipated sensitivity of GAPS for a 3σ discovery and the BESS 97–00 95% C.L. exclusion limits are indicated.

[**References:** Ph. von Doetinchem et al., "Cosmic-ray antinuclei as messengers of new physics: status and outlook for the new decade", JCAP08(2020)035, arXiv:2002.04163 [astro-ph.HE]; Ph. von Doetinchem, "Cosmic-Ray Antinuclei from Dark Matter and the GAPS Experiment (UCLA Dark Matter, March 29 — April 1, 2023).]


THE END

AUXILIARY SLIDES

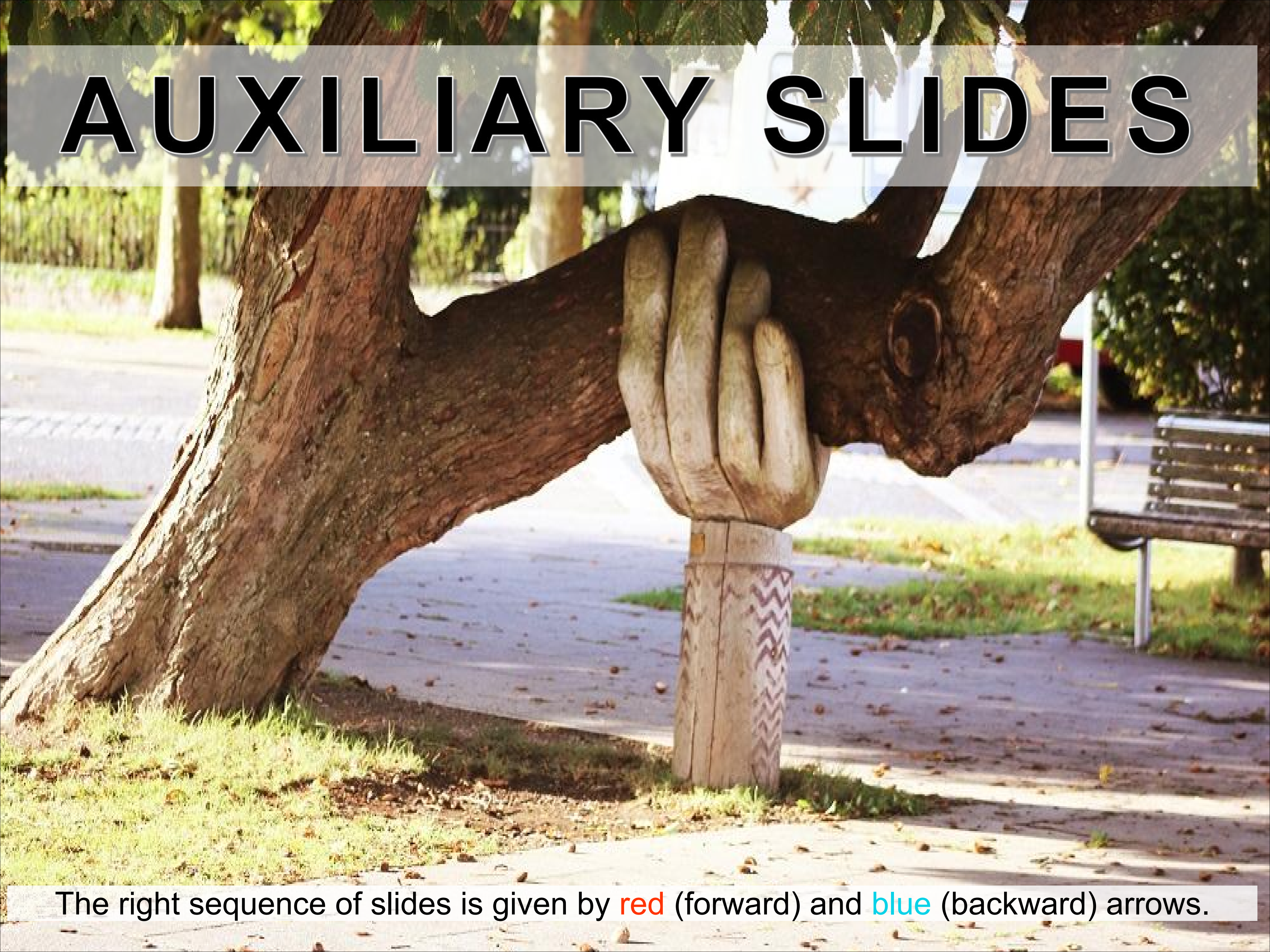

The right sequence of slides is given by red (forward) and blue (backward) arrows.

Big Bang Nucleosynthesis

Era of Nuclear Reactions:
~3 min to ~3.5 min (T ~ 10^9 to 10^8 K)

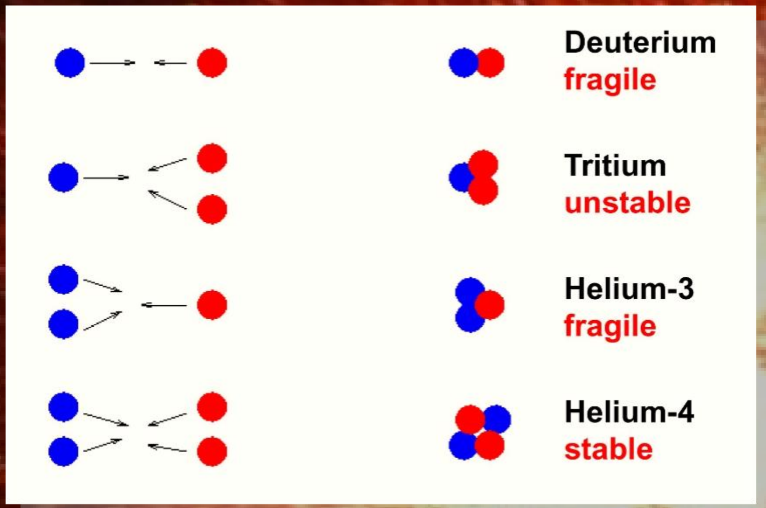

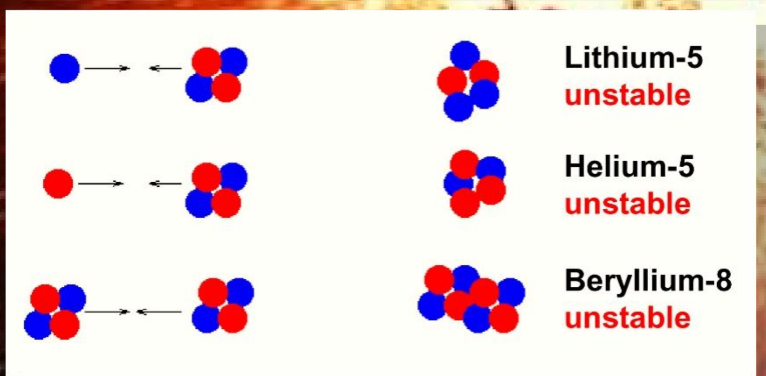

The net result of the early nuclear reactions is to transform all of the neutrons, along with the necessary protons, into ^{4}He plus traces of ^{2}H, ^{3}He, ^{7}Li, ^{6}Li, ^{7}Be.

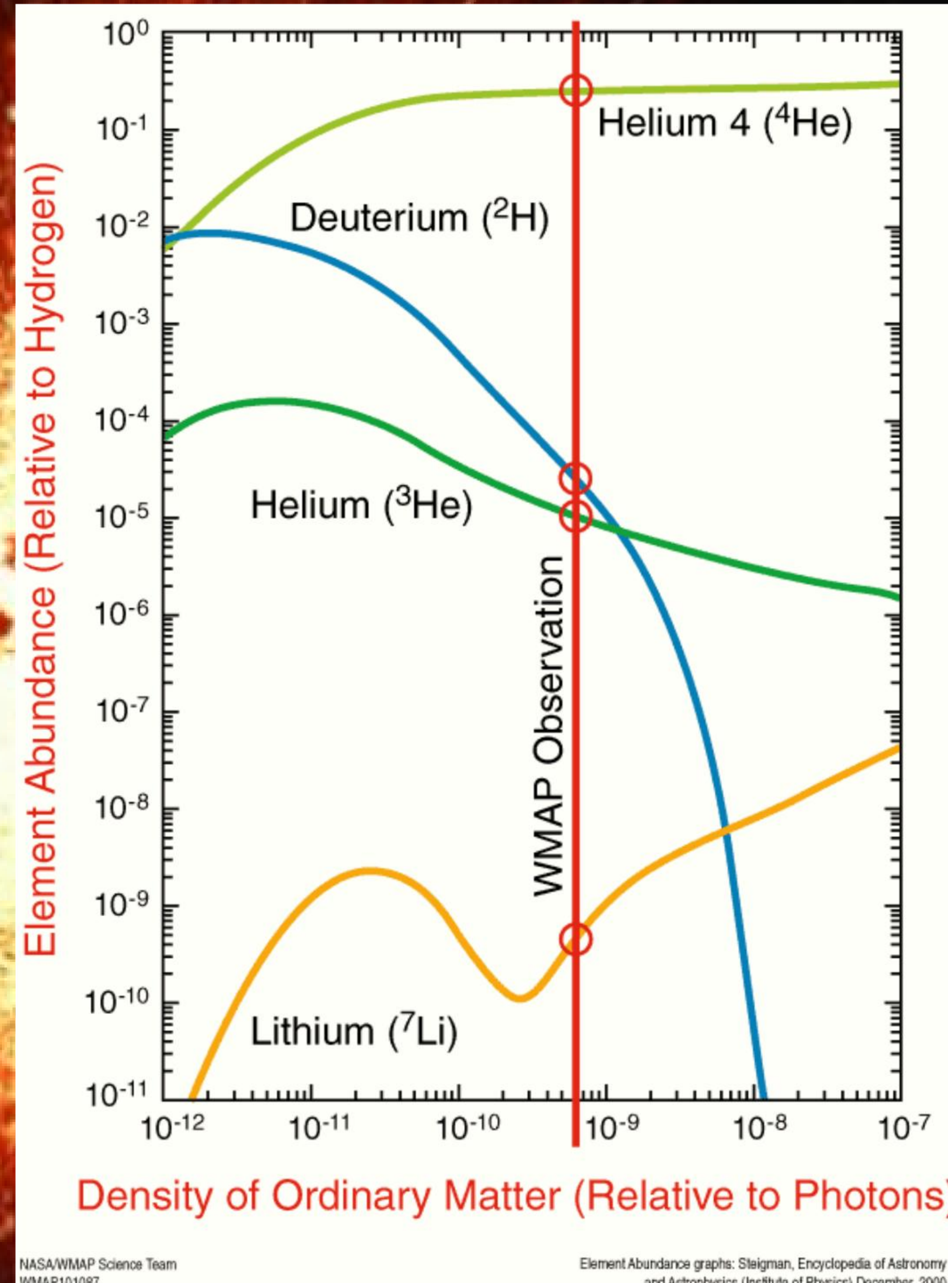

Cosmic Rays are associated with the extreme phenomena in Universe

(SNs, GRBs, radio-galaxies, quasars,…)

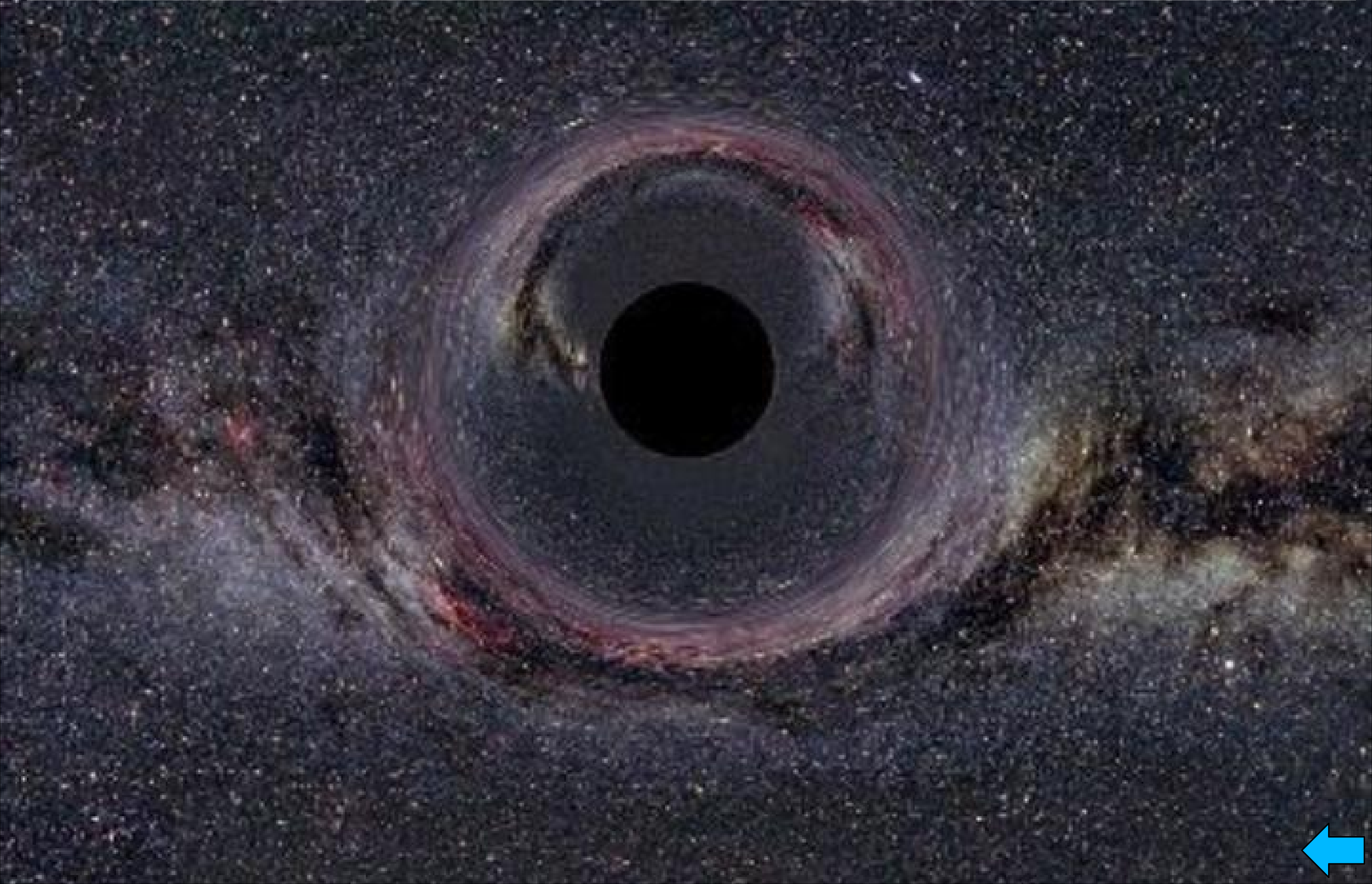

Supernovae

SN1998S in NGC3877
by Enrico Prosperi

SN1998S in NGC3877
by Pedro Re

SN 2001V in N3987s1
by Rafael Ferrando

SN 1998dh in NGC 7541
by Tim K.

Borrowed mainly from David Bishop's collection of real optical supernova images International Supernovae Network,
URL: <http://www.supernovae.net/snimages/animations.html>

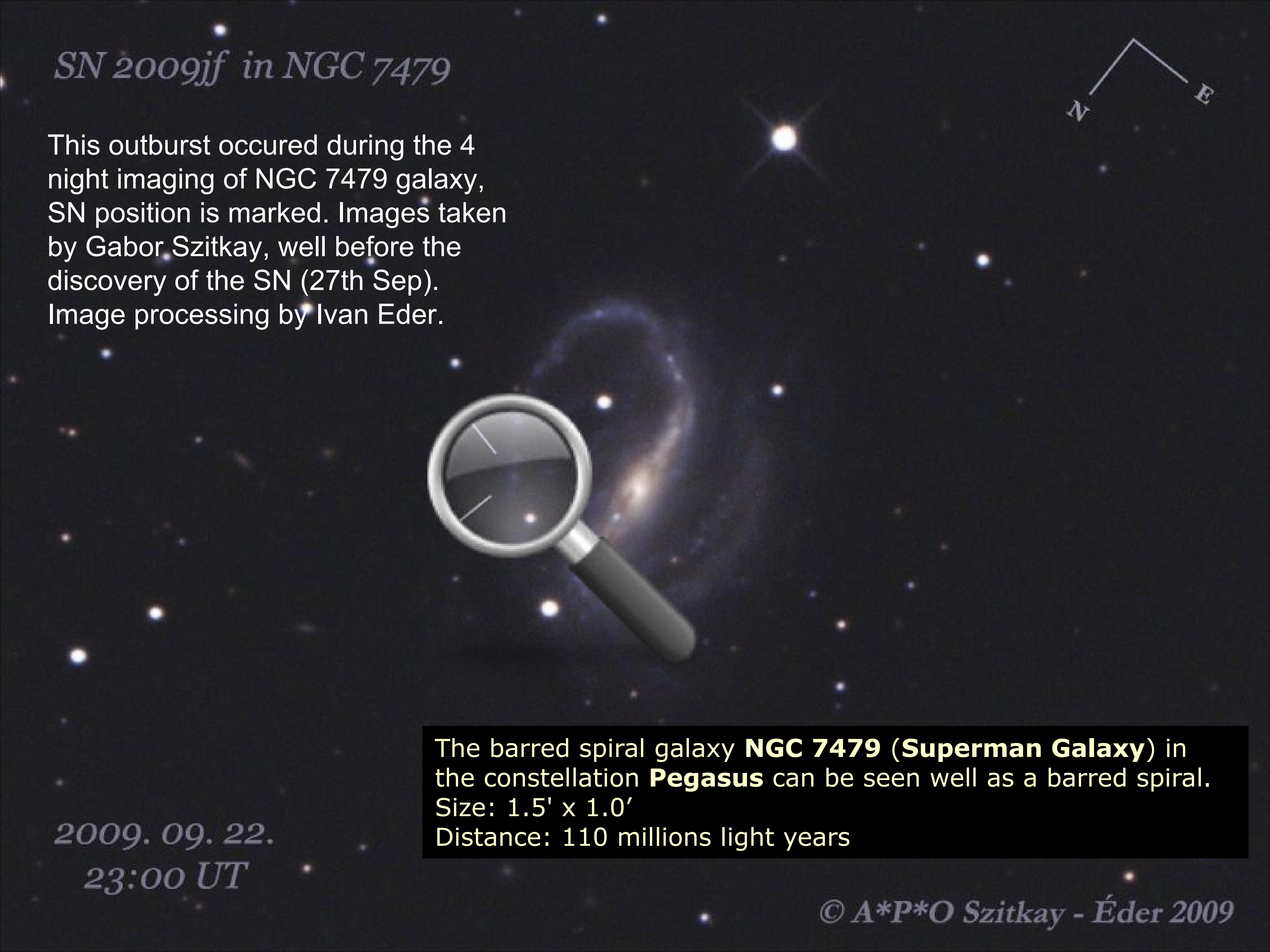
SN 2009jf in NGC 7479
N
E
This outburst occured during the 4 night imaging of NGC 7479 galaxy, SN position is marked. Images taken by Gabor Szitkay, well before the discovery of the SN (27th Sep). Image processing by Ivan Eder.
The barred spiral galaxy **NGC 7479** (**Superman Galaxy**) in the constellation **Pegasus** can be seen well as a barred spiral.
Size: 1.5' x 1.0’
Distance: 110 millions light years
2009. 09. 22.
23:00 UT
© A*P*O Szitkay - Éder 2009

A Supernovae Taxonomy

Early Spectra:

No Hydrogen / Hydrogen

up to 10^{43} J usually old stars

up to 10^{44} J often young, heavy stars

SN I
Si/ No Si

SN II
~3 mos. spectra
He dominant/H dominant

SN Ia
1985A
1989B

He poor/He rich
(absorption near 5700 A)

SN Ic
1983I
1983V

SN Ib
1983N
1984L

SN IIb
1993J
1987K

"Normal" SN II

Light Curve decay after maximum
Linear / Plateau

SN IIL
1980K
1979C

SN IIP
1987A
1988A
1969L

Theory

Believed to originate from **deflagration** or **detonation** of an ***accreting white dwarf***

Core collapse
Most (NOT all) H is removed during evolution by tidal stripping

Core Collapse
Outer Layers stripped by winds *(Wolf-Rayet Stars)* or binary interactions
Ib: H mantle removed
Ic: H & He removed

Core Collapse
of a massive progenitor with plenty of H

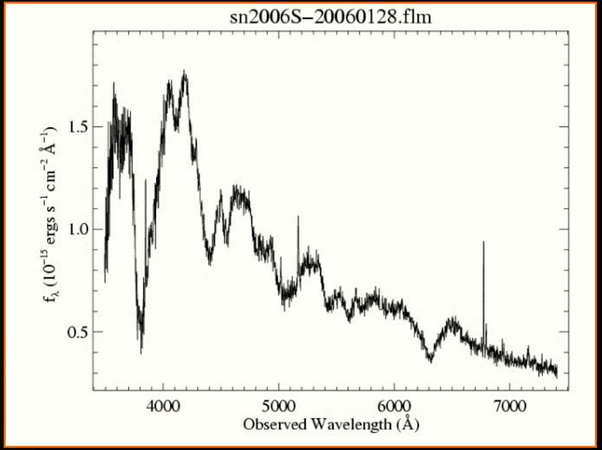

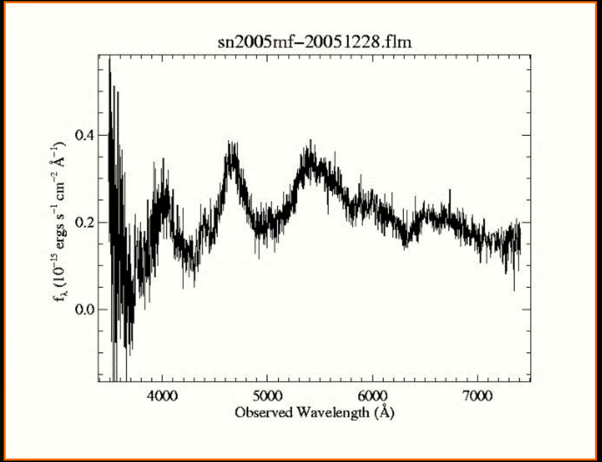

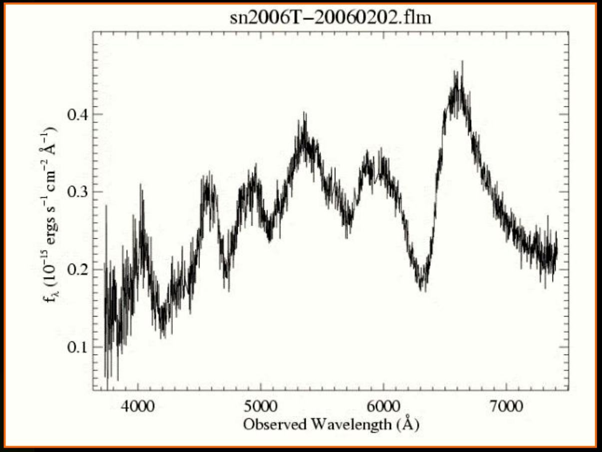

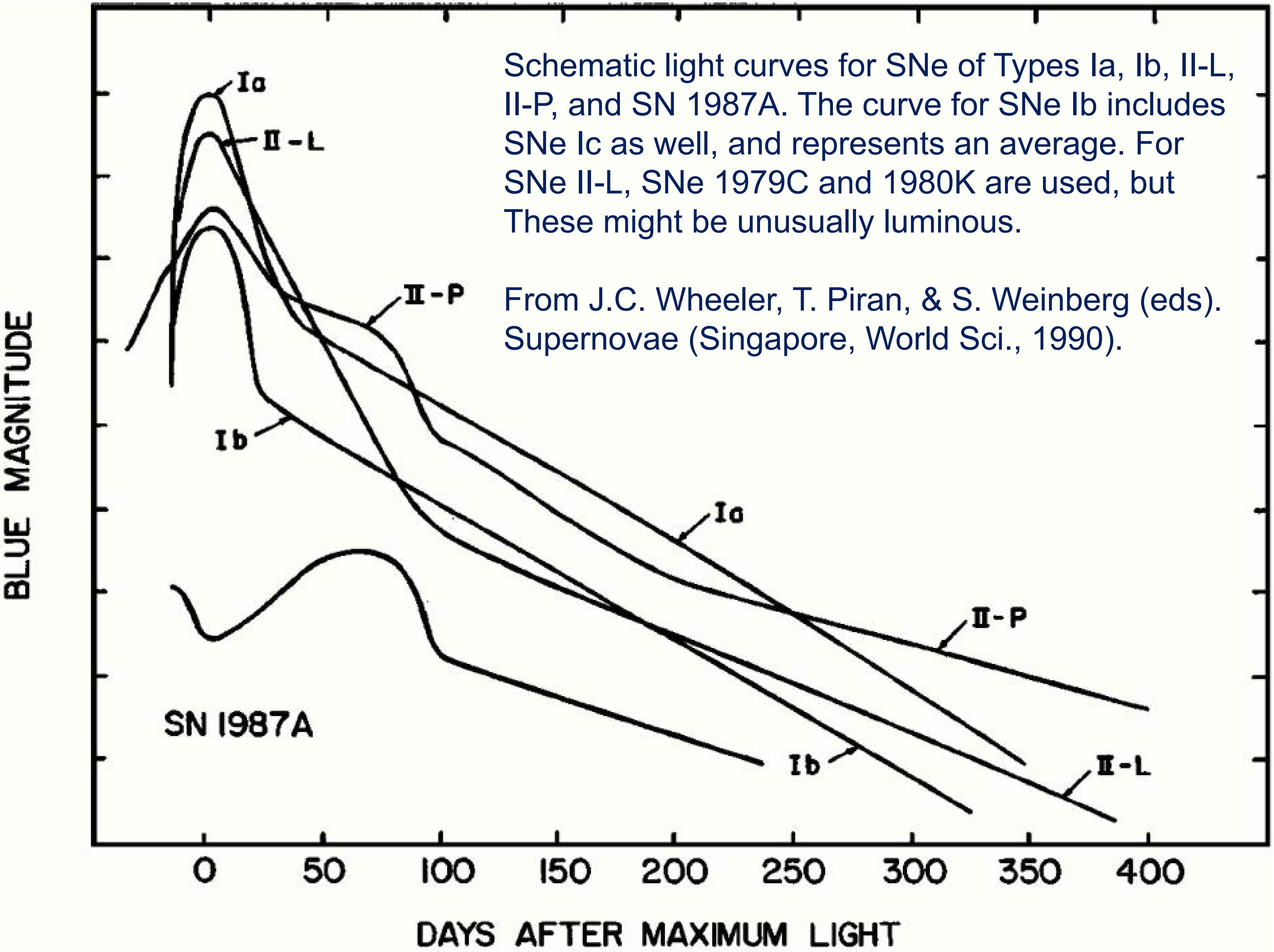

Schematic light curves for SNe of Types Ia, Ib, II-L, II-P, and SN 1987A. The curve for SNe Ib includes SNe Ic as well, and represents an average. For SNe II-L, SNe 1979C and 1980K are used, but These might be unusually luminous.

From J.C. Wheeler, T. Piran, & S. Weinberg (eds). Supernovae (Singapore, World Sci., 1990).

Artist's concepts of supernova explosions

There is an initial flash of light from the supernova explosion causing the ring to glow. Debris hurls into space, the fastest moving at 0.1*c*. The supernova's shockwave causes the ring to glow again.

The closer the pieces of the ring are to the shockwave, the sooner they light up. Eventually, the whole ring lights up.

[From NASA HubblSite]

An artist's impression of vampire star

Chandra timelapse movie of SN1987A

SN1987A

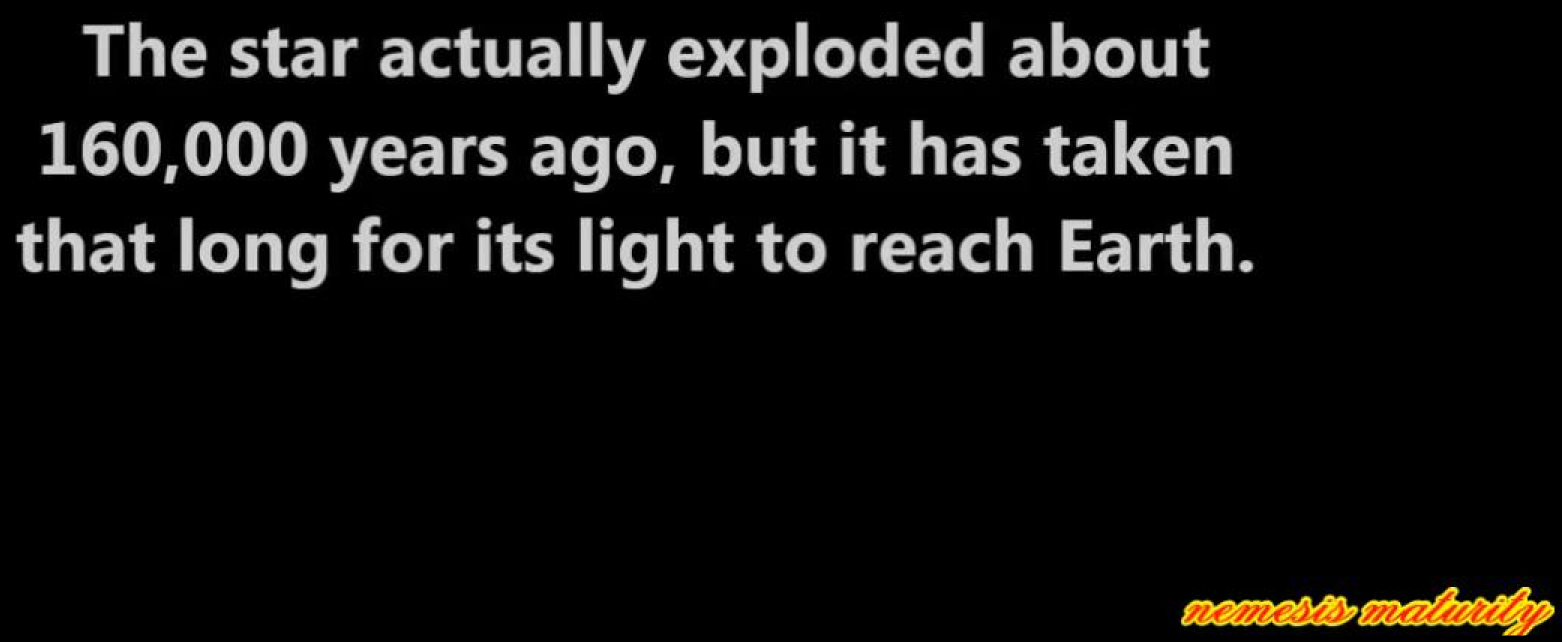

SN1987A is the first and still unique (fall 2021) extraterrestrial identified neutrino source other than the Sun. And it is an enigmatic object.

SN1987A: Some puzzles & surprises

Hubble image

The progenitor star, **Sk−69°202**, was one of the surprises. Massive stars similar to the progenitor of SN 1987A are expected to end their evolution as red supergiants, but **Sk−69°202** was a blue supergiant.

Moreover, the outer layers of the star were highly enriched in helium, suggesting that some nuclear processed material from the core had been mixed into the envelope by a nonstandard mixing process.

Most notably, the supernova was surrounded by a complex **triple-ring nebula** consisting of material that was ejected from the progenitor some **20,000 years** before the explosion in an almost axisymmetric but very nonspherical manner. Together, this evidence indicates that a dramatic event affected the progenitor some 20,000 years before the explosion, most likely the merger of two massive stars.

[Reference: T. Morris and Ph. Podsiadlowski, "The Triple-Ring Nebula around SN1987A: Fingerprint of a binary merger," Science **315** (2007) 1103-1106, astro-ph/0703317.]

SN1987A debris evolution

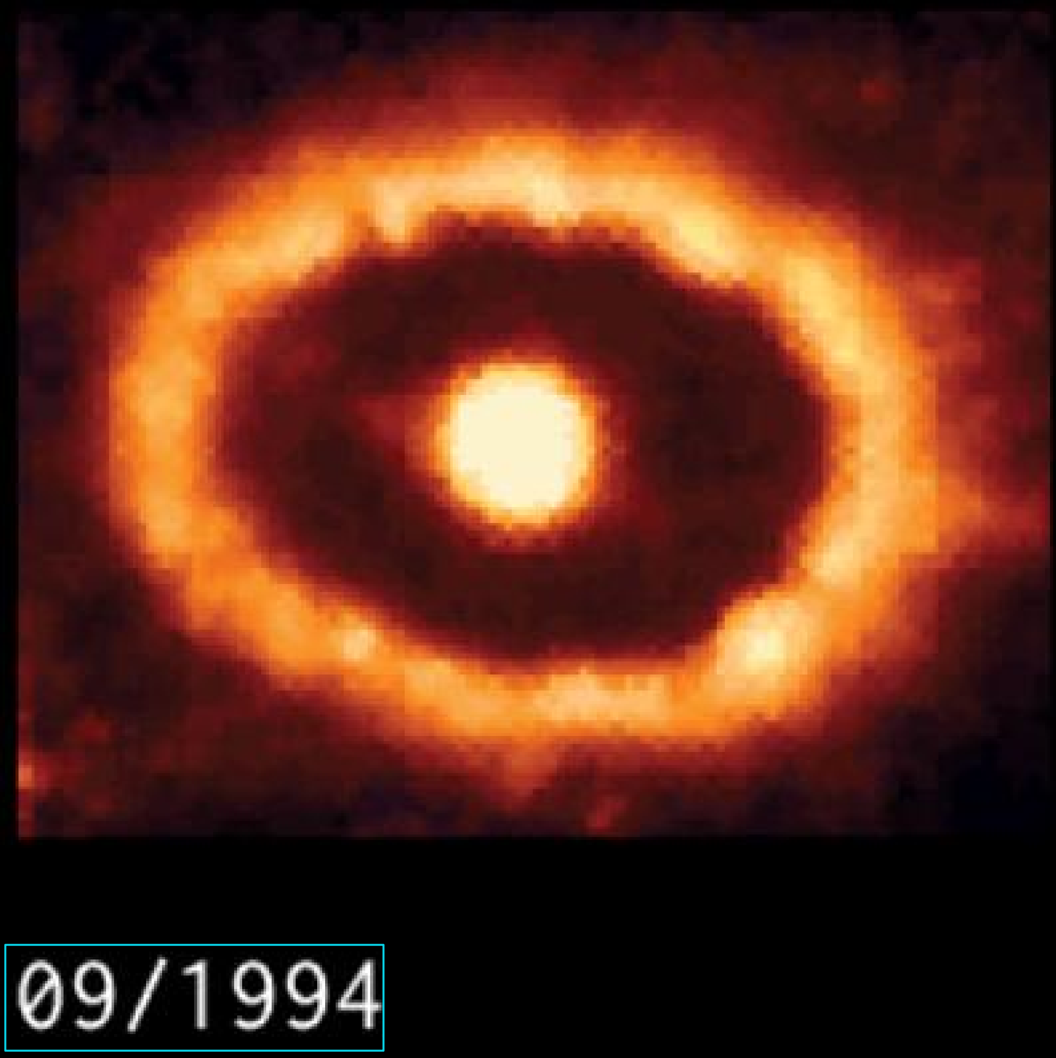

A time sequence of Hubble Space Telescope images, taken in the 15 years from **1994** to **2009**, showing the collision of the expanding supernova remnant with a ring of dense material ejected by the progenitor star **20,000 years** before the supernova.

When a massive star explodes as a supernova, substantial amounts of radioactive elements — primarily ^{56}Ni, ^{57}Ni and ^{44}Ti — are produced. After the initial flash of light from shock heating, the fading light emitted by the supernova is due to the decay of these elements. However, after decades, the energy powering a supernova remnant comes from the shock interaction between the ejecta and the surrounding medium.

[Reference: Larson et al. Nature, "X-ray illumination of the ejecta of supernova 1987A", **474** (2011) 484-486, arXiv:1106.2300 [astro-ph.SR] .]

Composite image of SN 1987A remnant (since 30 years).

ALMA data shows newly formed dust in the center of the remnant. HST and Chandra show the expanding shockwave.

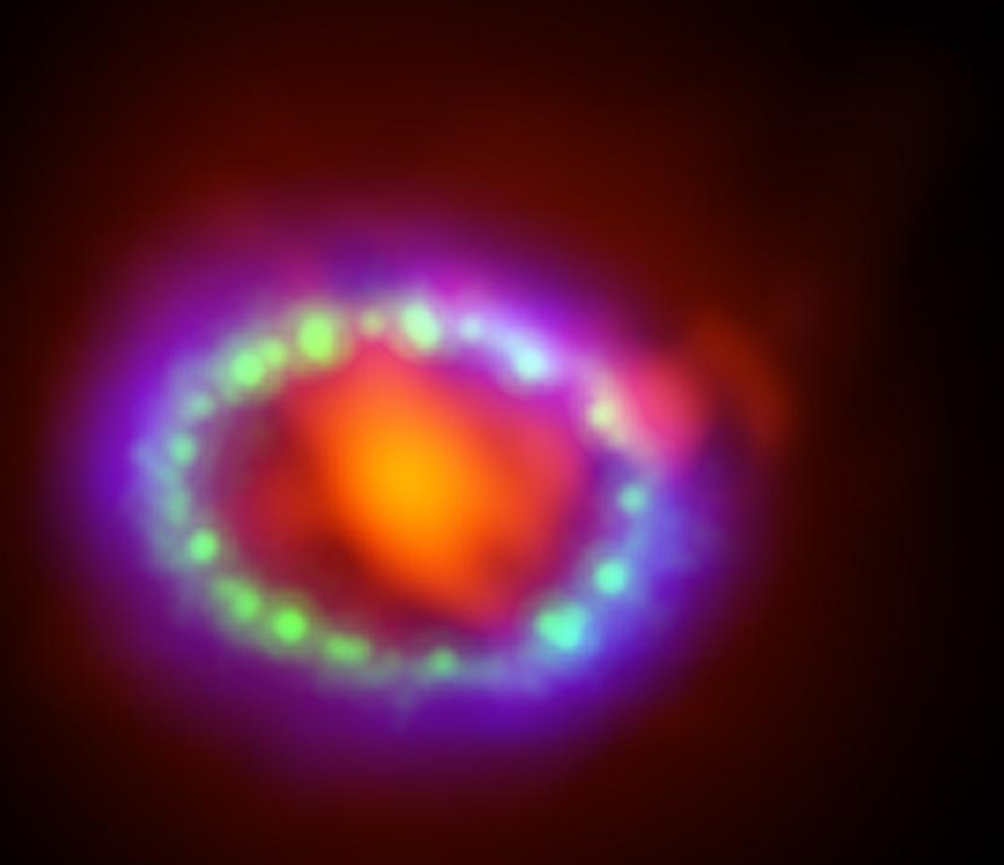

Millimeter/submillimeter image: the ESO ALMA (in red)

Visible light image: the NASA/ESA Hubble Space Telescope (in green)

X-Ray image: The NASA Chandra X-Ray Observatory (in blue)

[From https://www.almaobservatory.org/en/press-releases/supernovas-super-dust-factory-imaged-with-alma/]

A 3D evolution model of SN 1987A

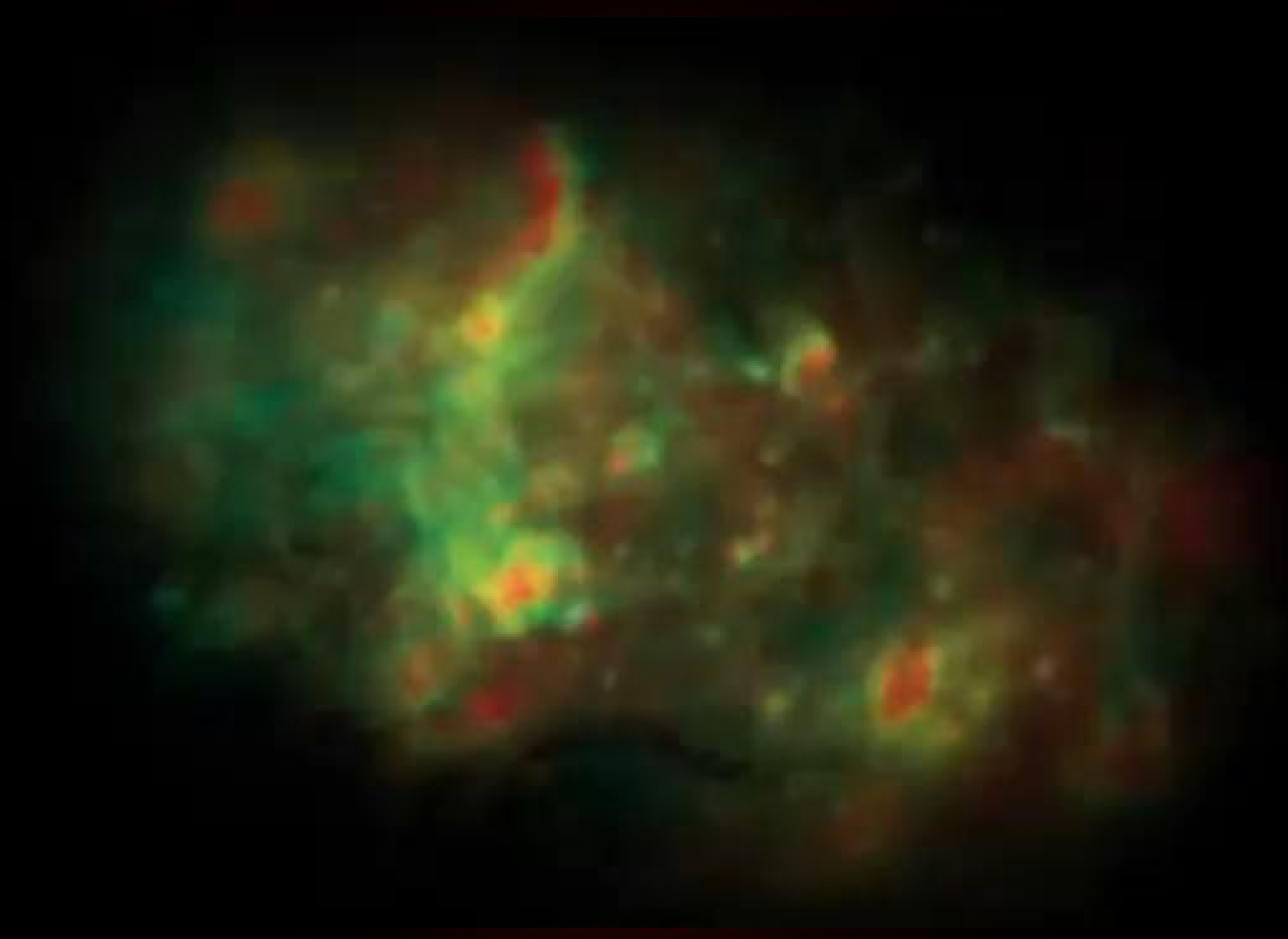

[From https://in-space.ru/novye-dannye-o-sverhnovoj-sn-1987a-i-3d-model-ee-vzryva/ /]

Artist's impression of the material around SN 1987A
(based on the observations in ESO's Very Large Telescope).

The original blast was powerful and more concentrated in one particular direction (indication that the supernova must have been very turbulent. Video shows two outer rings, one inner ring and the deformed, innermost expelled material. Just how the supernova explodes is not very well understood: why the inner material was not ejected symmetrically in all directions, but rather seems to have had a preferred direction; why this direction is different to what was expected from the position of the rings.

[From https://www.eso.org/public/videos/eso1032a/]

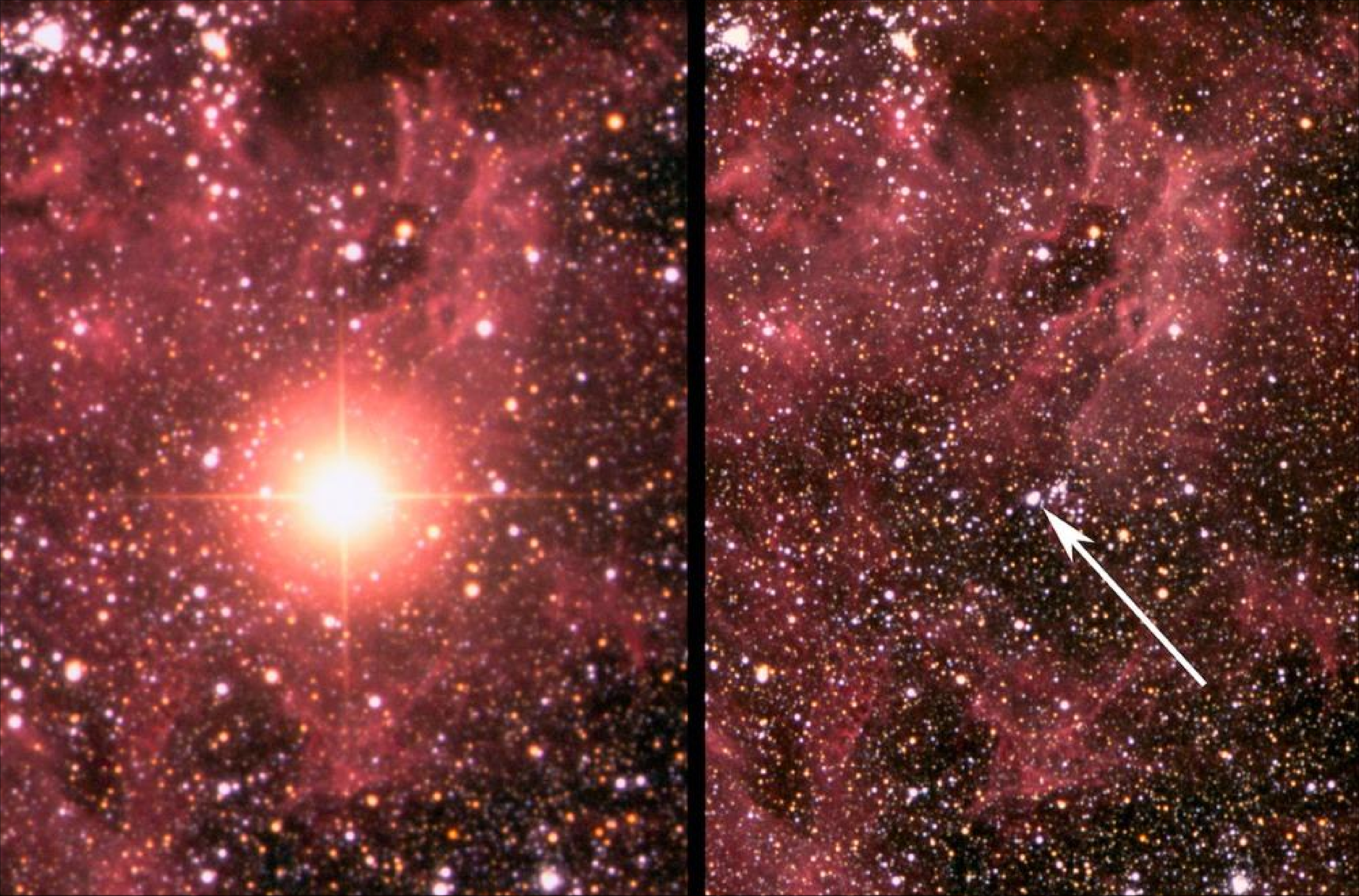

Near the Tarantula Nebula in the LMC. SN1987A after exploding in February 23, 1987 (left), and an image taken before the explosion (right), which clearly shows the progenitor (Sanduleak -69^{o} 202) of the supernova. Credit: David Malin / Australian Astronomical Observatory.

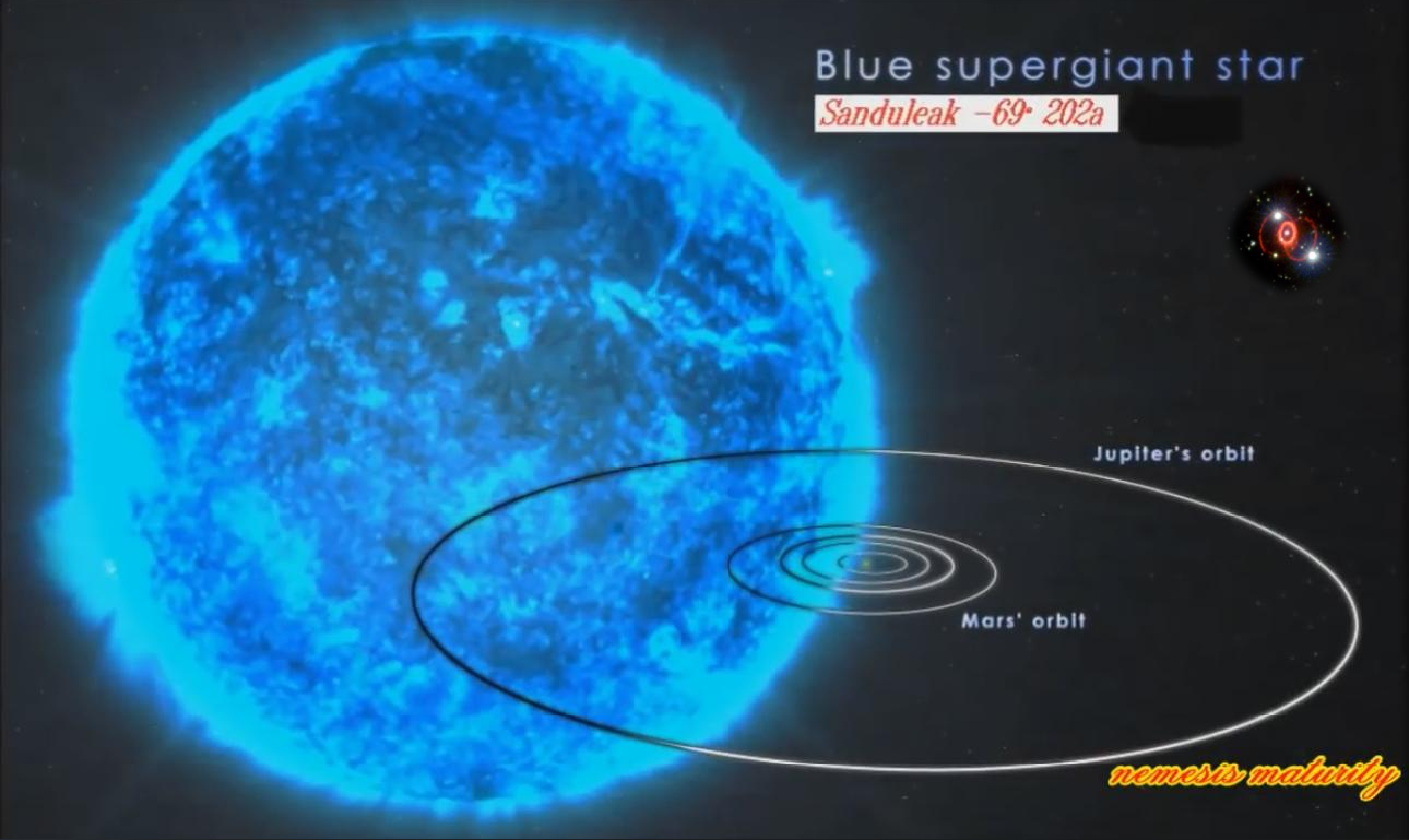

Sanduleak -69° 202 (also known as *GSC 09162-00821*) was a magnitude 12 blue supergiant star, located on the outskirts of the Tarantula Nebula in the Large Magellanic Cloud. It is notable as the progenitor of the supernova 1987A. [Artist's concept.]

Crab nebula

the brightest steady TeV gamma-ray source in the sky

The energetic nonthermal particles of the very compact Pulsar near the center of this object generate the nebula and the diffuse optical continuum of synchrotron emission that can be seen in its inner part.

The result of the measurement was: 1 gamma quantum of 500 GeV per minute, with three times more gammas per time than Cosmic-Ray background events. Thus the gamma-ray measurement is practically «background free».

The Crab Nebula is the remnant of a supernova explosion.

“The Crab pulsar is accelerating particles up to the speed of light and flinging them out into interstellar space at an incredible rate.”

[**Martin Weisskopf** (NASA's Marshall Space Flight Center)]

The X-ray image shows tilted rings or waves of high-energy particles that appear to have been flung outward over the distance of a *light year* from the central star, and high-energy jets of particles blasting away from the neutron star in a direction perpendicular to the spiral.

It provides important clues to the puzzle of how the cosmic generator, a pulsing neutron star, energizes the nebula, which still glows brightly 969 years after the SN 1054 explosion.

[From Chandra X-ray Observatory]

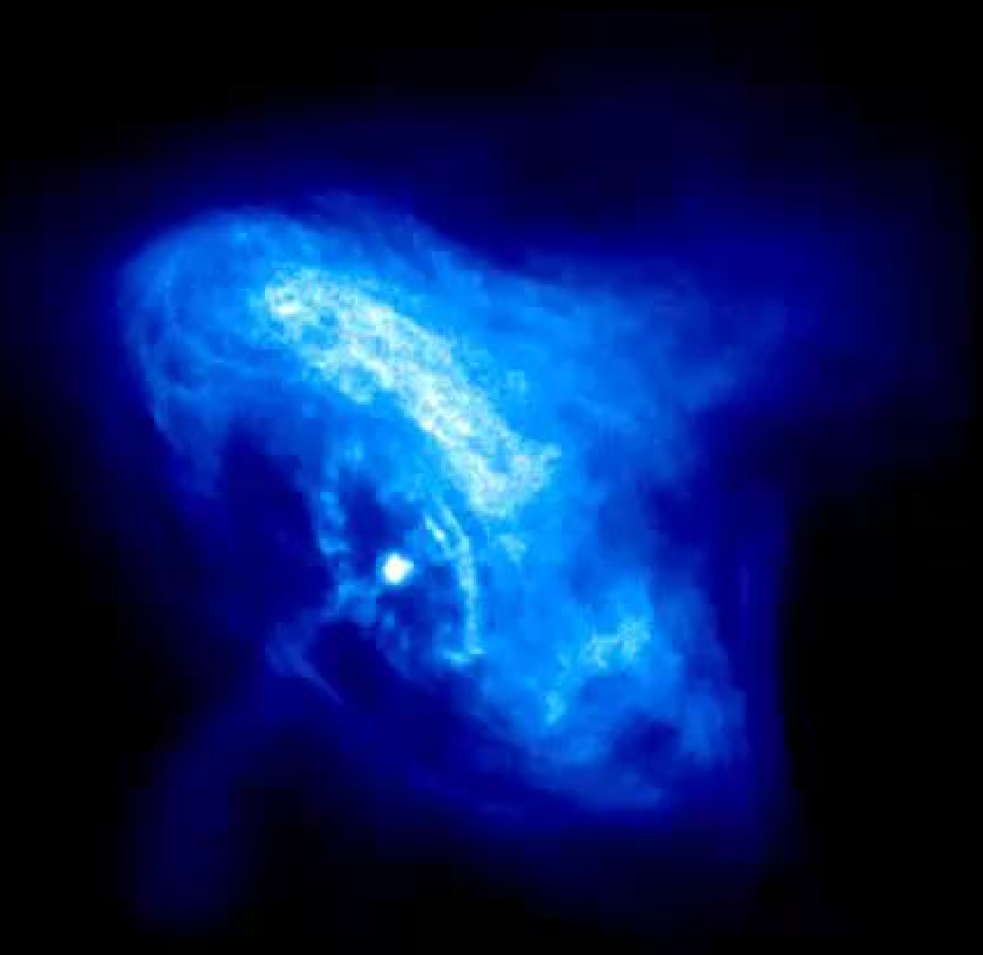

Dynamic rings, wisps and jets of matter and antimatter around the Crab pulsar as observed in optical light by Hubble

Composite image of the Crab Nebula

(by the Chandra X-ray Observatory)

The image shows

X-ray (in blue)
optical (in green)
radio (in red)

The three images are superimposed. The inner blue ring Is about one light year across.

The energetic nonthermal particles of the very compact pulsar near the center of this object generat the nebula and the diffuse continuum of synchrotron emission.

The size of the X-ray image is smaller those of optical and radio. This is because the higher energy X-ray emitting electrons radiate away their energy more quickly than the lower energy radio and optically emitting electrons as they move.

[From the Chandra Photo Album, URL: http://chandra.harvard.edu/photo/index.html]

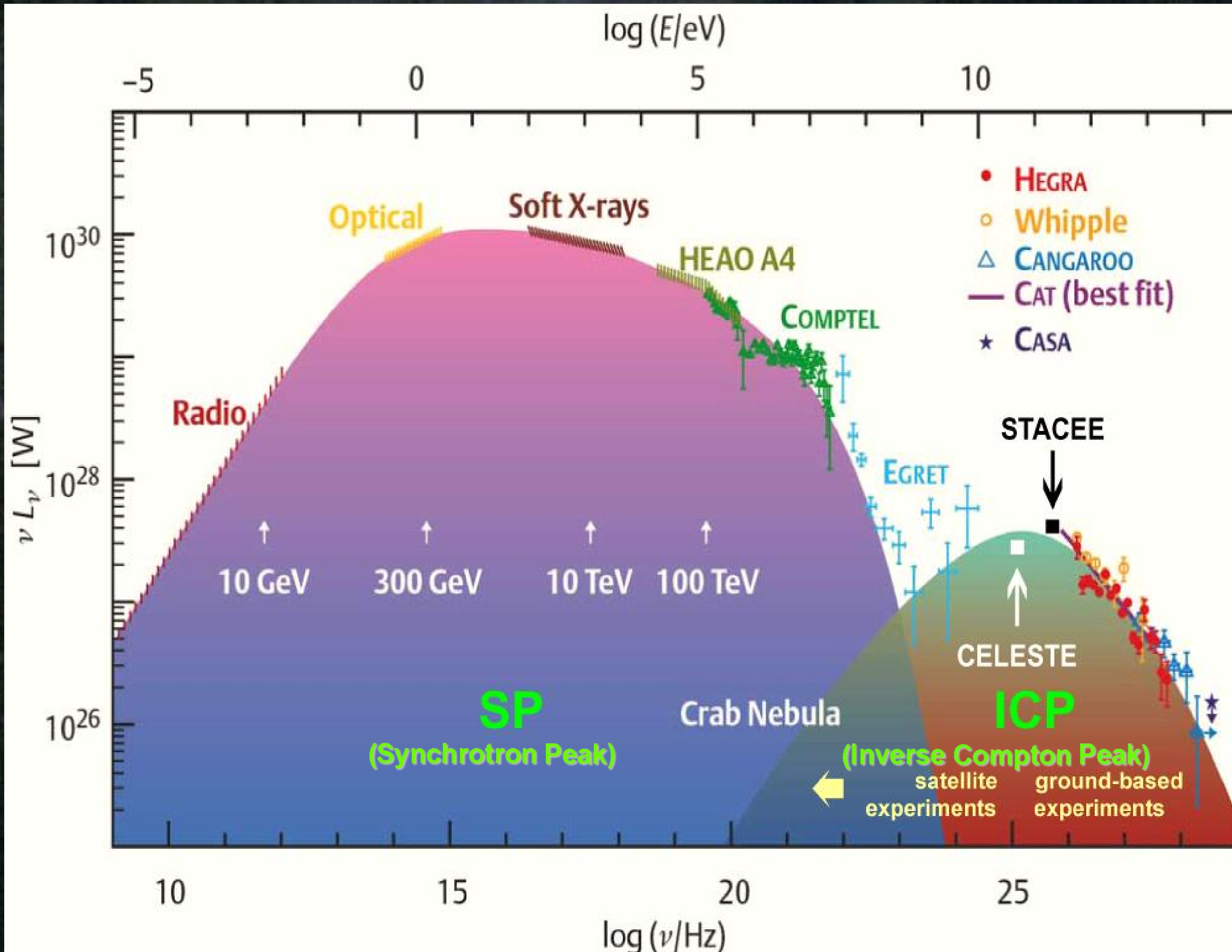

Wide-range spectrum from the Crab nebula shows two peaks, **SP** and **ICP**, which are interpreted as **synchrotron emission** from high energy electrons and **inverse Compton scattering** of synchrotron photon by the same electrons.

The electron energies producing the dominant SP at lower energies are indicated by the arrows. The Compton Gamma Ray Observatory (CGRO) telescopes COMPTEL and EGRET determine the synchrotron fall-off and the transition to the ICP expected at some tens of GeV and indicated by the Cherenkov telescope measurements.

The gap between the satellite and ground-based experiments are now being filled by Cherenkov telescopes using large-area solar power collectors.

Spectral energy distribution of the unpulsed electromagnetic emission from the Crab Nebula.
(Two more recent data points from CELESTE and STACEE measurements are added to the original figure).

[From von H. Völk, “Gamma-Astronomie mit abbildenden Cherenkov-Teleskopen,” Sterne und Weltraum **38** (1999) 1064-1070; see also F.A. Aharonian and A.M. Atoyan, “Nonthermal Radiation of the Crab Nebula,” astro-ph/9803091.]

Another example: Supernova Remnant RX J1713.7-3946 (G347.3-0.5)

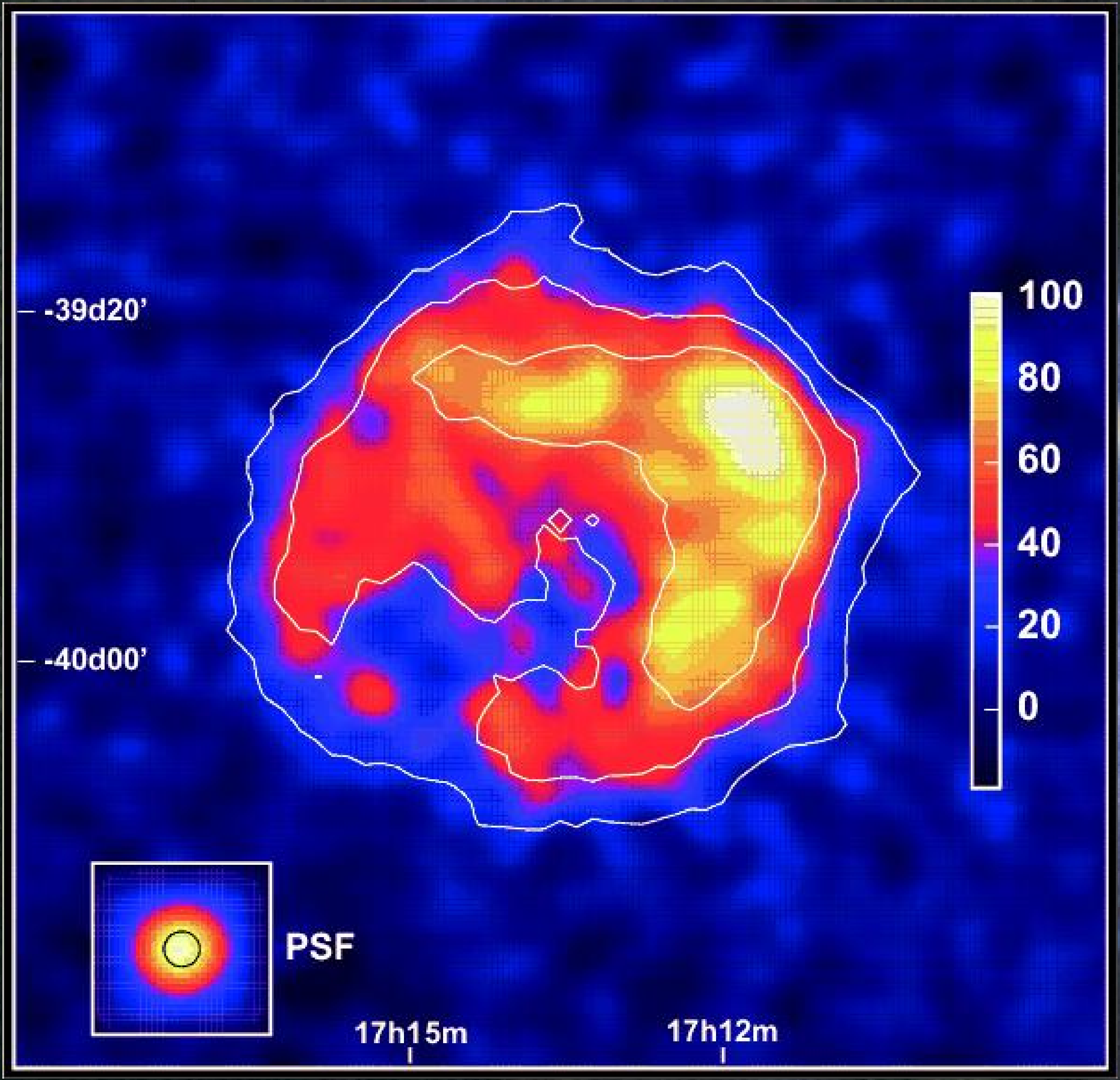

Gamma-ray image of the SNR RX J1713.7-3946. The linear colour scale is in units of excess counts. The white contour lines indicate the significance of the different features, the levels are linearly spaced and correspond to 5, 10, and 15σ, respectively. The significance of each point has been calculated assuming a point source at that position, integrating events within a circle of 0.1° radius. In the lower left hand corner a simulated point source is shown as it would appear in this particular data set (taking the point-spread function and the smoothing into account) along with a black circle of 2' radius denoting the σ of the Gaussian the image is smoothed with.

[From F. Aharonian et al. (H.E.S.S. Collaboration), "A detailed spectral and morphological study of the gamma-ray supernova remnant RX J1713.7-3946 with H.E.S.S," A&A 449 (2006) 223-242, astro-ph/0511678]

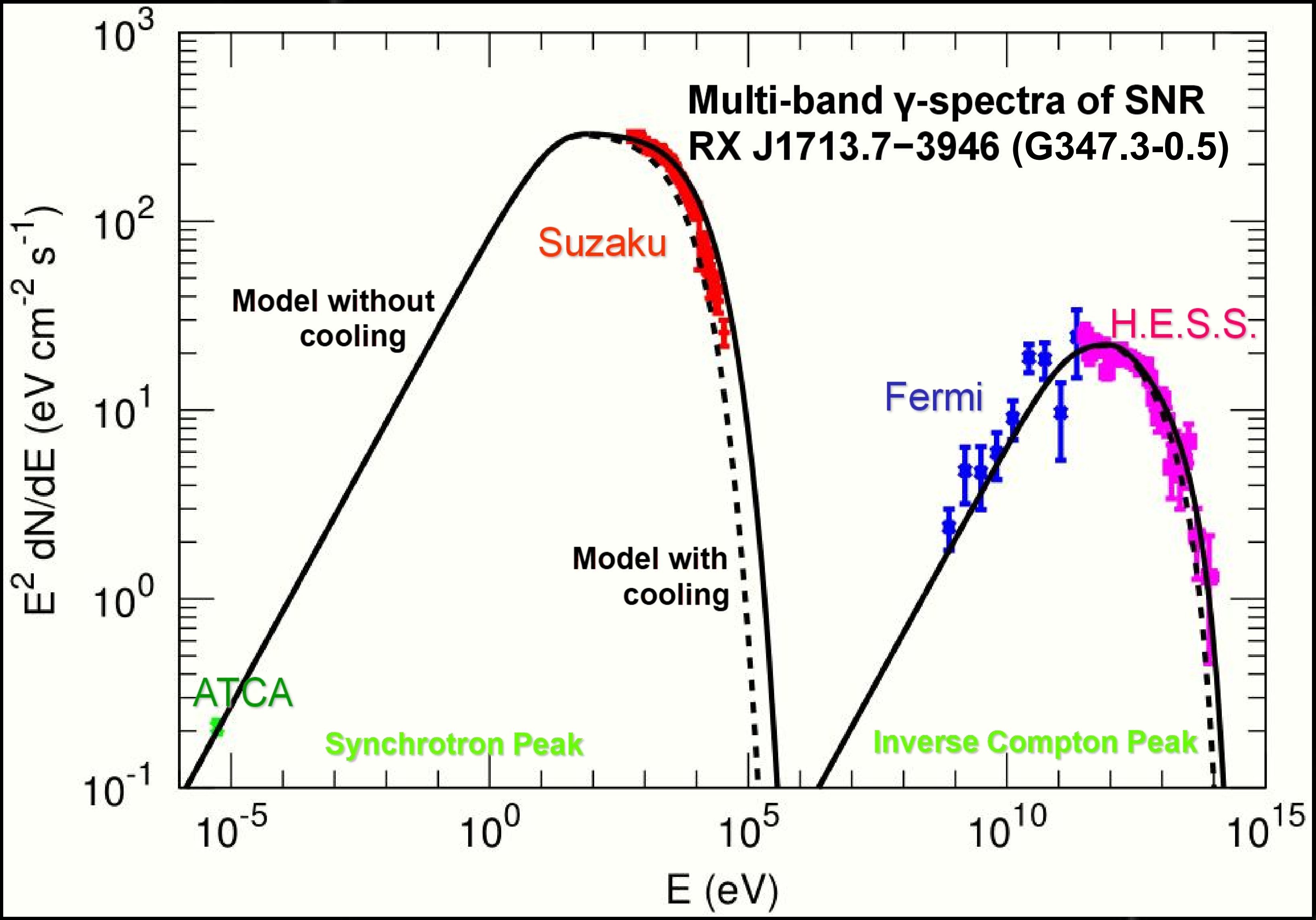

The black solid and dashed curves show model spectra without (E_{cut} = 135 TeV) and with cooling (E_{cut} = 88 TeV) in the downstream region of SNR shocks, respectively. The red, green, blue, and magenta data points are given by Suzaku (2008), ATCA (2009), Fermi (2015), and H.E.S.S. (2011), respectively.

[From Y.Ohira & R.Yamazaki, “Inverse Compton emission from a cosmic-ray precursor in RX J1713.7-3946,” arXiv:1609.02266 [astro-ph.HE].]

SN-GRB Connection

The collapsar model of a gamma-ray burst posits an event very like a Type Ic supernova. When a massive star collapses into a black hole surrounded by a disk of accreting matter, streaming particle jets along the rotation axis could give rise to the supernova and the GRB.

[**From:** SWIFT Satellite animation, Jet Propulsion Laboratory and NASA]

Gamma-ray Bursts (GRBs) are bright flashes of high energy (~1 keV to ~10 MeV) photons.

"The largest bangs in the Universe since the Big one" (Brian Schmidt)

The GRBs can last from a few milliseconds up to ~10 min. Their origin and nature have puzzled the scientific community for about 25 years until 1997, when the first X-ray afterglows of long (> 2 s duration) bursts were detected and the first optical and radio counterparts were found. These measurements established that long GRBs are typically at high redshift (***z* ~1.6**) and are in subluminous star-forming host galaxies. They are likely produced in core-collapse explosions of a class of massive stars that give rise to highly relativistic jets (collapsar model).

Internal inhomogeneities in the velocity field of the relativistic expanding flow lead to collisions between fast moving and slow moving fluid shells and to the formation of internal shock waves. These shocks are believed to produce the observed prompt emission in the form of irregularly shaped and spaced pulses of gamma-rays, each pulse corresponding to a distinct internal collision. The expansion of the jet outward into the circumstellar medium is believed to give rise to "external" shocks, responsible for producing the smoothly fading afterglow emission seen in the X-ray, optical and radio bands.

[Reference: G. Cusumano *et al*., "Detection of a huge explosion in the early Universe," Nature **440** (2006) 164, astro-ph/0509737.]

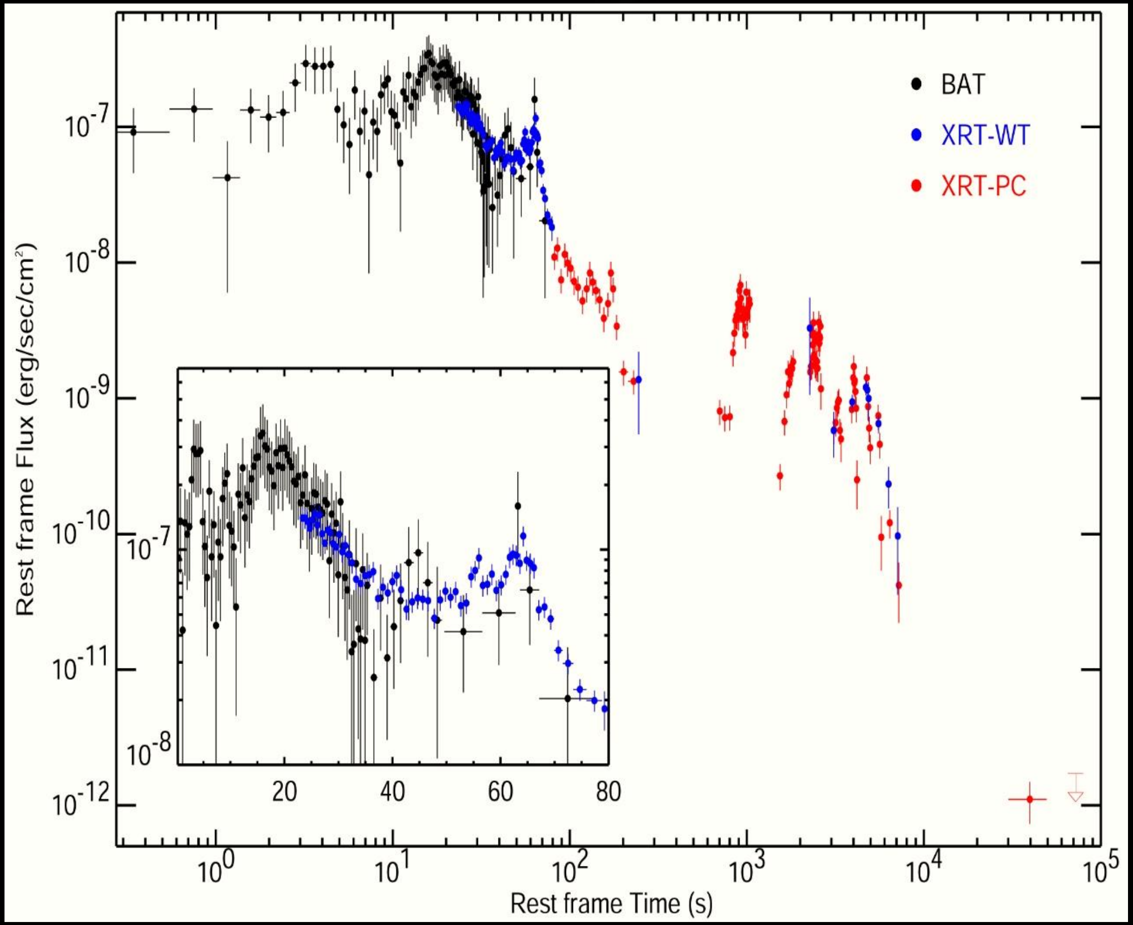

Light curve of **GRB 050904** as observed by the Swift Burst Alert Telescope (**BAT**) and X-ray Telescope (**XRT**). **WT** is windowed timing mode data, and **PC** is photon counting data.

This plot shows the evolution of the GRB flux in the source rest frame. The rest frame flux is calculated from the 0.2-10 keV observed flux by multiplying by $(1+z)^2$ with z=6.29, and corresponds to flux emitted in the 1.4-73 keV energy band. The observed XRT count rates were converted into observed flux using the best fit spectral parameters. The BAT data (originally in the 14-150 keV band) were first extrapolated into the XRT 0.2-10 keV band using a conversion factor evaluated from the BAT best fit spectral model and then converted to rest frame.

The horizontal axis shows the time in seconds starting from the BAT trigger in the rest frame, obtained by applying the correction factor $1/(1+z)$ to the observer frame time. The gaps in the XRT-PC data correspond to the part of the orbit when the satellite was not observing this GRB.
The inset shows the first 80 seconds of the burst, with the excellent match between the XRT and the extrapolated BAT fluxes.

Lower and upper limits to the isotropic-equivalent radiated energy E_{iso} up to 300 seconds from the burst onset are obtained to be **6.6×10^{46} J** and **3.2×10^{47} J**, respectively in the full 1-10^4 keV band.

The redshift of **6.29** translates to a distance of **13 billion light-years** from Earth, corresponding to a time when the Universe was just **700 million** to **750 million years** old.

[**Reference**: G. Cusumano *et al*., "Detection of a huge explosion in the early Universe," Nature **440** (2006) 164, astro-ph/0509737

An off-axis Type Ic supernova 2003jd as observed by the Australian National Observatory.

More often than not, supernovae are asymmetric. Thus, when you look at Type Ic supernovae from different angles, they look different.

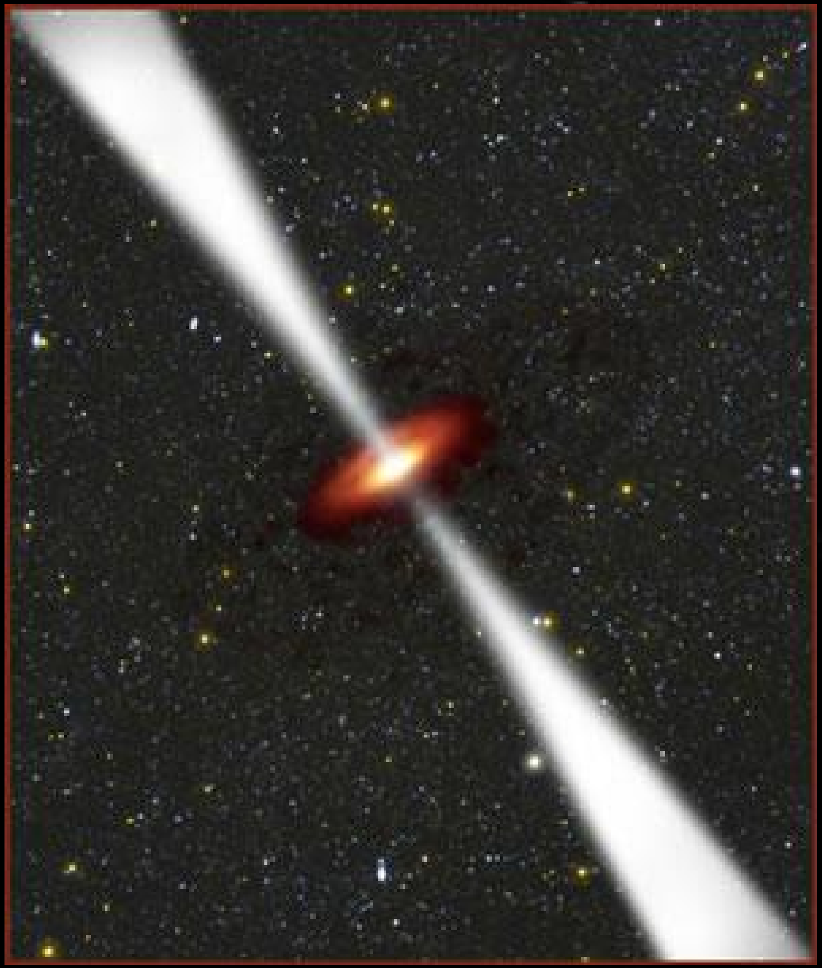

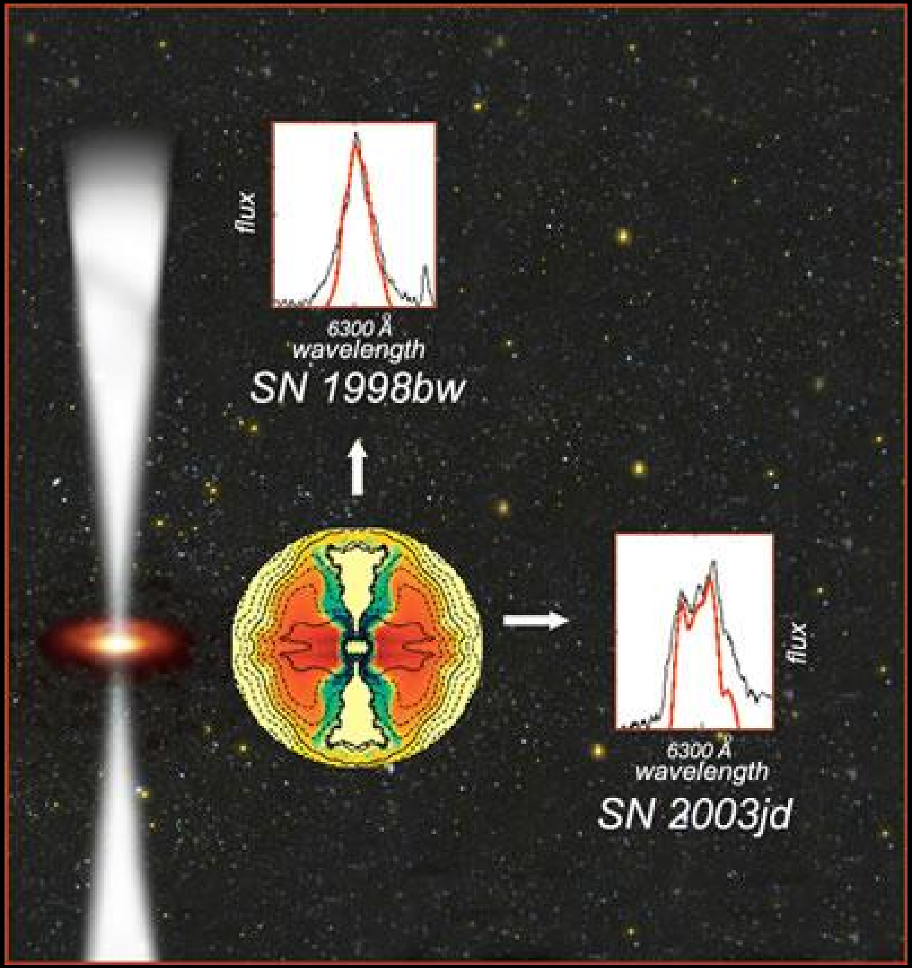

Some long-duration GRB may be associated with Type Ic supernovae, which occur when a massive star collapses to form a black hole or neutron star.

[**From:** P. Preuss, “It's an exceptional supernova, but is it a GRB?” **science@berkeley lab**, August 5, 2005]

Whether a Type Ic SN is seen as a GRB could depend upon how the asymmetric object is viewed. SN 1998bw may have been viewed along the axis of the jets; its spectrum showed a strong, single peak in the oxygen emission line. SN 2003jd may have been viewed from the side, through a rapidly rotating disk that caused the oxygen line to split.

Models of Short-Duration GRBs

Colliding Binary Neutron Stars

Short GRBs (less than two seconds in duration) may be caused by mergers of binary systems with black holes or neutron stars. While uncertainty remains, most astrophysicists believe in either scenario a new black hole is born.

[From Chandra X-ray Observatory Photo Album]

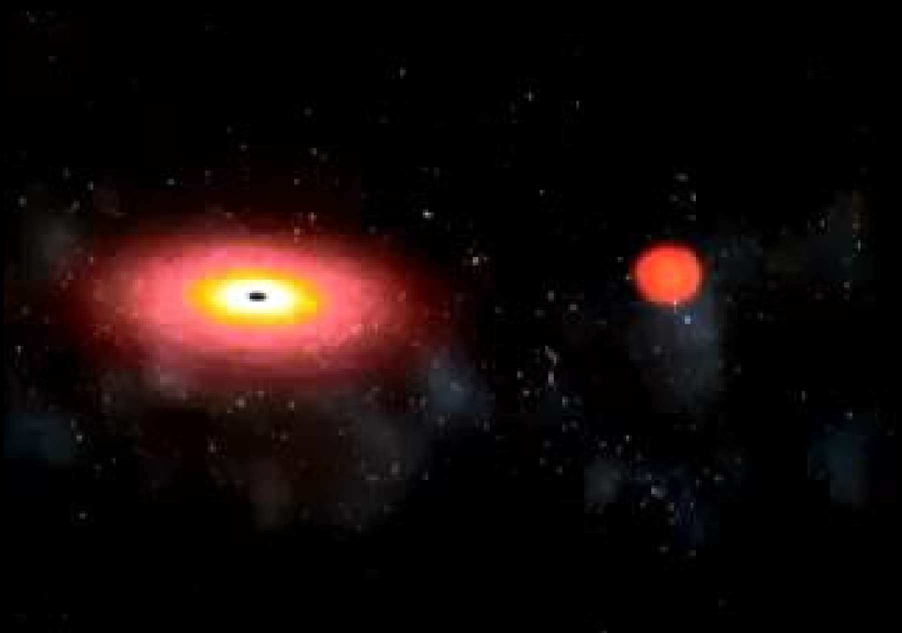

Black Hole Devours a Neutron Star

Astrophysicists say they have seen tantalizing, first-time evidence of a black hole eating a neutron star-first stretching the neutron star into a crescent, swallowing it, and then gulping up crumbs of the broken star in the minutes and hours that followed.

[From Chandra X-ray Observatory Photo Album]

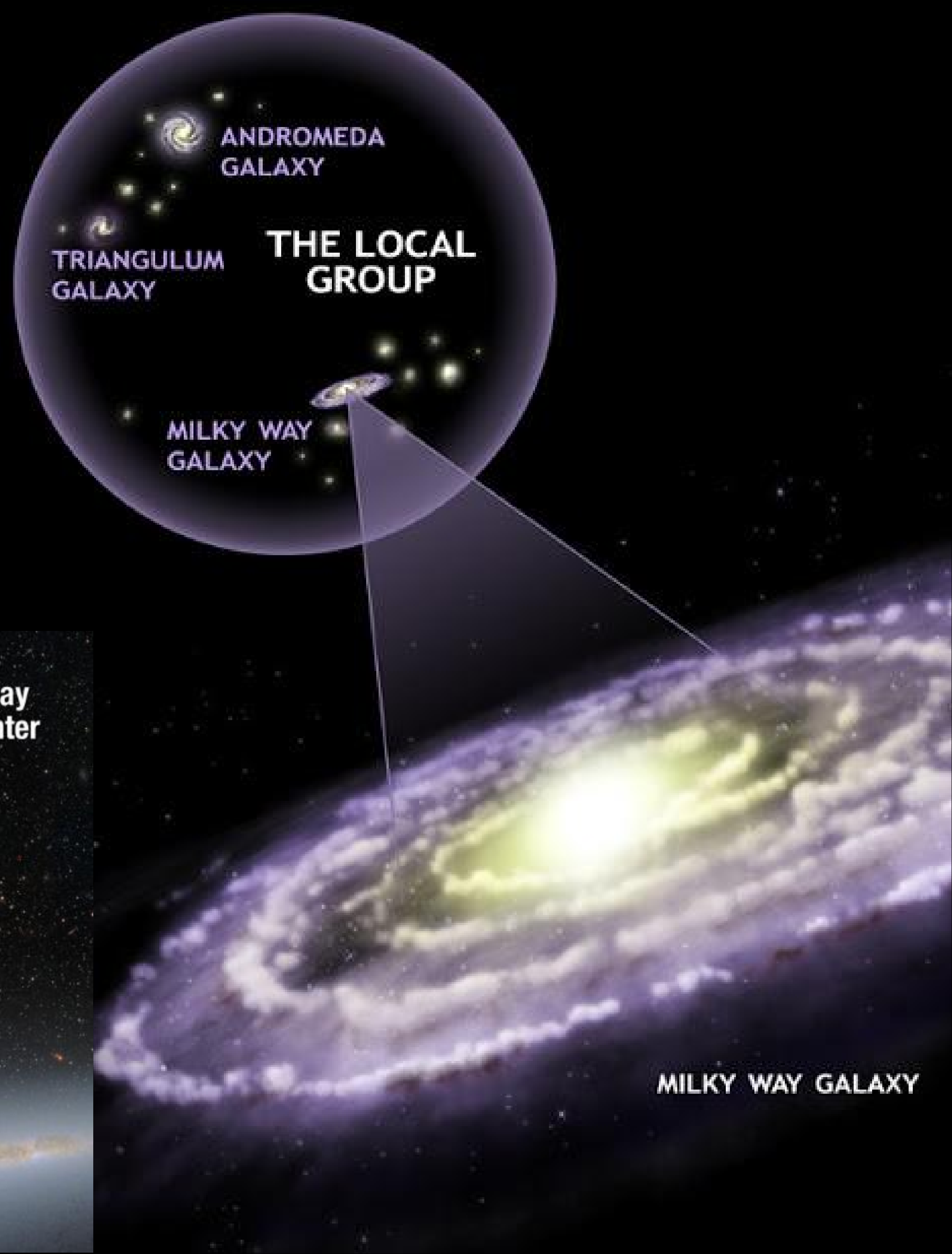
ANDROMEDA
GALAXY
TRIANGULUM
GALAXY
THE LOCAL
GROUP
MILKY WAY
GALAXY
MILKY WAY GALAXY

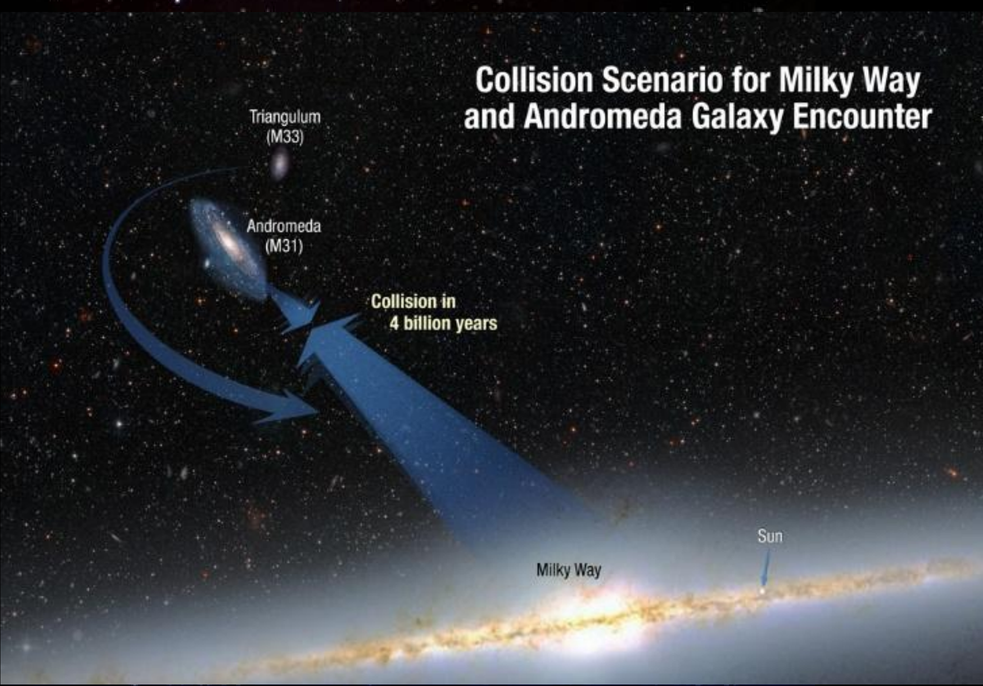
Collision Scenario for Milky Way
and Andromeda Galaxy Encounter
Triangulum
(M33)
Andromeda
(M31)
Collision in
4 billion years
Sun
Milky Way

Milky Way & Andromeda Galaxies head-on collision
(simulation developed by using data from the Hubble Space Telescope)

[From https://youtu.be/4disyKG7XtU]

Genus Diversity & Cosmic Rays

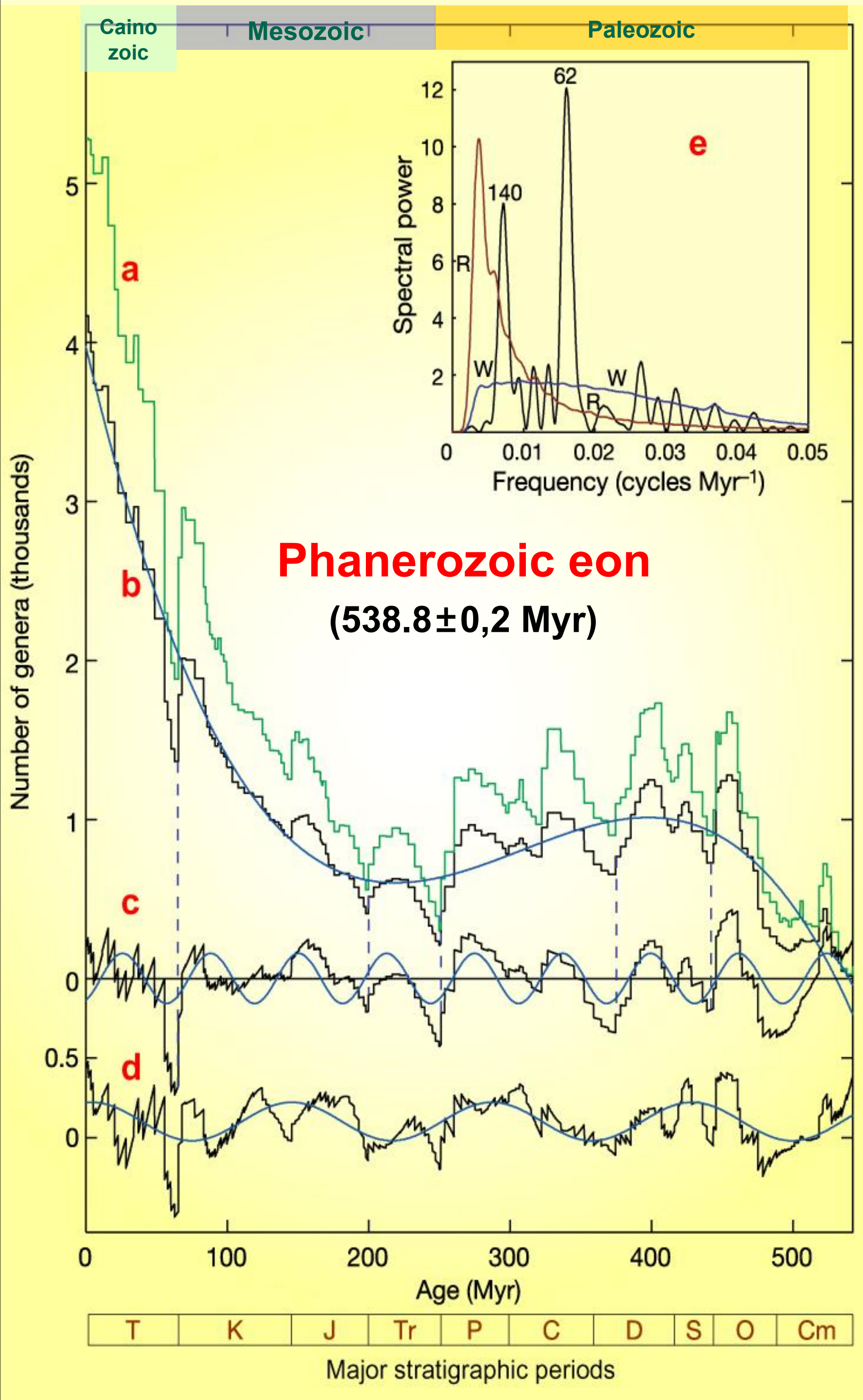

Robert Rohde and Richard Muller (University of California) analyzed the fossil records of marine animals over the past **542 Myr** (**Phanerozoic** eon - time of "explicit" life, next after the **Cryptozoic** eon) and found that biodiversity appears to rise and fall in mysterious cycles of about **62 Myr.**

These cycles probably cannot be explain by any terrestrial process!

a. The green plot shows the number of known marine animal genera versus time from Sepkoski's compendium, converted to the 2004 Geologic Time Scale.

b. The black plot shows the same data, with single occurrence and poorly dated genera removed. The trend line (blue) is a 3rd-order polynomial fitted to the data.

c. As b, with the trend subtracted and a **62-Myr** sine wave (blue curve) superimposed.

d. The detrended data after subtraction of the **62-Myr** cycle and with a **140-Myr** sine wave superimposed.

e. Fourier spectrum of c. Curves W (in blue) and R (in red) are estimates of spectral background.

The "Big 5" mass extinctions are marked with dashed lines.

[**Reference**: R.A. Rohde & R.A. Muller, "Cycles in fossil diversity," Lett. to Nature, **434** No. 10 (2005) 208-210.]

It seems the puzzle is already resolved by Mikhail Medvedev and Adrian Melott (Kansas University).

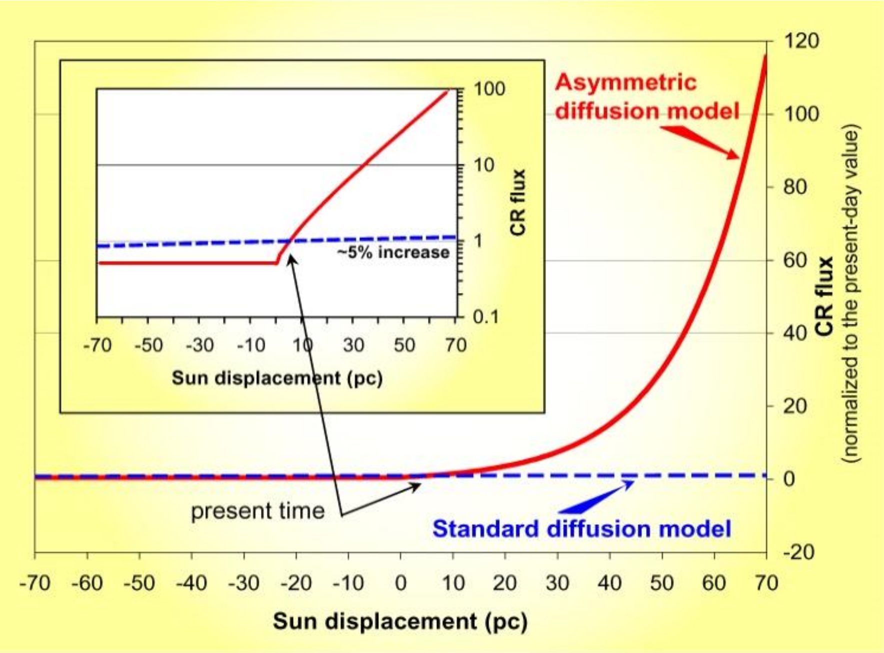

While astro- and geophysical phenomena may be periodic for such a long time, no plausible mechanism has been found. The fact that the period of the diversity cycle (62 Myr) is close to the ~ 64 Myr period of the vertical oscillation of the Solar system relative to the galactic disk is suggestive. However, any model involving cosmogenic processes modulated by the Sun's midplane crossing or its maximal vertical distance from the galactic plane predicts a half-period cycle, i.e. about 32 Myr.

Medvedev & Melott propose that the diversity cycle is caused by the anisotropy of cosmic ray (CR) production in the galactic halo/wind/termination shock and the shielding effect of the galactic magnetic fields.

CRs affect climate and harm live organisms directly via increase of radiation dose.

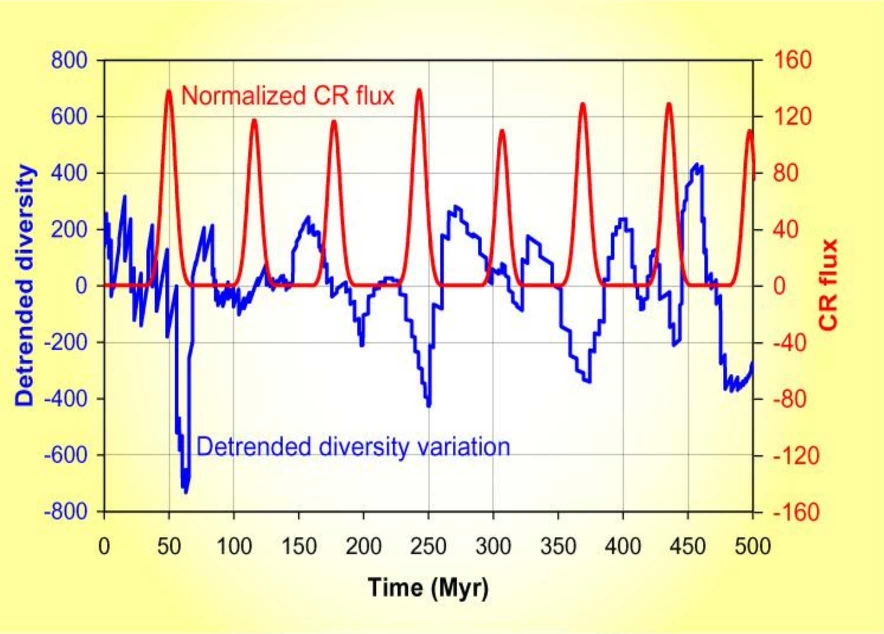

The CR anisotropy is caused by the galactic north-south asymmetry of the termination shock due to the interaction with the “warm-hot intergalactic medium” as our galaxy falls toward the Virgo cluster (nearly in the direction of the galactic north pole) with a velocity of order 200 km/s.

After a revision of the mechanism of CR propagation in the galactic magnetic fields it was show that the shielding effect is strongly position-dependent. It varies by a factor of a **hundred** and reaches a minimum at the maximum northward displacement of the Sun. Very good phase agreement between maximum excursions of the Sun toward galactic north and minima of the fossil diversity cycle further supports the model.

[**Reference**: M.V.Medvedev & A.L.Melott, “Do extragalactic cosmic rays induce cycles in fossil diversity?” Astrophys.J. **664** (2007) 879-889, astro-ph/0602092]

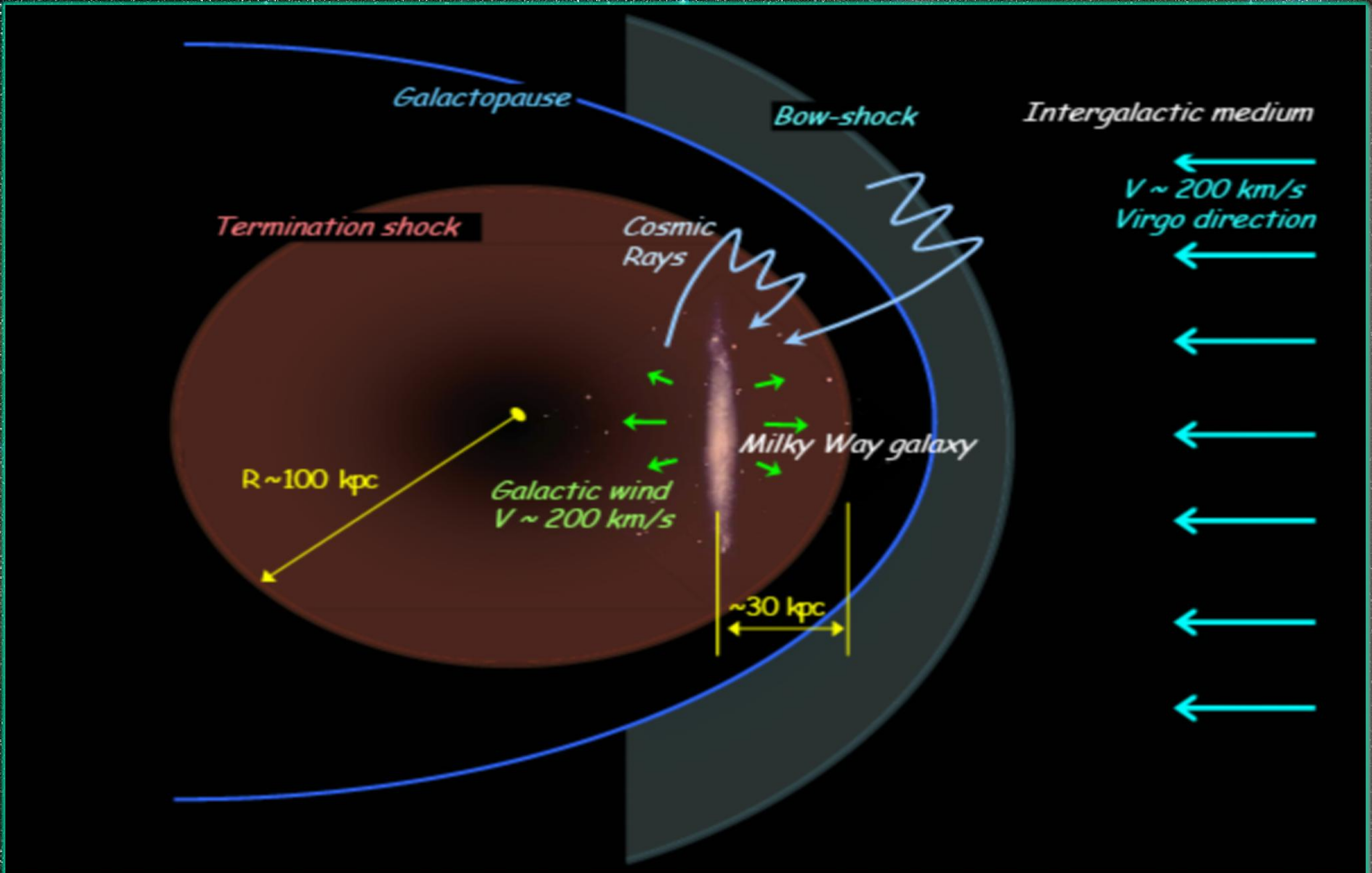

The “galactosphere” with the galactic termination and bow shocks being sources of extragalactic cosmic rays. Due to inherent asymmetry, the north side of the Milky Way (with Virgo cluster being nearly at the north galactic pole) is exposed to a larger cosmic ray flux than its south side.

[M.V. Medvedev & A.L. Melott, “Do extragalactic cosmic rays induce cycles in fossil diversity?” Astrophys.J. **664** (2007) 879-889, astro-ph/0602092]

Displacement of the Sun from the Galactic Plane

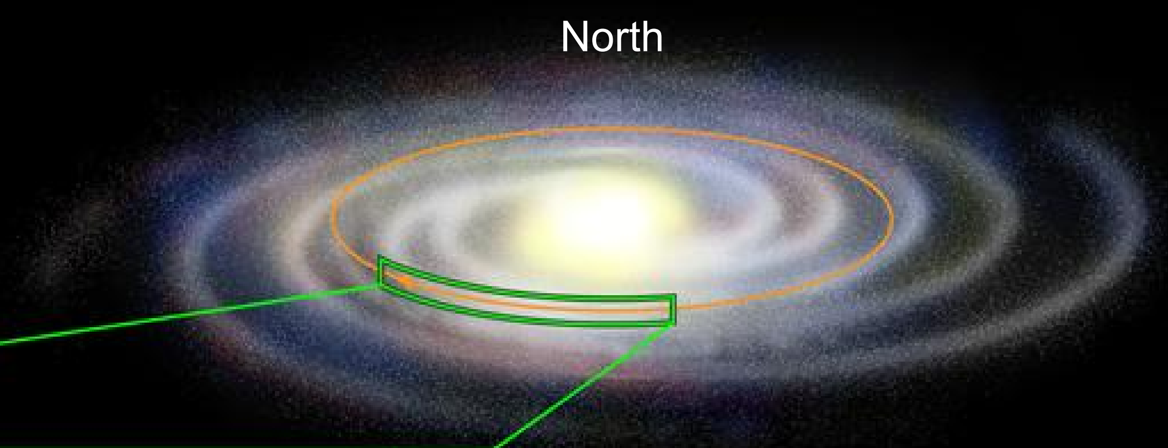

No, it is not a sine-wave or helical motion!

As the Sun orbits around the center of the Milky Way, it bobs up and down relative to the plane of the galactic disk due to its gravity. Every about 64 Myr, our solar system pops above the "northern" edge of the disk, exposing Earth to a barrage of dangerous cosmic rays that may be affecting biodiversity on the planet.

Keep in mind that the figure is **very relative** as the Sun is situated very close to the corotation region of the Galaxy and hence it orbits almost **together** with the spiral arms (see next slide).

[Some details can be found at URL: <https://astronomy.stackexchange.com/questions/12506/does-the-sun-orbit-the-milky-way-in-a-kind-of-flat-or-inclined-orbit-or-more-o>.]

If the Medvedev-Melott model is correct we have a very good new instrument for studying CR time variations.

Selected recent determinations of Z

Reference	Z (ps)	Sample
Conti & Vacca (1990)	15 ± 3	WR stars (N = 101) within 4.5 kpc of Sun
Cohen (1995)	15.5 ± 0.7	IRAS point-source counts + point-source sky model
Humphreys & Larsen (1995)	20.5 ± 3.5	Galactic-pole star counts (N ~ 10,000) plus Bahcall-Soneira galaxy model
Mendez & van Altena (1998)	27 ± 3	Solar-neighborhood reddening model plus star counts
Binney et al. (1997)	14 ±4	COBE/DIRBE surface-brightness analysis; double-exponential disk + power-law bulge
Reed (1997)	~10–12	OB stars with $\mid b \mid < 10^{\circ}$; averaged M_B values for rough OB classes; assumed extinction model
Chen et al. (1999)	27.5 ± 6.0	COBE/IRAS-based extinction model
Ma'z-Apell‡niz (2001)	24.2 ± 1.7	*Hipparcos* parallaxes for 3382 O-B5 stars ($\mid b \mid > 5^{\circ}$) within ~ 350 pc, plus distribution model
Joshi (2005)	22.8 ± 3.3	extinction analysis for ~ 600 open clusters with $\mid b \mid < 5^{\circ}$

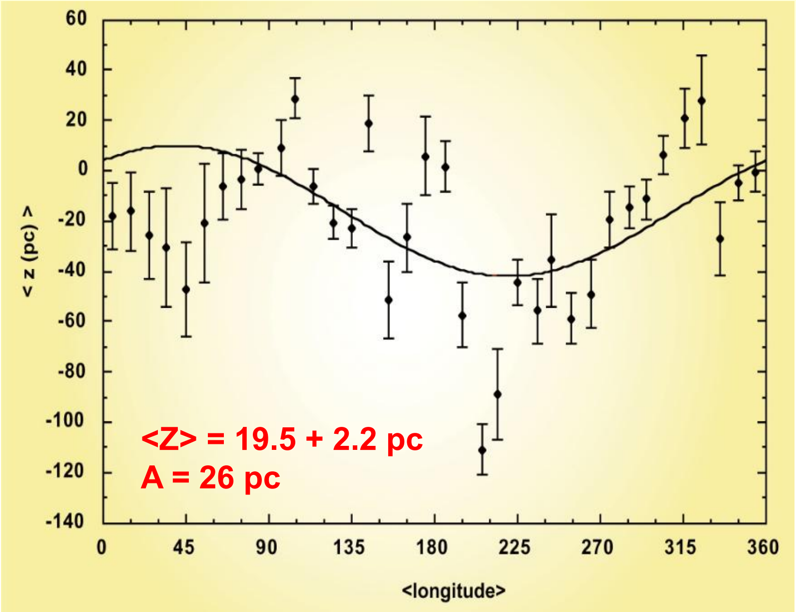

Note 1: The data on Sun's displacement from the galactic plane are rather uncertain. Therefore the above difference between 62 and 64 Myr does not seem essential now.

Note 2: The Sun is situated very close to the corotation resonance where the rotation velocities of the disk and of the spiral pattern coincide. The displacement of the Sun from the corotation circle is about 0.1 kpc.

[**References:** B.C. Reed, "The Sun's displacement from the galactic plane from spectroscopic parallaxes of 2400 OB stars," J.Roy.Astron.Soc.Canada **100** (2006) 146-148, astro-ph/0507655. Y.C.Joshi, "Displacement of the Sun from the Galactic Plane", Mon. Not. Roy. Astron. Soc. **378** (2007) 768-776, astro-ph_0704.0950.

Aurora Borealis, Northern Lights, 17th of March 2013 (by Hannu Hoffrén)

[More beautiful movies can be found @ https://www.youtube.com/watch?v=xI_qG0DuuMU]

Auroras are not unique to Earth. In the Solar System, other planets have auroras too — Jupiter, Saturn, Uranus, Neptune. And there are exoplanets that also show evidence of auroral activity.

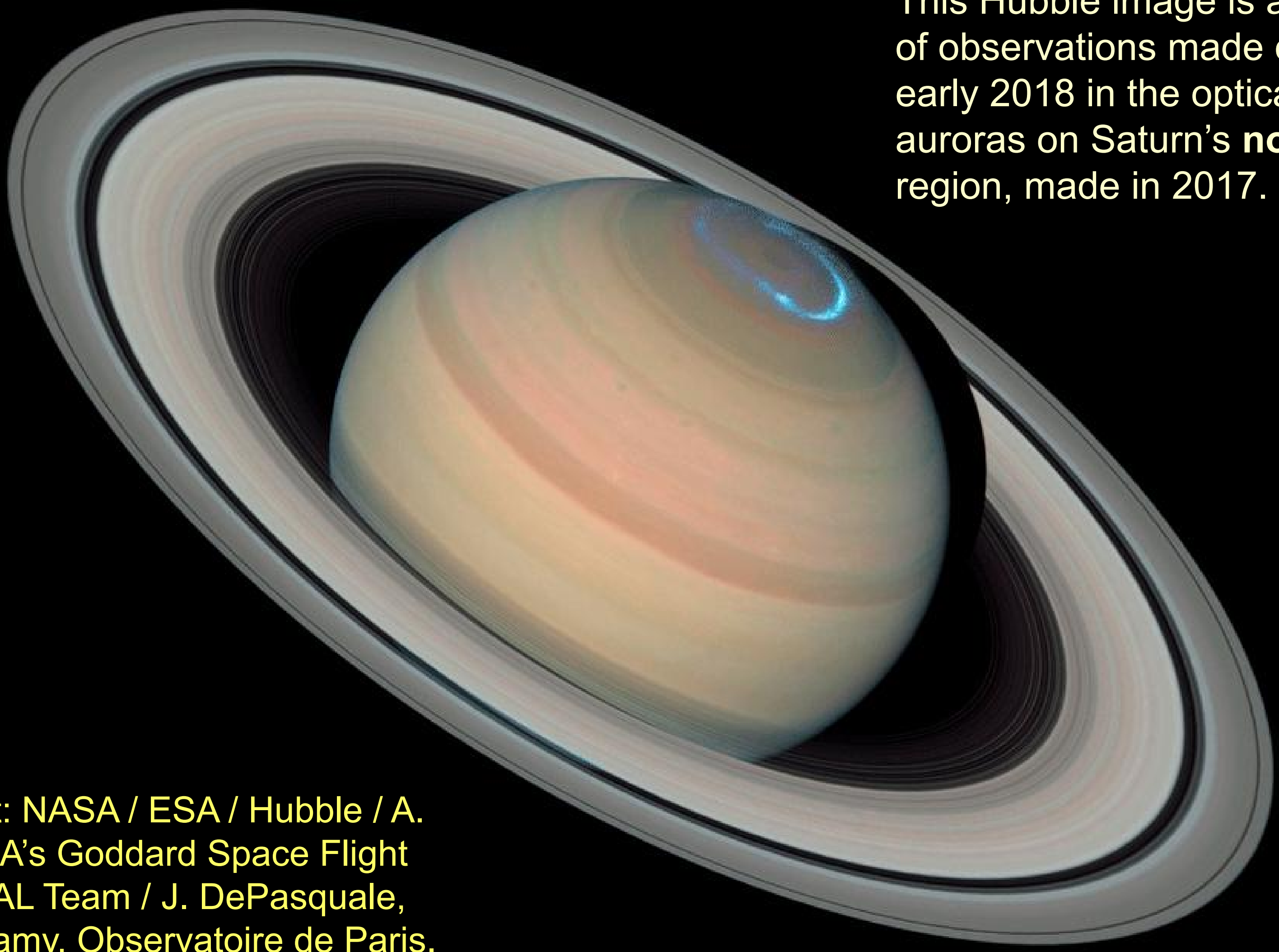

This Hubble image is a composite of observations made of Saturn in early 2018 in the optical and of the auroras on Saturn's **north** pole region, made in 2017.

Image credit: NASA / ESA / Hubble / A. Simon, NASA's Goddard Space Flight Center / OPAL Team / J. DePasquale, STScI / L. Lamy, Observatoire de Paris.

For detail, see, e.g., http://www.sci-news.com/astronomy/northern-auroras-saturn-06360.html

The diameter of the area of propagation of this aurora is approximately **3-4** times the diameter of the Earth.

Astronomers are using NASA's Hubble Space Telescope to study auroras — stunning light shows in a planet's atmosphere — on the poles of the Jupiter.

The animation is composed of two different Hubble observations. The auroras were photographed during a series of Hubble Space Telescope Imaging Spectrograph far-ultraviolet-light observations taking place as NASA's Juno spacecraft approaches and enters into orbit around Jupiter. The full-color disk of Jupiter in this image was separately photographed at a different time by Hubble's Outer Planet Atmospheres Legacy (OPAL) program, a long-term Hubble project that annually captures global maps of the outer planets.

Image credits: NASA, ESA, and J. Nichols (University of Leicester)

For more detail, see https://www.nasa.gov/feature/goddard/2016/hubble-captures-vivid-auroras-in-jupiter-s-atmosphere

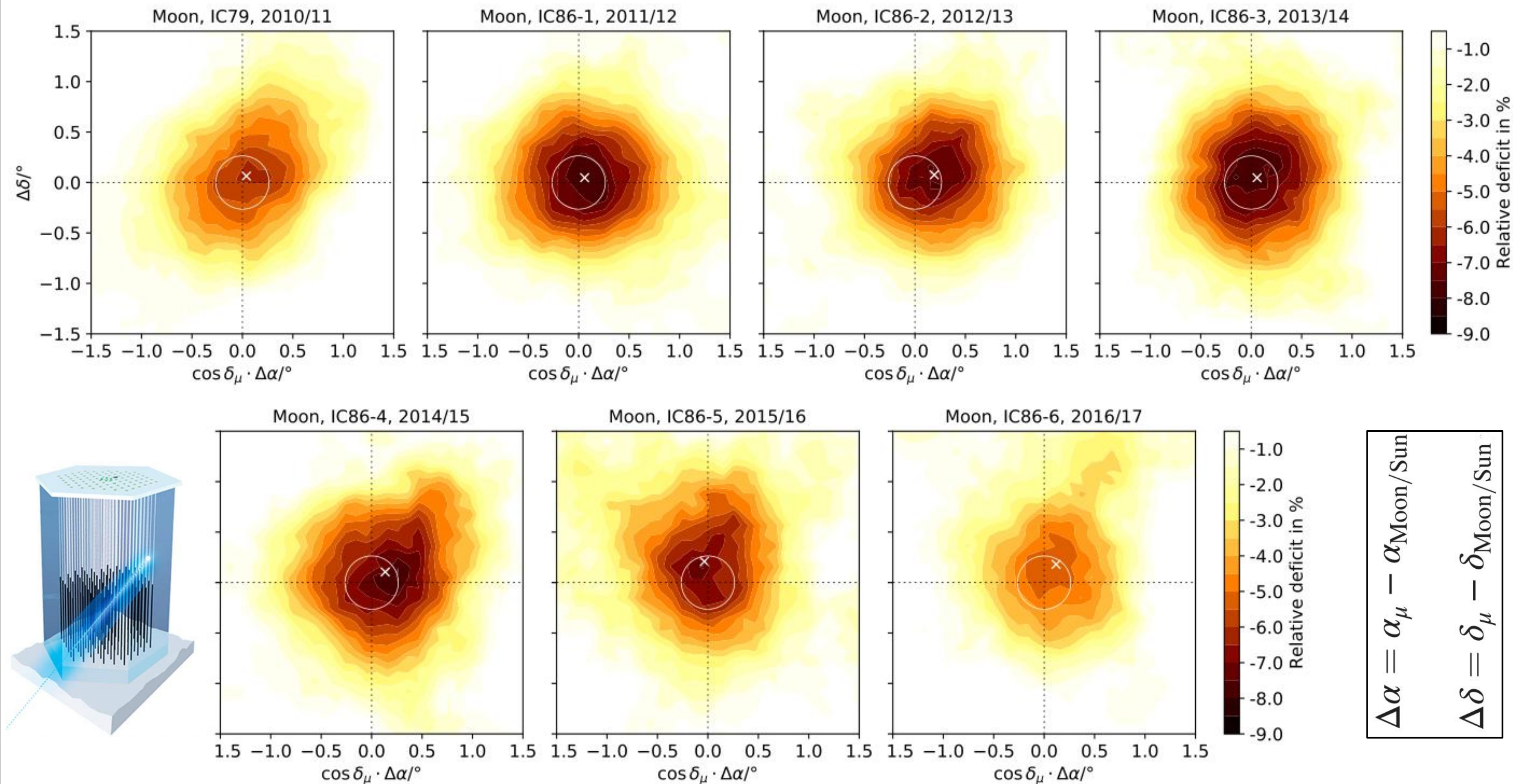

$$\Delta\alpha = \alpha_\mu - \alpha_{\mathrm{Moon/Sun}}$$
$$\Delta\delta = \delta_\mu - \delta_{\mathrm{Moon/Sun}}$$

Boxcar-smoothed two-dimensional contour map of the moon shadow for the years IC79 to IC86-6 showing the computed center of gravity of the shadow as a white cross. The white circle indicates the seven-year mean of the weighted average of the angular moon radius; here and below, α_μ and δ_μ represent the individual reconstructed right ascension and declination of each muon event.

[Reference: M. G. Aartsen et al, “Measurements of the time-dependent cosmic-ray Sun shadow with seven years of IceCube data: Comparison with the Solar cycle and magnetic field models,” Phys. Rev. D 103 (2021) 042005, arXiv:2006.16298 [astro-ph.HE].]

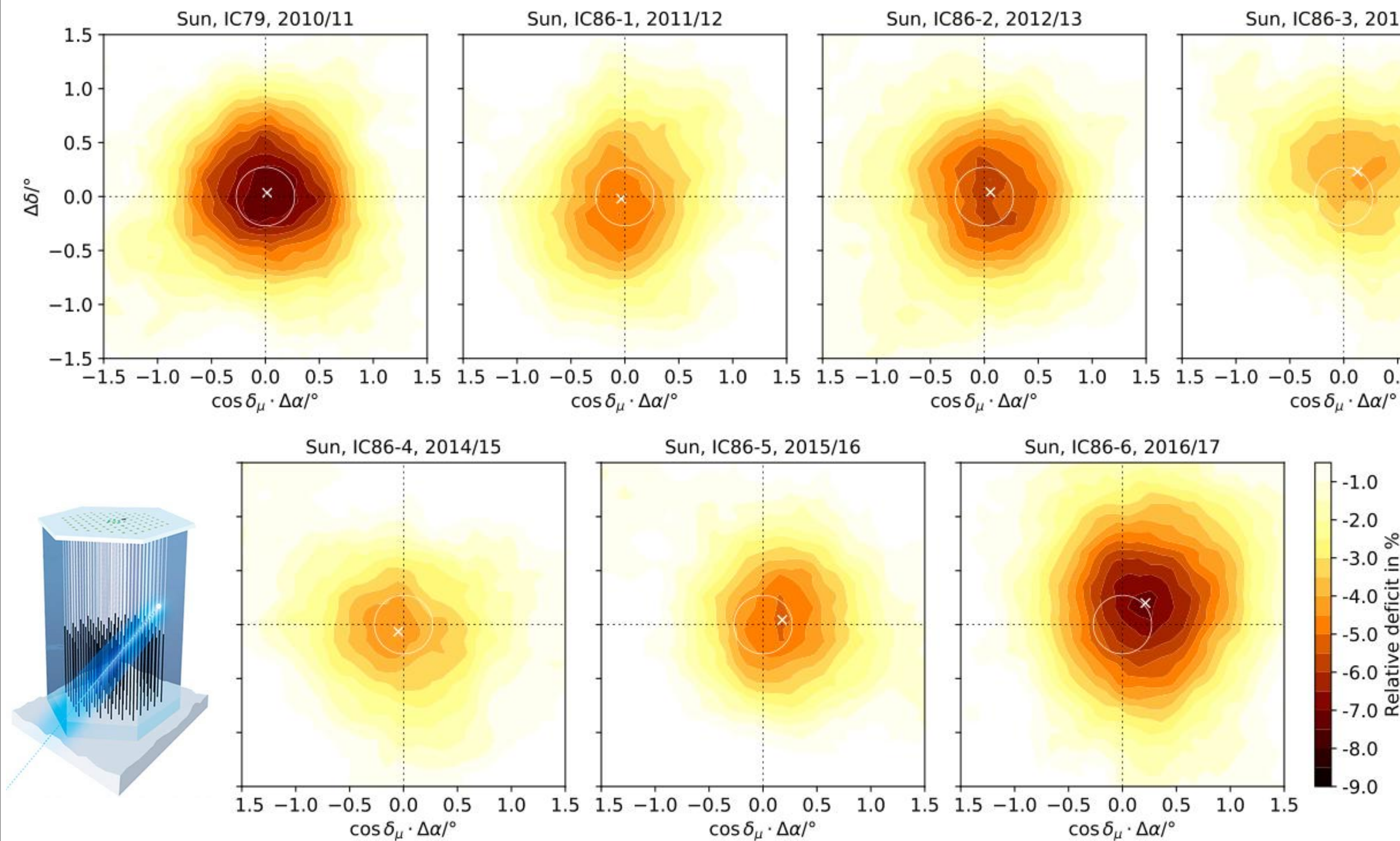

$$\Delta\alpha = \alpha_\mu - \alpha_{\mathrm{Moon/Sun}}$$

$$\Delta\delta = \delta_\mu - \delta_{\mathrm{Moon/Sun}}$$

Boxcar-smoothed two-dimensional contour map of the Sun shadow for the years IC79 to IC86-6 showing the computed center of gravity of the shadow as a white cross. The white circle indicates the weighted average of the angular Sun radius.

While the moon shadow is described reasonably well by the lunar-disk model, the Sun shadow is statistically incompatible with geometrical shadowing only due to the solar disk (7.3σ). A linear relationship between shadow strength and solar activity is preferred over a constant one with 6.4σ. In times of high solar activity, the measured Sun shadow seems to increase with energy (1.8σ indication).

COSMIC RAYS

Archived content

from earlier versions of this presentation

The material removed from the main content of the lectures either did not fit into the lecture schedule, or today is of only historical interest, but for the same reason I decided to preserve some of it in the archive. Sometimes it's interesting to compare old and new data and see progress.

Solar rotation varies by latitude

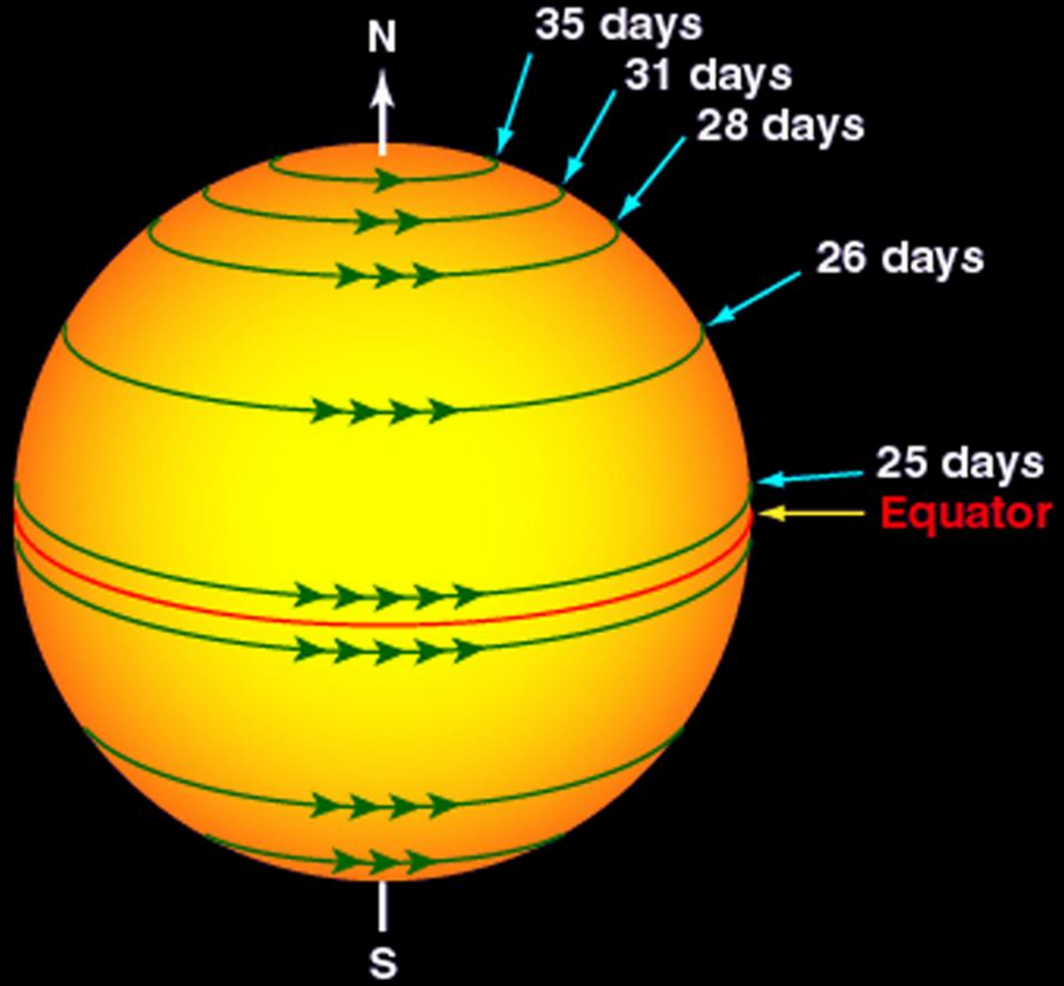

The Sun rotates on its axis once in about 27 days. This rotation was first detected by observing the motion of sunspots. The Sun's rotation axis is tilted by about 7.25 degrees from the axis of the Earth's orbit so we see more of the Sun's north pole in September of each year and more of its south pole in March.

[From URL: <https://www.nasa.gov/mission_pages/sunearth/science/solar-rotation.html>]

Solar wind and aurora polaris

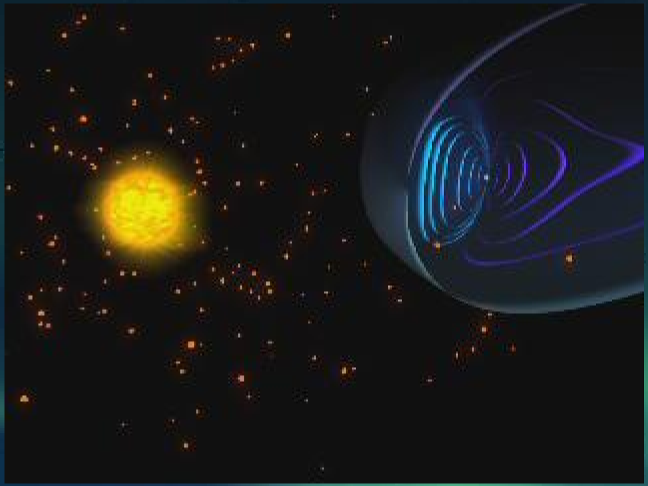

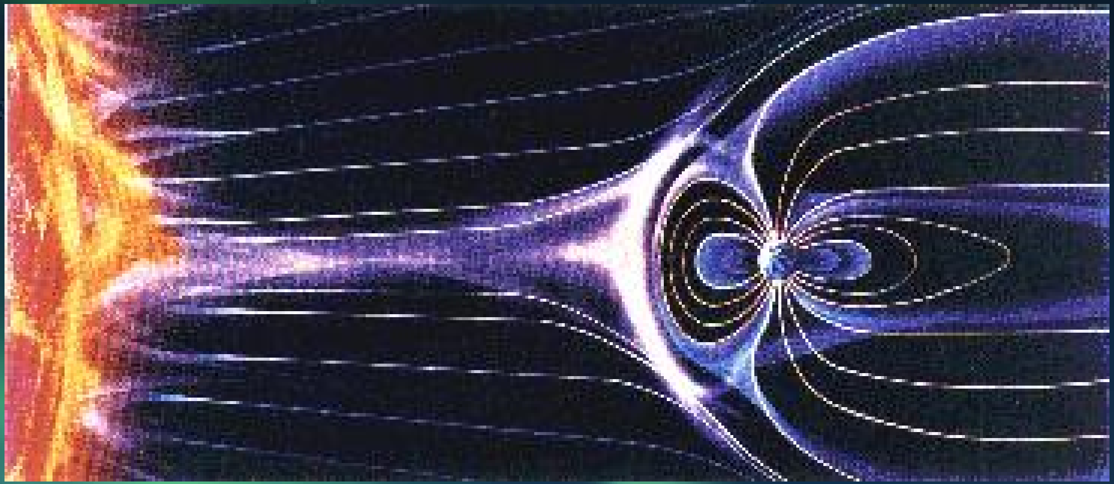

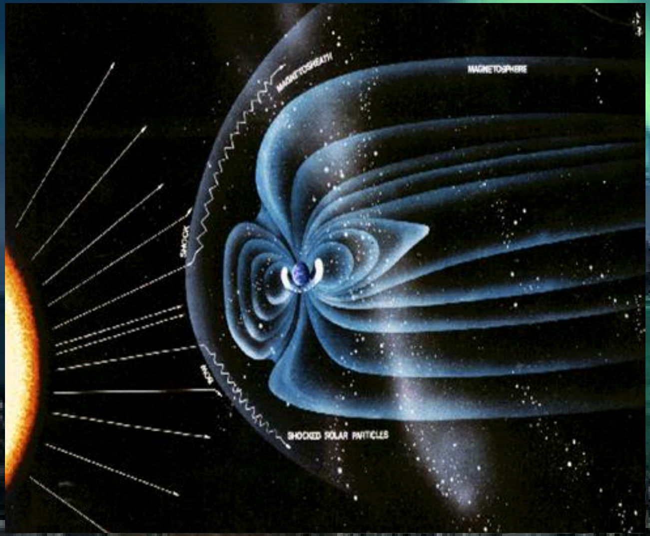

One of the largest sunspots in the last nine years, labeled AR1944, was seen in early January 2014, as captured by NASA's Solar Dynamics Observatory. The sunspot steadily moved toward the right, along with the rotation of the Sun. An image of Earth has been added for scale.

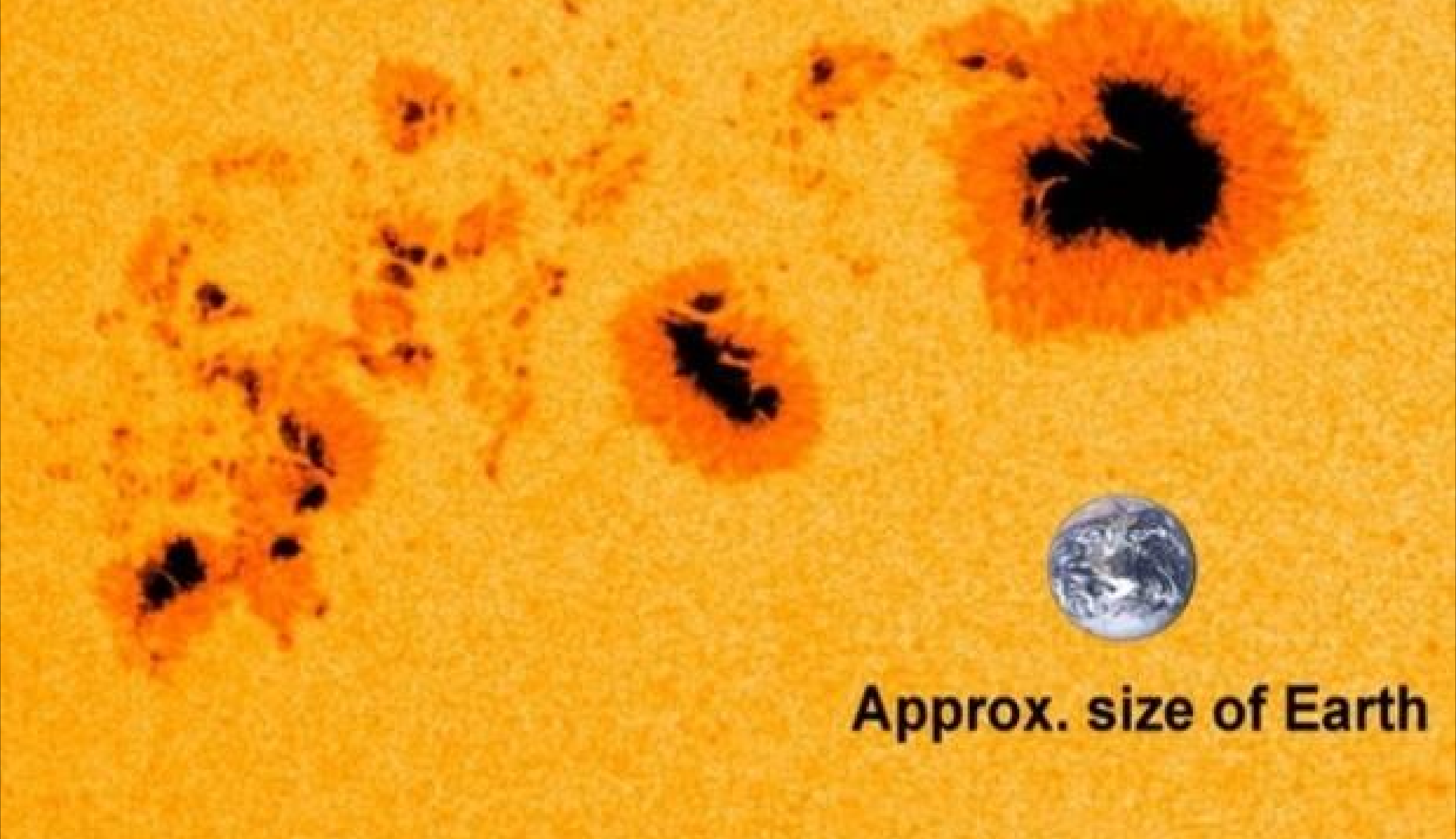

[Image Credit: NASA/SDO, URL: https://www.nasa.gov/content/goddard/giant-january-sunspots]

Monthly average Sunspot Number

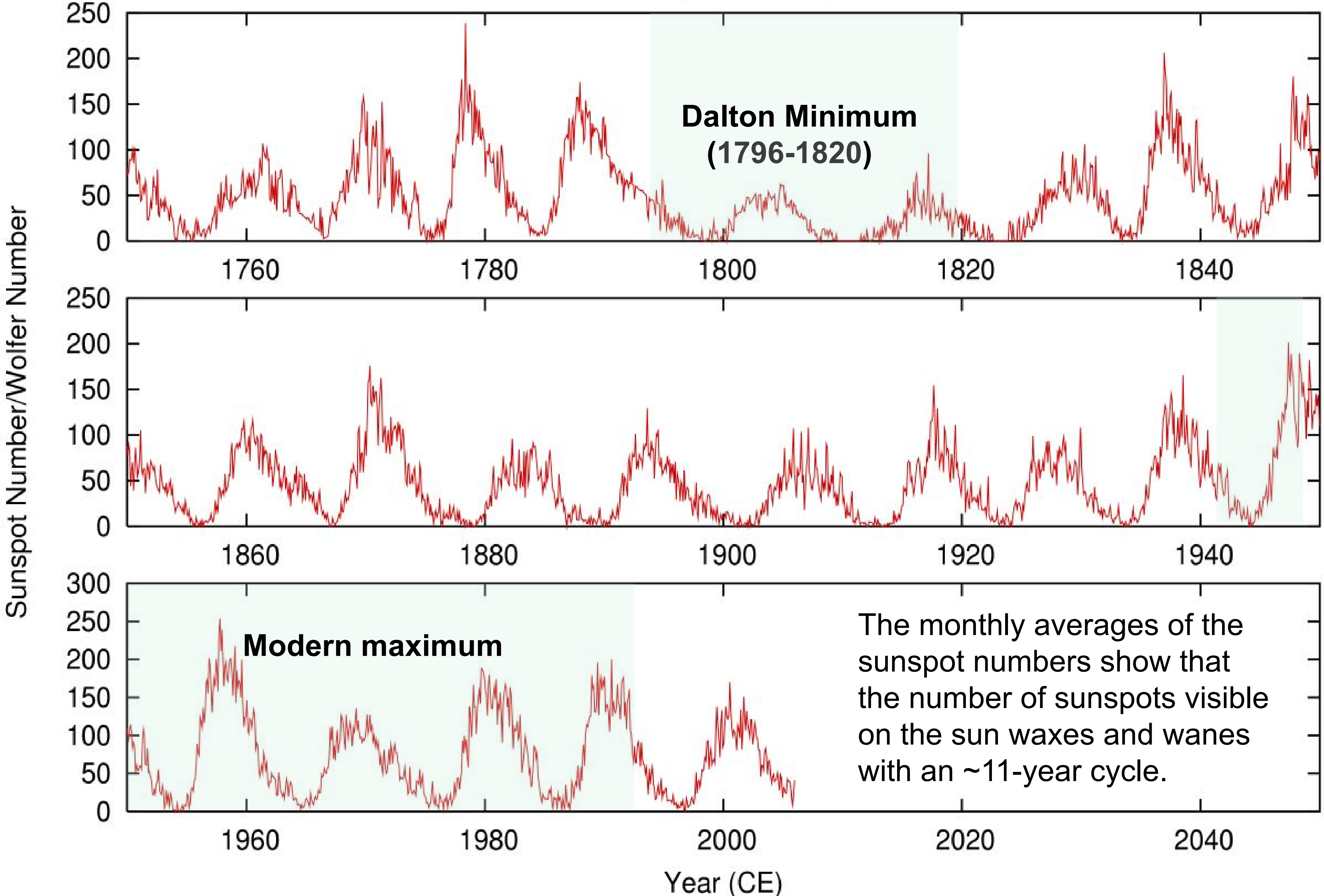

[From URL: http://science.nasa.gov/ssl/PAD/SOLAR/]

Unusual, but not unique ("*Nil novi sub sole*"). Let's wait awhile...

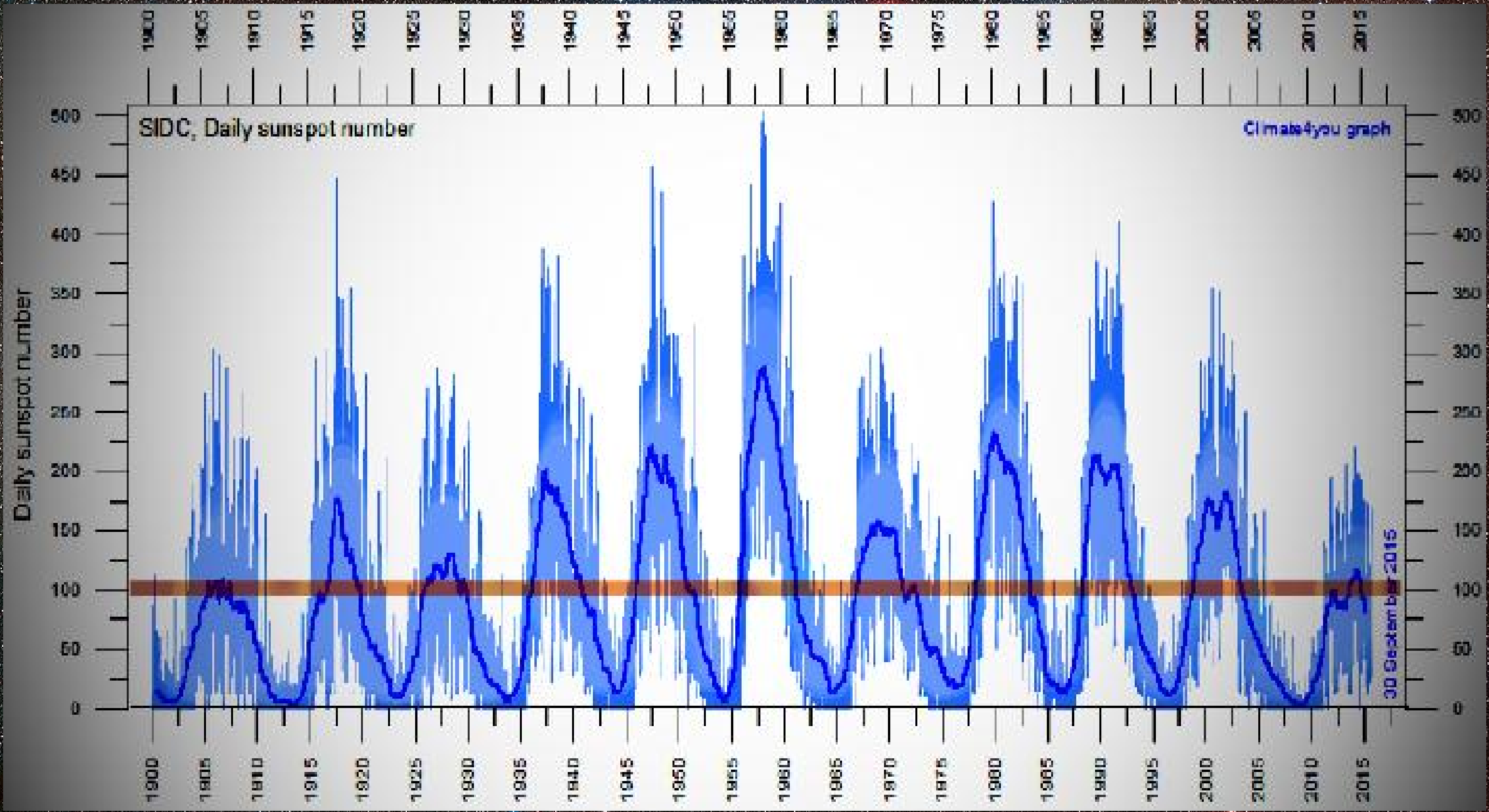

[From URL: <http://www.persicetometeo.com/public/sole_monitoring.htm>]

29 Nov 2020 Sunspots and M4 Flare just beyond the SE limb

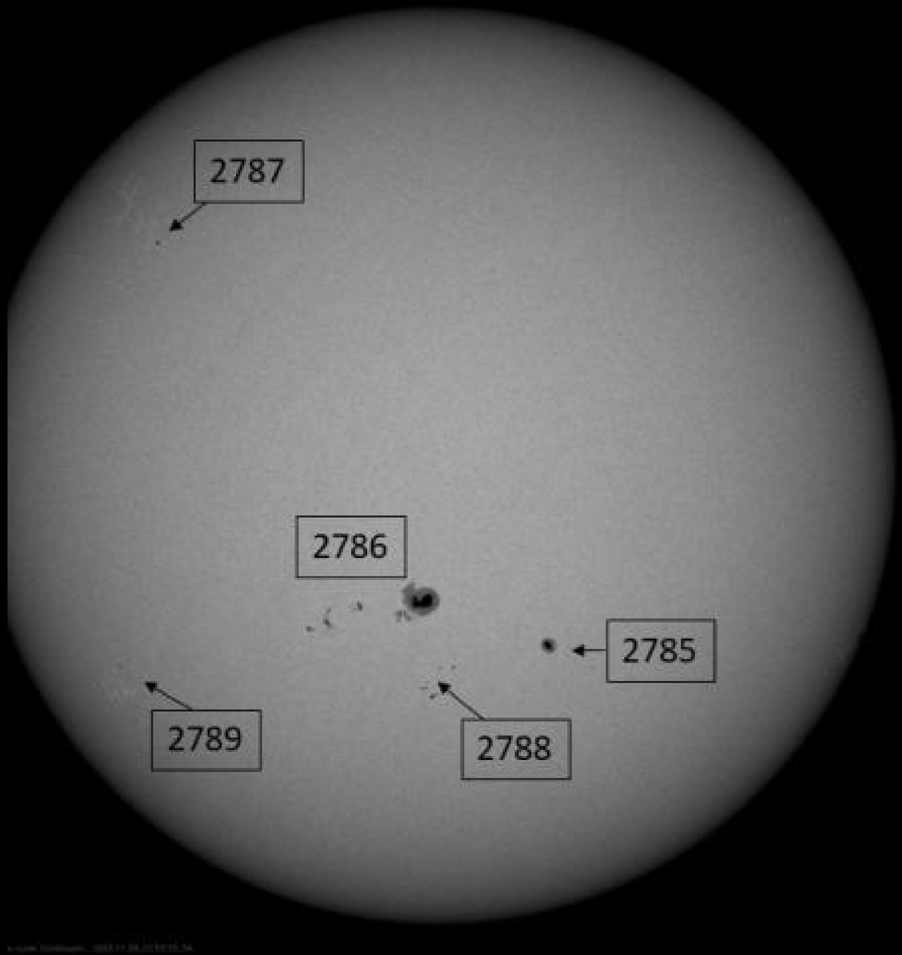

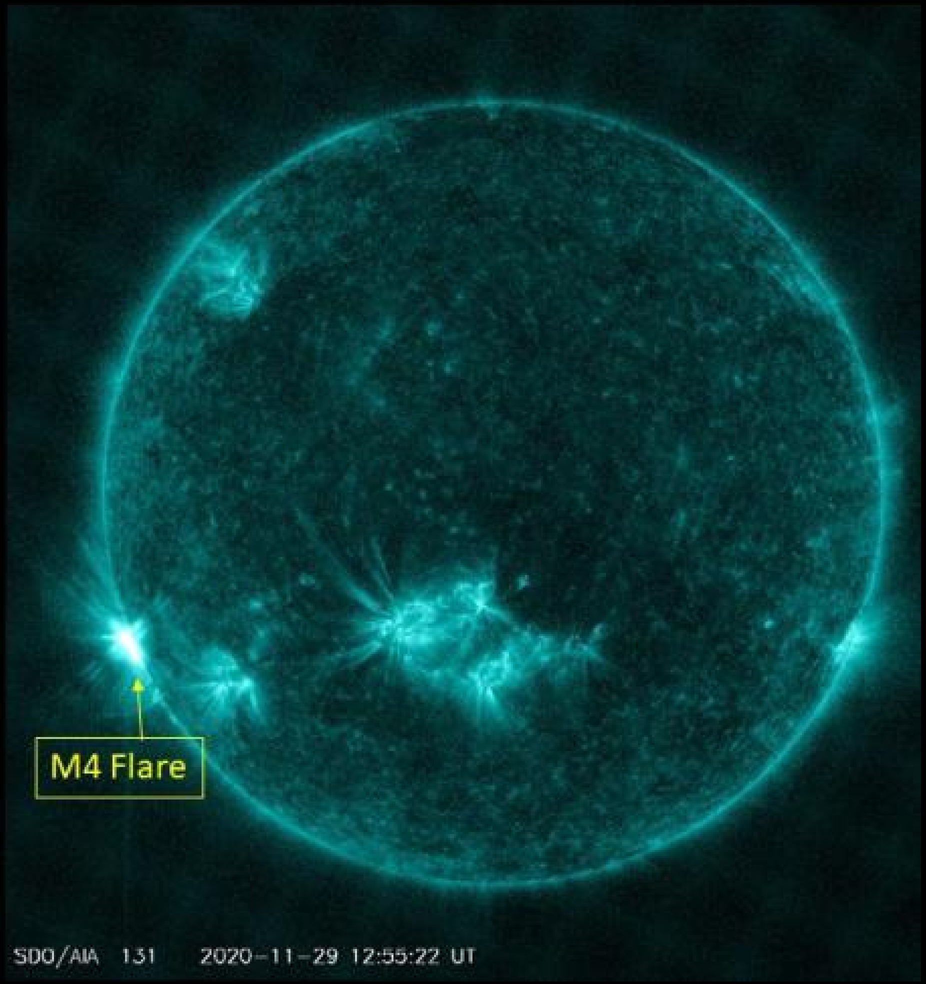

Solar activity picked up at the end of November into early December, 2020, as several sunspot groups emerged or rotated onto the visible disk. These areas of stronger, localized magnetic fields produced multiple C-class flares and even an M4 flare on November 29, 2020. This is not unusual as we are now in solar cycle 25. Solar activity is anticipated to slowly increase over the upcoming years towards the solar maximum peak around July, 2025.

[From URL: https://www.swpc.noaa.gov/news/solar-cycle-25-activity-update-nov-dec-2020
See also https://earthsky.org/space/nso-predicts-large-sunspot-thanksgiving-nov2020]

Dark magnetic filament bisecting sunspot AR2765 erupting on June 9th, 2020 at 18:00 UT.

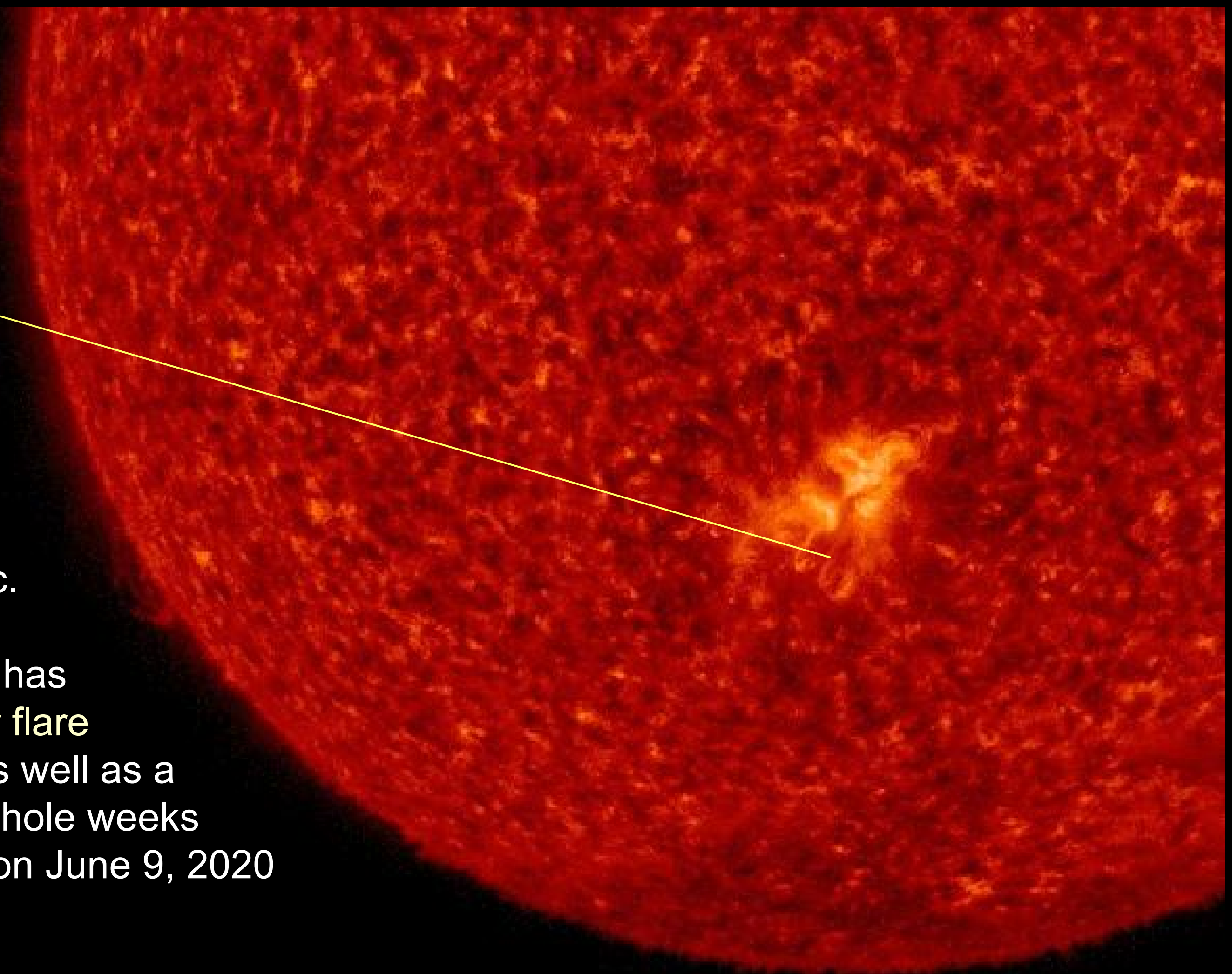

Solar Cycle 25 may have shown signs of life of late, but all is once again quite on the earth-facing solar disc.

During June, Solar Cycle 25 has produced the strongest solar flare in three years (M1-class), as well as a sunspot that lasted for two whole weeks (AR2765) that then erupted on June 9, 2020

[From URL: https://electroverse.net/solar-minimum-aint-over-yet/]

AIA 304 2020-06-09 17:18:18 UT

The Sun seems to be getting more and more active (see below).

Cosmic Ray Neutron Monitors, 1997

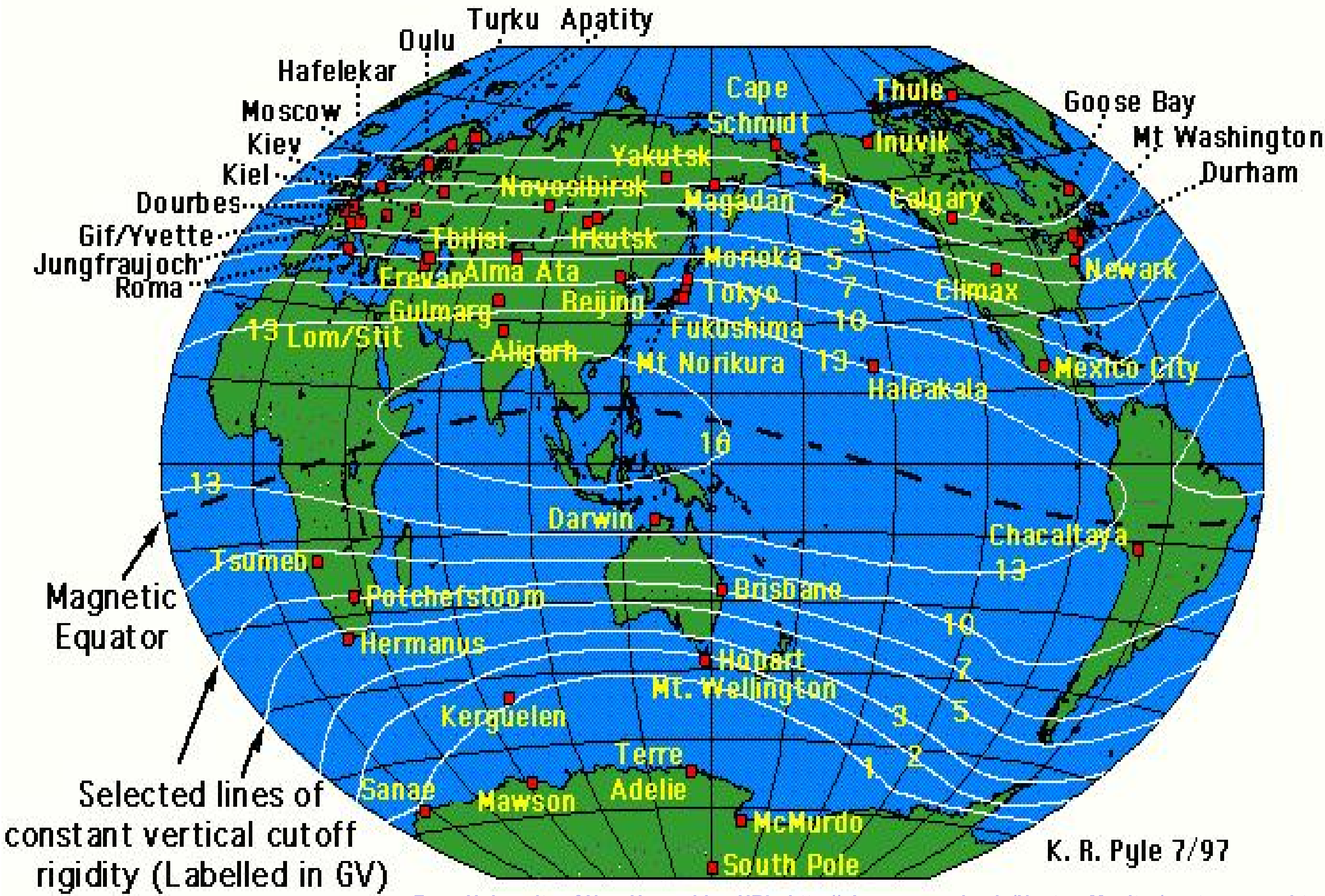

From University of New Hampshire, URL: http://ulysses.sr.unh.edu/NeutronMonitor/neutron_mon.html

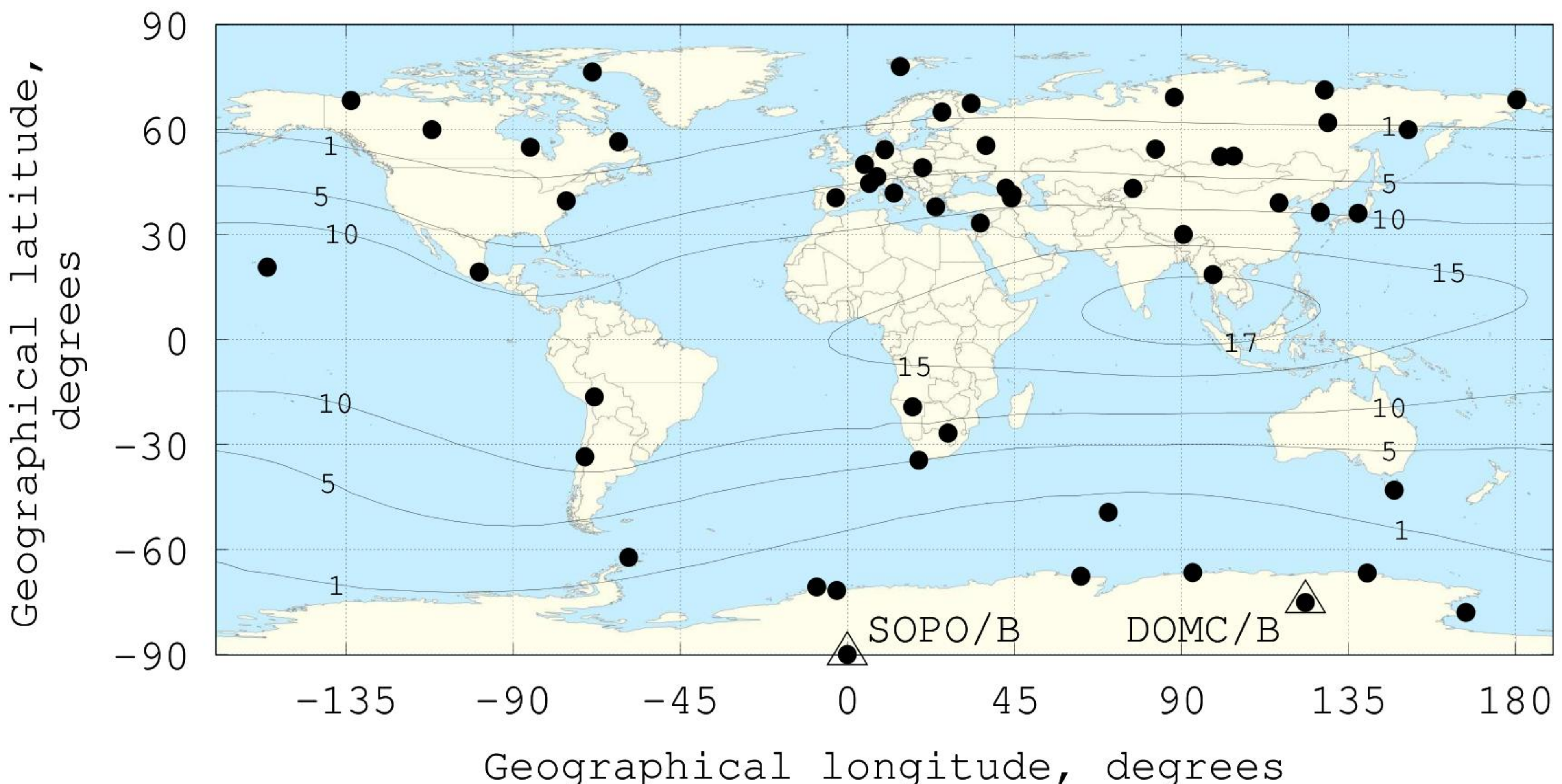

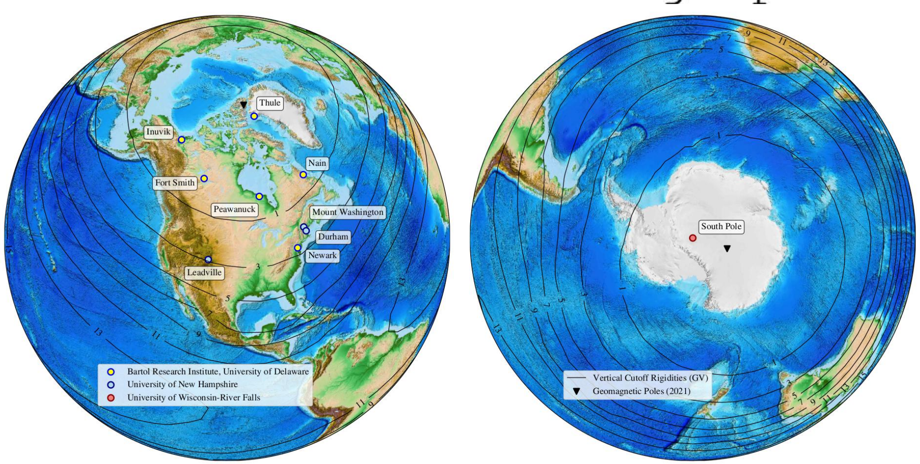

↑ Map of neutron monitors. Contours with numbers indicate the geomagnetic cutoff rigidities (in GV).

← Simpson Neutron Monitor Network, USA

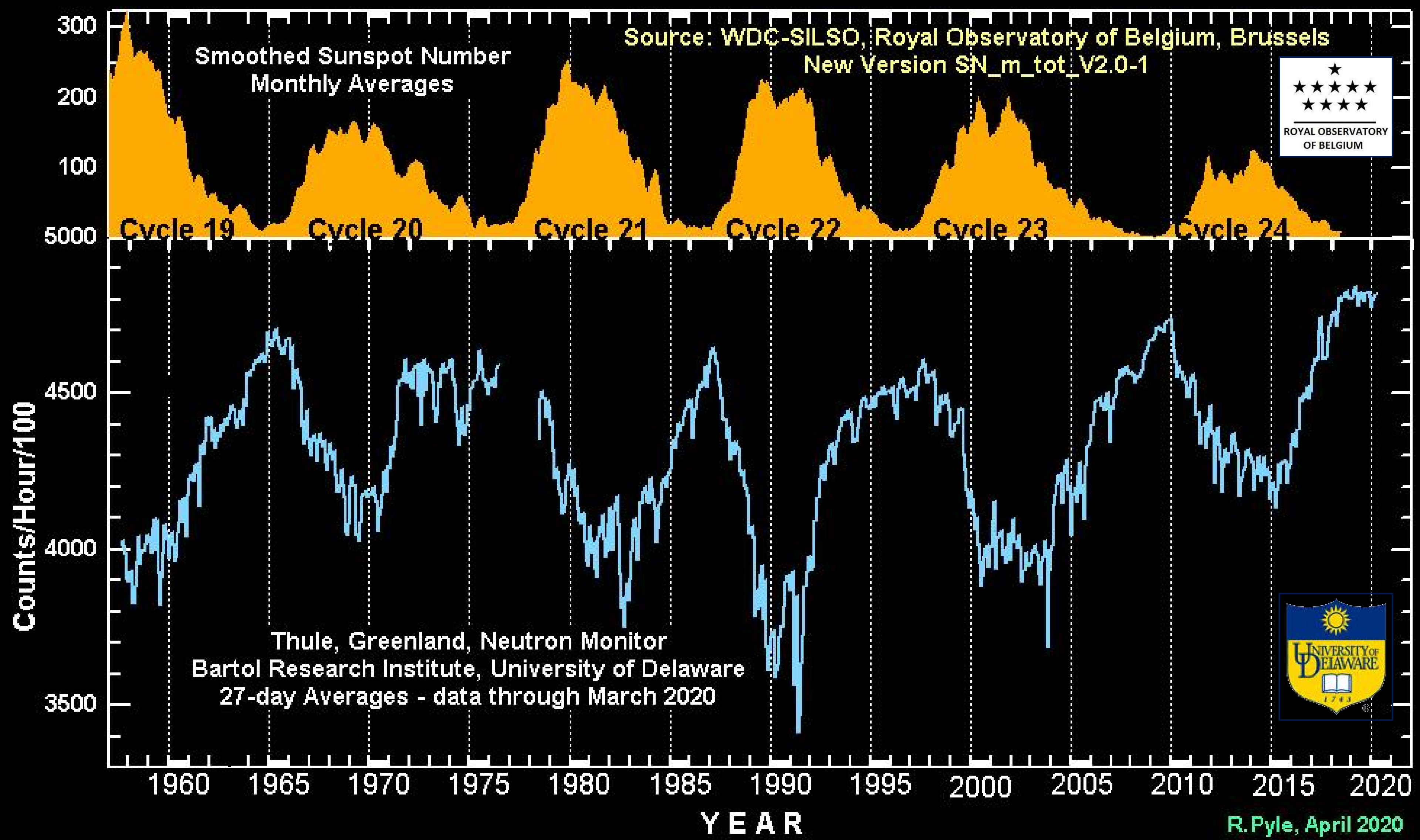

Solar modulation refers to the influence the Sun exerts upon the intensity of galactic cosmic rays. As solar activity rises (top panel, Source: WDC-SILSO Royal Observatory of Belgium, Brussels), the count rate recorded by a neutron monitor in Inuvik, Canada decreases (bottom panel, Source: Bartol Research Institute, University of Delaware, USA).

[From URL: http://neutronm.bartol.udel.edu/]

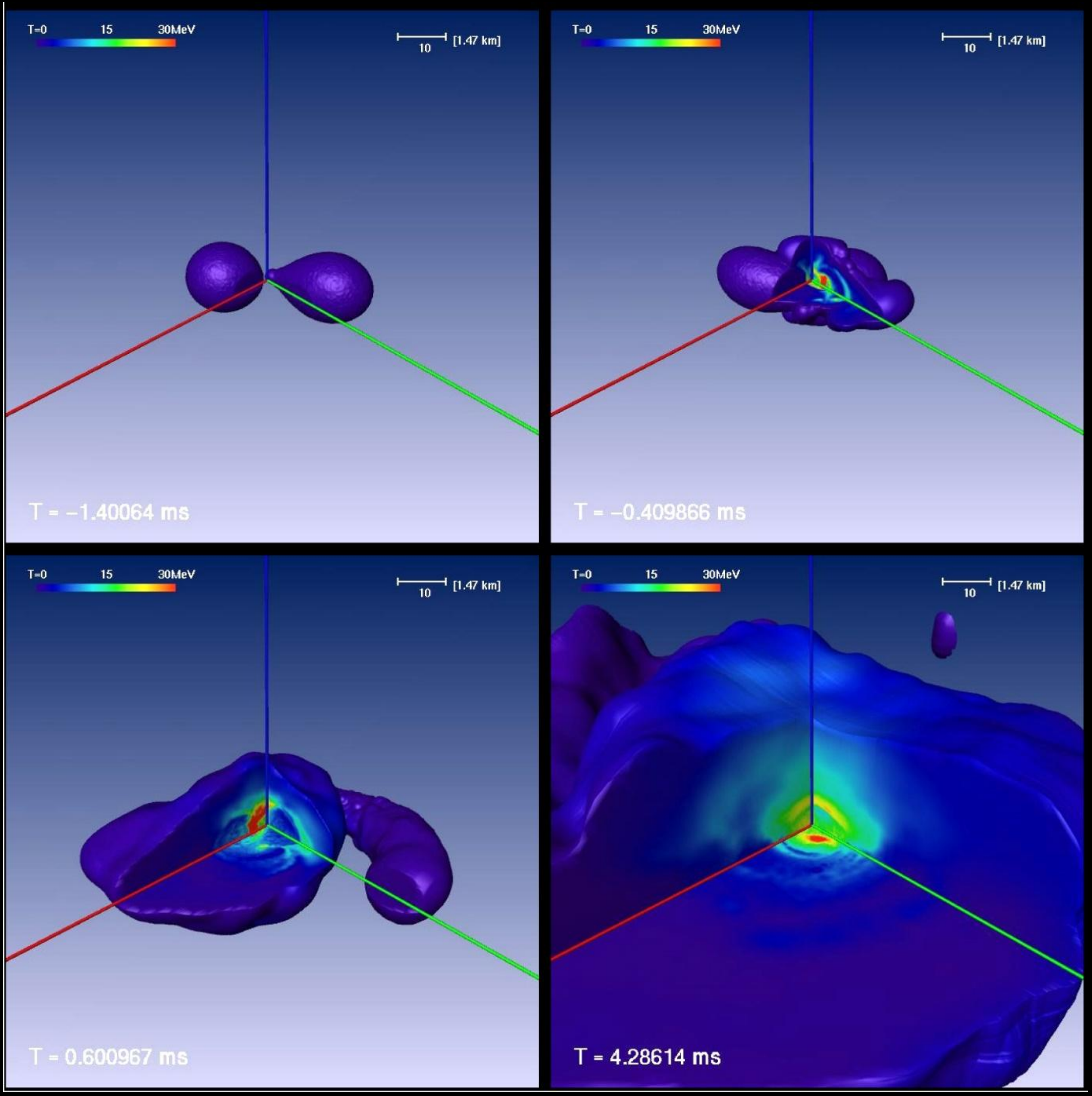

Four stages of the NS+NS merger Model S1216. The surface is chosen to correspond to a density of 10^{10} g/cm^3, the temperature distribution is visible color coded in the octant cut out from the 3-dimensional mass distribution. Temperatures up to 30 MeV are reached at the center only milliseconds after the two neutron stars have merged. Time is given in the lower left corner of the panels, and length is measured in units of 1.47 km (top right corner of each panel).

Upon colliding with each other, the two merging neutron stars heat up by shocks and compression to central temperatures of several 10 MeV. Within only a few milliseconds after the final plunge, the neutrino emission reaches luminosities of 10^{53} ergs/s or higher and the post-merger object should start losing mass in the neutrino-driven wind.

[**From** R. Oechslin and H.-Th. Janka, “Torus formation in neutron star mergers and well-localized short gamma-ray bursts,” astro-ph/0507099 (accepted by MNRAS).]

The Morris and Podsiadlowski model almost perfectly reproduces not only the main features of the triple-ring nebula but also the small asymmetries of the outer rings.

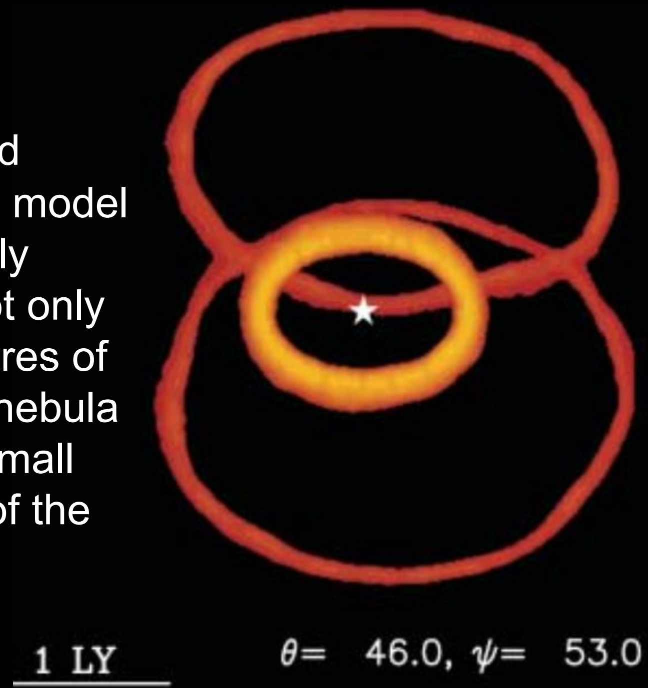

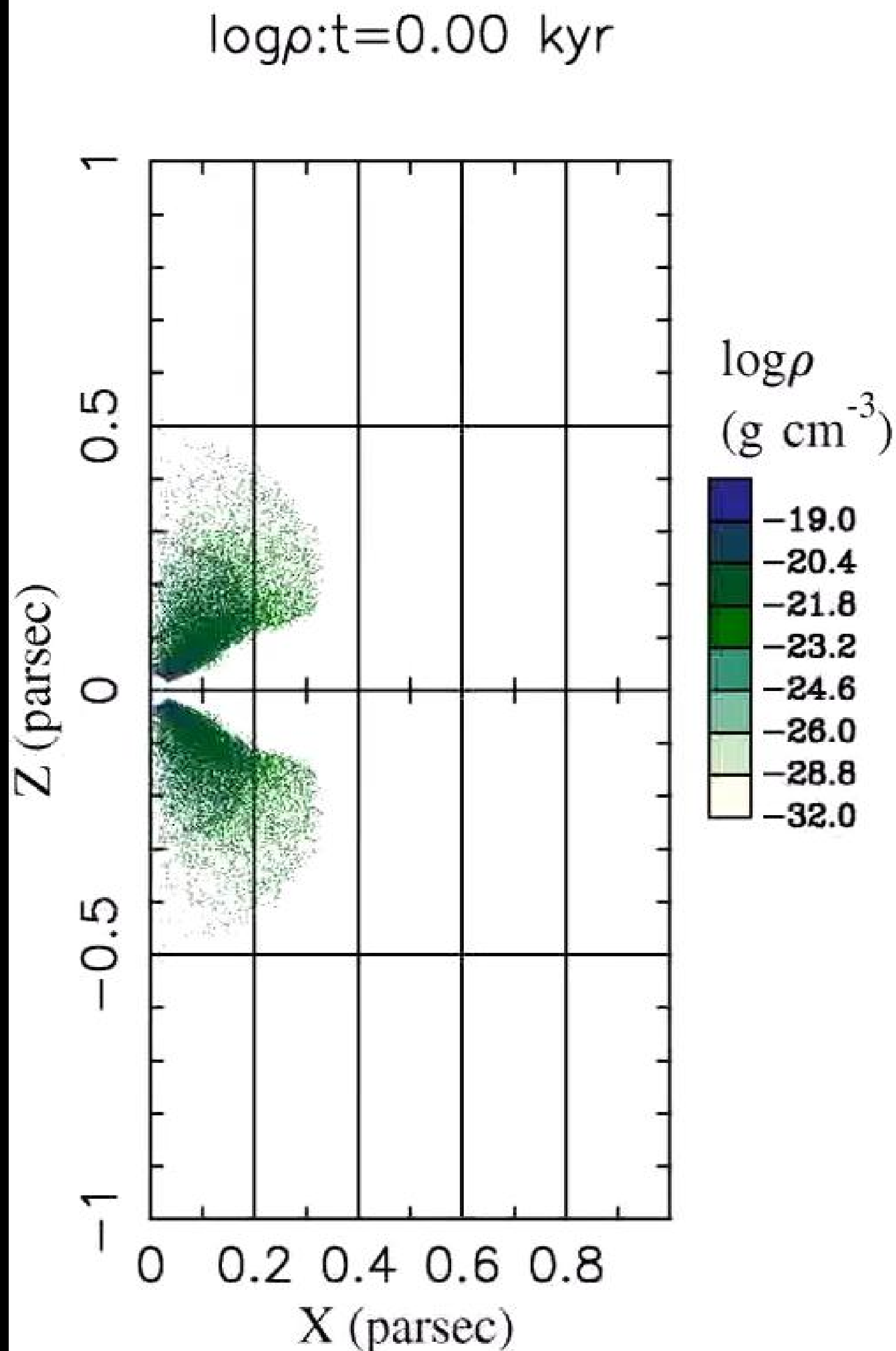

The movie shows the formation of the triple-ring nebula as a result of the interaction of the blue-supergiant wind (grey particles) with the matter ejected in the merger phase (green/blue particles). The color of the ejecta particles indicates the logarithm of the mass density in units of g/cm^3 (see scale bar). The spatial scale is in units of **pc**.

[**Reference**: T. Morris and Ph. Podsiadlowski, "The Triple-Ring Nebula around SN1987A: Fingerprint of a binary merger," Science **315** (2007) 1103-1106, astro-ph/0703317.]

Rotating, magnetized neutron star at the heart of the Crab Nebula (artist's conception).

Contribution of nearby Pulsars to CR observed at Earth

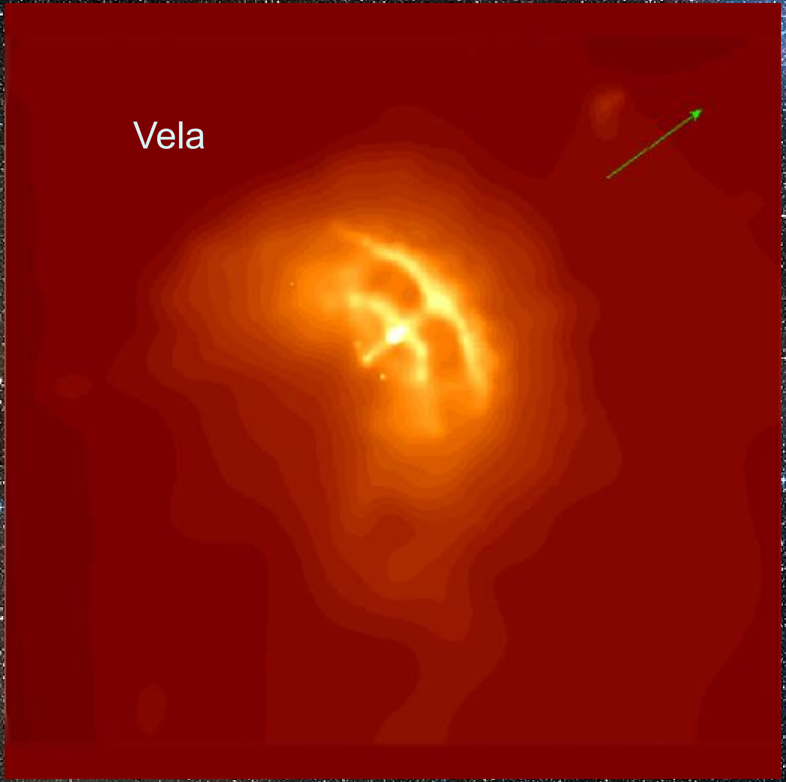

Vela (X-ray image) was found by SAS-2 as the brightest object in the gamma-ray sky. It is comparatively close to the Earth and so the surrounding nebula is well studied. Its characteristic age is around 10,000 years with periodicity P = 89.3 ms, slow down rate is $dP/dt = 1.25\times10^{-13}$, and the surface magnetic field is around 3.4×10^{12} Gauss. The distance of the object from the Earth is around 500 pc though recent works suggest a smaller value of 300 pc.

[From http://heasarc.gsfc.nasa.gov/]

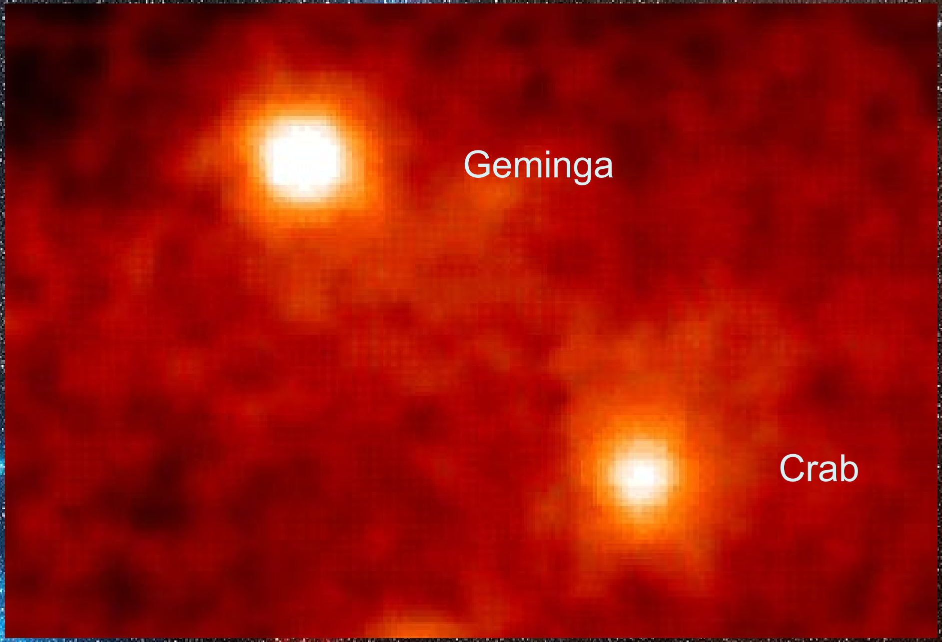

Geminga or PSR J0633+1746 (Gamma-ray image) discovered by the SAS-2 group and later confirmed by the COS-B group, about 150 pc away from the Earth. Its radial velocity is unknown, but if it were 200 km/s, it could have been within 100 pc of Earth at 340,000 years ago. Geminga is a unique object: a highly compressed, spinning neutron star which does not emit radio waves like the other well-known pulsars. Yet it is a powerful source of pulsating gamma-rays and X-rays. Geminga is now known to be a rotation-powered pulsar with period P = 0.237 s, $dP/dt = 1.0975\times10^{-14}$, and surface magnetic field $B = 1.6\times10^{12}$ Gauss.

[From http://antwrp.gsfc.nasa.gov/]

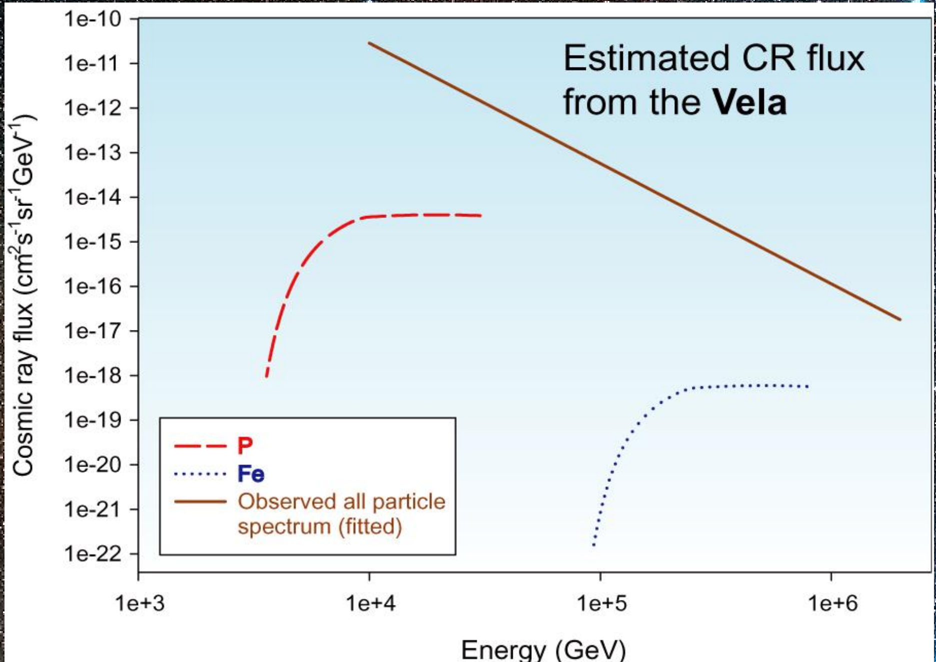

The maximum energy estimated:
~3Z×10^{13} eV.

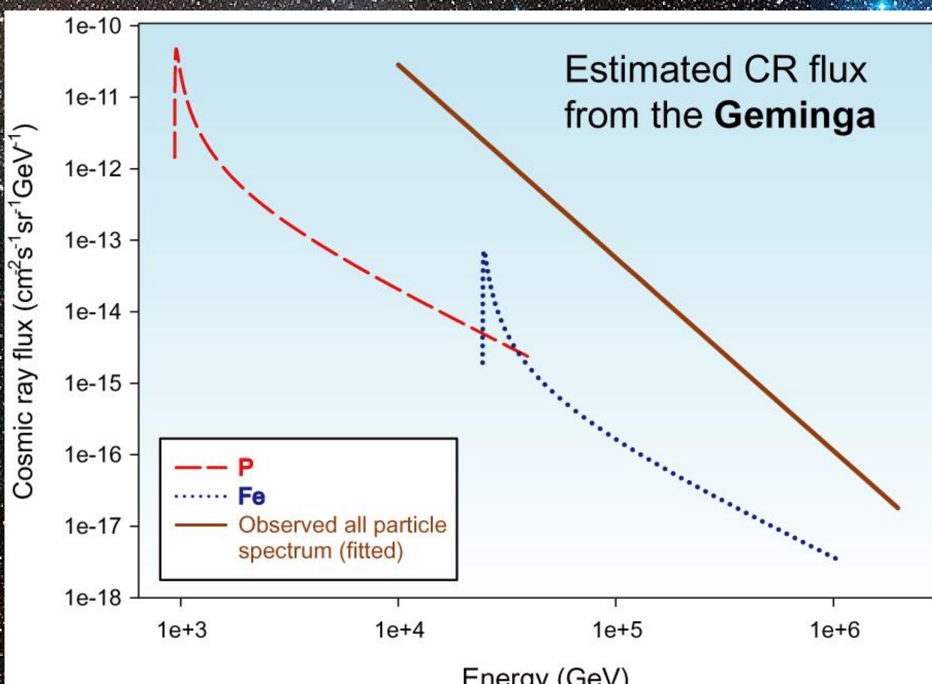

The maximum energy estimated:
~4Z×10^{13} eV.

Background: The rich region of sky around the young open star cluster NGC 2547 in the southern Constellation of Vela (The Sail).

Image: ESO/Digitized Sky Survey 2

[**Reference:** A. Bhadra, “Contribution of a nearby pulsar to cosmic rays observed at Earth,” Astropart. Phys. 25 (2006) 226-232 (astro-ph/0602301).]

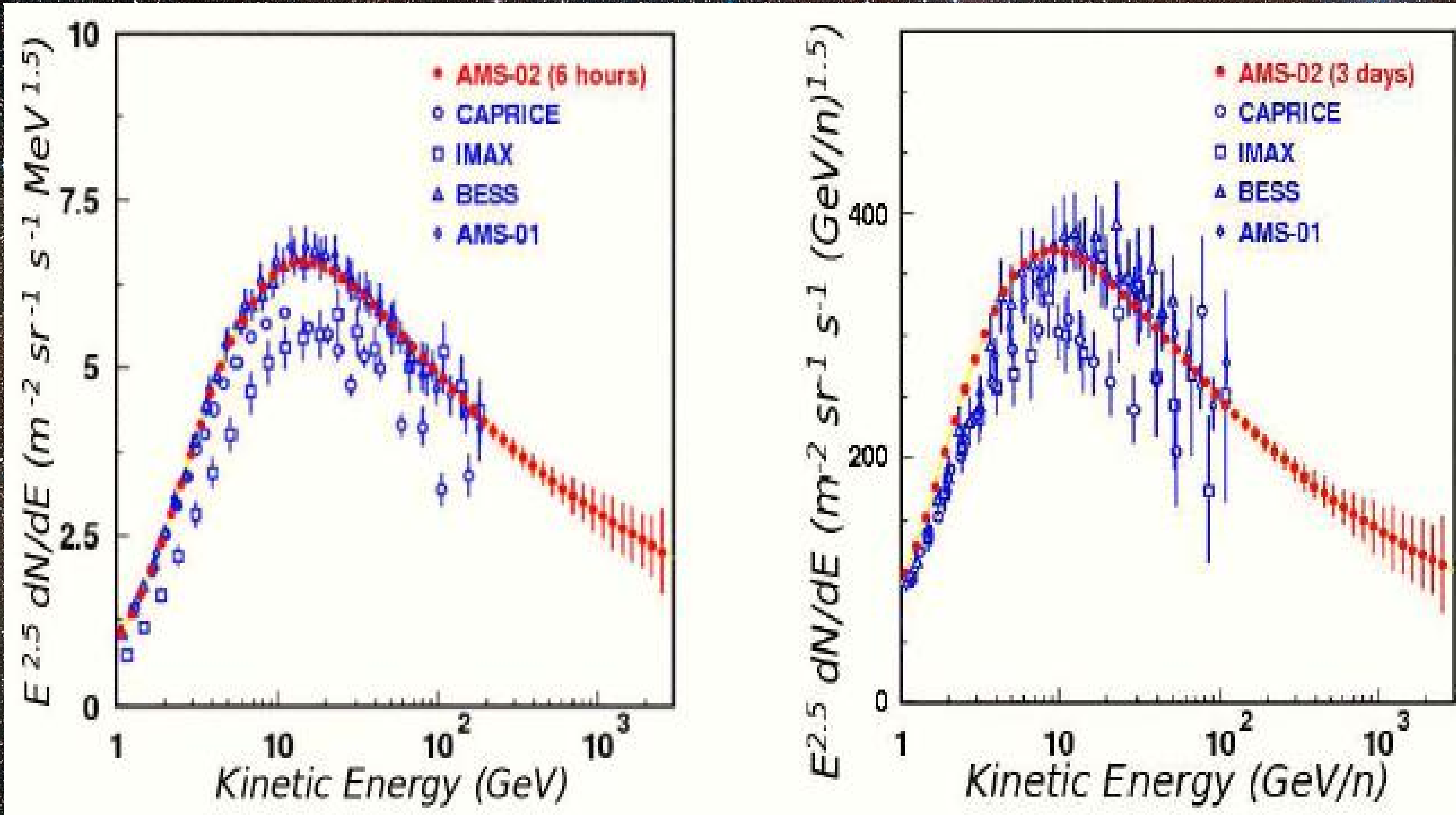

CR proton (**left panel**) and helium (**right panel**) flux measurements are compared to the expected AMS-02. A two-phases cylindrical model of the Galaxy has been used to simulate the propagation of protons and helium nuclei in the interstellar medium where they diffuse for roughly **2×10^7** years. These nuclei are the dipest charged probes of the Galaxy since they diffuse on the average through **one third** of the Galactic disk and in the halo before being measured.

[Reference: D. Casadei (for the AMS Collaboration), "Cosmic ray astrophysics with AMS-02," astro-ph/0404529.**]**

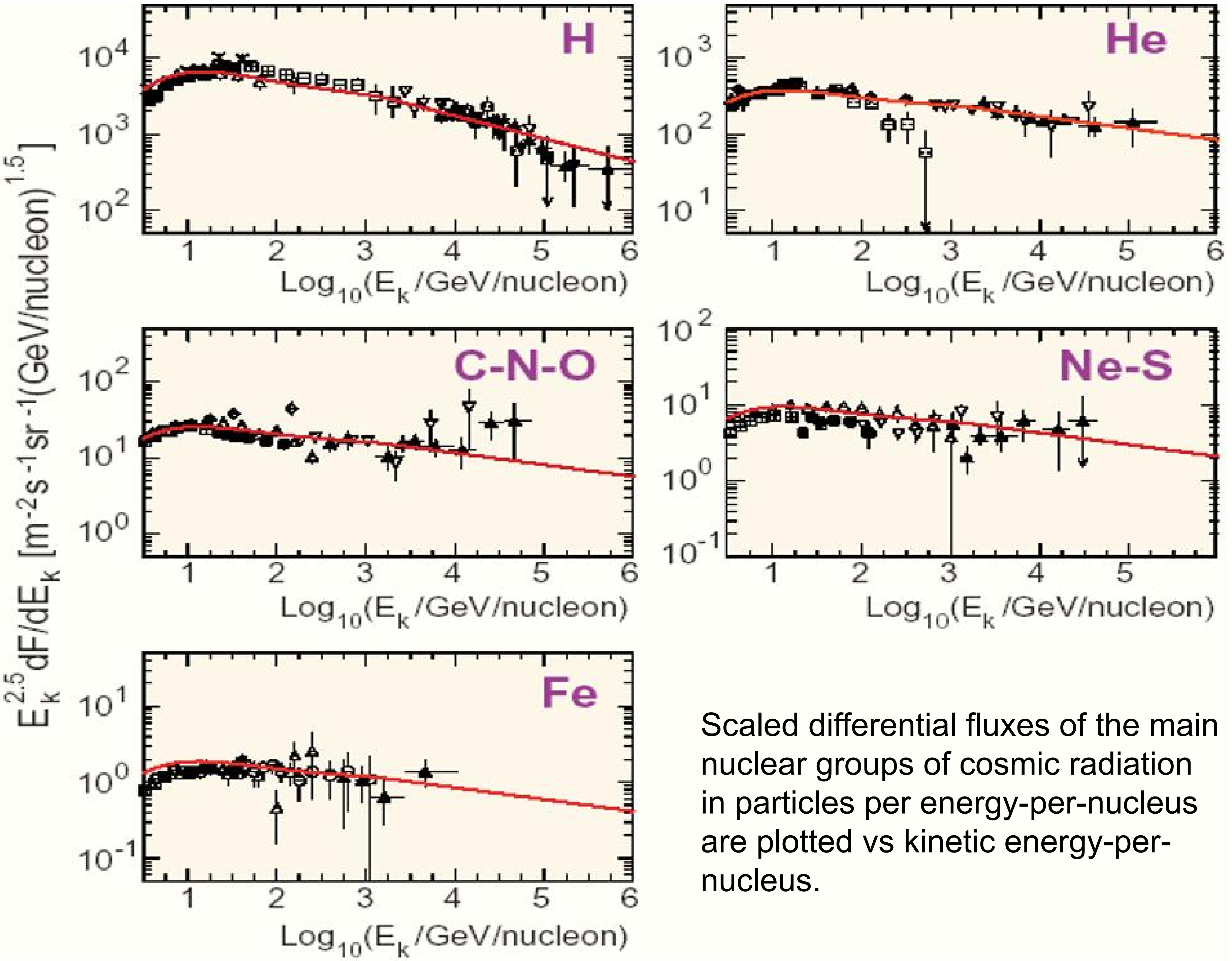

Scaled differential fluxes of the main nuclear groups of cosmic radiation in particles per energy-per-nucleus are plotted vs kinetic energy-per-nucleus.

Low and intermediate energy part of the CR spectrum for the main nuclear groups

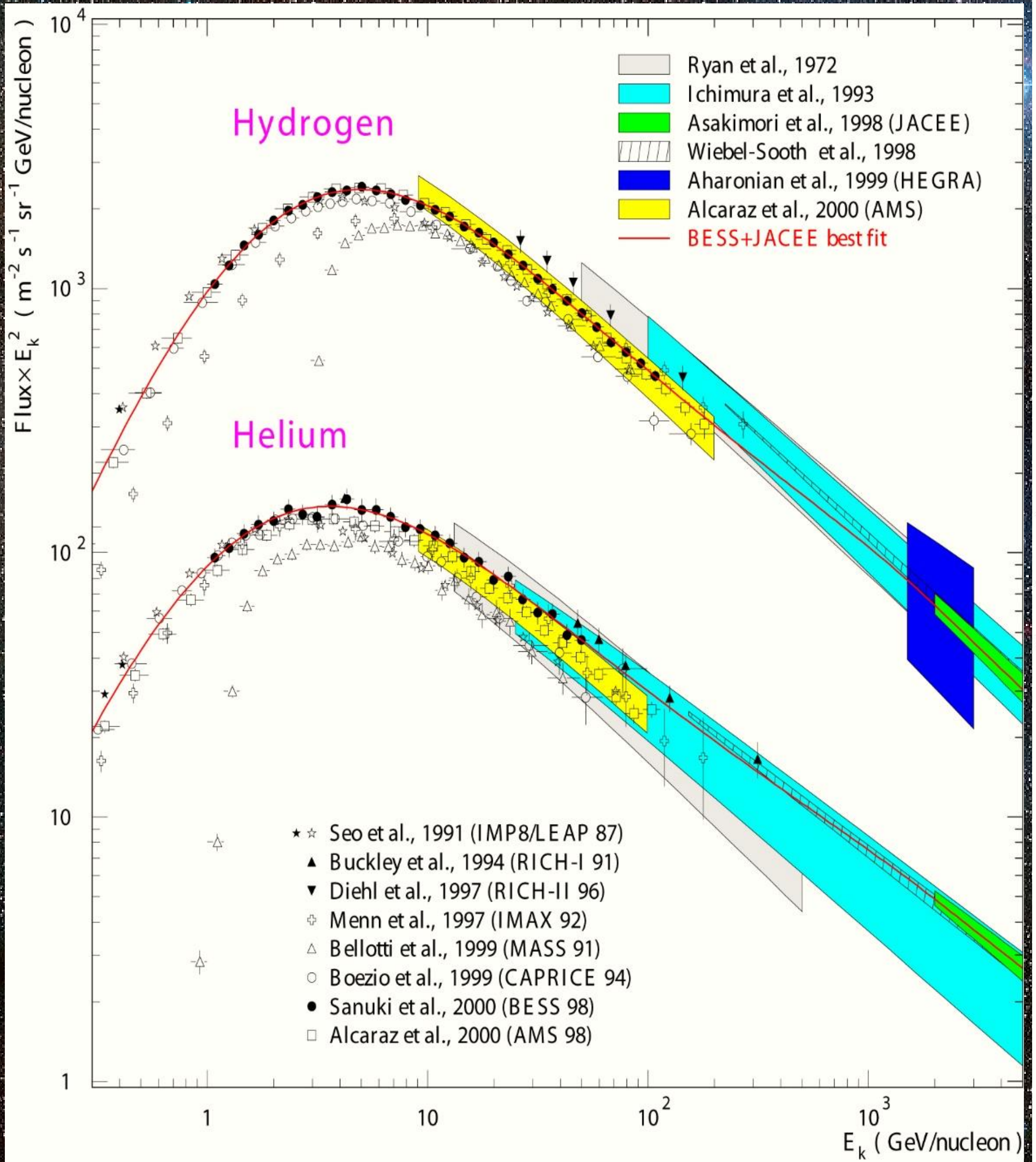

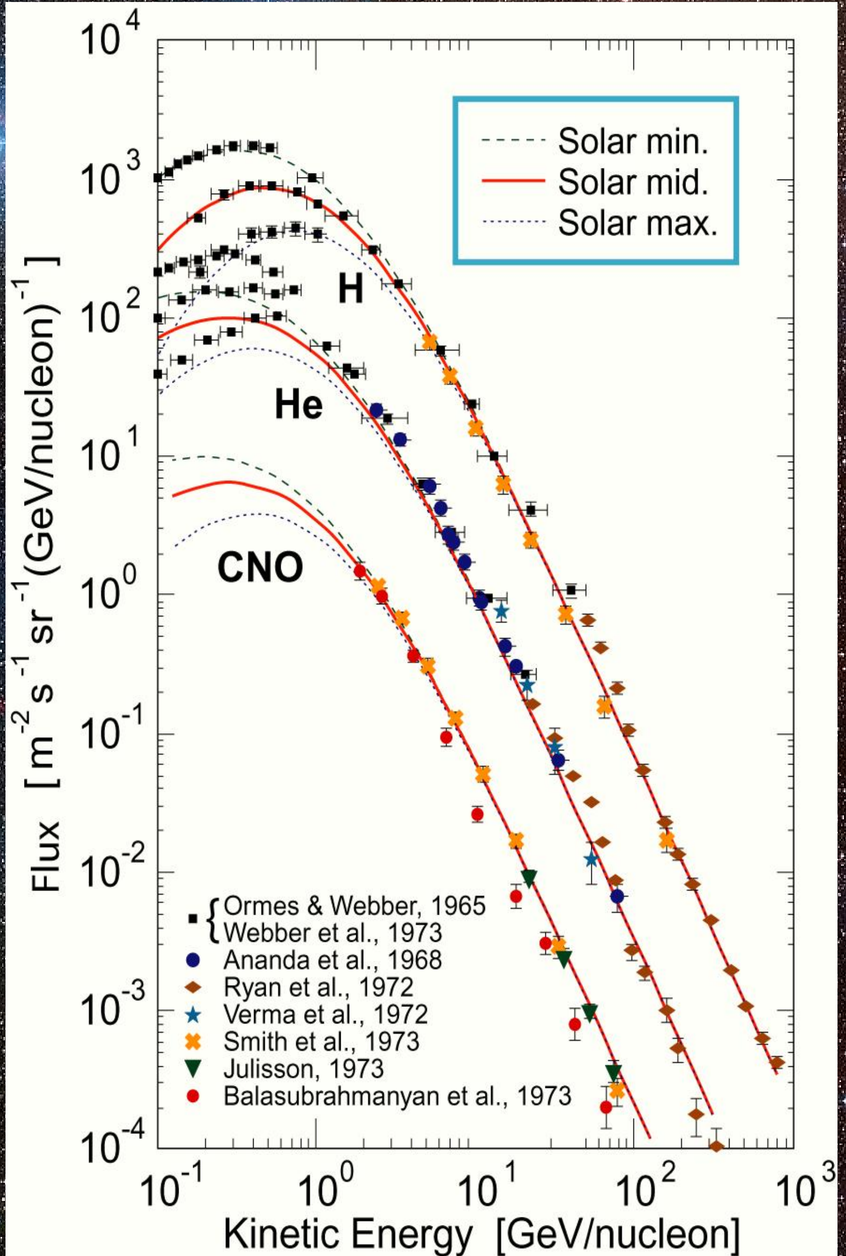

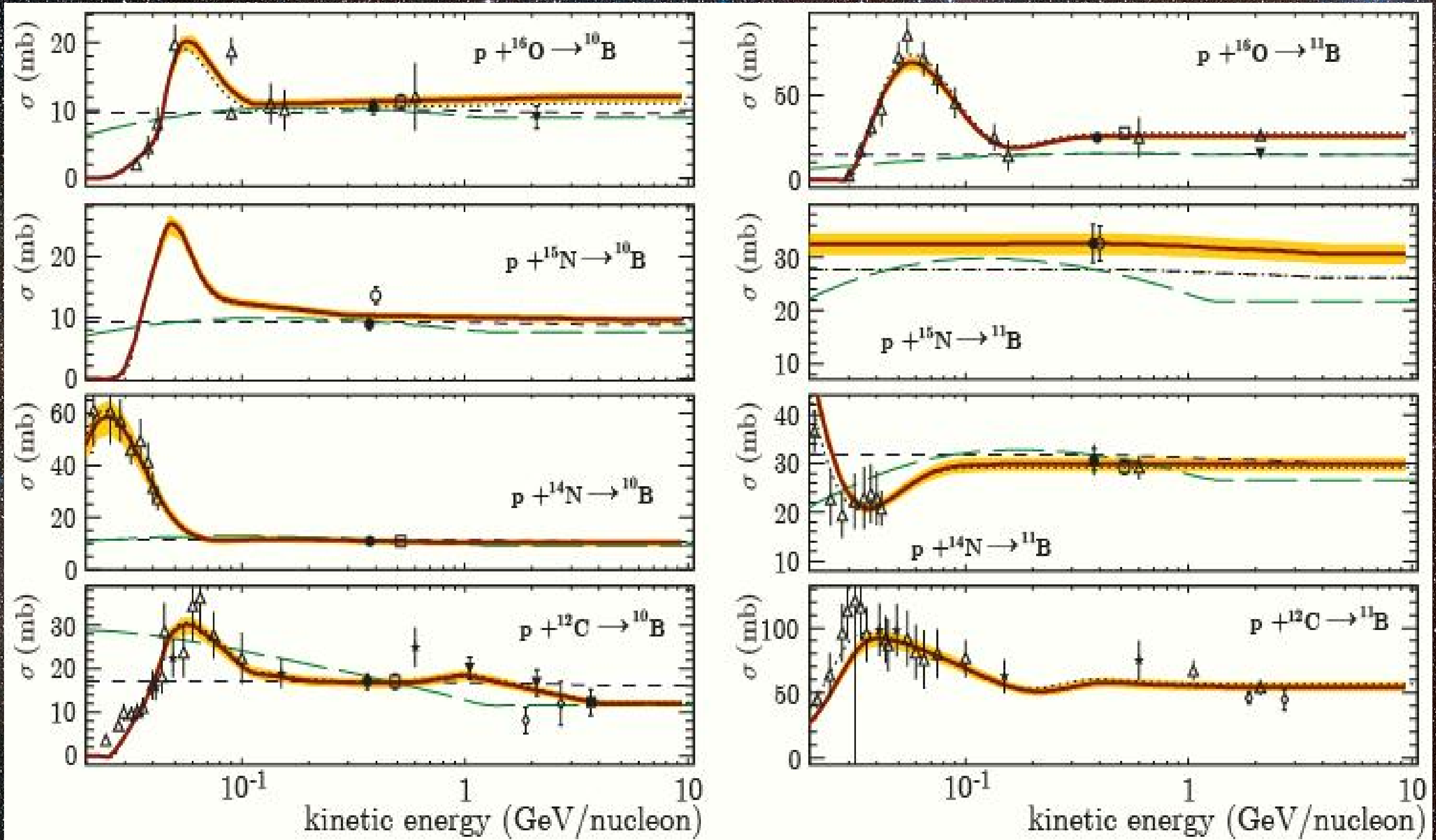

Fragmentation cross sections for B isotopes production from B-C-N-O collisions off hydrogen. The lines are from the WNEW (short-dashed), YIELDX (long-dashed), GALPROP (dotted), and cross sections by Tomassetti (thick solid lines) with their uncertainty band. These and other cross sections were used for calculationsof the B/C and Be/B ratios shown in next slide.

[**Reference**: N.Tomassetti, "Examination of uncertainties in nuclear data for cosmic ray physics with the AMS experiment," arXiv:1509.05776v2 [astro-ph.HE].]

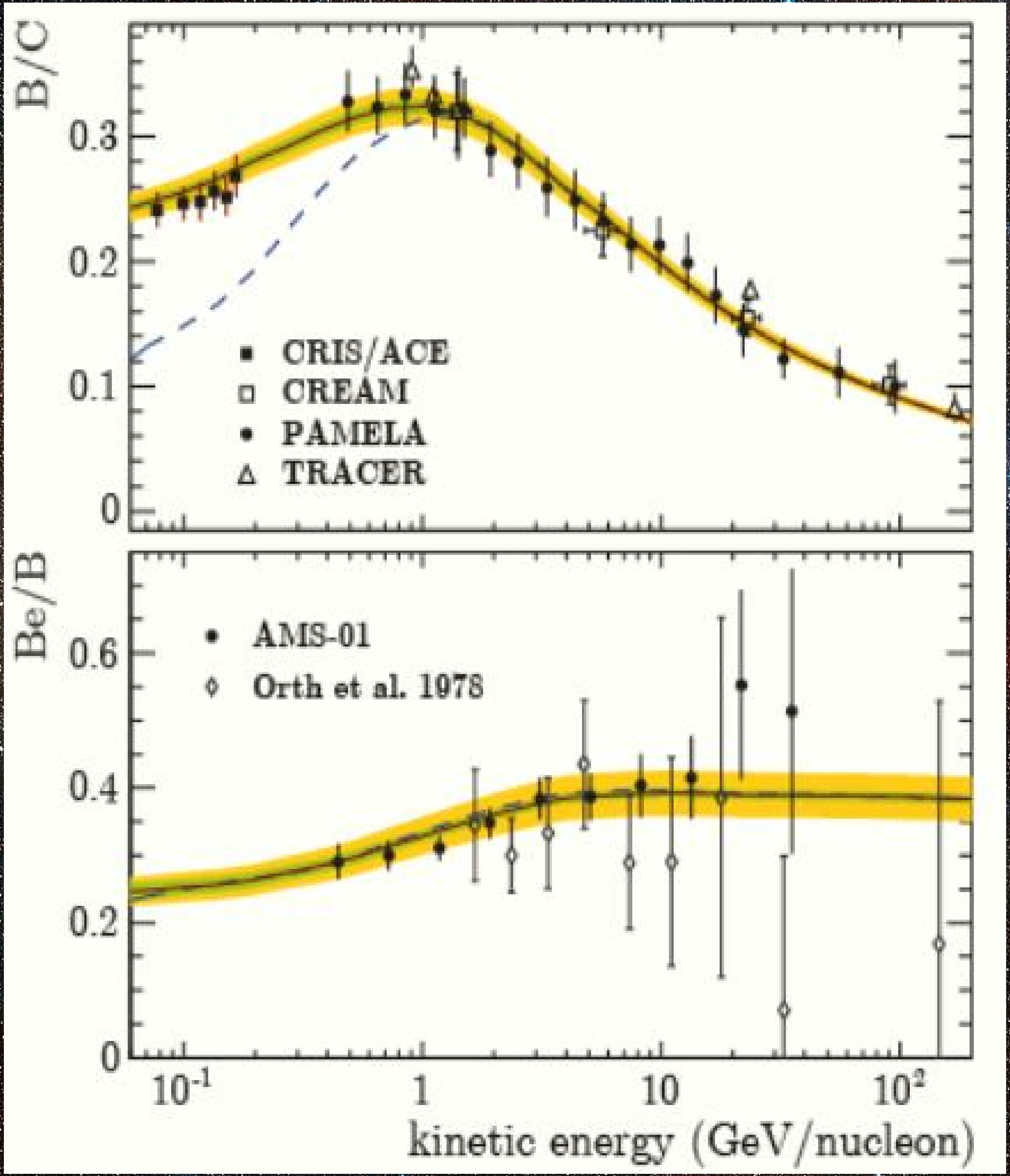

Elemental ratios from the reference Model by Tomassetti in comparison with the data.

The yellow bands are the estimated nuclear uncertainties (see previous slide and the original paper cited there). The green bands reflect the estimated parameter uncertainties for the anticipated AMS data.

The calculations by Tomassetti show that the AMS experiment can provide tight constraints on the key parameters of propagation models.

Reference	Instrument	He events	Rigidity (GV)	$\overline{\text{He}}/\text{He}$ 95% limit
Smoot *et al* (1975)	Balloon Supercond. magnet	1.5×10^4	4–33 33–100	5×10^{-4} 2×10^{-2}
Badhwar *et al* (1978)	Balloon Supercond. magnet	1.7×10^4	4–10 33–100	1.7×10^{-4} 10^{-2}
Buffington *et al* (1981)	Balloon No magnet		1–1.8	2.2×10^{-5}
Alcaraz *et al* (1999)	Space shuttle Permanent magnet	2.86×10^6	1–140	1.1×10^{-6}
Sasaki *et al* (2001)	Balloon Supercond. magnet	$>6.6 \times 10^6$	1–14	0.7×10^{-6}

Antihelium search results. The last column gives the antihelium to helium flux ratio at 95% confidence level.

[**Reference:** Yu.V. Galaktionov, "Antimatter in cosmic rays", Rep. Prog. Phys. **65** (2002) 1243—270.]

Isotopic Composition

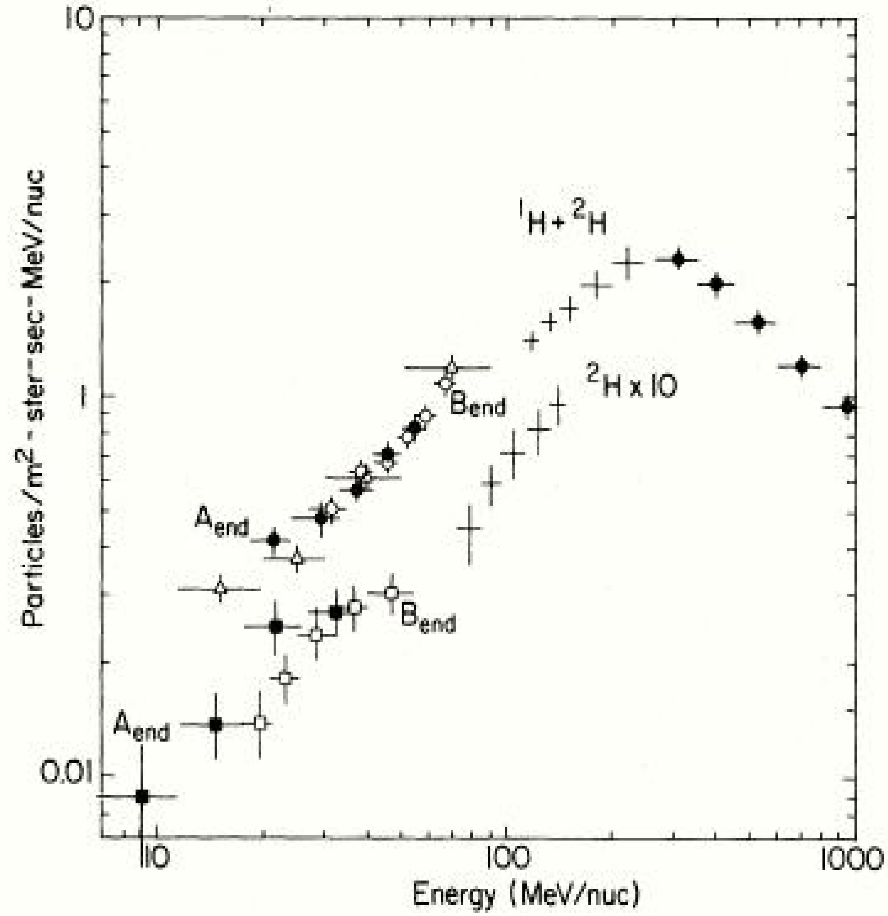

Kinetic-energy spectra of ^{1}H and ^{2}H obtained from balloon and spacecraft (Voyager) experiments at sunspot minimum modulation conditions in 1977.

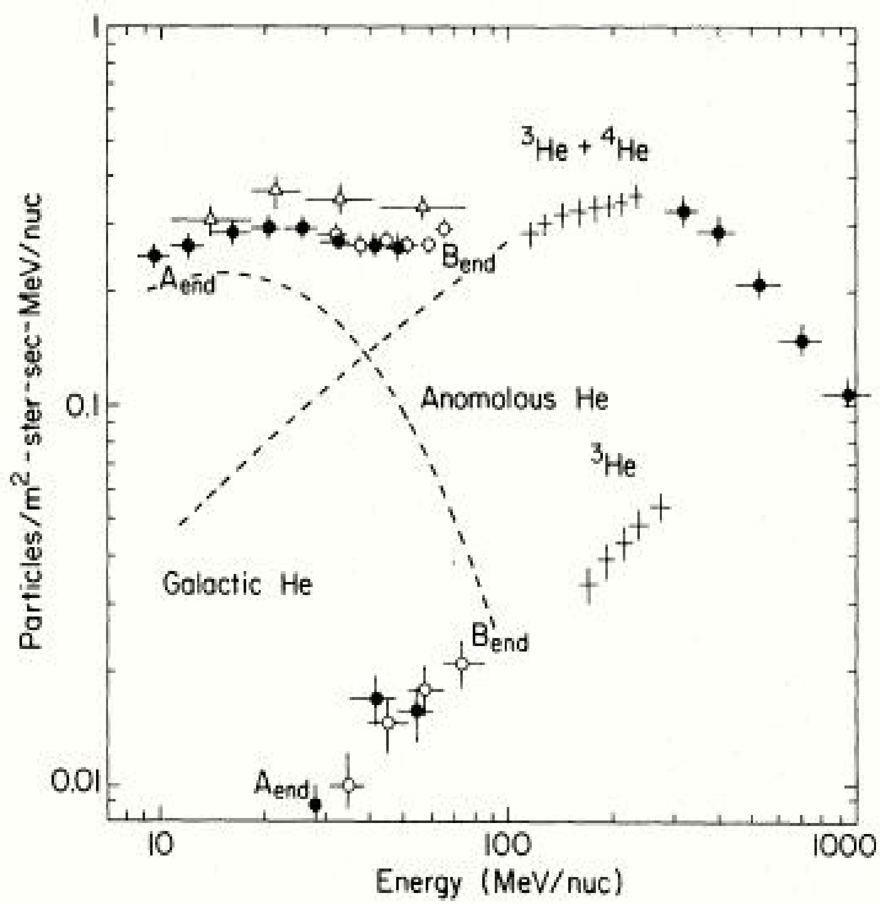

Kinetic-energy spectra of ^{3}He and ^{4}He obtained from the same experiments. Estimated magnitude of anomalous He component and galactic He are shown by dashed lines at low energies.

In both panels, the data points designated by triangles are from Bastian et al. (1979) for a similar time period.

[**Reference**: W.R. Webber & S.M. Yushak, ApJ **275** (1983) 391—404]

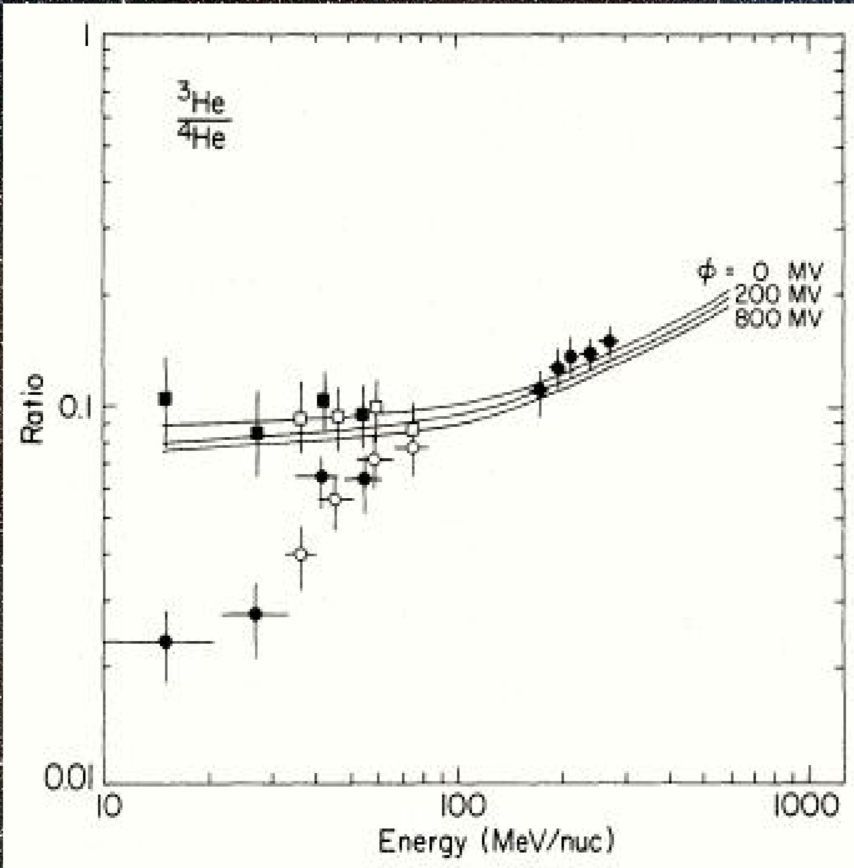

The ^{3}He/^{4}He ratios measured as a function of kinetic energy in the balloon and spacecraft experiments. Predictions of an interstellar propagation model for various values of the modulation parameter are shown as solid lines. Corrections to the ^{3}He/^{4}He ratios for the presence of anomalous ^{4}He are shown by open and solid squares.

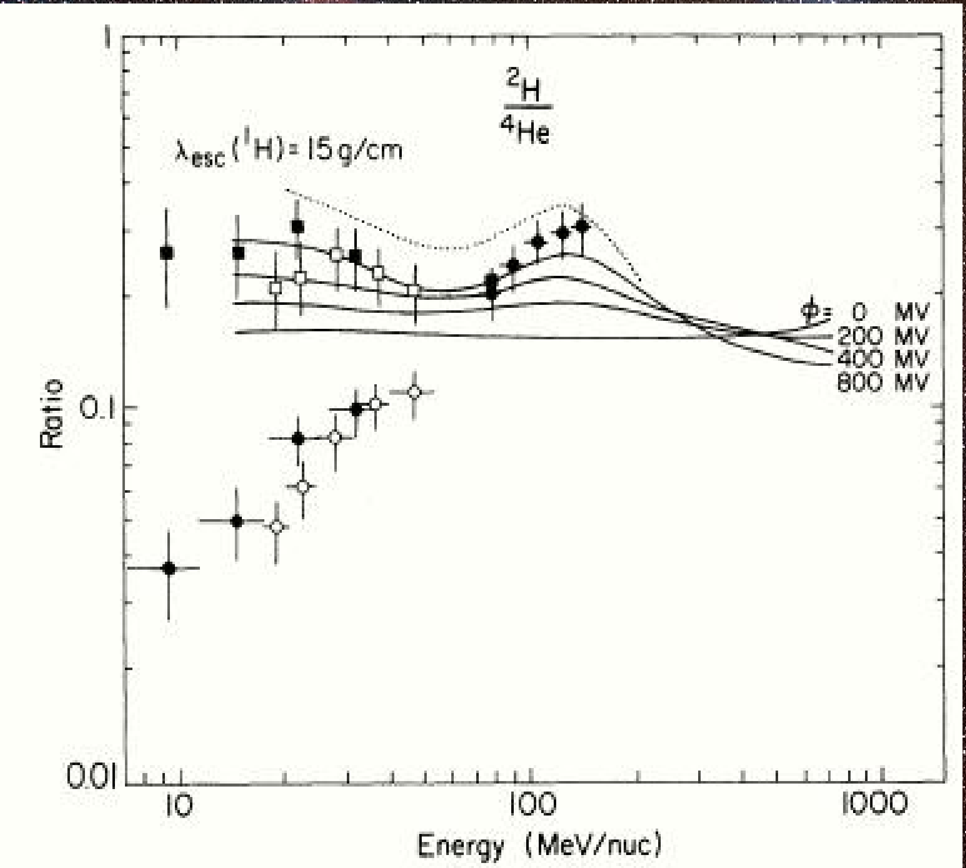

Measured ^{2}H/^{4}He ratios at low energies and predictions based on the same interstellar propagation model and local modulation as for He. Ratios corrected for anomalous ^{4}He are shown by open and solid squares at low energies.

[**Reference**: W.R. Webber & S.M. Yushak, ApJ **275** (1983) 391—404.]

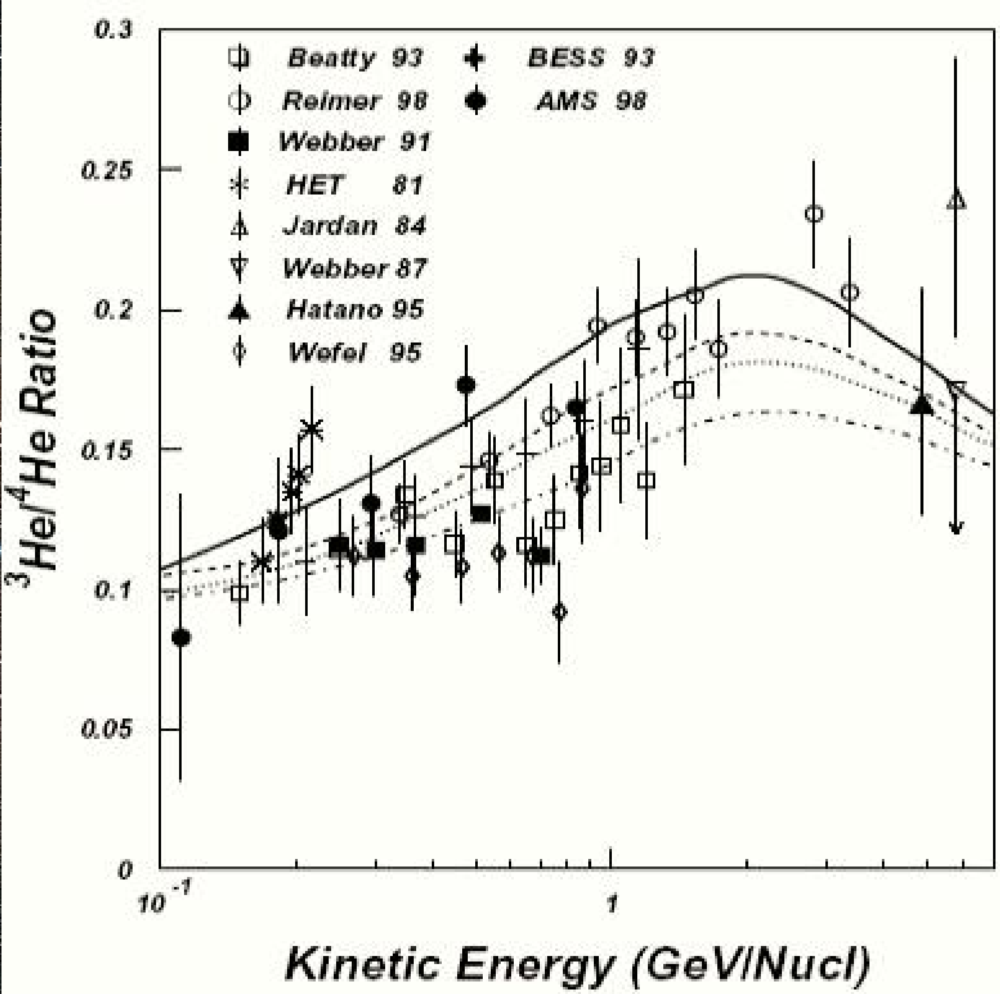

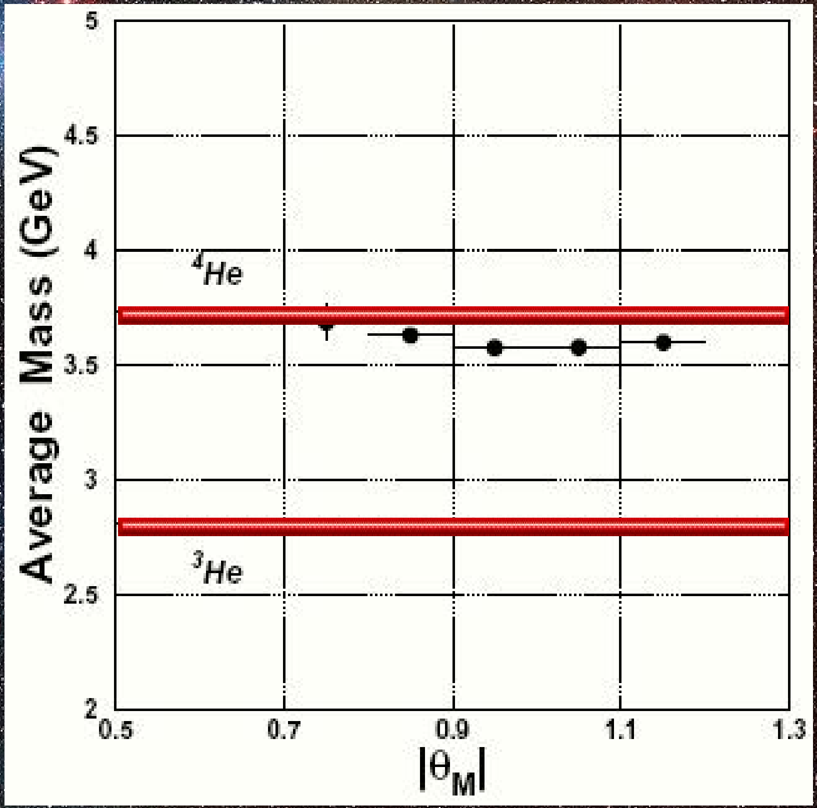

The $^3He/^4He$ ratios with measured in different experiments. The model predictions for various solar modulation levels are also shown with solid (φ = 0.35 GV), dashed (φ = 0.5 GV), dot line (φ = 1.0 GV), and dot-dashed (φ = 1.5 GV) lines.

The dependence of average helium mass on the geomagnetic latitude measured with AMS.

[**Reference**: Z. Xiong et al., JHEP **11** (2003) 048.]

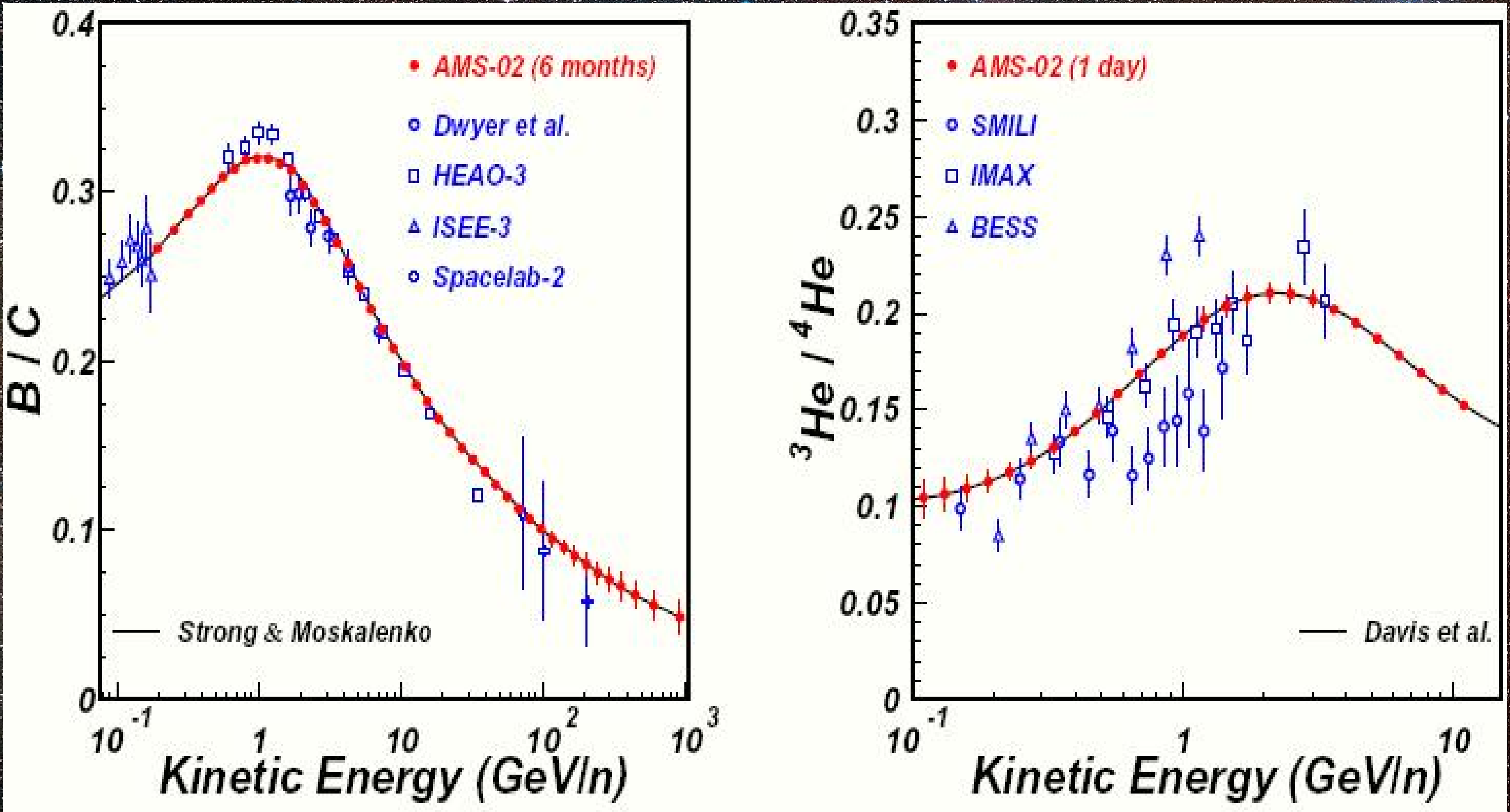

AMS-02 expected performance on **B/C** ratio (**left panel**) after six months of data taking and **$^3He/^4He$** ratio (**right panel**) after one-day of data taking compared to recent measurements. The **B/C** ratio was simulated according to a ***diffuse-reacceleration model*** (Strong & Moskalenko, 2001) with Alfvèn speed v_A **= 20 km/s**, propagation region bounded by a galactocentric radius R_h **= 30 kpc**, distance from the galactic plane z_h **= 1 kpc**. The **$^3He/^4He$** ratio has been simulated according to the classical cosmic-ray transport ***Leaky Box Model*** with a rigidity dependent path-length distribution (Davis et al, 1995).

[**Reference**: G. Lamanna, "Astrophysics and particle physics in space with the Alpha magnetic spectrometer," Mod. Phys. Lett. A **18** (2003) 1951—1966.]

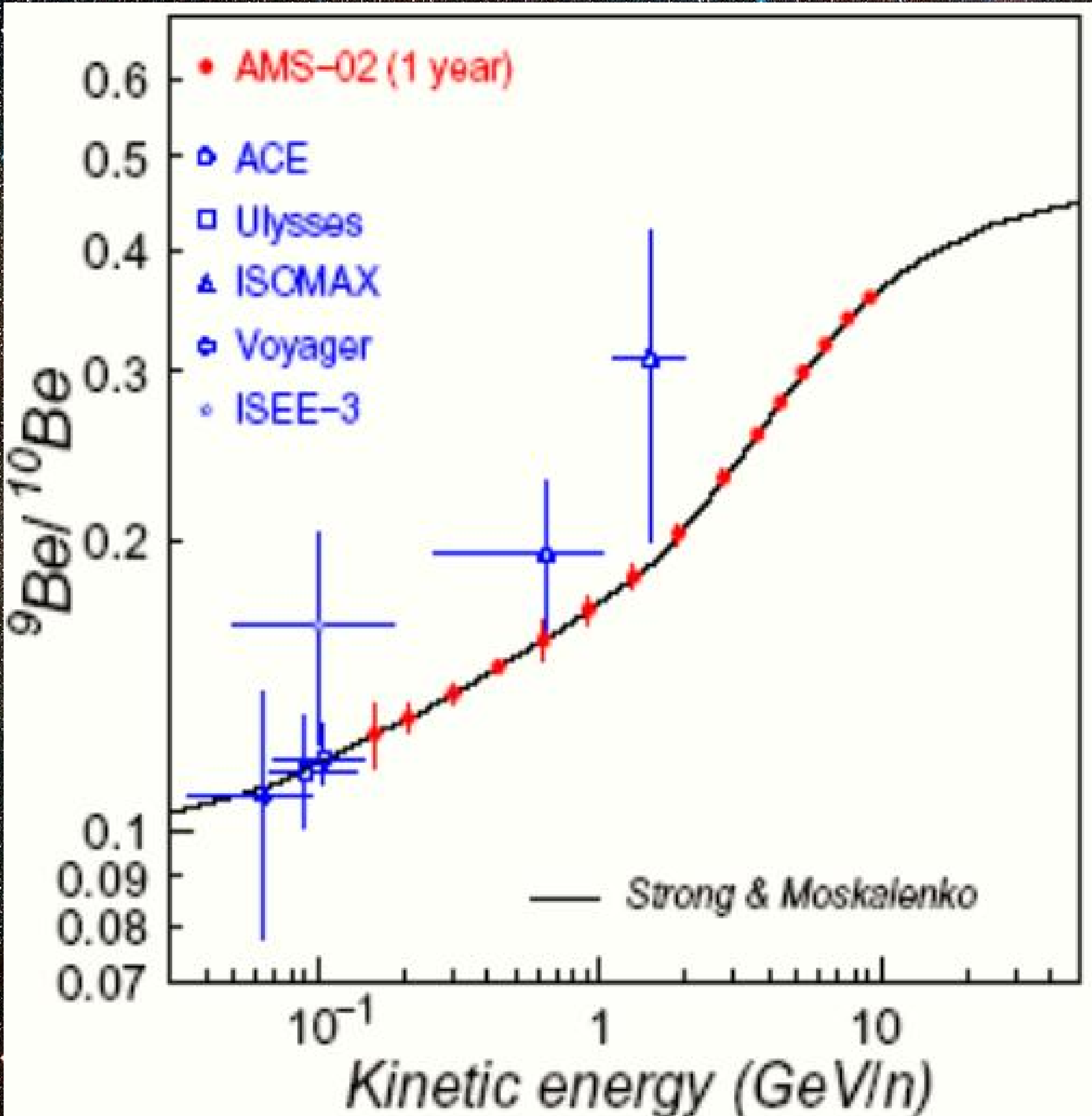

Beryllium measurements. The expected AMS-02 one year statistics is also shown assuming a model by Strong and Moskalenko.

[**Reference**: D. Casadei (for the AMS Collaboration), "Cosmic ray astrophysics with AMS-02," astro-ph/0404529.]

Around the knee
(“poly-gonato”[a] model by Jorg Hörandel[b])

Little bit outdated but still ideologically interesting

The Poly-Gonato Model (PGM) is an empirical model to systematize and fit the data on primary spectra of all CR nuclei at high energies. It is assumed that the cutoff energy for each individual element depends on its charge Z. The following ansatz is adopted to describe the energy dependence of the flux for particles with charge Z.

$$F_Z(E) = \Phi_Z^0 E^{\gamma_Z} \left[1 + \left(\frac{E}{E_Z} \right)^{\epsilon_c} \right]^{\frac{\gamma_c - \gamma_Z}{\epsilon_c}}$$

The absolute flux normalization, Φ_Z^0 and the spectral index γ_Z quantify the power law. The flux above the cutoff energy is modeled by a second and steeper power law. Parameters γ_c and ϵ_c characterize the change in the spectrum at the cutoff energy E_Z. Both parameters are assumed to be identical for all spectra, γ_c being the hypothetical slope beyond the knee and ϵ_c describes the smoothness of the transition from the first to the second power law.

Cf. 2020 Bartol spline model

[a] Greek “many knees”.
[b] **Reference**: J. R. Hörandel, Astropart. Phys. 19 (2003) 193.

Z		Φ_Z^0	$-\gamma_Z$	Z		Φ_Z^0	$-\gamma_Z$	Z		Φ_Z^0	$-\gamma_Z$
1[2]	H	$8.73 \cdot 10^{-2}$	2.71	32[4]	Ge	$4.02 \cdot 10^{-6}$	2.54	63[4]	Eu	$1.58 \cdot 10^{-7}$	2.27
2[2]	He	$5.71 \cdot 10^{-2}$	2.64	33[4]	As	$9.99 \cdot 10^{-7}$	2.54	64[4]	Gd	$6.99 \cdot 10^{-7}$	2.25
3[3]	Li	$2.08 \cdot 10^{-3}$	2.54	34[4]	Se	$2.11 \cdot 10^{-6}$	2.53	65[4]	Tb	$1.48 \cdot 10^{-7}$	2.24
4[3]	Be	$4.74 \cdot 10^{-4}$	2.75	35[4]	Br	$1.34 \cdot 10^{-6}$	2.52	66[4]	Dy	$6.27 \cdot 10^{-7}$	2.23
5[3]	B	$8.95 \cdot 10^{-4}$	2.95	36[4]	Kr	$1.30 \cdot 10^{-6}$	2.51	67[4]	Ho	$8.36 \cdot 10^{-8}$	2.22
6[3]	C	$1.06 \cdot 10^{-2}$	2.66	37[4]	Rb	$6.93 \cdot 10^{-7}$	2.51	68[4]	Er	$3.52 \cdot 10^{-7}$	2.21
7[3]	N	$2.35 \cdot 10^{-3}$	2.72	38[4]	Sr	$2.11 \cdot 10^{-6}$	2.50	69[4]	Tm	$1.02 \cdot 10^{-7}$	2.20
8[3]	O	$1.57 \cdot 10^{-2}$	2.68	39[4]	Y	$7.82 \cdot 10^{-7}$	2.49	70[4]	Yb	$4.15 \cdot 10^{-7}$	2.19
9[3]	F	$3.28 \cdot 10^{-4}$	2.69	40[4]	Zr	$8.42 \cdot 10^{-7}$	2.48	71[4]	Lu	$1.72 \cdot 10^{-7}$	2.18
10[3]	Ne	$4.60 \cdot 10^{-3}$	2.64	41[4]	Nb	$5.05 \cdot 10^{-7}$	2.47	72[4]	Hf	$3.57 \cdot 10^{-7}$	2.17
11[3]	Na	$7.54 \cdot 10^{-4}$	2.66	42[4]	Mo	$7.79 \cdot 10^{-7}$	2.46	73[4]	Ta	$2.16 \cdot 10^{-7}$	2.16
12[3]	Mg	$8.01 \cdot 10^{-3}$	2.64	43[4]	Tc	$6.98 \cdot 10^{-8}$	2.46	74[4]	W	$4.16 \cdot 10^{-7}$	2.15
13[3]	Al	$1.15 \cdot 10^{-3}$	2.66	44[4]	Ru	$3.01 \cdot 10^{-7}$	2.45	75[4]	Re	$3.35 \cdot 10^{-7}$	2.13
14[3]	Si	$7.96 \cdot 10^{-3}$	2.75	45[4]	Rh	$3.77 \cdot 10^{-7}$	2.44	76[4]	Os	$6.42 \cdot 10^{-7}$	2.12
15[3]	P	$2.70 \cdot 10^{-4}$	2.69	46[4]	Pd	$5.10 \cdot 10^{-7}$	2.43	77[4]	Ir	$6.63 \cdot 10^{-7}$	2.11
16[3]	S	$2.29 \cdot 10^{-3}$	2.55	47[4]	Ag	$4.54 \cdot 10^{-7}$	2.42	78[4]	Pt	$1.03 \cdot 10^{-6}$	2.10
17[3]	Cl	$2.94 \cdot 10^{-4}$	2.68	48[4]	Cd	$6.30 \cdot 10^{-7}$	2.41	79[4]	Au	$7.70 \cdot 10^{-7}$	2.09
18[3]	Ar	$8.36 \cdot 10^{-4}$	2.64	49[4]	In	$1.61 \cdot 10^{-7}$	2.40	80[4]	Hg	$7.43 \cdot 10^{-7}$	2.08
19[3]	K	$5.36 \cdot 10^{-4}$	2.65	50[4]	Sn	$7.15 \cdot 10^{-7}$	2.39	81[4]	Ti	$4.28 \cdot 10^{-7}$	2.06
20[3]	Ca	$1.47 \cdot 10^{-3}$	2.70	51[4]	Sb	$2.03 \cdot 10^{-7}$	2.38	82[4]	Pb	$8.06 \cdot 10^{-7}$	2.05
21[3]	Sc	$3.04 \cdot 10^{-4}$	2.64	52[4]	Te	$9.10 \cdot 10^{-7}$	2.37	83[4]	Bi	$3.25 \cdot 10^{-7}$	2.04
22[3]	Ti	$1.14 \cdot 10^{-3}$	2.61	53[4]	I	$1.34 \cdot 10^{-7}$	2.37	84[4]	Po	$3.99 \cdot 10^{-7}$	2.03
23[3]	V	$6.31 \cdot 10^{-4}$	2.63	54[4]	Xe	$5.74 \cdot 10^{-7}$	2.36	85[4]	At	$4.08 \cdot 10^{-8}$	2.02
24[3]	Cr	$1.36 \cdot 10^{-3}$	2.67	55[4]	Cs	$2.79 \cdot 10^{-7}$	2.35	86[4]	Rn	$1.74 \cdot 10^{-7}$	2.00
25[3]	Mn	$1.35 \cdot 10^{-3}$	2.46	56[4]	Ba	$1.23 \cdot 10^{-6}$	2.34	87[4]	Fr	$1.78 \cdot 10^{-8}$	1.99
26[2]	Fe	$2.04 \cdot 10^{-2}$	2.59	57[4]	La	$1.23 \cdot 10^{-7}$	2.33	88[4]	Ra	$7.54 \cdot 10^{-8}$	1.98
27[3]	Co	$7.51 \cdot 10^{-5}$	2.72	58[4]	Ce	$5.10 \cdot 10^{-7}$	2.32	89[4]	Ac	$1.97 \cdot 10^{-8}$	1.97
28[3]	Ni	$9.96 \cdot 10^{-4}$	2.51	59[4]	Pr	$9.52 \cdot 10^{-8}$	2.31	90[4]	Th	$8.87 \cdot 10^{-8}$	1.96
29[4]	Cu	$2.18 \cdot 10^{-5}$	2.57	60[4]	Nd	$4.05 \cdot 10^{-7}$	2.30	91[4]	Pa	$1.71 \cdot 10^{-8}$	1.94
30[4]	Zn	$1.66 \cdot 10^{-5}$	2.56	61[4]	Pm	$8.30 \cdot 10^{-8}$	2.29	92[4]	U	$3.54 \cdot 10^{-7}$	1.93
31[4]	Ga	$2.75 \cdot 10^{-6}$	2.55	62[4]	Sm	$3.68 \cdot 10^{-7}$	2.28				

Absolute flux [(m sr s TeV) $^{-1}$] at E_0 = 1 TeV/nucleus and spectral index of CR elements. (2) from PGM; (3) from **B. Wiebel-Soth et al**., Astron. Astrophys. **330** (1998) 389; (4) from PGM after an extrapolation for ultra-heavy elements.

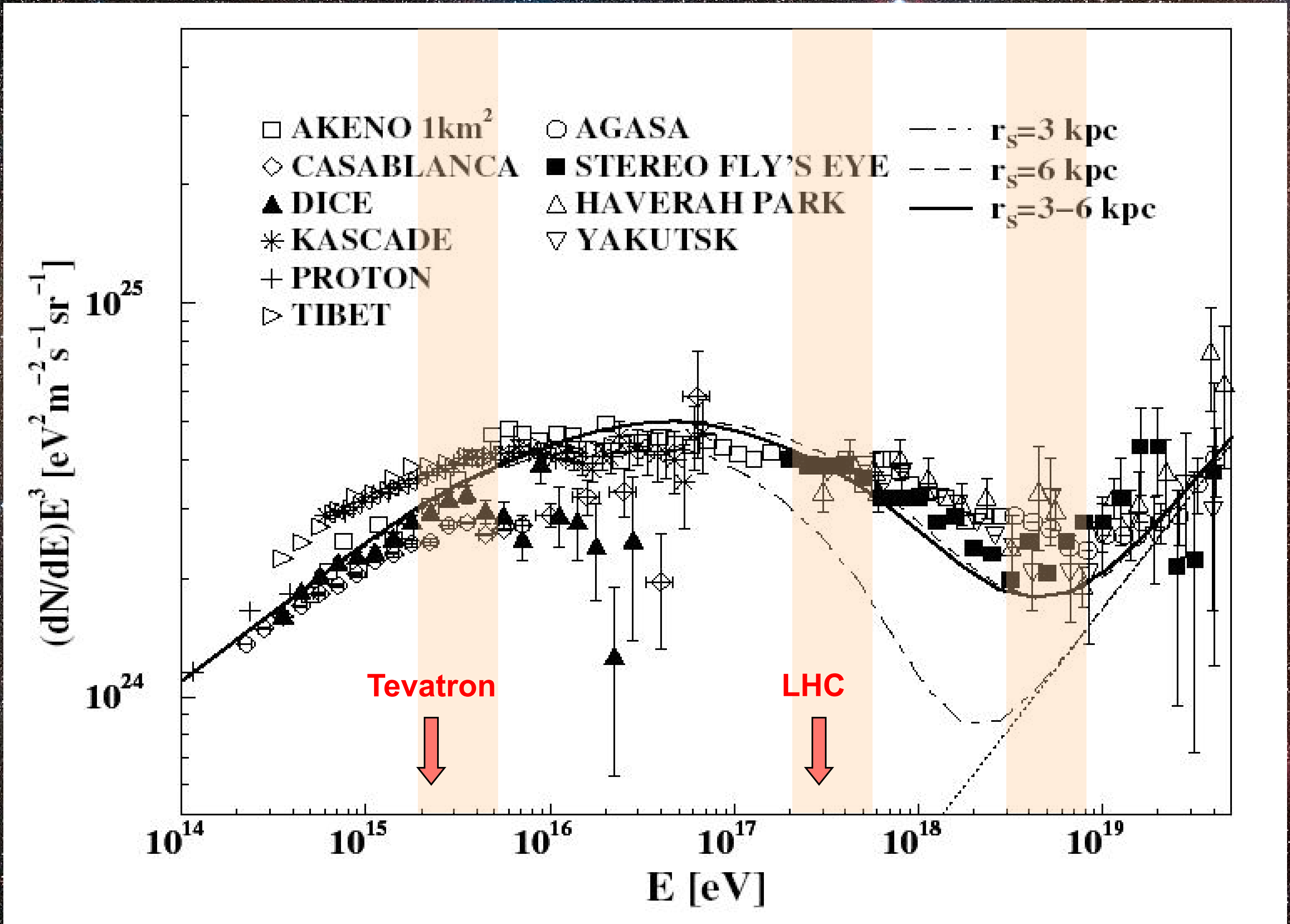

Comparison with several models from J. Candia, S. Mollerach, and E. Roulet, JCAP 05 (2003) 003 [astro-ph/0302082]. The dotted straight line corresponds to an *ad-hoc* isotropic extragalactic component with a power-law spectrum.

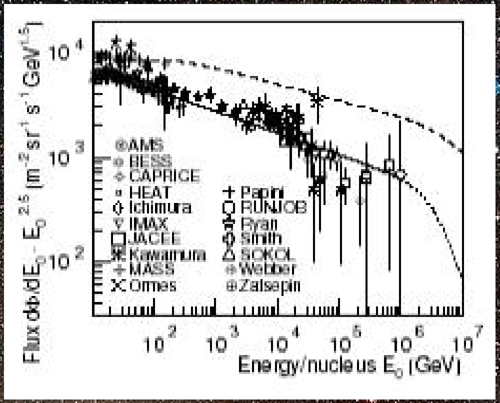

Differential energy spectrum for **protons**. The best fit to the spectrum according to a power law is represented by the solid line, the bend (dotted line) is obtained from a fit to the all-particle spectrum.

←

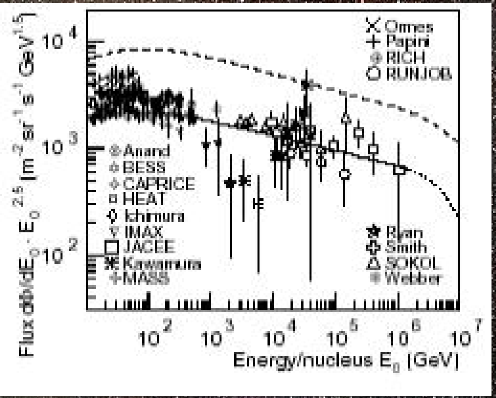

Differential energy spectrum for **helium nuclei**. The best fit to the spectrum according to a power law is represented by the solid line, the bend (dotted line) is obtained from a fit to the all-particle spectrum.

←

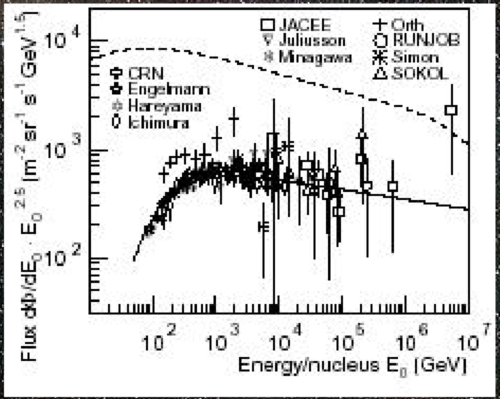

Differential energy spectrum for **iron nuclei**. The best fit to the spectrum is represented by the solid line.

←

In all 3 figures, the all-particle spectra are shown as dashed lines for reference.

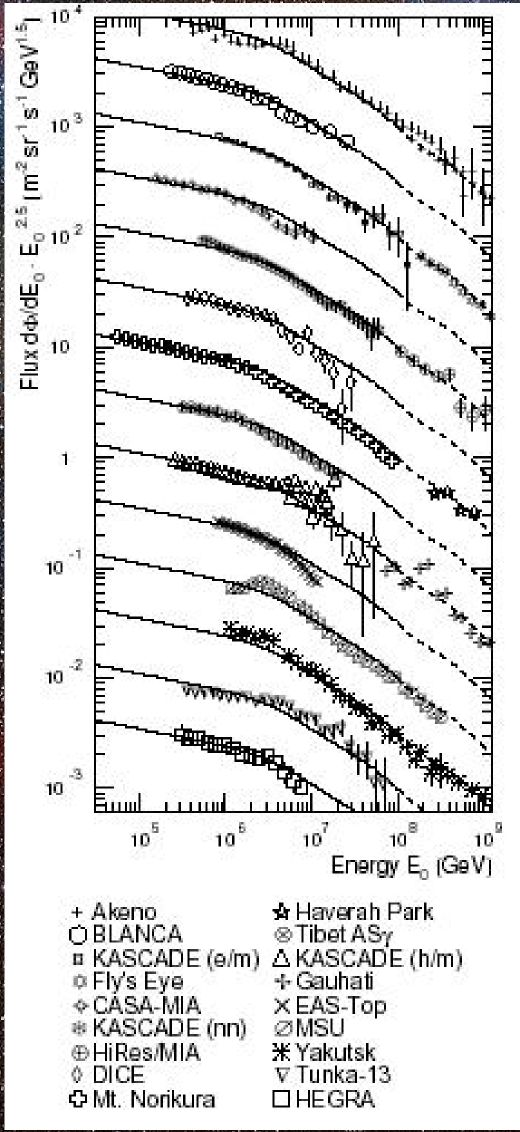

Normalized all-particle energy spectra for individual experiments compared to one of the PGM. The individual results are shifted in steps of half a decade in flux in order to reduce overlap.

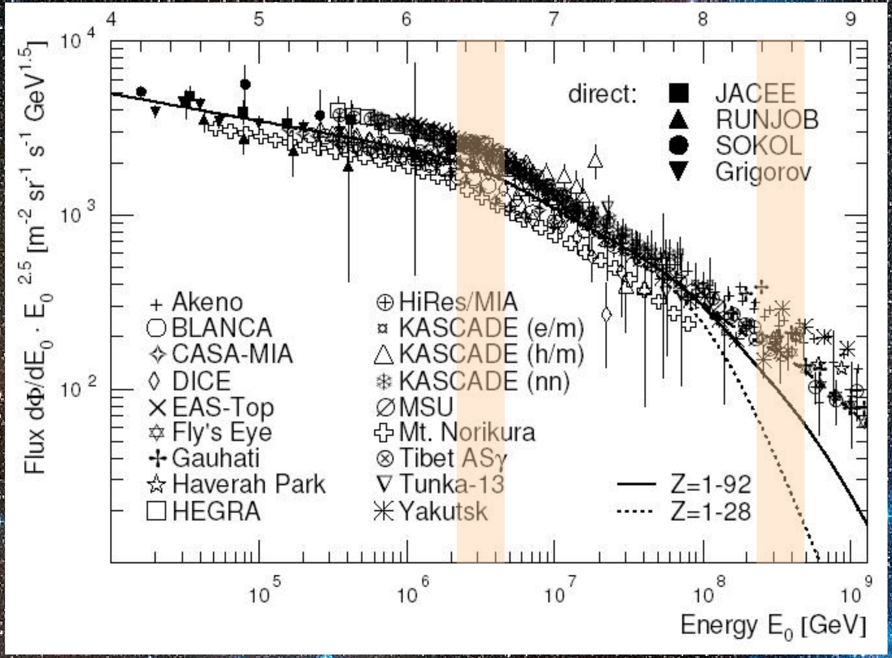

All-particle energy spectra obtained from direct and indirect measurements.

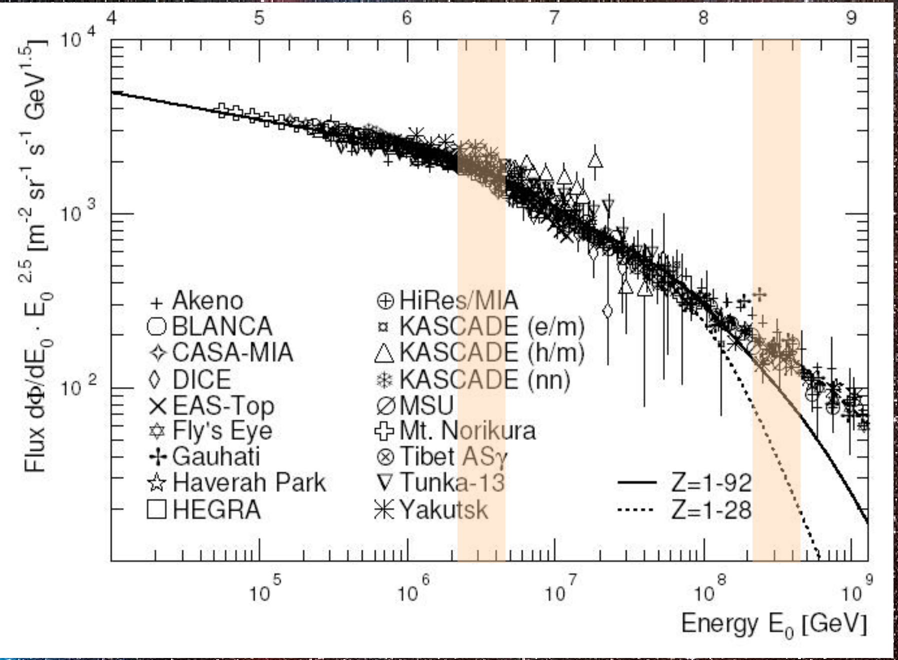

Normalized all-particle energy spectra for Individual experiments.

In both figures, the sum spectra for individual elements according to the poly-gonato model are represented by the dotted line for **$1 \leq Z \leq 28$** and by the solid line for **$1 \leq Z \leq 92$**. Above **10^8 GeV** the dashed line reflects the average spectrum.

Conclusion: The knee is explained as the subsequent cutoffs of the individual elements of the galactic component, starting with protons. The second knee seems to indicate the end of the stable elements of the galactic component.

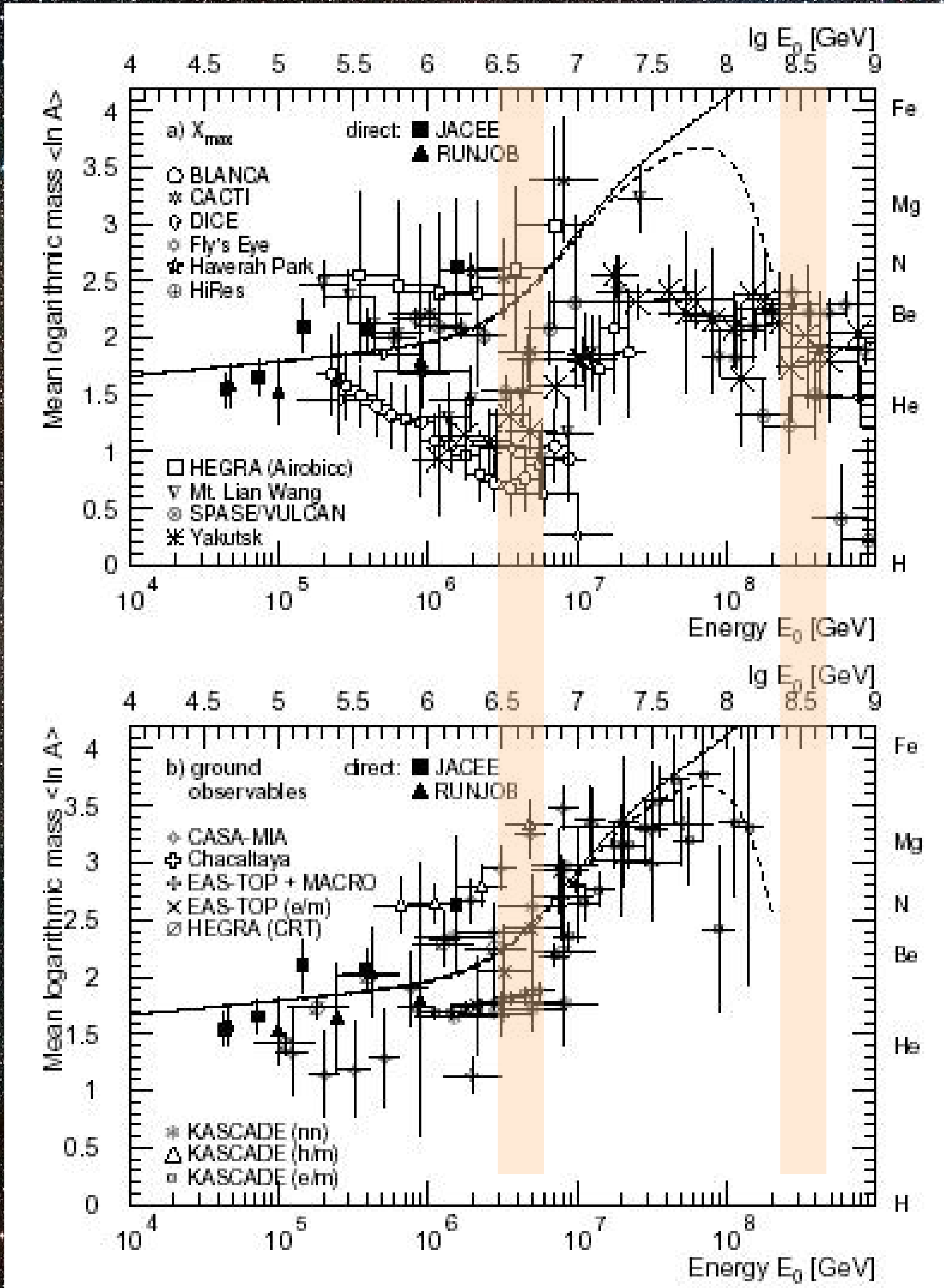

Mean logarithmic mass vs. primary energy.

Results from the average depth of the shower maximum X_{max} using CORSIKA/QGSJET simulations.

Results from measurements of distributions for electrons, muons, and hadrons at ground level.

Results from the balloon experiments JACEE and RUNJOB are given as well. Predictions according to the PGM are represented by the solid lines. The dashed lines are obtained by introducing an *ad-hoc* component of hydrogen only.

Conclusion: The mass composition calculated with the PGM is in good agreement with results from EAS experiments measuring the electromagnetic, muonic and hadronic components at ground level. But the mass composition disagrees with results from experiments measuring the average depth of the shower maximum with Cherenkov and fluorescence detectors. If we believe the model we may conclude that **<ln A> increases around and above the knee.**

State of the Art — 2019: UHECR anisotropy

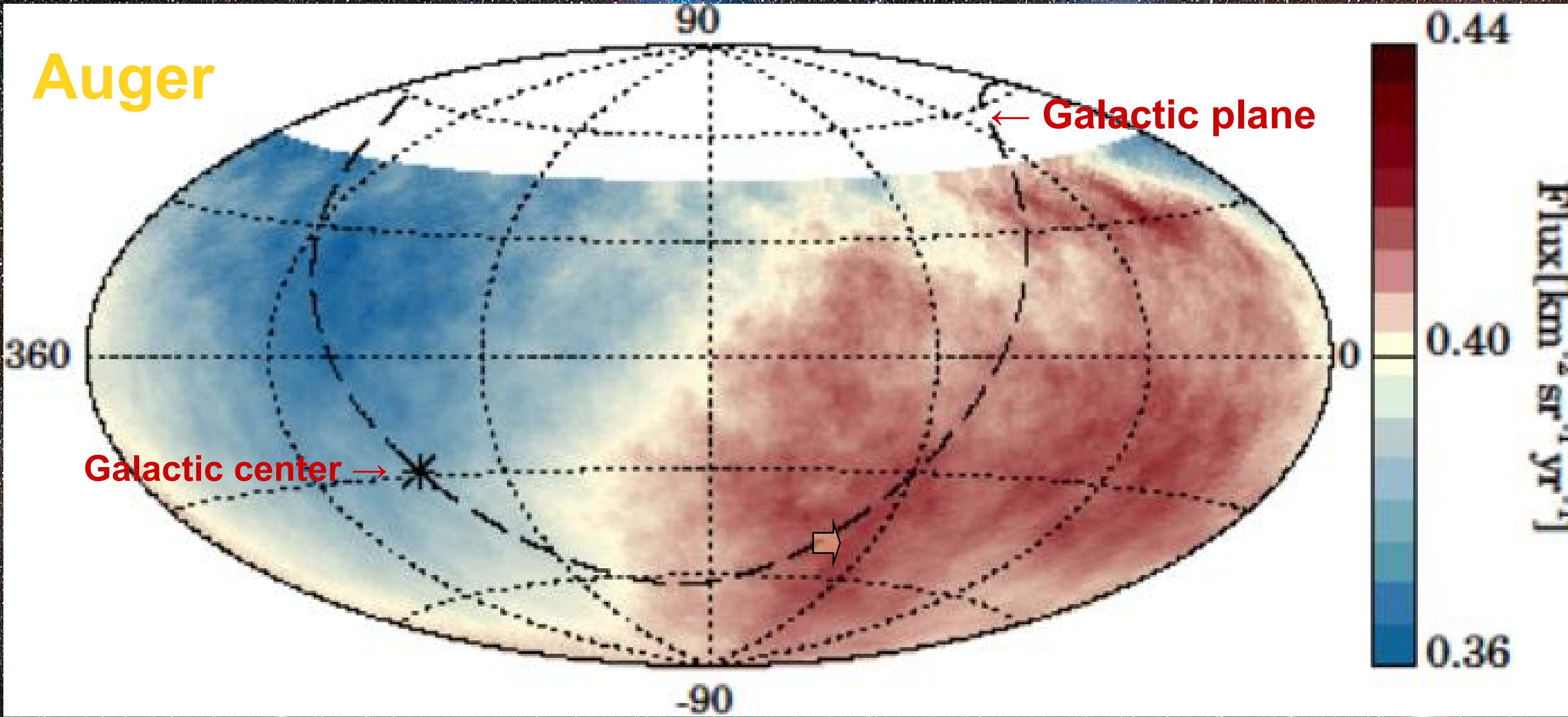

The CR flux above 8 EeV, averaged on top-hat windows of 45° radius (equatorial coordinates).

Under the assumption that higher multipoles are negligible, Auger Collaboration founds a total dipolar amplitude for $E \geq 8$ EeV of $d = 0.066 \pm 0.012$, pointing ~ 125° away from the direction of the Galactic center, as such indicating an extragalactic origin of the modulation. A combined analysis of the Pierre Auger and Telescope Array collaborations is consistent with that obtained by Auger alone, with smaller uncertainties when allowing for non-vanishing quadrupole moments..

[**Reference:** A. Castellina, "Highlights from the Pierre Auger Observatory", PoS(ICRC2019)004, arXiv:909.10791 [astro-ph.HE]]

LIS of CR electrons and positrons[a]

The CR spectra $F_a(E,r,t)$ or $F_a(R,r,t)$ measured in the Solar System are in general some functionals of the Local Interstellar Spectra (LIS). For example, in the spherical isotropic model of cosmic ray diffusion through the heliosphere,[b] the relation is

$$F_a(R,r,t) = \left[\frac{R}{R_a(t)}\right]^2 F_a^{\mathsf{LI}}(R_a(t)),$$

where $F_a^{\mathsf{LI}}(R)$ is the LIS (assumed to be isotropic and time-independent),

$$R_a(t) = \frac{1}{Z_a|e|}\sqrt{[E+\Delta E_a(t)]^2 - m_a^2}$$

is the local interstellar rigidity of the particle a and

$$\Delta E_a(t) = Z_a|e|\phi_a(t)$$

is the energy lost by the particles during their travel, which is proportional to the solar modulation parameter, $\phi_a(t)$. This parameter can be expressed as function of the diffusion coefficient and the solar wind velocity, even though usually it is considered a free parameter to be measured.

[a] Here we will mainly follow to D. Casadei and V. Bindi, astro–ph/0302307.

[b] E. N. Parker, Planet. Space Sci. **13** (1965) 9; L. J. Gleeson and W. I. Axford, ApJ **149** (1967) L115; ApJ **154** (1968) 1011.

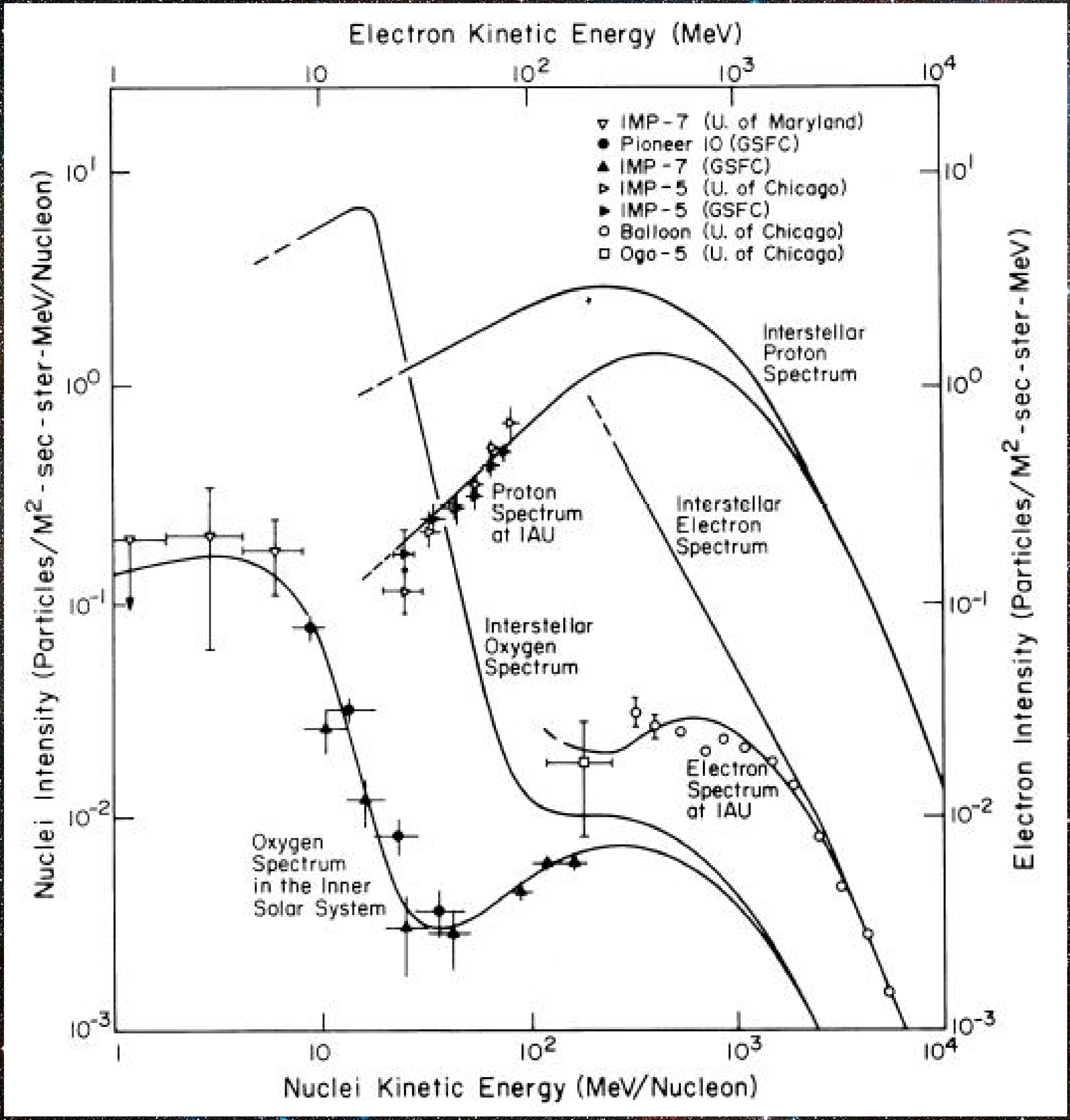

A numerical solution to the Parker-Gleeson-Axford equation for modulated spectra of protons, electrons, and oxygen.

The particles undergo a diffusive-like propagation in which trapping between time-varying constituents in the interplanetary magnetic field controls the particle motion.

[**Reference**: L. Fisk, "Solar modulation and a galactic origin for the anomalous component observed in low-energy cosmic rays", ApJ **206** (1976) 333-341.]

Direct Measurements of Cosmic Ray Electrons and Positrons

Measurement	Year	ϕ (MV)	Sun Polarity	e^-/e^+ Separation	E_{min} (GeV)	E_{max} (GeV)	References e^-	References e^+	References p^+	Notes
Fanselow et al. (1969)	1965, 1966	570(50)	−	Y	0.07	11.0	1	1	...	a
Nishimura et al. (1980)	1968–1975	700(200)	−, +	N	30.0	1500	2	...	...	a
Meegan & Earl (1975)	1969, 1973	650(100)	+	N	6.4	114	3	...	...	a
Buffington et al. (1975)	1972, 1973	650(50)	+	Y	5.1	63.0	4	4	...	a
Prince (1979)	1975	550(50)	+	N	10.2	202	5	...	...	a
Golden et al. (1984, 1987)	1976	500(50)	+	Y	3.45	91.7	6	7	...	a
Tang (1984)	1980	900(200)	+	N	4.89	200	8	...	...	a
MASS 89	1989	1400(50)	−	Y	1.6	16.1	9	9	10	b
MASS 91	1991	2000(200)	+	Y	7.5	46.9	11	11	12	b
CAPRICE 94	1994	664(5)	+	Y	0.54	34.3	13	13	14	b
HEAT 94	1994	650(50)	+	Y	5.45	66.4	15	15	...	c
HEAT 95	1995	550(50)	+	Y	1.20	66.4	15	15	...	a
Nishimura et al. (2001)	1996, 1998	600(100)	+	N	30.0	3000	16	...	...	a, c
BETS 97+98	1997, 1998	600(100)	+	N	13.9	112.6	17	...	...	a, c
AMS 98	1998	632(13)	+	Y	0.15	35.7	18	18	19	b

Notes.—The value of the solar modulation parameter ϕ was estimated using: (a) neutron rates; (b) the proton spectrum measured by the same detector; and (c) the proton spectrum measured by a different detector in the same period. Positive and negative solar polarities refer to epochs when the magnetic field emerging from the north pole of the Sun points outward and inward, respectively (Bieber et al. 1999). The energy range is reported for electrons only.

References.—(1) Fanselow et al. 1969; (2) Nishimura et al. 1980; (3) Meegan & Earl 1975; (4) Buffington et al. 1975; (5) Prince 1979; (6) Golden et al. 1984; (7) Golden et al. 1987; (8) Tang 1984; (9) Golden et al. 1994; (10) Webber et al. 1991; (11) Grimani et al. 2002; (12) Bellotti et al. 1999; (13) Boezio et al. 2000; (14) Boezio et al. 1999; (15) Du Vernois et al. 2001; (16) Nishimura et al. 2001; (17) Torii et al. 2001; (18) Alcaraz et al. 2000a; (19) Alcaraz et al. 2000b.

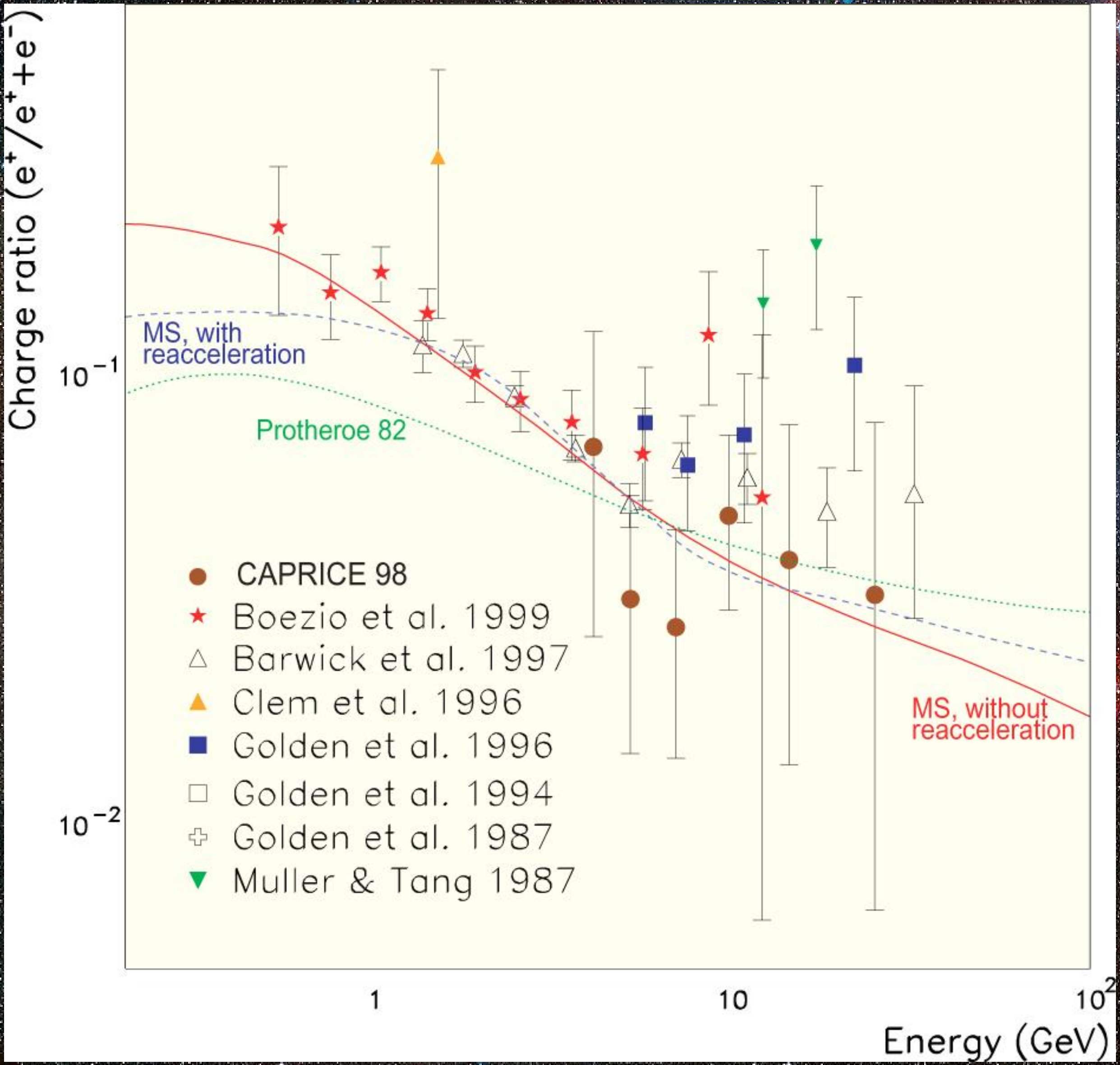

The positron fraction as a function of energy measured by CAPRICE 98 (closed circles) and several other experiments. The dotted line is the secondary positron fraction calculated by R.J. Protheroe [ApJ **254** (1982) 391], the dashed and solid lines are the secondary positron fraction calculated by I.V. Moskalenko and A.W. Strong [ApJ **493** (1998) 694] with and without reacceleration of cosmic rays, respectively.

Note: These data are not included into the fit under discussion.

[**Reference:** M. Boezio et al. (WiZard-CAPRICE98 Collaboration), ICRC'26,OG.1.1.16.]

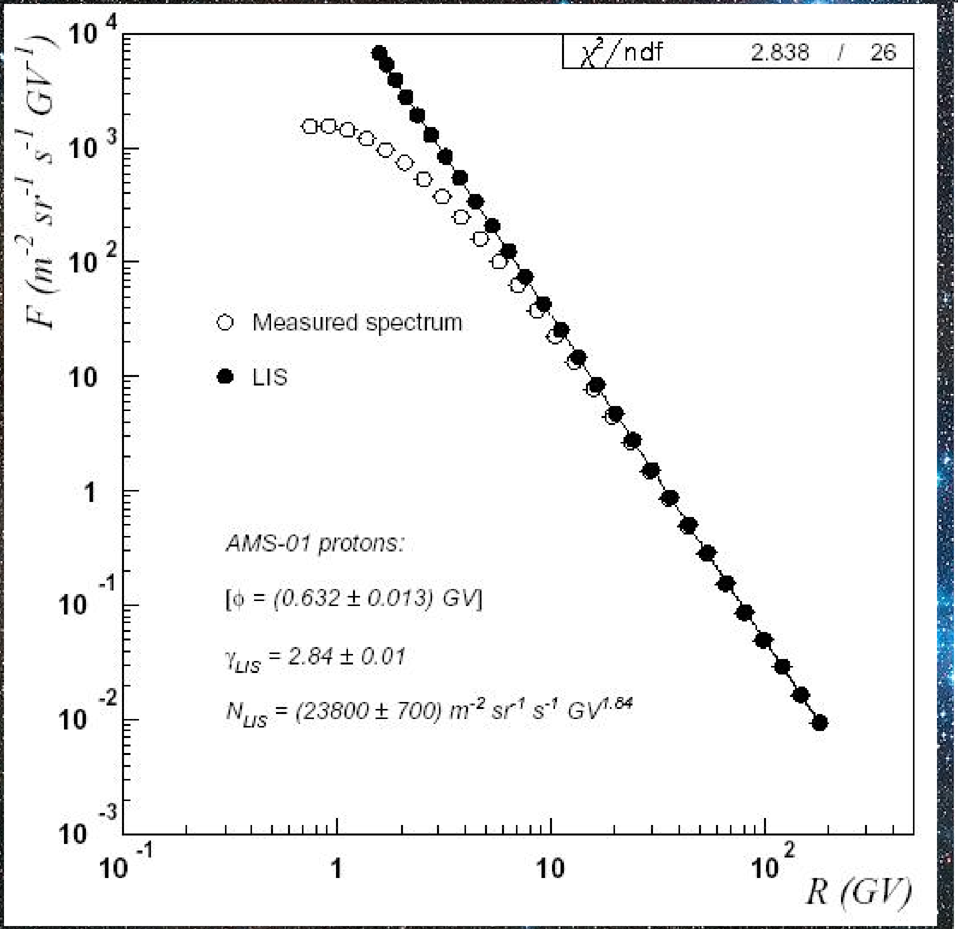

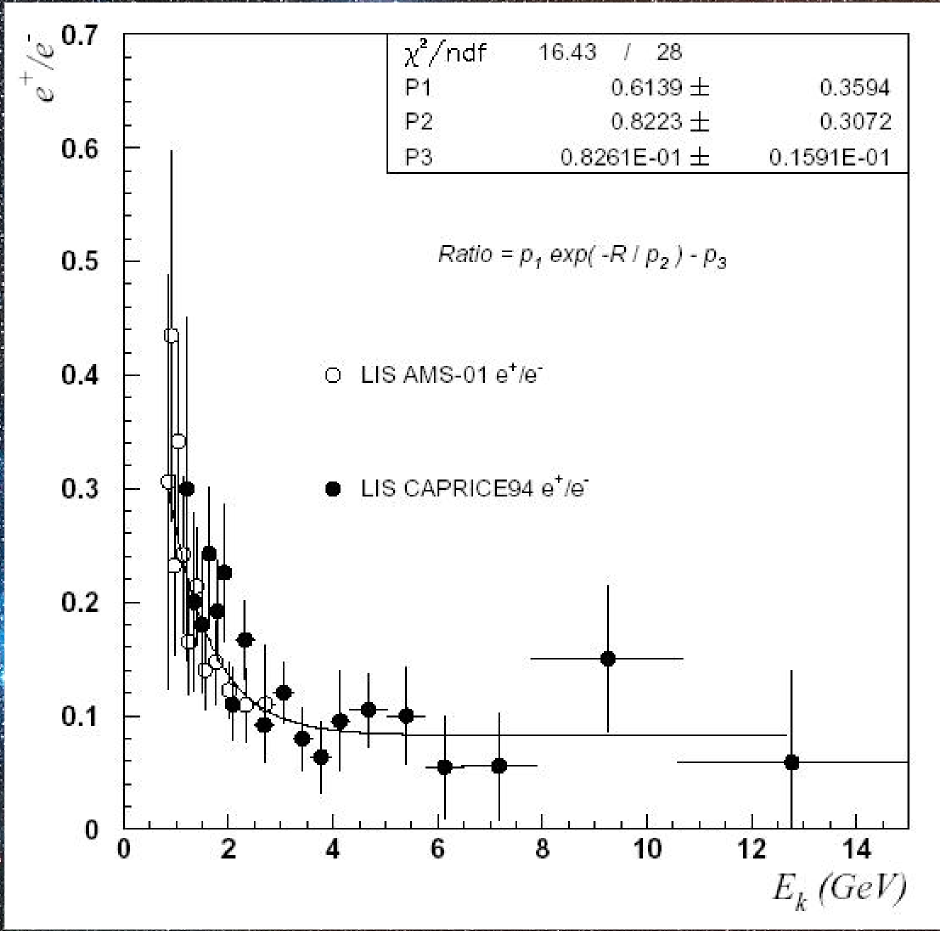

Measured and local interstellar flux of AMS-01 protons.

Local interstellar **e^+/e^- ratio** measured by AMS-01 and CAPRICE 94.

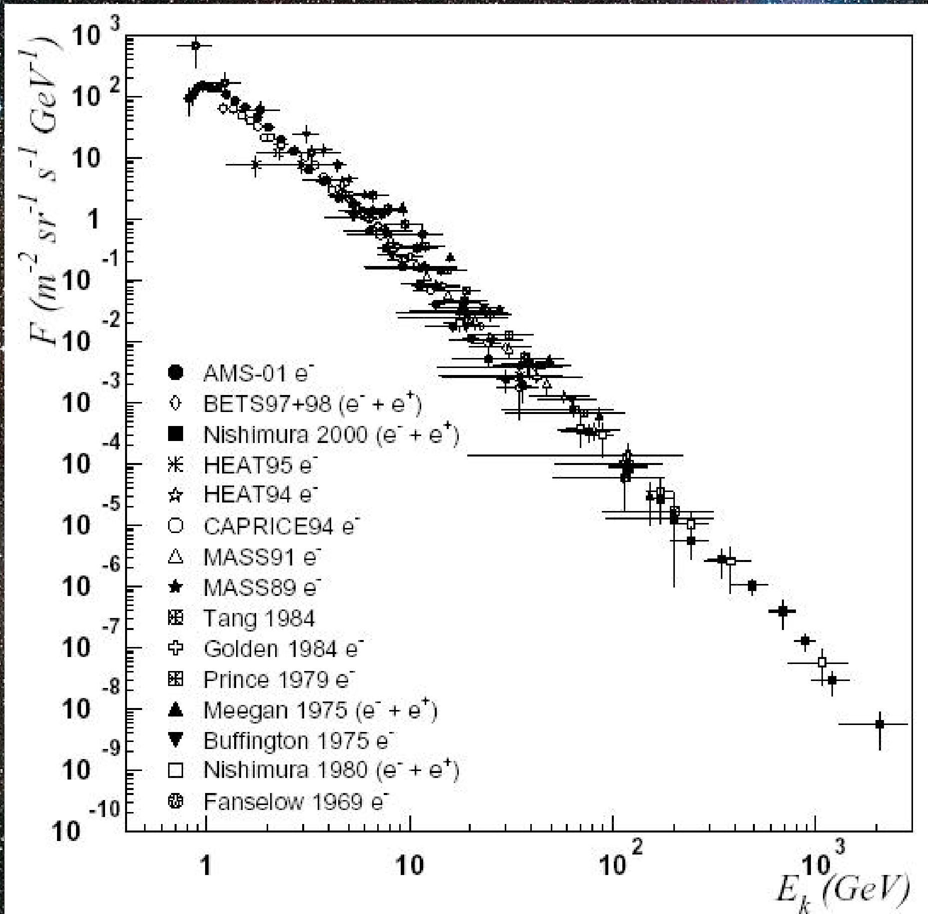

LIS of **e+** and **e-** measured by all considered experiments.

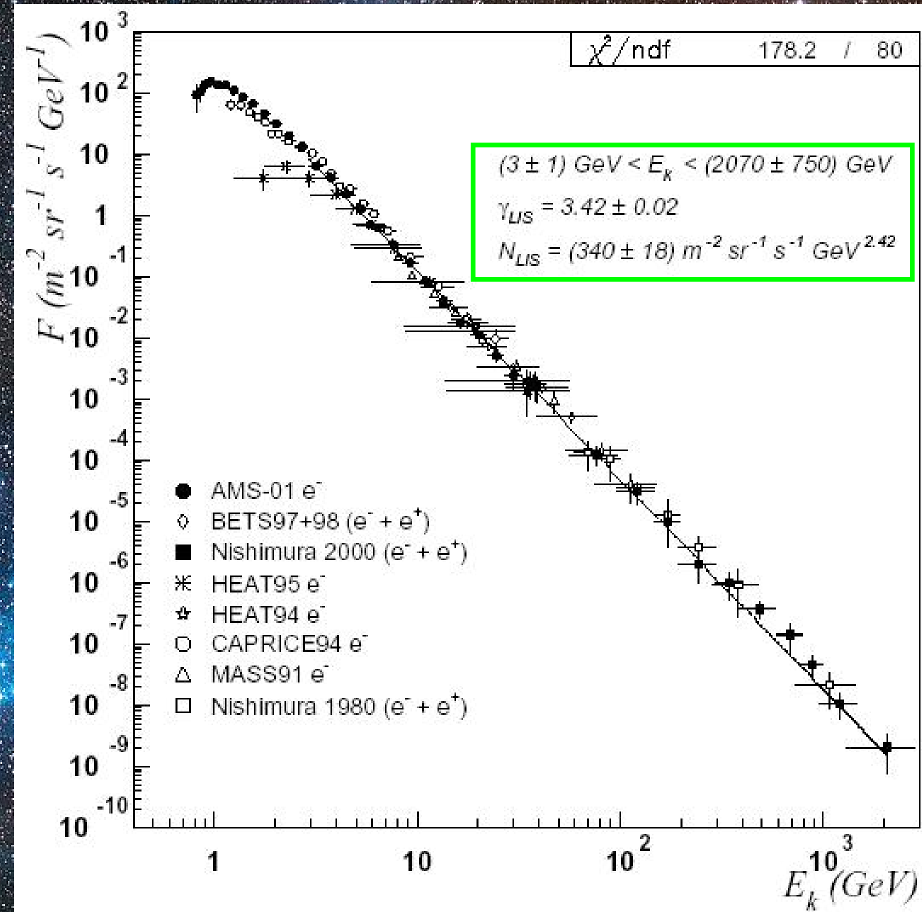

LIS of **e+** and **e-** measured by all considered experiments, after renormalization to the AMS-01 and CAPRICE 94 flux at 20 GeV, with a single power-law fit.

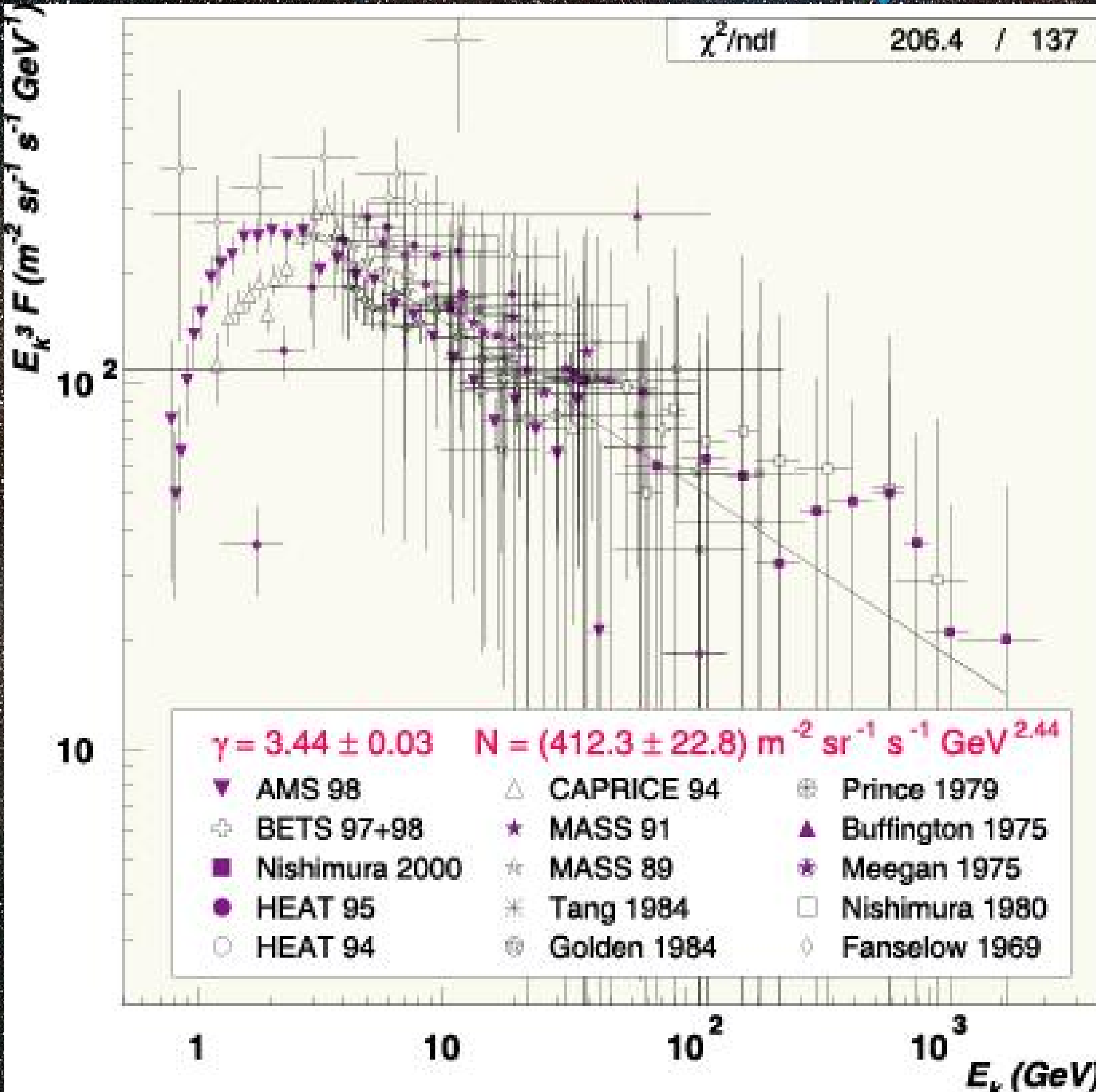

The final (published) result: the single power-law fit of the electron Local Interstellar Spectrum (multiplied by E_k^3), after the rescaling.

The obtained spectral index is 3.44 +/- 0.03 between ~3 GeV and ~2 TeV.

[**Reference**: D. Casadei & V. Bindi, "The origin of cosmic ray electrons and positrons," ApJ **612** (2004) 262-267.]

Note: This published version is formally more accurate in comparison with the e-print one. If true, the analysis suggests that the experimental data are self-contradictory and cannot be described by a single power law.